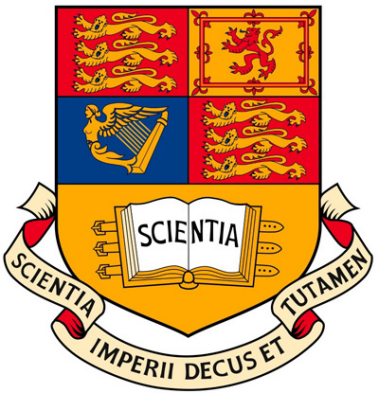
Nonlinear wave interactions with multiple bodies in close proximity

Milena Perić



Department of Civil and Environmental Engineering

Thesis submitted for the degree of Doctor of Philosophy of the University of London and for the Diploma of Imperial College

Declaration of originality

All the work presented in this thesis is that of the author.

Any work or contributions made by others is referenced appropriately.

Abstract

This thesis describes the interaction of waves with multiple bodies in close proximity. The case of two-dimensional fixed bodies is first considered, where large wave excitation is found to occur within the gap between the two bodies at the so-called resonance frequency. The width of the gap is identified as the most important factor in determining this frequency; an increase in the gap width leading to a decrease in the resonance frequency. Subsequently, the effect of the motion of one of the bodies (with a single degree of freedom) is investigated using a newly developed floating-body application of the boundary element method. In the floating-body case, the resonance frequency is found be higher than in the fixed-body equivalent. In addition, a large amplification of the nonlinear water surface elevation within the gap is identified.

In order to determine whether the observations within the two-dimensional study can be applied to the practical case of side-by-side offloading of Liquid Natural Gas (LNG), similar investigations are undertaken in a three-dimensional analysis. The latter involves both numerical and experimental studies. The three-dimensional studies confirm the effects identified in the two-dimensional analysis; specifically the effects of the gap width, the motion of one of the bodies, and the nonlinear effects arising within the gap are all clearly established. Furthermore, consideration of both beam-sea and head-sea incident wave conditions eliminates the orientation of the bodies relative to the incident wave direction as a key factor in determining the resonance frequency. Finally, consideration of the motion of the bodies shows that some unexpected higher order motion of the moored body arises when the two bodies have significantly different hydrodynamic properties. As a result, it is concluded that the numerical modelling of side-by-side offloading must be fully nonlinear, incorporate the body motion and include the forcing of the fenders and the mooring lines.

Acknowledgements

I would like thank Prof. Chris Swan for his support and guidance. Through being a part of his research group, I have achieved many things I would never have thought possible.

I would also like to thank Eirini, Johannes, Marios, Latheef, Livio and John for making the lab a unique working environment. Special thanks go to Stuart for his patience in showing me that I can always do better. Thanks go to Becky, Tony, Bill and Dave for being helpful and getting things made and set up, taken down and then set up again. I would also like to thank my non-lab friends for their understanding of my PhD ways and for including me in their real-world lives.

Above all, I would like to thank my family whose ability as my safety net has been truly tested throughout this PhD. I could not have done this without you and it would have been pointless if there was noone to tease me about being an Imperial geek.

Contents

1 Overview **19**

1.1 Introduction 19

1.2 Aims 19

1.3 Motivation 20

1.4 Practical applications 21

1.5 Approach to the solution 23

1.5.1 Numerical study 23

1.5.2 Experimental study 25

1.6 Layout of thesis 26

1.7 Achievements 27

2 Theoretical Background **29**

2.1 Introduction 29

2.2 Governing equations 30

2.3 Boundary conditions and analytical solutions 30

2.3.1 Linear regular wave theory 30

2.3.2 The boundary condition on a moving rigid body 32

2.3.3 Wave maker theory 34

2.4 The Boundary Element Method 36

2.4.1 Boundary integral equation 37

2.4.2 Double nodes 39

2.4.3 Discontinuous elements 39

2.4.4 Multiple-flux BEM 40

2.5 Calculating force and body motion 44
2.5.1 Backwards finite difference 47
2.5.2 The Isaacson Method 47
2.5.3 Acceleration potential 50
2.5.4 The Indirect Method 51
2.6 Conclusions 54

3 Model validation **56**
3.1 Introduction 56
3.2 Validation of forced motions 58
3.2.1 Wave maker theory 58
3.2.2 Radiation of a rectangular body 67
3.3 Validation of force calculations 71
3.3.1 The numerical domain 72
3.3.2 Comparison of forces 73
3.4 Validation of the hydrodynamic properties 75
3.4.1 Experimental setup 75
3.4.2 Comparison of decay tests 77
3.5 Validation of wave-induced motion 80
3.5.1 Heave only motion 82
3.5.2 Pitch only motion 87
3.6 Conclusions 90

4 Two-dimensional analysis of fixed bodies in close proximity **92**
4.1 Introduction 92
4.2 Background 94
4.3 The numerical model 95
4.3.1 The numerical wave tank 96
4.3.2 Numerical results 98
4.4 Single fixed body of finite draft 99
4.5 Two fixed bodies in close proximity 103

4.5.1 Definition of cases . . . 103
4.5.2 The effect of incident wave frequency . . . 105
4.5.3 The effect of gap width . . . 113
4.5.4 The effect of the LNG beam . . . 116
4.5.5 The effect of draft . . . 118
4.5.6 The effect of transmission . . . 118
4.5.7 Summary of resonance frequency results . . . 124
4.6 The validity of the fixed-body simplification . . . 126
4.6.1 The first harmonic wave field . . . 126
4.6.2 The first harmonic body motion . . . 131
4.6.3 The nonlinear wave field within the gap . . . 135
4.7 Conclusions . . . 136

5 Three-dimensional analysis of fixed bodies 139
5.1 Introduction . . . 139
5.2 The multiple-flux boundary element method . . . 142
5.2.1 Governing equations . . . 142
5.2.2 Boundary conditions . . . 143
5.2.3 Discretisation . . . 146
5.2.4 Time-marching the solution . . . 147
5.2.5 Outputs . . . 148
5.3 Validation of the 3D wave field surrounding a fixed body . . . 149
5.3.1 Comparisons to theoretical solutions for a semi-infinite breakwater . . . 149
5.3.2 Comparisons to experimental data involving a bottom-mounted GBS . . . 153
5.4 3D wave interaction with fixed bodies . . . 159
5.4.1 Wave field surrounding a single fixed body . . . 160
5.4.2 The effect of a second body in close proximity . . . 168
5.4.3 The effect of gap width . . . 171

5.5 Conclusions 176

6 An experimental study of the effect of vessel motion on the surface elevation in the gap between two bodies 178

6.1 Introduction 178
6.2 Experimental setup 180
6.3 Regular wave results 183
6.3.1 Beam-sea cases 186
6.3.2 Head-sea cases 192
6.4 Focused wave events 196
6.5 Random sea states 202
6.6 Conclusions 203

7 An experimental study of alternative side-by-side offloading configurations 206

7.1 Introduction 206
7.2 Experimental study 208
7.3 Surface elevation within the gap 213
7.3.1 The effect of incident wave frequency 213
7.3.2 The effect of the second body 215
7.3.3 The effect of orientation 221
7.3.4 The effect of wave steepness 223
7.4 Vessel motion 225
7.4.1 The effect of the second body 225
7.4.2 The effect of wave excitation within the gap 230
7.5 Surface elevation in the upwave region 231
7.6 Conclusions 237

8 Concluding remarks 239

8.1 Introduction 239
8.2 Work undertaken 239

8.3 Physical insights 241
8.4 Further work 242
8.4.1 Numerical modelling 243
8.4.2 Experimental studies 244
8.4.3 Practical guidance 245
8.4.4 Wider applications 246

9 Appendices **247**

List of Figures

2.1 Examples of the angle of orientation, θ, around the outline of the rigid body, Γ_b. 33
2.2 Definition of the moving wave maker problem. 35
2.3 Discretised numerical domain for a moving wave maker. 38
2.4 Potential fluxes at a corner. 43

3.1 Details of the numerical wave tank for a moving flap-type wave maker. 61
3.2 Predictions of propagating and evanescent wave mode amplitudes for a moving flap-type wave maker; comparison between the numerical calculations and the analytical solution. 63
3.3 Prediction of the first harmonic amplitude of the three components of the force on the moving wave maker, comparison between the numerical calculations and the analytical theory. 65
3.4 Details of numerical wave tank for the radiation of surface water waves due to the motion of a rectangular body. 68
3.5 Predictions of the non-dimensionalised linear amplitude of the propagating wave mode for heave only radiation. 70
3.6 Predictions of the non-dimensionalised linear amplitude of the propagating wave mode for pitch only radiation. 70
3.7 Numerical wave tank involving a fixed body. 72
3.8 Predicted forces acting on a fixed rectangular body. 74
3.9 Photographs of the 2D experimental setup. 76
3.10 Sketches illustrating the arrangement of the experimental setup to restrict the motion of the body to heave only and pitch only. 76

3.11 Predictions of the heave response to an initial displacement in heave; comparisons between numerical predictions and experimental data. . 77
3.12 Predictions of the pitch response to an initial displacement in pitch; comparisons between numerical predictions and experimental data. . 79
3.13 Predicted amplitude of the first harmonic of the wave-induced heave motion, $|xi_2^1|$, for a single degree of freedom system; comparisons between numerical prediction, experimental data, and motion determined via the superposition method. 83
3.14 Spatial variation of the amplitude of the first harmonic surface elevation within the wave field surrounding a body undergoing wave-induced heave only motion. 85
3.15 Time-history of the free surface elevation at two points within the wave field upwave of a body undergoing motion in heave only for (a) $f = 0.72$Hz and (b) $f = 1.25$Hz. 86
3.16 Predicted amplitude of the first harmonic of the wave-induced pitch motion, $|\xi_3^1|$, for a single degree of motion system; comparisons between numerical prediction, experimental data, and motion determined via the superposition method. 87
3.17 Spatial variation of the amplitude of the first harmonic surface elevation within the wave field surrounding a body undergoing wave-induced pitch only motion. 88
3.18 Time-history of the free surface elevation at two points within the wave field upwave of a body undergoing motion in pitch only for (a) $f = 0.72$Hz and (b) $f = 0.83$Hz. 90

4.1 Numerical wave tank used for the simulation of wave interactions with a fixed LNG in close proximity to a terminal; the latter modelled as a bottom-mounted Gravity Based Structure (GBS). 96

4.2 Spatial variation of the amplitude and phase of the first harmonic surface elevation for a single fixed body subject to regular waves of frequency, f. 100
4.3 Variation with frequency of the amplitude of the first harmonic of the reflected wave in the upwave region and the amplitude of the first harmonic of the incident wave in the downwave region for a single LNG. 102
4.4 Spatial (x) variation of the first harmonic surface elevation amplitude and phase for Case 1b. 106
4.5 Spatial (x) variation of the first harmonic surface elevation amplitude and phase for Case 1c. 107
4.6 Spatial (x) variation of the first harmonic surface elevation amplitude and phase for Case 1e. 108
4.7 Spatial (x) variation of the first harmonic surface elevation amplitude and phase for Case 1f. 110
4.8 Variation with frequency the amplitude of the first harmonic of the reflected wave in the upwave region and the amplitude of the first harmonic of the incident wave within the gap for Case 1 and a single LNG. 111
4.9 Comparison between the Case 1 and the Case 2 numerical wave tanks. 113
4.10 Comparison of the spatial (x) variation of the first harmonic surface elevation amplitude and phase between Cases 1c and 2c. 114
4.11 Comparison of the spatial (x) variation of the first harmonic surface elevation amplitude and phase between Cases 1d and 2d. 115
4.12 Variation with frequency of the amplitude of the first harmonic of the reflected wave in the upwave region and the amplitude of the first harmonic of the incident wave in the gap for Cases 1, 2 and 3. . 117
4.13 Variation with frequency of the amplitude of the first harmonic of the reflected wave in the upwave region and the amplitude of the first harmonic of the incident wave in the gap for Cases 1 and 4. . . 118

4.14 Variation with frequency of the amplitude of the first harmonic of the reflected waves in the upwave region and in the gap and the amplitude of the first harmonic of the incident waves in the downwave region and in the gap for Cases 5 and 6 and for a single LNG. 120
4.15 Comparison between the Case 5 and the Case 6 numerical wave tanks. 121
4.16 Comparison of the spatial variation in x and $\tilde{x}$ of the first harmonic surface elevation amplitude and phase between Cases 5a and 6a. . . 122
4.17 Comparison of the spatial variation in x and $\tilde{x}$ of the first harmonic surface elevation amplitude and phase between Cases 5e and 6e. . . 123
4.18 Conversion of Case 1 into the equivalent moonpool problem. 124
4.19 Comparison of the spatial (x) variation of the first harmonic surface elevation and body motion amplitude and phase between Cases 1a and 7a. 127
4.20 Comparison of the spatial (x) variation of the first harmonic surface elevation and body motion amplitude and phase between Cases 1d and 7d. 128
4.21 Comparison of the spatial (x) variation of the first harmonic surface elevation and body motion amplitude and phase between Cases 1f and 7f. 129
4.22 Comparison of the spatial (x) variation of the first harmonic surface elevation and body motion amplitude and phase between Cases 1g and 7g. 130
4.23 Comparison of the decay test response and variation with frequency of the dynamic amplification factor for the single LNG and the LNG in Case 7. 132
4.24 Variation with frequency of the first harmonic of the heave motion in Case 7 and the heave motion based upon the superposition method. 134
4.25 Time-history of η at various positions within the numerical wave tank for Case 7a. 135

5.1 3D numerical wave tank for waves interacting with a fixed body of finite draft subject to beam seas. 144
5.2 Comparison of the semi-infinite analytical breakwater and the numerical breakwater 150
5.3 Transverse (y) variation of the diffraction coefficient K_D for f = 0.875Hz at four x-sections. 152
5.4 Plan view of the bottom-mounted GBS located within the wave basin. 154
5.5 Spatial (x, y) variation of the amplitude of the first harmonic of the water surface elevation directly upwave of a bottom-mounted GBS for f = 0.875Hz, comparisons between experimental measurements and numerical predictions. 156
5.6 Spatial (x, y) variation of the amplitude of the first harmonic of the water surface elevation directly upwave of a bottom-mounted GBS for f = 1.25Hz, comparisons between experimental measurements and numerical predictions. 157
5.7 Transverse (y) and inline (x) variation of the amplitude of the first harmonic of the surface elevation directly upwave of a bottom-mounted GBS for f = 0.875Hz, comparison between experimental measurements and numerical predictions. 158
5.8 Transverse (y) and inline (x) variation of the amplitude of the first harmonic of the surface elevation directly upwave of a bottom-mounted GBS for f = 1.25Hz, comparison between experimental measurements and numerical predictions. 160
5.9 Inline (x) variation of first harmonic surface elevation amplitude and phase around a fixed LNG at two y-sections. 161
5.10 Contours of first harmonic surface elevation amplitude and phase around a bottom-mounted GBS at f = 0.875Hz and f = 1.25Hz. . . . 164
5.11 Contours of first harmonic surface elevation amplitude and phase around a bottom-mounted GBS of finite beam at f = 0.875Hz and f = 1.25Hz. 166

5.12 Contours of first harmonic surface elevation amplitude and phase around fixed body of finite draft at $f = 0.875$Hz. 167
5.13 Contours of surface elevation around the LNG-FLNG arrangement at nine discrete intervals in time for $f = 0.875$Hz. 170
5.14 Contours of surface elevation around the LNG-FLNG arrangement at nine discrete intervals in time for $f = 1.25$Hz. 172
5.15 Plan view of experimental setup for a fixed LNG in close proximity to a GBS. 173
5.16 Transverse (y) variation of the amplitude of the first harmonic surface elevation arising in the gap at four incident wave frequencies for three gap widths. 175
5.17 Transverse (y) variation of the phase of the first harmonic surface elevation, $arg(\eta^1)$, for a gap width of 0.08m. 176

6.1 Plan view of the experimental setup for the floating ship. 181
6.2 Spatial variation of the standing wave fluid velocity vector. 184
6.3 Spatial variation of first harmonic of the surface elevation amplitude and phase for various incident frequencies in beam seas. 185
6.4 Variation with incident wave frequency of the maximum amplitude of various harmonics of the surface elevation at any point within the gap in beam seas. 188
6.5 Spatial variation of the amplitude of the zeroth to third harmonic surface elevation in beam seas. 190
6.6 Spatial variation of first harmonic surface elevation amplitude and phase for various incident frequencies in head seas. 192
6.7 Variation with incident frequency of the maximum amplitude of the first harmonic surface elevation at any point within the gap in head seas. 194
6.8 Spatial variation of the amplitude of the zeroth to third harmonic surface elevation in head seas. 195

6.9 Incident amplitude spectra for focused wave events with varying peak frequencies. 196
6.10 Amplitude spectra arising at each wave gauge location within the gap for f_p = 0.625Hz. 198
6.11 Amplification of the spectral amplitudes for focused events of different spectral peak frequencies based on data recorded at the amidships location. 200
6.12 Dimensionless amplitude spectra at all wave gauge locations for the floating ship case subject to beam seas; focused and regular waves. . 201
6.13 Probability of exceedance of wave height in the gap associated with a floating in beam seas subject to a random sea state with a spectral peak frequency of f_p = 1.25Hz. 203

7.1 Plan view of the experimental setups within the 3D wave basin for GBS-LNG, FLNG-LNG$_E$, FLNG-LNG$_S$ and LNG-LNG. 209
7.2 Spatial variation of first harmonic of the surface elevation amplitude and phase for various incident regular wave frequencies. 214
7.3 Variation with incident wave frequency of the non-dimensionalised maximum total surface elevation at any point within the gap in beam seas. 216
7.4 Variation with incident wave frequency of the non-dimensionalised maximum amplitude of various harmonics of the surface elevation at any point within the gap in beam seas. 218
7.5 Spatial variation of the largest non-dimensionalised harmonics of the surface elevation amplitude in beam seas. 220
7.6 Spatial variation of the largest non-dimensionalised zeroth, first and second harmonic surface elevation amplitude in head seas. 222
7.7 Spatial variation of the non-dimensionalised amplitude of the surface elevation harmonics for varying incident wave steepness in beam seas. 225

7.8 Variation with incident frequency of the first harmonic horizontal x acceleration of the LNG vessel in regular wave beam-sea cases. . . 226
7.9 Variation with incident frequency of the amplitude of the first harmonic of the relative vertical acceleration for regular waves in beam seas. 227
7.10 Spectra defining the motion of the FLNG and LNG vessels subject to focused waves of $f_p = 0.714$Hz in a beam-sea orientation. 229
7.11 Frequency content of the horizontal y acceleration, a_y, of the LNG for GBS-LNG in head-sea focused waves. 230
7.12 Plan view of the FLNG-LNG$_S$ setup showing the area within which measurements of the upwave region were undertaken. 232
7.13 Spatial variation of the amplitude of the first harmonic of the surface elevation for the FLNG-LNG$_S$ setup in the upwave region and within the gap at three x-sections. 233
7.14 Contours of the amplitude of the first harmonic of the surface elevation within the upwave area identified in figure 7.12 and in the gap for various incident wave frequencies. 235

List of Tables

3.1 Details of the wave cases simulated using a moving wave maker. . . 60
3.2 Geometric properties of the rectangular bodies considered. 68
3.3 Comparison between experimental and numerical dynamic properties of a rectangular body moving in heave. 78

4.1 Definition of cases considered. 104
4.2 Incident wave frequencies considered and their case suffixes. 104
4.3 Equivalent moonpool dimensions for Cases 1 to 6, together with a comparison of the predicted and obtained resonance frequencies. . . 125

6.1 Properties of the experimental model of the LNG tanker Gallea, the floating ship. 182
6.2 Details of observations undertaken in beam and head sea orientations. 184
6.3 Return periods, T_r, for a selection of wave gauge locations 202

7.1 Properties of the experimental model of the FLNG barge. 208
7.2 Details of the incident wave cases considered, regular waves and focused wave events. 212
7.3 Resonant amplifications of the total surface elevation and of its harmonic components, non-dimensionalised with respect to the incident wave amplitude, for the experimental setups in beam seas. . . 217
7.4 Incident wave frequencies at which the resonant amplification of the non-dimensionalised harmonic components of the surface elevation occur for the experimental setups in beam seas. 219

7.5 Incident wave frequencies at which the resonant amplification of the non-dimensionalised harmonic components of the surface elevation occur for the experimental setups in head seas. 221

1

Overview

1.1 Introduction

This chapter describes the overall aims of the study and explains why they are important from both theoretical and practical viewpoints. It outlines the steps that are necessary to achieve these aims, indicates the layout of the thesis and highlights the main achievements.

1.2 Aims

The purpose of the work presented within this thesis is to further the understanding of the hydrodynamic interaction between water waves and multiple bodies in close proximity. This is achieved through both a numerical and an experimental study. Both fixed structures and floating bodies are considered; the purpose being to first illustrate the basic hydrodynamics associated with multiple bodies in close proximity and then to highlight the effect of the motion of one or more of the bodies.

1.3 Motivation

The prediction of the motion of a floating body in specified incident wave conditions, commonly referred to as *wave-induced* motion, is complex. The conventional approach to such predictions is to split the problem into three parts:

(i) In the first part, the floating body is assumed to be fixed in position. A diffraction analysis (typically linear) of the interaction between the incident waves and the fixed structure is undertaken. This analysis determines the force acting on the body due to the surrounding wave field; the latter being defined by the sum of the linear incident and diffracted wave fields.

(ii) The second part of the approach essentially consists of a decay test. Here, the incident waves are assumed to be zero, corresponding to a still water environment, and the floating body is given a known initial displacement. The body's subsequent motion is then used as the impulse response of a mass-spring-damper system, from which the body's hydrodynamic coefficients can be determined. These include the hydrodynamic damping coefficient, to be applied to the body's velocity, and the added mass coefficient, to be applied to the body's acceleration. A separate decay test is performed for each degree of freedom.

(iii) In the final part, the motion of the floating body is determined through the equation of motion. This equates the force on the body to its motion using the hydrodynamic coefficients. The force is taken from part (i) and the hydrodynamic coefficients from part (ii); the underlying assumption being that the force on the body and its motion are independent.

One disadvantage of this commonly adopted approach is that no account is taken of the effect of the body motion on the surrounding wave field. In many situations this simplification (or omission) is relatively unimportant when seeking to predict the motion of a single body. However, when considering the complex hydrodynamic interaction between waves and multiple bodies in close proximity,

the effect of body motion must be considered. Another limitation of this approach arises because the values of the hydrodynamic coefficients, as determined by a decay test, are dependent on the presence of surrounding boundaries (or bodies). As a result, they cannot be generally applied in the case where local boundaries are present and may also be moving.

1.4 Practical applications

The limitations of the conventional approach, described above, need to be overcome in order to efficiently exploit hydrocarbon basins through the use of mobile, thus floating, production plants. Indeed, it has been shown that at present it is uneconomic to construct permanent structures in many locations because approximately 85% of deepwater discoveries outside of the Gulf of Mexico contain less than 500 million barrels (Faber et al. 2002). Taking the example of Liquid Natural Gas (LNG), the layout of such an offshore Floating LNG production, storage and offloading barge (FLNG) is similar to that of an onshore LNG plant; the safety requirements being the principle drivers in the design of the layout. However, some components used in the processing of LNG are motion sensitive. In order to protect these components, detailed knowledge of the wave loading and the subsequent vessel response is required. Therefore, the calculation of the wave loading must include the effect of the body motion on the surrounding wave field.

Furthermore, the need to correctly model the hydrodynamic coefficients in the presence of surrounding boundaries arises when predicting the vessel motion during the offloading of processed LNG from the FLNG to a transport vessel and also during the transfer of LNG at an offshore receiving terminal. From a practical perspective, offshore loading / unloading is desirable for safety reasons as well as to distance operations from politically unstable regions; the latter being particularly true off the west coast of Africa. However, if such operations are to be a viable option, the accurate prediction of the vessel motion (or response) when adjacent to a second body becomes a key issue.

For the offloading of LNG from the FLNG to a transport vessel, there are two possible methods:

(i) Tandem offloading involves the mooring of the tanker or transport vessel's bow to the stern of the FLNG. The spacing between the two bodies is of the order of 50m, which is a favourable distance in terms of avoiding ship to ship contact in case of component failure. However, tandem offloading requires a structure (which must be cantilevered from the FLNG) to bridge the 50m gap between the vessels and carry the cryogenic pipes across to the tanker. Newell (2003) described that designs of such a structure can weigh up to 1200tonnes and require a fair amount of space on an already-confined deck area. Furthermore, in an offshore environment, the FLNG is turret-moored at the bow so that it is able to weathervane or move to a position of lowest forcing. However, during tandem offloading operations it would also be connected at the stern to the transport vessel. In such a scenario, 'fishtailing' can occur which leads to very large relative motions between the two floating bodies.

(ii) A second and more viable option is side-by-side offloading. This involves the transport vessel being moored parallel to the FLNG at a spacing of around 4m; the latter determined by a typical (maximum) fender size. The close proximity of the vessels in side-by-side offloading involves a rather difficult vessel approach, but allows for more reasonably sized offloading arms. Furthermore, the mooring system used is of a standard design set by the OCIMF (Oil Companies International Marine Forum) instead of the innovative design necessary for tandem offloading (Newell 2003).

The present study will consider the side-by-side mooring arrangement. The small spacing, outlined in (ii), illustrates the need to understand the hydrodynamics of both fixed structures and floating bodies in very close proximity.

1.5 Approach to the solution

The approach taken to further understand the nonlinear wave-structure interactions appropriate to multiple bodies in close proximity is outlined in the subsections that follow; the numerical and experimental studies being considered separately. In each case, the subsection begins with a description of the resources available to the author at the outset of the work.

1.5.1 Numerical study

The two-dimensional (2D) calculations undertaken in the present study were based upon a fully nonlinear application of the Boundary Element Method (BEM). This model was developed in the Hydrodynamics Section at Imperial College London, under the supervision of Professor Chris Swan. At the outset of the present study, the model had been successfully validated for wave-wave interaction studies (up to the point of wave overturning) and a limited range of wave-fixed body interactions. The numerical code is formulated as a numerical wave tank. As a result, the so-called corner problem, inherent of any physical-space BEM application, must be addressed. In the present model this important difficulty is addressed using the multiple-flux approach, full details of which are given in Hague & Swan (2009). A three-dimensional (3D) numerical model, based upon a similar approach, was also available but in a much less advanced stage of development. Indeed, at the outset of the present project, it had only been applied to linear wave groups and was undergoing extensive development. As a result, the majority of the numerical development undertaken by the author applies to the 2D numerical code.

The fully nonlinear nature of the numerical code is achieved by applying nonlinear boundary conditions and, more importantly, by modelling the motion of the deformable free surface boundary. In order to simulate a floating body while retaining this fully nonlinear nature, the numerical code must first be able to model the interaction of *two* moving boundaries; specifically the free surface and the floating body. At this point, two distinct types of body motion must be introduced,

both having been considered in the present study:

(i) prescribed or *forced* body motions, which are independent of the surrounding wave field, and

(ii) *wave-induced* motions, which are dependent on the force exerted on the body by the surrounding wave field and whose prediction must take into account the fact that the body is moving within fluid; the latter resulting in a coupled hydrodynamic system.

The simulation of a forced body motion involves ensuring that the motion of the deformable free surface boundary remains consistent with the velocity potential describing the (generated) wave field. At the same time, the motion of the moving body boundary must relate to the (prescribed) motion of the rigid body. It is important to note that modelling the interaction of these two, very different, moving boundaries is non-trivial, not least because they intersect at points that are central to the solution procedure.

Predicting the wave-induced body motion requires the calculation of the forces acting on the surface of the body due to the surrounding wave field. Two different methods have been incorporated into the numerical code to enable the evaluation of these forces. Furthermore, the two methods model the coupled hydrodynamic system appropriate to wave-induced motions without resorting to the use of predetermined hydrodynamic coefficients. As a result, through the incorporation of these methods, undertaken within the present study, the (2D) numerical model can predict the fully nonlinear wave-body interactions for any combination of fixed and floating bodies. This is in contrast to diffraction-radiation codes, in which the effects of diffraction and radiation are linearly superposed.

Finally, the separately-developed 3D BEM numerical code is used to simulate the 3D interaction of unidirectional incident waves with fixed bodies in a beam-sea orientation; the development of modelling fixed bodies of finite draft being undertaken by the author. In the beam-sea orientation, the incident waves propagate beam-on towards the fixed bodies and, as a result, the 3D simulations are

comparable to the 2D simulations. Consequently, the 3D results illustrate how the 2D results vary in the third (transverse) direction; identifying which of the extensive 2D results are directly applicable to the complex 3D problem of side-by-side offloading.

1.5.2 Experimental study

The Hydrodynamics Laboratory at Imperial College London houses a 3D wave basin, in which 1:100 scale modelling is commonly undertaken. The laboratory is equipped with wave gauges to record the water surface elevation at a fixed position in space and accelerometers to record rigid body motions.

The 3D numerical study, introduced above, is limited in its extent, not least because run-times were very long. The purpose of the experimental study is therefore to build on these numerical results. However, although each experimental run is fast in comparison to a numerical simulation, the number of experimental runs required to record the surface elevation over a large area of interest can become very large. Fortunately, the area of interest in side-by-side offloading is relatively confined; being the narrow gap between the two bodies.

Within the experimental study, it is also possible to examine the 3D effect of the body motion on the wave excitation within the gap. This was made possible by comparing the data arising from a number of experimental setups; involving various combinations of the following bodies:

- A bottom-mounted Gravity Based Structure, hereafter referred to as the GBS. This is representative of a typical (fixed) offshore terminal.
- A scale model of the LNG transport vessel or tanker, the MS *Gallea*. This is hereafter referred to as the floating ship or LNG.
- A fixed box-like approximation to the floating ship, hereafter referred to as the fixed box.

- A floating rectangular LNG production, storage and offloading barge. This is substantially larger than the LNG and is hereafter referred to as the FLNG.

1.6 Layout of thesis

The general approach presented in Section 1.5 is reflected in the chapter outline which follows. Chapter 2 introduces the basic theory of waves and of dynamically responding rigid bodies. It also describes the 2D numerical model developed within the Hydrodynamics Section, with particular attention paid to the improvements necessary to simulate the interaction of two moving boundaries. The chapter then presents the theory underpinning the various methods used to calculate the force acting on a single body and to predict its wave-induced motion.

Chapter 3 continues with the validation of the developed numerical model. This includes the wave field generated by the forced motion of a single body, the wave-induced force on a fixed body, the decay of a body's response to an initial displacement and the wave-induced motion of a body in regular waves. Within the validation, the numerical predictions are compared to a combination of available analytical solutions, previous numerical work and experimental observations.

Chapter 4 concerns the 2D numerical analysis of wave interactions with two fixed bodies in close proximity. The cases considered involve variations in the incident wave frequency, the gap width and the beam and draft of the bodies involved. In the final section of this chapter, comparative calculations are provided to establish the importance of allowing one of the bodies to respond dynamically.

Chapter 5 describes the 3D numerical model and presents a validation based upon the interaction of waves with a fixed body. The numerical predictions presented within this chapter illustrate how the finite length, finite width, finite draft and presence of a second body in close proximity affect the surrounding wave field. To support this work, the chapter also presents the results of an experimental study involving two fixed bodies in close proximity. The experimental data define the wave excitation along the length of the narrow gap between the two

bodies. The experimental study includes a large number of incident wave frequencies and addresses three gap widths.

Chapter 6 consists solely of experimental results. It describes the experimental setup in the wave basin and provides details of the side-by-side mooring arrangements. The data presented within the chapter concern the water surface elevation recorded within the gap between the two bodies. Two cases are considered, relating to the GBS-fixed box and the GBS-floating ship setups. In both cases, the setups are positioned beam-on and head-on to the incident wave conditions; the latter consisting of regular waves, irregular waves and random sea states.

Chapter 7 compares the results of the GBS-LNG, FLNG-LNG and LNG-LNG experimental setups; the width of the gap being similar in each case. The observations include the water surface elevation within the gap and the vessel motion for each setup; the purpose of the data being to identify the relative merits of the different offloading arrangements. In addition, the surface elevation within the upwave field of the FLNG-LNG setup is also recorded.

Chapter 8 provides a summary of the key achievements and comments on their practical importance. It also makes suggestions for future work.

1.7 Achievements

The main achievements of the work presented within this thesis are as follows.

(i) A new fully nonlinear 2D numerical model is established, which is capable of describing the dynamic response of a body. Extensive validation work is presented and it is shown that the applied forcing, and hence the associated dynamic response, is best calculated using the so-called Indirect Method originally proposed by Wu & Eatock-Taylor (1996).

(ii) A simplified analysis of side-by-side offloading, adopting a 2D representation, shows a resonant wave excitation within the gap between the two bodies. The frequency at which this resonance occurs, hereafter referred to as the

resonance frequency, is found to be significantly dependent on the width of the gap and on the motion of the body. Furthermore, it is shown that the effect of the body motion cannot be neglected when estimating the linear motion of a body in close proximity to a second body. This is in stark contrast to comparable results relating to the linear motion of a single body.

(iii) Following modifications to an existing 3D numerical model, the description of the 3D interaction of waves with two fixed bodies in close proximity is achieved. This suggests that the 3D wave excitation within the gap is closely related to the 2D equivalent up to the resonance frequency. Beyond the resonance frequency, the effects of the transverse variation become dominant in the 3D calculations.

(iv) The comparison of the data corresponding to the GBS-fixed box and the GBS-floating ship setups shows that the body motion affects the resonance frequency. This is consistent with the 2D numerical results described in (ii) above. The results of the GBS-floating ship setup also provide evidence of significant amplification of the second harmonic of the surface elevation within the gap at half the resonance frequency. Furthermore, the resonant amplification in the GBS-floating ship case is similar irrespective of both the nature of the incident waves (regular, focused or random) and the orientation of the setup relative to the incident waves (beam seas or head seas).

(v) Comparisons between the GBS-LNG, FLNG-LNG and LNG-LNG experimental setups suggest that the characteristics of the second body have a negligible effect on the wave excitation within the gap. However, in terms of the motion of the moored LNG vessel, evidence of unexpected higher order motions is provided for the setups involving two bodies with varying hydrodynamic properties.

2

Theoretical Background

2.1 Introduction

This chapter presents background theory relevant to the modelling of nonlinear wave interactions with multiple bodies in close proximity. With many of the incident wave conditions within the present study corresponding to regular waves, the chapter first provides an introduction to the modelling of regular waves. It continues with a description of the boundary conditions relevant to a moving rigid body. Two types of rigid body motion are considered:

(i) Forced motion, where the body motion is prescribed and leads to a generated wave field.

(ii) Wave-induced motion, where the body motion is unknown and is a reaction to the force exerted on it by the surrounding wave field.

An analytical solution for forced body motion is presented in the form of classical wave maker theory. However, since there are no analytical solutions for wave-induced body motion, the problem must be solved numerically.

The numerical model used within the present study is outlined in Section 2.4. In order to calculate wave-induced body motion, the numerical model developed by the author calculates the force on the body exerted by the surrounding wave

field and uses this force to predict the body's wave-induced motion. The present chapter describes three possible methods appropriate for this development; the advantages and disadvantages of each being discussed in detail in Section 2.5.

2.2 Governing equations

The principles of the analytical analysis of waves were initially established by Airy (1845) and Stokes (1847). The theory presented within this chapter refers to the two-dimensional (2D) analysis of a fluid flow, with variations in the horizontal, x, and vertical, z, directions. The fluid is assumed to be inviscid, homogeneous and incompressible. Furthermore, the flow is assumed to be irrotational such that the gradient of the velocity potential, ϕ, defines the fluid velocity, $\mathbf{u}$;

$$\mathbf{u} = \nabla\phi, \tag{2.1}$$

where $\mathbf{u} = (u, w)$ denotes the velocity components of the fluid in the horizontal and vertical directions respectively. Adopting these assumptions the governing equation for the fluid flow, representing mass continuity, can be expressed as

$$\nabla^2\phi = 0. \tag{2.2}$$

This is the Laplace equation, which must be satisfied along with the boundary conditions defining the problem being considered.

2.3 Boundary conditions and analytical solutions

2.3.1 Linear regular wave theory

The boundary conditions appropriate to an analytical solution for linear regular waves are based on the assumption that the fluid flow is bounded by a horizontal and impermeable bed and by the free water surface. The bed boundary is located at $z = -h$; h being the still water depth and z being measured vertically upwards

from the still water level. The boundary condition acting on the bed requires the normal fluid velocity to be zero. This is expressed as

$$\frac{\partial \phi}{\partial n} = \frac{\partial \phi}{\partial z} = 0 \quad \text{on } z = -h, \tag{2.3}$$

where $\mathbf{n}$ is the outward normal direction and $\frac{\partial \phi}{\partial n}$, or ϕ_n, is referred to as the normal potential flux.

The water surface elevation is a function of both space and time and is described by $z = \eta(x,t)$. The evolution of this surface is determined by two nonlinear boundary conditions. The first is the Kinematic Free Surface Boundary Condition (KFSBC), which stipulates that the velocity of the free surface along a normal to the surface must be equal to the fluid velocity along that normal;

$$\frac{\partial \eta}{\partial t} = w - u\frac{\partial \eta}{\partial x}. \tag{2.4}$$

The second condition is the Dynamic Free Surface Boundary Condition (DFSBC). This requires the pressure on the free surface to be constant. Setting the pressure to zero and re-arranging Bernoulli's equation, the DFSBC can be expressed as

$$\frac{\partial \phi}{\partial t} = -gz - \frac{1}{2}\left(u^2 + w^2\right) \quad \text{on } z = \eta, \tag{2.5}$$

where g is the acceleration due to gravity. It is important to note that equation 2.5 is applied on $z = \eta$, the instantaneous position of the free surface, which is not known *a priori*. Consequently, the analytical solution of linear wave theory combines the KFSBC and the DFSBC and applies the new Linearised Free Surface Boundary Condition (LFSBC) at the still water level,

$$\frac{\partial^2 \phi}{\partial t^2} = -gw \quad \text{on } z = 0. \tag{2.6}$$

The solution for a propagating linear regular wave, as derived by Airy (1845), is given by

$$\phi = \frac{H\omega}{2k}\frac{\cosh\left(k\left(z+h\right)\right)}{\sinh\left(kh\right)}\sin\left(kx - \omega t\right), \tag{2.7}$$

where H is the incident wave height, k is the wave number and ω is the angular wave frequency. Considering the expression of ϕ more closely, it can be seen that:

(i) $\frac{H\omega}{2k}$ relates to the magnitude of ϕ.

(ii) The ratio of the hyperbolic terms determines the depth variation; the relationship being exponential for waves in deep water.

(iii) The $\sin(kx - \omega t)$ shows that ϕ is oscillatory in x and t, with $(kx - \omega t)$ defining the so-called phase angle.

The solution also yields the dispersion equation,

$$\omega^2 = gk \tanh(kh). \tag{2.8}$$

This describes the relationship between the angular frequency and the wave number, which is also dependent on the water depth, h. Finally, the linear solution for the water surface elevation is simply defined by

$$\eta(x,t) = \frac{H}{2} \cos(kx - \omega t). \tag{2.9}$$

2.3.2 The boundary condition on a moving rigid body

Consider the problem of a wave field generated by the motion of a rigid body. In this case, in addition to the bed and free surface boundary conditions described above, a boundary condition must be formulated to describe the interaction between the moving body and the surrounding fluid. In the arguments that follow, and in all subsequent chapters, the body is assumed to be rigid. As in the case of the bed, the body is impermeable but, unlike the bed, the body boundary is moving. As a result, the appropriate boundary condition states that the velocity of the fluid along a normal to the boundary must be equal to the velocity of the boundary along that normal.

In order to define the normal velocity of the body, its motion modes or degrees of freedom need to be considered, as originally described by Landweber (1961) and later by Pytel & Kiusalaas (2001). Within a 2D analysis, the body displacement vector $\boldsymbol{\xi}$ has three components (ξ_1, ξ_2, ξ_3) corresponding to surge (translation in x), heave (translation in z) and pitch (rotation about the axis perpendicular to

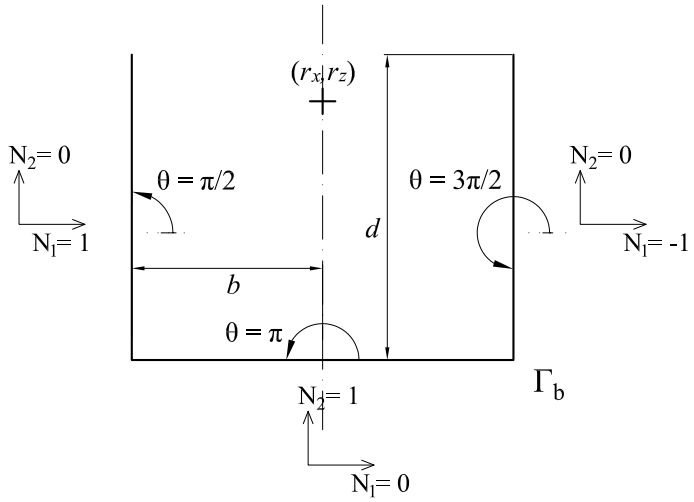


Figure 2.1: Examples of the angle of orientation, θ, around the outline of the rigid body, Γ_b.

the $x-z$ plane, corresponding to y). Consequently, the moving body boundary condition is expressed as

$$\frac{\partial \phi}{\partial n} = \mathbf{v} \cdot \mathbf{N} \quad \text{on } \Gamma_b, \tag{2.10}$$

where Γ_b is the body boundary and $\mathbf{v} = (v_1, v_2, v_3)$ is the velocity vector describing the velocity components of the body in each of the three motion modes; $v_1 = \dot{\xi}_1$, $v_2 = \dot{\xi}_2$ and $v_3 = \dot{\xi}_3$. The components of $\mathbf{N}$ are

$$N_1 = \sin\theta, \quad N_2 = -\cos\theta, \quad N_3 = (x - r_x - \xi_1)\, N_2 - (z - r_z - \xi_2)\, N_1, \tag{2.11}$$

where (r_x, r_z) defines the position of the body's centre of rotation and θ is the angle of orientation of the boundaries, measured anti-clockwise from the horizontal. Values of θ, N_1 and N_2 along the boundaries of a rectangular body are illustrated in figure 2.1. It is clear from this figure that these values are different for each of the three sides of the body; the change in the values occurring at the corners linking the sides. If ξ_3 defines the pitching motion of the body, θ at each of the nodes can be linked to ξ_3; the value of θ along each of the rigid sides being identical. The significance of $\mathbf{N}$ is discussed as follows.

Figure 2.1 depicts a *discontinuous* body of draft, d, and half-beam, b; a *discon-*

tinuous body being one which is surrounded by fluid on all sides. Alternatively, the body boundary may extend vertically from the bed to the free surface forming a *continuous* lateral boundary; an example of this latter case being a wave maker. Whatever the shape of the moving body, equation 2.10 defines the appropriate boundary condition; the body velocity, $\mathbf{v}$, being converted into the motion of the body boundaries through the vector $\mathbf{N}$ and the motion of the body boundaries defining the motion of the surrounding fluid, $\left(\frac{\partial \phi}{\partial n}\right)$. To present this more clearly, consider the first degree of freedom ($j = 1$). The three different values of N_1 in figure 2.1 indicate how the surge motion of the body, v_1, affects the fluid adjacent to the vertical boundaries but not the fluid adjacent to its horizontal boundary.

Despite the fact that the moving body boundary condition, equation 2.10, is applicable irrespective of the shape of the body, the approach adopted in an analytical solution involving a *continuous* body is very different to that involving a *discontinuous* body. The reason for this is that in the latter case there are two effective water depths: h and $h - d$. This leads to two effective wave numbers, k; the relationship between k and the water depth being expressed by the dispersion equation, equation 2.8. As a result, problems involving *discontinuous* bodies are either modelled using matched (asymptotic) expansions (Miles (1967) and Lee (1995)) or, more commonly, modelled numerically. In contrast, several analytical theories relating to *continuous* bodies are available, not least because they relate to the practically important problem of wave maker theory. One such theory is outlined below.

2.3.3 Wave maker theory

Figure 2.2 illustrates a common problem considered in wave maker theory; the fluid flow being bounded by the bed, the free surface and a moving lateral boundary. The dotted lines within the figure represent the position of the still water level (SWL) and the equilibrium position of the wave maker. The wave maker is hinged at the bed and its displacement is rotational (ξ_3); the case corresponding to a

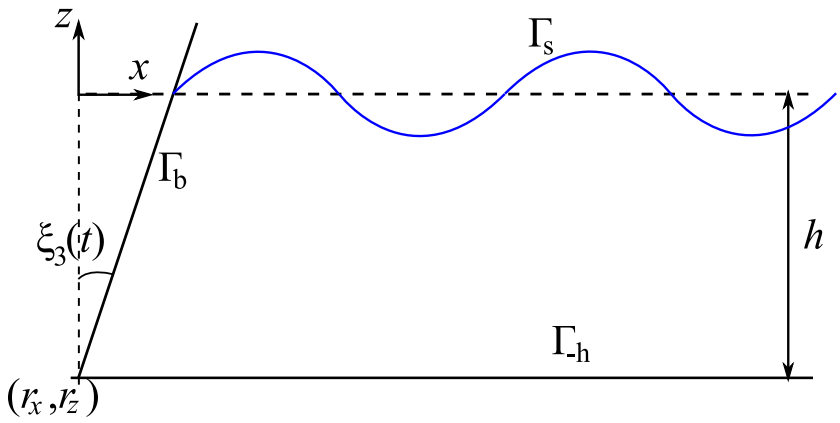


Figure 2.2: Definition of the wave maker problem, where the fluid flow is bounded by the free surface, the bed and a *continuous* moving rigid body; the latter representing the wave maker boundary, Γ_b.

bottom-hinged flap-type wave maker. A general discussion of wave maker theory is provided by, among others, Schäffer (1996). This considers a variety of wave makers, the solution expressed in terms of the wave maker motion at still water, X_0. In the brief discussion that follows, the general notation of Schäffer (1996) is retained. However, it should be noted that later sections will be concerned with the rotation ξ_3 rather than a general X_0; the former being specific to the motion of a flap-type wave maker, as outlined in figure 2.2. The displacement X_0 is defined in Schäffer (1996) as

$$X_0 = \frac{1}{2}\left(-iX_a e^{i\omega t} + c.c.\right), \tag{2.12}$$

where X_a is the complex amplitude of the linear wave maker motion at the still water level and *c.c.* is the complex conjugate of the previous term.

Based upon this motion Schäffer (1996) describes the linear generated wave field in terms of a velocity potential defined by

$$\phi = \frac{1}{2}\left\{\frac{igX_a}{\omega}\sum_{s=0}^{\infty} c_s \frac{\cosh k_s\left(z+h\right)}{\cosh k_s h} e^{i(\omega t - k_s x)} + c.c.\right\}, \tag{2.13}$$

where s is a simple counter and c_s are the first-order coefficients, details of which are provided in Appendix A. In formulating this solution, the LFSBC is applied at the still water level and the moving body boundary condition is applied at the equilibrium position of the wave maker (see figure 2.2).

Within equation 2.13 $s = 0$ represents the propagating wave component, with real k_0, generated by the wave maker motion. However, there is an inevitable mismatch between the velocity of the wave maker and the fluid velocity of the propagating wave mode; the former varying linearly with depth and the latter based upon the ratio of the hyperbolic terms in equation 2.7. The correction for this mismatch is based upon an infinite series of evanescent modes, represented by $\sum_{s=1}^{\infty}$ in equation 2.13. For each of these evanescent wave modes, the corresponding wave number, k_s, is imaginary; being one of the infinite roots of the dispersion equation. Upon substitution of imaginary k_s into equation 2.13, it is clear that the evanescent modes are oscillatory in z and decay exponentially in x. As a result, evanescent modes are only significant close to the wave maker boundary.

The corresponding expression for the water surface elevation, η, is

$$\eta(x,t) = \frac{1}{2}\left(X_a \sum_{s=0}^{\infty} c_s e^{i(\omega t - k_s x)} + c.c.\right). \tag{2.14}$$

As before, the first term corresponding to $s = 0$ refers to the propagating wave mode, while the remaining terms $\sum_{s=1}^{\infty}$ represent the evanescent modes.

Adopting a solution that allows for real and imaginary wave numbers enables the compact complex notation adopted in equations 2.13 and 2.14. An alternative formulation, that explicitly separates the propagating wave mode and the evanescent modes, is given by Dean & Dalrymple (1991). Unfortunately, neither formulation can easily be extended to the solution of a problem involving a *discontinuous* body (figure 2.1). As a result, this case is usually investigated using numerical calculations.

2.4 The Boundary Element Method

The Boundary Element Method (BEM) is a common approach adopted in the numerical analysis of many hydrodynamic problems. There are many advantages to this technique, not least the fact that the BEM considers only the outline (or boundary) of a problem, which is beneficial in two ways. First, as outlined in

Section 2.3 above, the analysis of many hydrodynamic problems involves satisfying *boundary* conditions. The BEM approach is perfectly suited to this task. Second, it reduces the dimensionality of the problem by one. This is valuable in terms of the computational effort required, particularly when the resolution of a problem requires a large number of nodal points. In the sections which follow, the fundamental equations appropriate to the BEM and the nature of the numerical solution are outlined.

2.4.1 Boundary integral equation

The Boundary Integral Equation (BIE) is fundamental to the description of the BEM. Longuet-Higgins & Cokelet (1976) were the first to apply the BIE to surface water waves. In the context of this early work, a conformal mapping scheme was used to solve the Cauchy integral formula. The limitations of this initial approach are as follows:

(i) The water depth must be constant and the solution periodic due to the conformal mapping adopted.

(ii) Three-dimensional (3D) analysis cannot be undertaken because the Cauchy integral formula involves calculations in the complex plane.

In order to overcome the limitations of a Cauchy integral formulation, Grilli et al. (1989) applied Green's second identity. This approach describes what is commonly referred to as a numerical wave tank, effectively a numerical representation of a physical space. As such, it is possible to accommodate changes in water depth, non-periodic wave fields and 3D calculations including directionally spread wave fields. Figure 2.3 illustrates a 2D numerical wave tank used to simulate wave generation by the forced motion of a rectangular body (denoted in red). The closed boundary of the numerical wave tank, Γ, is represented by discrete nodes along the bed boundary, Γ_{-h}, the end boundaries, Γ_r, the free surface boundary, Γ_s, and the moving body boundary, Γ_b. The sponge layers seen at either end of

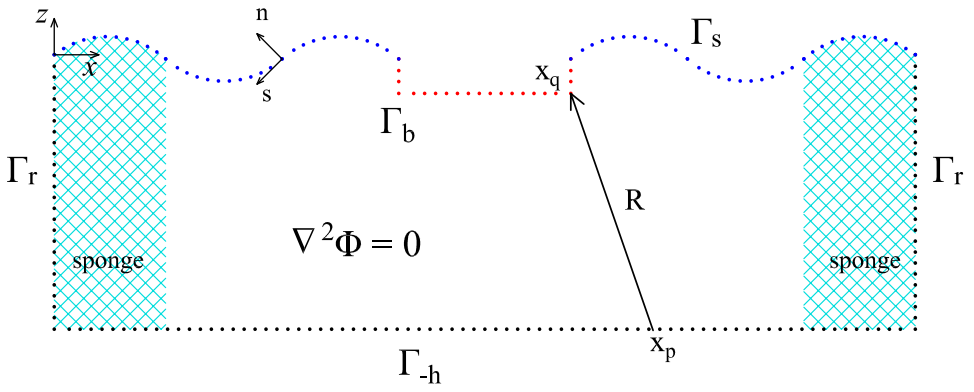


Figure 2.3: Discretised numerical domain enclosed by the free surface boundary, Γ_s, the moving wave maker boundary, Γ_b, the bed boundary, Γ_{-h}, and the end boundaries, Γ_r. Note: the stationary boundaries are denoted by ···, the free water surface by ···, and the moving rigid body by ···.

the numerical domain serve to damp out the wave energy generated by the forced motion of the rectangular body. The figure also illustrates the directions of the outward normal, **n**, and the corresponding tangential, **s**; the latter being defined as positive in an anti-clockwise direction.

Within a physical-space domain, the solution to the governing Laplace equation (equation 2.2) is the Green's function

$$G(p,q) = \frac{1}{2\pi}\ln(R), \tag{2.15}$$

where $R = |\mathbf{x}_p - \mathbf{x}_q|$; $\mathbf{x}_p$ and $\mathbf{x}_q$ being the position vectors of the source and evaluation points respectively (see figure 2.3). Using Green's function as a solution to the Laplace equation and applying Green's second identity yields the BIE as

$$C(p)\phi(p) = \int_\Gamma \left(\phi(q)\frac{\partial G(p,q)}{\partial n} - \frac{\partial \phi(q)}{\partial n}G(p,q)\right)\mathrm{d}\Gamma, \tag{2.16}$$

where $C(p)$ is a geometric coefficient reflecting the position of the source point on the boundary and is found using a rigid mode technique (Becker 1992). It should be noted that the BIE is expressed in terms of the potential, ϕ, and the normal potential flux, ϕ_n.

The use of physical-space domains ensures that the same numerical solution

can be used to simulate continuous and discontinuous bodies, among many other problems. Unfortunately, physical-space domains inevitably contain discontinuities, corresponding to corners in a 2D domain, and edges and corners in a 3D domain. Strictly speaking, the BIE (equation 2.16) is only valid over a smooth boundary, effectively assuming that ϕ and ϕ_n are continuous. However, figure 2.3 clearly indicates that the intersection of boundaries is not smoothly varying. In particular, there will be two discrete values of ϕ_n at each corner in a 2D domain. This dilemma is commonly referred to as the *corner problem*. It becomes particularly important when seeking to model a *discontinuous* body, not least because this introduces more corners (or discontinuities) at positions that represent a vital part of the required solution. The different approaches used to overcome this problem are outlined below.

2.4.2 Double nodes

In a 2D domain, the double-nodes approach involves placing an additional node at each corner so that there are two nodes occupying exactly the same position in space at every boundary intersection (Grilli & Svendsen 1990). Each of the two nodes is then assigned to one of the two normal fluxes and the BIE is evaluated for these additional nodes. In adopting this approach, compatibility conditions must be introduced to remove any unwanted discontinuities in the continuous variables (Grilli et al. 1989); examples of the latter being ϕ or (u, w) at the two overlying nodes.

2.4.3 Discontinuous elements

An alternative approach involves the use of discontinuous elements. Here, the nodes which would normally be placed at the corner are instead moved a short distance away from the discontinuity. In this way, the corner problem is avoided, but the interaction of the intersecting boundaries is not rigorously examined.

2.4.4 Multiple-flux BEM

In order to correctly model the interaction of waves and moving bodies, it is essential to provide an accurate treatment of the corner problem because, as seen in figure 2.3, corners become a central part of the required solution. To avoid the loss of any important effects, the use of compatibility conditions or discontinuous elements is avoided within the present study. This is achieved by adopting a multiple-flux approach.

The concept of multiple fluxes was first described in Brebbia & Dominguez (1992), with applications to various boundary value problems. However, its application to the modelling of surface water waves was first outlined in Hague & Swan (2009). This contribution provides a detailed account of the theory together with an extensive validation of the model including standing wave, regular wave and solitary wave effects. Following this work, Christou et al. (2008) applied the model to the study of submerged breakwaters and Christou et al. (2009) to the study of wave interaction on a wall. Details of the multiple-flux BEM are as follows:

Discretisation

The 2D numerical domain, depicted in figure 2.3, is made up of P nodes; each occupying a unique position in space. Quadratic isoparametric shape functions are used and therefore three nodes make up one element to give a total of $M = P/2$ elements. In the multiple-flux approach, one normal flux, ϕ_n, is specified for every node in each element to give a total of $3M$ normal potential fluxes. This means that there are two (multiple) normal fluxes at the intersection of every element, hence allowing for the definition of two distinct normal fluxes at each corner. The total number of tangential potential fluxes, ϕ_s, is also $3M$ as they too are discontinuous at the corners.

The evaluation of the BIE for the interaction of every node p with every node q is undertaken using numerical integration by Gaussian quadrature. This results

in the linear system of equations

$$\mathbf{H\Phi} = \mathbf{G\Phi_n}, \tag{2.17}$$

where $\mathbf{\Phi}$ is of size $(P \times 1)$, $\mathbf{H}$ is the matrix of $\int \frac{\partial G}{\partial n}$ and is of size $(P \times P)$; its diagonal entries absorbing the coefficient $C(p)$. Given the multiple flux formulation, $\mathbf{\Phi_n}$ is of size $(3M \times 1)$. Accordingly, $\mathbf{G}$ must be of size $(P \times 3M)$ and is the matrix of $\int G$. It should be noted that because $\mathbf{G}$ is dependent solely on the position of the nodes, it is a continuous variable and its values at the intersection between elements will be equal (including the intersection of corner elements).

The known entries of $\mathbf{\Phi}$ and $\mathbf{\Phi_n}$ in equation 2.17 are given by the complete set of boundary conditions. For the problem of wave generation by the forced motion of a rectangular body, depicted in figure 2.3, the boundary conditions are

$$\phi = \int \phi_t \mathrm{d}t \quad \text{on } \Gamma_s, \tag{2.18}$$

$$\phi_n = \mathbf{v} \cdot \mathbf{N} \quad \text{on } \Gamma_b, \tag{2.19}$$

$$\phi_n = 0 \quad \text{on } \Gamma_{-h} \text{ and } \Gamma_r. \tag{2.20}$$

Linear system of equations

From equations 2.18 to 2.20, it is clear that the boundary conditions along Γ_s are Dirichlet (specified in terms of ϕ), while Neumann boundary conditions (specified in terms of ϕ_n) act along the remaining boundaries: Γ_b, Γ_{-h} and Γ_r. As a result, the linear system of equations given in equation 2.17 cannot be solved for directly; the left-hand side containing known values of ϕ along Γ_s. Consequently, the numerical domain is divided into two sets of nodes: (i) those along Γ_s, numbering from 1 to P_s and depicted by the blue dots in figure 2.3, and (ii) the remaining nodes, numbering from $P_s + 1$ to P and depicted by the black and red dots in figure 2.3. For these two sets of nodes, the linear system of equations is expressed by

$$\mathbf{A}\boldsymbol{\varphi} = \mathbf{b}, \tag{2.21}$$

where $\mathbf{A}$ is the influence matrix, $\boldsymbol{\varphi}$ contains the nature of the unknown variables and $\mathbf{b}$ the values of the known variables. The entries of these matrices are as follows:

$$\varphi_q = \begin{cases} \left(\frac{\partial\phi}{\partial n}\right)_q & q = 1, ..., P_s \\ \phi_q & q = P_s + 1, ..., P, \end{cases} \tag{2.22}$$

for the unknown variables;

$$A_{pq} = \begin{cases} \int G_{pq} \mathrm{d}q & q = 1, ..., P_s \\ \int \left(\frac{\partial G}{\partial n}\right)_{pq} \mathrm{d}q & q = P_s + 1, ..., P, \end{cases} \tag{2.23}$$

for the influence matrix; and

$$b_p = \sum_{q=1}^{P_s} \int \left(\frac{\partial G}{\partial n}\right)_{pq} \mathrm{d}q\phi_q + \sum_{q=P_s+1}^{P} \int G_{pq} \mathrm{d}q \left(\frac{\partial \phi}{\partial n}\right)_q \tag{2.24}$$

for the known values. Given a set of P independent equations, a total of P unknowns can be solved. Therefore, one value of ϕ_n can be obtained for each node along Γ_s, or $q = 1, ..., P_s$; the two ϕ_n values at the intersection of elements along the free surface being assumed to be equal. The linear system of equations is solved using GMRES, with Jacobi pre-conditioning as described in Christou (2009).

Time-marching the solution

At this point in the solution, the values of ϕ and ϕ_n everywhere in the domain are known. However, this is not the end of the numerical solution since the numerical model is fully nonlinear and the evolution of the interacting wave field is the primary objective. The key to a fully nonlinear solution lies in the application of the boundary conditions on the *instantaneous* position of the boundaries. This is achieved through the implementation of the so-called Mixed Eulerian-Lagrangian (MEL) method, first used by Longuet-Higgins & Cokelet (1976). Within this method, the boundary conditions are solved in an Eulerian frame of reference, while the position of the nodes along moving boundaries changes with time; the latter being characteristic of a Lagrangian frame of reference. The reader is reminded that an Eulerian description considers the fluid motion at a location fixed

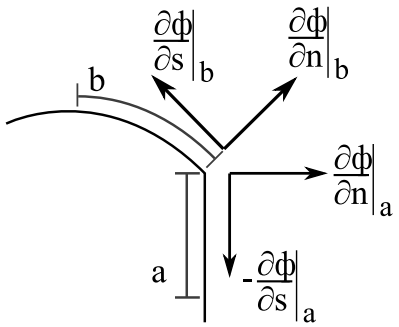


Figure 2.4: Potential fluxes at a corner intersection of element a and element b.

in space, while a Lagrangian description considers the motion (and trajectory) of individual fluid particles.

In the context of the numerical model, the nodes are modelled in two frames of reference: semi-Lagrangian and fully-Lagrangian. Semi-Lagrangian motion involves nodes moving in the vertical direction with the fluid velocity w, but being fixed in the horizontal direction. Fully-Lagrangian motion involves the nodes moving both horizontally and vertically with (u, w). The advantage of semi-Lagrangian motion over fully-Lagrangian motion is that, when fixed in x, nodes along the free surface boundary cannot drift. It is desirable to avoid the drifting of nodes not least because as the nodes get closer together, Green's function becomes singular and the numerical simulation cannot continue. However, any simulation involving surge or pitch motion of a rigid body must involve the use of a fully-Lagrangian frame of reference.

The fluid velocity (u, w) at any nodal point is determined using ϕ_n and ϕ_s; the latter being the tangential gradient of ϕ calculated within a sliding element. To illustrate one of the key advantages of the multiple-flux BEM, consider the calculation of (u, w) at a corner node. The normal and tangential potential fluxes at the corner intersection of element a and element b are depicted in figure 2.4. In solving the multiple-flux boundary element formulation, all of the fluxes are defined without the need for additional compatibility conditions; the latter being necessary in a double-node formulation (Grilli et al. 1989). However, the normal fluxes are calculated with greater accuracy, being independent of any sliding ele-

ment approximation. Therefore, the horizontal and vertical fluid velocities of the corner node are defined using information relating to the element whose normal flux is predominantly in the direction of the required velocity component. This leads to the following results:

$$\begin{aligned} u &= \left.\frac{\partial\phi}{\partial n}\right|_a N_1|_a - \left.\frac{\partial\phi}{\partial s}\right|_a N_2|_a \\ w &= \left.\frac{\partial\phi}{\partial n}\right|_b N_2|_b + \left.\frac{\partial\phi}{\partial s}\right|_b N_1|_b, \end{aligned} \tag{2.25}$$

where $N_1|_a$, $N_2|_a$ and $N_1|_b$, $N_2|_b$, are found using equation 2.11. This approach ensures that the normal fluid velocities calculated along lateral boundaries satisfy the lateral boundary condition. The latter is especially important when considering the intersection of a moving rigid body and the moving free water surface.

Having defined the fluid velocities at each node on the water surface, a fourth-order Runge-Kutta scheme is used to time-march the free surface boundary conditions (equations 2.4 and 2.5). This takes the form

$$(f)_{t_0+\Delta t} = (f)_{t_0} + \frac{\Delta t}{6}\left[\left(\dot{f}\right)_{t_0} + 2\left(\dot{f}\right)^{(1)}_{t_0+\Delta t/2} + 2\left(\dot{f}\right)^{(2)}_{t_0+\Delta t/2} + \left(\dot{f}\right)^{(3)}_{t_0+\Delta t}\right], \tag{2.26}$$

where the superscript $\dot{}$ denotes a time derivative and the superscripts (1), (2) and (3) denote the first, second and third intermediate steps, while the subscripts outside the parentheses denote the times at which the values are determined. This results in a new set of boundary conditions to be solved and, in this way, the solution is progressed in time.

2.5 Calculating force and body motion

Section 2.4.4 has illustrated how the multiple-flux BEM is applied to the problem of wave generation by the forced motion of a rigid *discontinuous* body. Before presenting the various methods used to calculate force and wave-induced body motion, the origins of the forces acting on a body moving in a fluid are discussed.

The evaluation of the force on a body has been considered by, among others, Mei (1994) and more recently by Falnes (2005) and Cruz (2008). The relationship

between the fluid-induced forces acting on a body and its subsequent motion is described in Cruz (2008) as

$$\mathrm{M}\mathbf{a} = \mathbf{F}^{exc} - \mathbf{F}^{rad}, \tag{2.27}$$

where M is the physical mass matrix, $\mathbf{a}$ is the body acceleration vector; $a_1 = \ddot{\xi}_1$, $a_2 = \ddot{\xi}_2$ and $a_3 = \ddot{\xi}_3$. Further $\mathbf{F}^{exc}$ is the exciting force and $\mathbf{F}^{rad}$ is the radiated force. The origins of $\mathbf{F}^{exc}$ and $\mathbf{F}^{rad}$ are considered below.

Within Cruz (2008), $\mathbf{F}^{exc}$ is described as the force that the body experiences when held fixed in its equilibrium position. As a result, the contributions to $\mathbf{F}^{exc}$ include the forces due to the incident wave conditions and the scattered wave field; the latter arising due to the presence of a rigid body. Mathematically, the exciting force is found by integrating the pressure, p, over the instantaneous wetted surface of the body; the pressure distribution being defined by Bernoulli's equation. The exciting force is given by

$$\begin{aligned} F_j^{exc} &= \int_{\Gamma_b} pN_j \mathrm{d}\Gamma - \mathrm{K}_s\boldsymbol{\xi} \\ &= \int_{\Gamma_b} \left[-\rho\left(\phi_t + gz + \frac{1}{2}\left(u^2 + w^2\right)\right) N_j \right] \mathrm{d}\Gamma - \mathrm{K}_s\boldsymbol{\xi}, \end{aligned} \tag{2.28}$$

where $j = (1, 2, 3)$ identifies each of the three degrees of freedom, ρ is the density of the fluid and K_s is the spring constant associated with the body displacement, $\boldsymbol{\xi}$. The last term in equation 2.28 reflects the change in the body's buoyancy as it moves. The equation shows that the scalar pressure distribution is converted into the three components of the external force through the use of $\int_{\Gamma_b} N_j \mathrm{d}\Gamma$. Once again, it is emphasised that the values of ϕ_t, z, u, w and N_j adopted in equation 2.28 must correspond to a wave field based upon the incident and scattered potentials only.

The radiated force, $\mathbf{F}^{rad}$, is the force due to the motion of the body. It may be expressed using the approximate form of the equation of motion,

$$\mathbf{F}^{rad} = \mathrm{M}_a\mathbf{a} + \mathrm{C}_s\mathbf{v}, \tag{2.29}$$

where M_a is the added mass matrix associated with the acceleration of the body, $\mathbf{a}$ and C_s is the hydrodynamic damping matrix associated with the body velocity,

$\mathbf{v}$. It should be noted that, in this form, the added mass and hydrodynamic damping are constants; typically being evaluated through a decay test. In this latter case, the body's response to an initial displacement is modelled using the classical solution for a free damped oscillation (outlined in Appendix D), from which the damped frequency and the damping coefficient can be obtained. These terms are then related to the added mass and the hydrodynamic damping of the body, again described in Appendix D. The added mass and the hydrodynamic damping are related to the wave field generated by the motion of the body and require further discussion.

A linearised solution for the wave field generated by a moving wave maker was presented in terms of an analytical solution in Section 2.3.3. This described the wave field as consisting of a single propagating wave mode and an infinite series of evanescent wave modes; the latter only being appreciable close to the wave maker boundary. Consequently, the hydrodynamic damping (of an inviscid system) may be described in terms of the propagating wave mode, radiating energy away from the body. Furthermore, the evanescent wave modes represent the body's added mass, remaining close to the body boundary. It is easily shown that the propagating wave mode and evanescent wave modes are 90° out of phase at the body boundary. This reflects the fact that the hydrodynamic damping is associated with the body velocity, while the added mass is associated with the body acceleration.

As described above, $\mathbf{F}^{exc}$ and $\mathbf{F}^{rad}$ are evaluated from the contributions of the incident, scattered and radiated wave fields separately. However, the numerical model described in Section 2.4.4 solves for the total wave field or the interaction of the incident, scattered and radiated potentials. Therefore, the relationship between the force and the body motion is simply taken from Newton's 2^{nd} law

$$\mathbf{F} = \mathrm{M}\mathbf{a}. \tag{2.30}$$

In order to capture the various origins of $\mathbf{F}$ (described separately as $\mathbf{F}^{exc}$ and $\mathbf{F}^{rad}$ above), the numerical model must properly account for the effects of the radiated

potential; the latter defining the radiated propagating wave and the associated evanescent wave modes. Various methods for numerically calculating F_j and the wave-induced acceleration of the body, a_j, are presented below.

2.5.1 Backwards finite difference

Backwards finite difference is used to carry out the numerical differentiation of a variable whose forward value is unknown; an example being the differentiation of any variable which is a function of time and whose future value is unknown. The time-marching scheme introduced in Section 2.4.4 is defined by a fourth order Runge-Kutta integration. As a result, any backwards finite difference method should also be accurate to fourth order. Such a scheme is given in Koo (2003) as

$$\left(\frac{dS}{dt}\right)_{t_0+\Delta t} = \frac{1}{4\Delta t}\left[-2\,(S)_{t_0} - 4\,(S)^{(1)}_{t_0+\Delta t/2} - 4\,(S)^{(2)}_{t_0+\Delta t/2} + 10\,(S)^{(3)}_{t_0+\Delta t}\right] - \frac{1}{2}\left(\frac{dS}{dt}\right)_{t_0}, \tag{2.31}$$

where S represents any function and Δt is the time step. If S is taken to be ϕ around the body, equation 2.31 can be used to calculate ϕ_t. This, in turn, may be directly used in Bernoulli's equation (equation 2.28) to obtain the force on the body. However, F_j found in this way cannot be used in Newton's 2^{nd} law (equation 2.30) to predict wave-induced body motion because it does not include any free surface effects and therefore cannot properly account for the radiated force on the body. Similar conclusions have been made by Tanizawa (1995), who states that with the use of backwards finite difference in ϕ for wave-induced motion simulations, the hydrodynamic equilibrium of forces is not guaranteed. For example, the work of Sen (1993) applied the backwards finite different method to the problem of wave-induced body motion and encountered saw-tooth instabilities.

2.5.2 The Isaacson Method

One of the difficulties in modelling the radiated force lies in the fact that one of its contributions is associated with the body velocity, while the other is associated with its acceleration. The approach presented in Isaacson (1982) overcomes this

difficulty by substituting for the body velocity in the moving body boundary condition, using an expression for the unknown body acceleration; the latter being derived using Newton's 2^{nd} Law. The following paragraphs summarise the approach adopted by Isaacson (1982), hereafter referred to as the Isaacson Method, by first providing the expression for F_j and then outlining how the wave-induced motion is determined.

Calculation of force

Isaacson (1982) provides the expression for the force, F_j, based upon Bernoulli's equation (equation 2.28) as

$$F_j = \int_{\Gamma_b} \left[-\rho \frac{d\left(\phi N_j\right)}{dt} + \rho\phi \frac{dN_j}{dt} - \rho \left(gz + \frac{1}{2}\left(u^2 + w^2\right) \right) N_j \right] \mathrm{d}\Gamma, \tag{2.32}$$

where the sum of the first two terms defines the dynamic pressure. In adopting this expression, backwards finite difference is used to find the d/dt terms. As a result, this expression for F_j is valid for problems involving a fixed body or a body undergoing forced motion. However, for the prediction of wave-induced motion, equation 2.32 is merely the first step in the approach described below.

Prediction of wave-induced motion

Substituting the expression of F_j (equation 2.32) into Newton's 2^{nd} Law (equation 2.30), Isaacson (1982) gives

$$m_j a_j + \int_{\Gamma_b} \left(\rho \frac{d\left(\phi N_j\right)}{dt} \right) \mathrm{d}\Gamma = \int_{\Gamma_b} \left[\rho\phi \frac{dN_j}{dt} - \rho \left(gz + \frac{1}{2}\left(u^2 + w^2\right) \right) N_j \right] \mathrm{d}\Gamma, \tag{2.33}$$

where m_j is the body mass. When this expression is integrated with respect to time, it yields

$$\left(m_j v_j + \rho \int_{\Gamma_b} \phi N_j \mathrm{d}\Gamma \right)_{t_0+\Delta t} = H_j, \tag{2.34}$$

where

$$H_j = \left(m_j v_j + \rho \int_{\Gamma_b} \phi N_j \mathrm{d}\Gamma \right)_{t_0} + \frac{\Delta t}{6} \left[\left(h_j\right)_{t_0} + 2\left(h_j\right)^{(1)}_{t_0+\Delta t/2} + 2\left(h_j\right)^{(2)}_{t_0+\Delta t/2} + \left(h_j\right)^{(3)}_{t_0+\Delta t} \right] \tag{2.35}$$

and

$$h_j = \int_{\Gamma_b} \left[\rho\phi \frac{dN_j}{dt} - \rho \left(gz + \frac{1}{2}\left(u^2 + w^2\right) \right) N_j \right] \mathrm{d}\Gamma. \tag{2.36}$$

At this stage it should be noted that the expression for H_j given in equation 2.35 differs from that originally presented in Isaacson (1982). The difference arises solely due to the time-marching scheme; a fourth order Runge-Kutta scheme having been used throughout the present study. The expression for the body velocity, to be used in the moving body boundary condition, is then taken as

$$(v_j)_{t_0+\Delta t} = \frac{H_j}{m_j} - \frac{\rho}{m_j} \int_{\Gamma_b} (\phi N_j)_{t_0+\Delta t} \, \mathrm{d}\Gamma. \tag{2.37}$$

The difficulty with this expression lies in the use of $(\phi)_{t_0+\Delta t}$, which is *unknown* on the moving body boundary. To overcome this difficulty, three sets of nodes make up the numerical domain within the Isaacson Method. These are closely related to the nodes identified in figure 2.3, but the formulation of the problem is handled differently to that given in Section 2.4.4. The first set contains the nodes along the free surface Γ_s, indicated in blue on figure 2.3. The second set occurs along the moving body Γ_b, indicated in red; while the third and final set contains the remaining nodes, indicated in black. Assume that the nodes are numbered $1, ..., P_s$ along Γ_s, $P_s + 1, ..., P_b$ along Γ_b, and $P_b + 1, ..., P$ along the rest of the boundary Γ. Adopting this approach, the entries in the influence matrix and the known values are defined by Isaacson (1982) as

$$A_{pq} = \begin{cases} \int G_{pq} \mathrm{d}q & q = 1, ..., P_s \\ \int \left(\frac{\partial G}{\partial n}\right)_{pq} \mathrm{d}q - \sum_{l=P_s+1}^{P_b} \left(\frac{\partial G}{\partial n}\right)_{pl} \sum_{j=1}^{3} \frac{\rho}{m_j} (N_j)_l \int (N_j)_q \, \mathrm{d}q & q = P_s + 1, ..., P_b \\ \int \left(\frac{\partial G}{\partial n}\right)_{pq} \mathrm{d}q & q = P_b + 1, ..., P \end{cases} \tag{2.38}$$

$$b_p = \sum_{q=1}^{P_s} \int \left(\frac{\partial G}{\partial n}\right)_{pq} \mathrm{d}q \phi_q + \sum_{q=P_s+1}^{P_b} \int G_{pq} \mathrm{d}q \sum_{j=1}^{3} (N_j)_q \frac{H_j}{m_j} + \sum_{q=P_b+1}^{P} \int G_{pq} \mathrm{d}q \left(\frac{\partial \phi}{\partial n}\right)_q. \tag{2.39}$$

A complete derivation of these equations is given in Appendix B. Comparisons between equations 2.23 and 2.38 illustrates how the influence matrix in the Isaacson Method differs from the influence matrix for the multiple-flux BEM described in

Section 2.4.4. Specifically, the difference lies in the additional sum over the moving body nodes, $\sum_{l=P_s+1}^{P_b}$, in equation 2.38 of the Isaacson Method; resulting from the fact that equation 2.38 applies to a formulation involving wave-induced (therefore unknown) motion of the body. The physical significance of this difference is thought to be as follows. The use of Green's function represents point wave sources (Isaacson 1978) and the effect of these point wave sources on the rest of the numerical domain is determined through the use of the BIE. Consequently, the additional $\sum_{l=P_s+1}^{P_b}$ term is thought to represent the wave sources due to the wave-induced motion of the body and therefore the radiated force.

2.5.3 Acceleration potential

For greater accuracy, the use of the backwards finite difference method in the prediction of the wave-induced motion (as in the Isaacson Method) must be avoided. Tanizawa (1995) provides an alternative to the Isaacson Method which is based on the description of the acceleration potential, Φ. Details of this are as follows.

The acceleration potential is based on the time derivative of the velocity potential, ϕ; the latter being a function of both time and space. The acceleration potential is therefore defined as

$$\Phi = \frac{\partial \phi}{\partial t} + \frac{1}{2}\left(\nabla \phi\right)^2. \tag{2.40}$$

Using this result, the moving body boundary condition is simply

$$\frac{\partial \Phi}{\partial n} = \mathbf{a} \cdot \mathbf{N} \quad \text{on } \Gamma_b, \tag{2.41}$$

where $\mathbf{a}$ is the body acceleration.

In order to model wave-induced motion, the solution adopted in Tanizawa (1995) considers the acceleration and velocity fields separately. This is achieved by solving two Boundary Value Problems (BVP):

(i) a BVP expressed in terms of ϕ, as described in Section 2.4.4, and

(ii) a BVP in terms of ϕ_t.

It should be noted that the second BVP is expressed in terms of ϕ_t because the nonlinear term in Φ (equation 2.40) implies that Φ does not satisfy the Laplace equation. Consequently, the moving body boundary condition in terms of ϕ_t is given by Tanizawa (1995) as

$$\frac{\partial \phi_t}{\partial n} = \sum_{j=1}^{3} a_j N_j + N_1 \left[v_3^2 \left(x - r_x - \xi_1 \right) - 2 v_3 \left(w - v_2 \right) \right] + N_2 \left[v_3^2 \left(z - r_z - \xi_2 \right) + 2 v_3 \left(u - v_1 \right) \right] + \frac{\partial \phi}{\partial n} \frac{\partial}{\partial s} \left(\frac{\partial \phi}{\partial s} \right) - \frac{\partial \phi}{\partial s} \frac{\partial}{\partial s} \left(\frac{\partial \phi}{\partial n} \right) \quad \text{on } \Gamma_b; \tag{2.42}$$

a detailed derivation of this result being given in Appendix C. The first three terms of equation 2.42 define the normal acceleration of the body, $\mathbf{a} \cdot \mathbf{N}$ in equation 2.41; the large number of terms arising because the body coordinate system moves within the global coordinate system (see Appendix C for further details). In contrast, the last two terms of equation 2.42 relate to $\frac{\partial}{\partial n} \left(\frac{1}{2} \left(\nabla \phi \right)^2 \right)$, which is required to obtain $\frac{\partial \phi_t}{\partial n}$ from equation 2.41. Considering equation 2.42 as a whole, it should be noted that the first term $(a_j N_j)$ contains the *unknown* body acceleration. The remaining terms are the known velocity and displacement of the body, or the characteristics of the wave field determined from the solution of the ϕ BVP.

The consequence of the unknown acceleration term in the body boundary condition for the ϕ_t BVP is that two (different) influence matrices must be formulated within the method described in Tanizawa (1995). The influence matrix for the ϕ_t BVP involves three sets of nodes, while that for the ϕ BVP involves only two sets of nodes. Unfortunately, the formulation of an influence matrix (which involves the integration of the BIE) is the most computationally intensive part of a BEM solution (Archibald 2008). As a result, any solution involving a second BVP expressed in terms of ϕ_t is undesirable.

2.5.4 The Indirect Method

Wu & Eatock-Taylor (1996) and, more recently, Kashiwagi (2000) and Bai & Eatock-Taylor (2006) describe an Indirect Method that introduces an auxiliary

function for each degree of freedom, ψ_j. In effect, these functions define the unsteady component of the acceleration potential arising due to each motion mode. As such, each auxiliary function satisfies the Laplace equation. This approach is similar to the mode decomposition method described in Cointe et al. (1990) and Vinje & Brevig (1981). In a 2D analysis, the Indirect Method is described in Kashiwagi (2000) to involve four BVPs: one in ϕ and three in ψ_j. However, as indicated below, the same influence matrix is used for all the BVPs. This represents a considerable advantage over a solution involving a second BVP in terms of ϕ_t (Section 2.5.3). A brief summary of the Indirect Method is given below. This first provides the derivation of the expression for F_j, which is followed by an outline of the solution procedure for the wave-induced body motion.

Calculation of force

Kashiwagi (2000) gives the boundary conditions for the BVPs in terms of ϕ_t and ψ_j as

$$\frac{\partial \phi_t}{\partial n} = 0, \quad \tfrac{\partial \psi_j}{\partial n} = 0, \quad \text{on } \Gamma_{-h}, \tag{2.43}$$

$$\frac{\partial \phi_t}{\partial n} = 0, \quad \tfrac{\partial \psi_j}{\partial n} = 0, \quad \text{on } \Gamma_r, \tag{2.44}$$

$$\phi_t = -gz - \frac{1}{2}\left(u^2 + w^2\right), \quad \psi_j = 0, \quad \text{on } \Gamma_s, \tag{2.45}$$

$$\frac{\partial \phi_t}{\partial n} = \sum_{j=1}^{3} a_j N_j + \mu_b, \quad \tfrac{\partial \psi_j}{\partial n} = N_j, \quad \text{on } \Gamma_b, \tag{2.46}$$

where μ_b represents the last four terms of equation 2.42. With respect to the boundary conditions in terms of ψ_j, the only non-zero condition is on the moving body and this is expressed in terms of the *known* normal, N_j. Consequently, the influence matrix for the ϕ BVP can be used in the ψ_j BVP.

To illustrate how ψ_j is used to evaluate F_j, consider that both ϕ_t and ψ_j satisfy the Laplace equation. Consequently, Bai & Eatock-Taylor (2006) show that

$$\int_\Gamma \left(\phi_t \frac{\partial \psi_j}{\partial n} - \frac{\partial \phi_t}{\partial n} \psi_j \right) \mathrm{d}\Gamma = 0. \tag{2.47}$$

When Γ is split into $\Gamma = \Gamma_{-h} + \Gamma_r + \Gamma_s + \Gamma_b$ and the appropriate boundary condition values are substituted into equation 2.47, using equations 2.43 to 2.46, the force

on the body is defined by

$$F_j = -\rho \int_{\Gamma_b} \psi_j \left(\sum_{l=1}^{3} a_l N_l + \mu_b \right) \mathrm{d}\Gamma + \rho \int_{\Gamma_b + \Gamma_s} \left(-gz - \frac{1}{2}\left(u^2 + w^2\right) \right) \frac{\partial \psi_j}{\partial n} \mathrm{d}\Gamma. \quad (2.48)$$

Further insight into the fundamentals of this approach is given as follows. Johansson (1989) considers the radiation problem (wave generation by forced body motion) and decomposes the velocity potential as follows

$$\phi = \hat{\phi}_1 v_1 + \hat{\phi}_2 v_2 + \hat{\phi}_3 v_3, \quad (2.49)$$

where $\hat{\phi}_j$ is the spatial velocity potential associated with the radiation problem in each degree of freedom, $j = 1, 2, 3$. As the velocity potential is expressed as the product of $\hat{\phi}_j$ and v_j, the moving body boundary condition in $\hat{\phi}_j$ is simply

$$\frac{\partial \hat{\phi}_j}{\partial n} = N_j \quad \text{on } \Gamma_b. \quad (2.50)$$

Consequently, it can be seen that the body boundary condition for $\hat{\phi}_j$ (equation 2.50) and ψ_j (equation 2.46) are identical. This suggests the use of ψ_j in the Indirect Method accounts for the radiated force.

Prediction of the wave-induced motion

When predicting the wave-induced motion, the body acceleration must be solved, and Kashiwagi (2000) argues it is more convenient to express equation 2.48 as

$$F_j = -\sum_{l=1}^{3} a_l D_{jl} + Q_j, \quad (2.51)$$

where D_{jl} is

$$D_{jl} = \int_{\Gamma_b} \psi_j N_l \mathrm{d}\Gamma \quad (2.52)$$

and

$$Q_j = -\rho \int_{\Gamma_b} \psi_j \mu_b \mathrm{d}\Gamma + \rho \int_{\Gamma_b + \Gamma_s} \left(-gz - \frac{1}{2}\left(u^2 + w^2\right) \right) \frac{\partial \psi_j}{\partial n} \mathrm{d}\Gamma, \quad (2.53)$$

Recalling that $F_j = m_j a_j$, equation 2.51 gives

$$m_j a_j + \sum_{l=1}^{3} a_l D_{jl} = Q_j. \quad (2.54)$$

This provides the three simultaneous equations, necessary to obtain the three components of the body acceleration in 2D. Once evaluated, this acceleration is time-marched to give the body velocity, which is then used in the body boundary condition of the ϕ BVP.

2.6 Conclusions

This chapter has presented the background theory for the work undertaken within this thesis. It introduced the moving body boundary condition and described how the use of the normal vector allows for this boundary condition to be applicable to any body shape. The analytical solution to linear regular wave theory and linear wave maker theory were presented; the latter introducing the differences between the propagating and evanescent wave modes.

An outline of the multiple-flux BEM was provided for the problem of wave generation by the forced motion of a rectangular body. Most importantly, the description of the method used in the calculation of the fluid velocity (u, w) illustrated how the multiple-flux approach rigorously addresses the corner problem inherent of any BEM solution.

In order to model wave-induced body motions, the force on the body due to the surrounding wave field must first be evaluated. The origins of this force were shown to be split into the exciting force, due to the incident and scattered wave potentials, and the radiated force, due to the radiated potential. Various methods for calculating the force and wave-induced motion were outlined. Within the Isaacson Method, the additional wave sources around the body are believed to account for the radiated force. Furthermore, the ψ_j body boundary condition was likened to the body boundary condition for the spatial radiation potential; thereby representing the radiated force in the Indirect Method.

The incorporation of the Isaacson Method and the Indirect Method into the multiple-flux BEM represents a major development undertaken by the author. The validation of the new numerical model is considered in the next chapter. The first

set of validations includes the evaluation of the force on a moving body; given by equation 2.32 for the Isaacson Method and equation 2.48 for the Indirect Method. However, this is merely one of the many single-body applications considered.

3

Model validation

3.1 Introduction

The validation of the new numerical model is described in this chapter. Although the overall aim is to apply the model to problems involving multiple bodies in close proximity, the validation will be based upon single-body applications since these provide comparative solutions.

The first set of comparisons involves the forced motion of both continuous and discontinuous bodies. By considering forced body motions, the validation is much simplified; the motion of the body being prescribed and the generated wave field being the main area of interest. In the first example, the propagating and evanescent wave modes generated by a bottom-hinged flap-type wave maker are validated against the analytical solution of wave maker theory. In addition to the generated wave field, this validation considers the three components of the force acting on the wave maker in a 2D analysis. Within the numerical solution, this force is calculated using both the Isaacson Method and the Indirect Method, described in Chapter 2. In the second example, the radiation of waves by the forced motion of a rectangular body is considered. As this involves a discontinuous body, it is more complex than the wave maker problem. In this case, the propagating wave mode is validated against the numerical results presented in Black et al. (1971).

In a third example, the forces acting on a fixed rectangular body in incident regular waves is considered. Although a fixed body involves zero body motion, the applied force corresponds to the exciting force, $\mathbf{F^{exc}}$. This was first introduced in Chapter 2 and represents one of the two contributions to the force acting on a body undergoing wave-induced motion.

Before extending the work to consider wave-induced motions, a fourth set of examples involving decay tests is presented. These tests represent a, predominantly experimental, technique used to determine the hydrodynamic properties of a body through its response to an initial displacement in an otherwise stagnant (or still) environment. As such, these examples constitute an important intermediate step between forced and wave-induced motions; the reasoning being as follows. Although both forced motion and decay tests involve zero incident wave conditions, in the latter case only the *initial* displacement of the body is known. Indeed, all subsequent body motion in the decay test must be predicted using the force on the body. In this respect, it is similar to wave-induced motions. However, in decay tests, the force on the body may be interpreted as a radiated force, $\mathbf{F^{rad}}$; corresponding to the force due to the motion of the body as it generates waves in the surrounding fluid. In contrast, the force on a body undergoing wave-induced motions includes the radiated force as well as the exciting force; the latter having been dealt with in the fixed-body simulations. The calculations involving the decays tests allow a comparison of the time-history of the body's response; the comparison being between experimental observations and an equivalent numerical simulation. These tests also serve to illustrate the extent to which the numerical solution is able to model the physical properties of an experimental setup.

The present chapter ends with a final example involving wave-induced body motions. This involves both the surrounding wave field and the body motion; the numerical results being compared with experimental data. In addition, comparisons are provided where the wave-induced body motion is based upon the linear superposition of the (separately-evaluated) exciting and radiated forces, hereafter referred to as the superposition motion. This is achieved by solving $\mathbf{F}$ =M$\mathbf{a}$ where

$\mathbf{F} = \mathbf{F}^{\mathbf{exc}} - \mathbf{F}^{\mathbf{rad}}$ (see Section 2.5). These results show that the linear motion predicted using the superposition method agrees well with the linear motion in the wave-induced simulations. This has important practical implications, not least because the superposition method is commonly adopted in industrial codes.

3.2 Validation of forced motions

In these cases the body motion is prescribed and the calculations seek to determine the generated wave field. Two examples of this type are addressed; the first considers a moving flap-type wave maker and the second a rectangular body moving with a single degree of freedom.

3.2.1 Wave maker theory

The problem considered within this section is that of wave generation by the forced motion of a bottom-hinged flap-type wave maker. In this case, the numerical calculations are compared with an analytical solution of linear wave maker theory; the latter being described in Section 2.3.3 and Appendix A. In making these comparisons the following parameters are considered:

(i) The amplitude of the propagating wave mode.

(ii) The amplitude sum of the evanescent wave modes, evaluated and predicted 0.1m from the surface of the wave maker; the latter location chosen to ensure that the amplitudes of the evanescent modes remain appreciable (see Chapter 2).

(iii) The force exerted on the wave maker by the generated wave field.

Definition of cases

The most comprehensive set of comparisons between the numerical calculations and the analytical solution concerns the variation over frequency. In the analyt-

ical solution, the required terms can be determined with a fine discretisation (in frequency) such that they are effectively continuous. However, the numerical predictions involve time-domain simulations and the results are therefore discrete in terms of the frequency.

A total of thirteen numerical runs were considered; the details being presented in Table 3.1. In considering these data, it should be noted that a scale of 1:100 is applied to the lengthscales. This scaling is applicable to all the results presented in this chapter. Table 3.1 defines:

(i) The frequency of the wave maker motion, f.

(ii) The amplitude of the angular displacement of the wave maker, $\hat{\xi}_3$.

(iii) The dimensionless wave maker motion at the still water level, $k_0 X_a$; where k_0 is the real wave number, $X_a = h \tan \hat{\xi}_3$ is the amplitude of the wave maker motion at still water level and h is the still water depth.

(iv) The steepness of the (generated) propagating wave mode, $k_0 H/2$, where H is the wave height found using the analytical solution.

The variation in the $\hat{\xi}_3$ values, provided in Table 3.1, indicates that the study involves a broad range of wave maker motion. In considering these cases, it is important to recall that the linear analytical solution assumes that both the free surface boundary and the wave maker boundary are *stationary*. In contrast, within the fully nonlinear numerical model the respective boundary conditions are applied on the instantaneous position of the *moving* boundaries. The expressions $k_0 X_a$ and $k_0 H/2$ indicate the steepness of the wave maker motion and of the propagating wave mode respectively. As a result, an effort was made to keep both $k_0 X_a$ and $k_0 H/2$ within the numerical simulations less than 0.1 such that the motion of the boundaries can be considered linear. Consequently, $k_0 X_a$ (or the wave maker motion) determines the values of $\hat{\xi}_3$ at the low frequency end of the table, while $k_0 H/2$ (or the free surface motion) determines $\hat{\xi}_3$ at the high frequency end. Finally, it should be noted that for the longest wave case $k_0 X_a$ is larger than $k_0 H/2$,

f [Hz]	$\hat{\xi_3}$ [rad]	$k_0X_a[-]$	$k_0H/2$ [-]
0.406	0.060	0.04	0.02
0.594	0.060	0.07	0.05
0.703	0.060	0.09	0.08
0.797	0.055	0.10	0.10
0.844	0.045	0.09	0.10
0.906	0.035	0.08	0.10
0.953	0.030	0.08	0.10
1.000	0.025	0.07	0.09
1.047	0.025	0.08	0.11
1.094	0.020	0.07	0.10
1.156	0.020	0.08	0.11
1.203	0.015	0.06	0.09
1.297	0.015	0.07	0.11

Table 3.1: Details of the wave cases simulated using a moving wave maker.

but much less than 0.1. This is due to an additional restriction imposed upon the numerical simulations; X_a being limited to the node spacing along the free surface boundary of the numerical domain (0.04m). It should also be noted that the time-step adopted in these simulations is 0.005s.

Separating the propagating wave mode and the evanescent modes

The analytical solution separates the velocity potentials associated with the propagating and the evanescent wave modes. In contrast, the numerical model describes the total velocity potential. As a result, a method must be established to determine the amplitudes of the propagating and the evanescent wave modes based upon the numerical calculations. In considering these comparisons, it is important to recognise that they represent the first ever description of the evanescent wave mode amplitudes based upon a fully nonlinear numerical wave maker (or

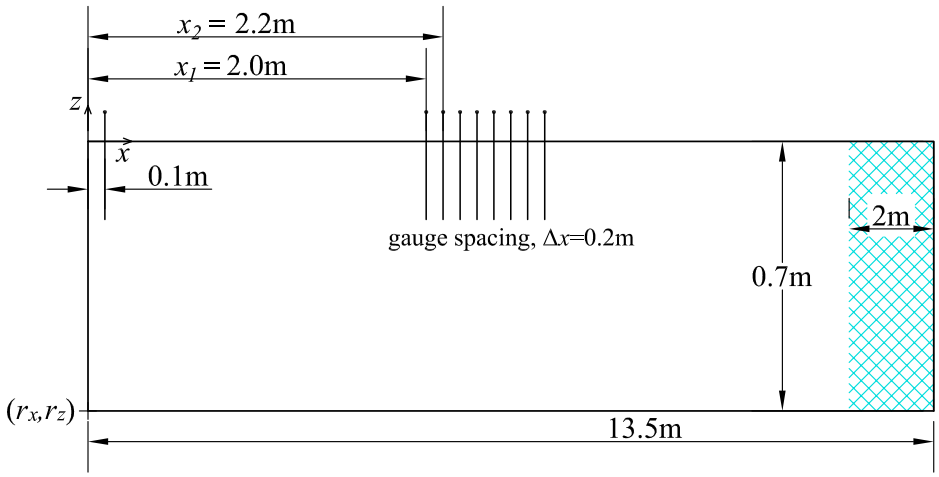


Figure 3.1: Details of the numerical wave tank for a moving flap-type wave maker. Note: the vertical lines within the domain indicate the position of the numerical wave gauges and the shaded area indicates the sponge layer.

wave-structure interactions) model.

Figure 3.1 outlines the numerical wave tank used in the moving wave maker simulations. It illustrates the position of numerical 'wave gauges' at which the water surface elevation, $\eta(t)$, is determined using quadratic interpolation between the spatial coordinates (x, z) of the nodes along the free surface boundary. In considering this layout, the reader is reminded that the amplitude sum of the evanescent wave modes decays exponentially in x. As a result, only the propagating wave mode is present at the group of wave gauges located at $x \geq 2.0$m (see figure 3.1). In contrast, the wave gauge located at x = 0.1m records both the propagating and the evanescent wave modes. Furthermore, the propagating and evanescent wave modes are 90° out of phase on the surface of the wave maker, x = 0m (see Appendix A for further details). As a result, there is a phase difference between the surface elevation at x = 0.1m and the propagating wave mode at x = 0.1m. This fact is key in determining the amplitude sum of the evanescent wave modes as outlined below.

In undertaking the present study, the prescribed motion of the wave maker is sinusoidal in time, generating regular waves. A frequency content analysis is

undertaken using a Fast Fourier Transform (FFT). The FFT is applied to the time-history of η calculated at each wave gauge location indicated in figure 3.1; the data record corresponding to the fully developed or established wave conditions. The length of the data record used varies from case to case because it corresponds to an integer number of generated wave periods. This ensures that the frequency bins within the FFT analysis will contain the frequency of the generated waves and multiples thereof. As the analytical solution used is linear, only the first harmonic of the numerical wave gauge data is considered; the frequency of the first harmonic being equivalent to the frequency of the wave maker motion. In this way, the FFT provides the complex amplitude of the first harmonic surface elevation, $(\alpha^1 + i\beta^1)$; the superscript 1 denoting the first harmonic.

Lin & Huang (2004) outline a method in which the spatial location of a number of wave gauges and the FFT results based upon the surface elevations recorded at these locations are used to determine the amplitude and phase of the first harmonic incident and reflected waves. In fact, the method also identifies the amplitude and phase of the second harmonic incident and reflected waves, separating the free and bound wave components. However, for the purpose of the present study, only the amplitude and phase of the first harmonic incident (or generated) waves are considered. Adopting this approach, the method is applied as follows:

(i) Data describing $\eta(t)$ at each of the eight wave gauges beyond x = 2.0m in figure 3.1 are first employed. This yields the complex amplitude of the propagating wave mode, $(\alpha^1 + i\beta^1)_{prop}$; the phase being defined relative to x = 0m.

(ii) This result is shifted from x = 0m to x = 0.1m, using an adjustment of the form $(\alpha^1 + i\beta^1)_{prop} e^{ik_0 0.1}$.

(iii) The result obtained from (ii) is subtracted from FFT result at the x = 0.1m wave gauge position. This identifies the complex amplitude sum of the evanescent wave modes at x = 0.1m.

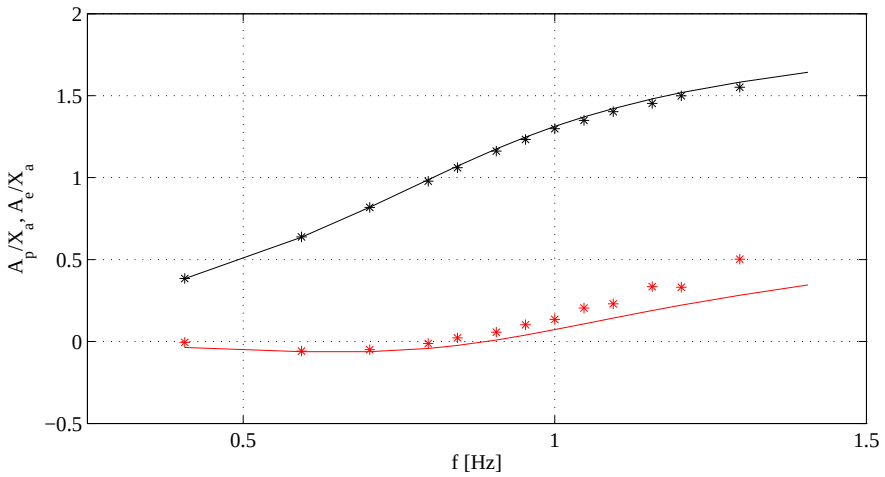


Figure 3.2: Predictions of propagating and evanescent wave mode amplitudes for a moving flap-type wave maker, comparison between the numerical calculations and the analytical solution; —— analytical A_p/X_a, * numerical A_p/X_a, —— analytical A_e/X_a, * numerical A_e/X_a

Predicted surface elevations

The wave maker motion, $\hat{\xi}_3$, has been shown to vary with the frequency, f, of the wave generation (see Table 3.1). In order to more clearly portray trends over frequency, the amplitudes of the surface elevation terms are non-dimensionalised by the amplitude of the wave maker motion at still water level, X_a. This results in the non-dimensionalised amplitude of the propagating wave modes, A_p/X_a, and the non-dimensionalised amplitude sum of the evanescent modes at x = 0.1m, A_e/X_a. Figure 3.2 concerns the variation of A_p/X_a and A_e/X_a with frequency, f, providing a comparison between the numerical predictions and the established analytical solution.

The data describing the propagating wave mode (A_p/X_a in figure 3.2) show that the numerical wave maker generates almost identical waves to those predicted by the analytical solution. Likewise, the comparison of the amplitude sum of the evanescent wave modes is very good. However, in this latter case the numerical predictions and the analytical solution start to deviate in the high frequency cases. The explanation for this discrepancy may, in part, lie in the fact that within

the numerical simulations the wave maker boundary moves, while the analytical solution is based upon an expansion about the equilibrium position of the wave maker. However, the wave maker motion is largest for the low frequency cases and not those arising at the high frequencies. A more significant feature in the high frequency cases is the drift of the nodes along the free surface boundary, Γ_s. This is due to the non-closed fluid particle orbits in the fully Lagrangian numerical simulations. For example, with an initial node spacing along Γ_s of 0.04m, the initial element length is 0.08m. For the time interval over which the frequency content analysis is undertaken, the element size close to the moving wave maker has increased by ≈14% for the longest case (f = 0.406Hz), while it has increased by ≈100% for the shortest case (f = 1.297Hz). Consequently, in the high frequency cases, the element closest to the wave maker becomes distorted.

The distortion of the element closest to the wave maker boundary on the free surface may be diminished by using a finer discretisation of the nodes along Γ_s. However, the nodes will still drift and, as the spacing reduces, they will be in danger of colliding. In this case, the boundary integral equation becomes singular and the numerical calculations break down. In practice, it is possible to carry out numerical simulations with adaptive time-stepping, where the value of the time-step varies according to the smallest distance between nodes. This allows the simulation to progress further in time. Unfortunately, the varying time-step means that the FFT technique cannot be used directly in the analysis of the data. As a result, adaptive time-stepping is undesirable when attempting to validate the wave field generated by a large range of wave maker motions.

It is clear from these comments that fully Lagrangian numerical simulations are never without their difficulties. However, given these difficulties, figure 3.2 shows that the numerical wave field generated by a moving flap-type wave maker compares very well with the available analytical solution.

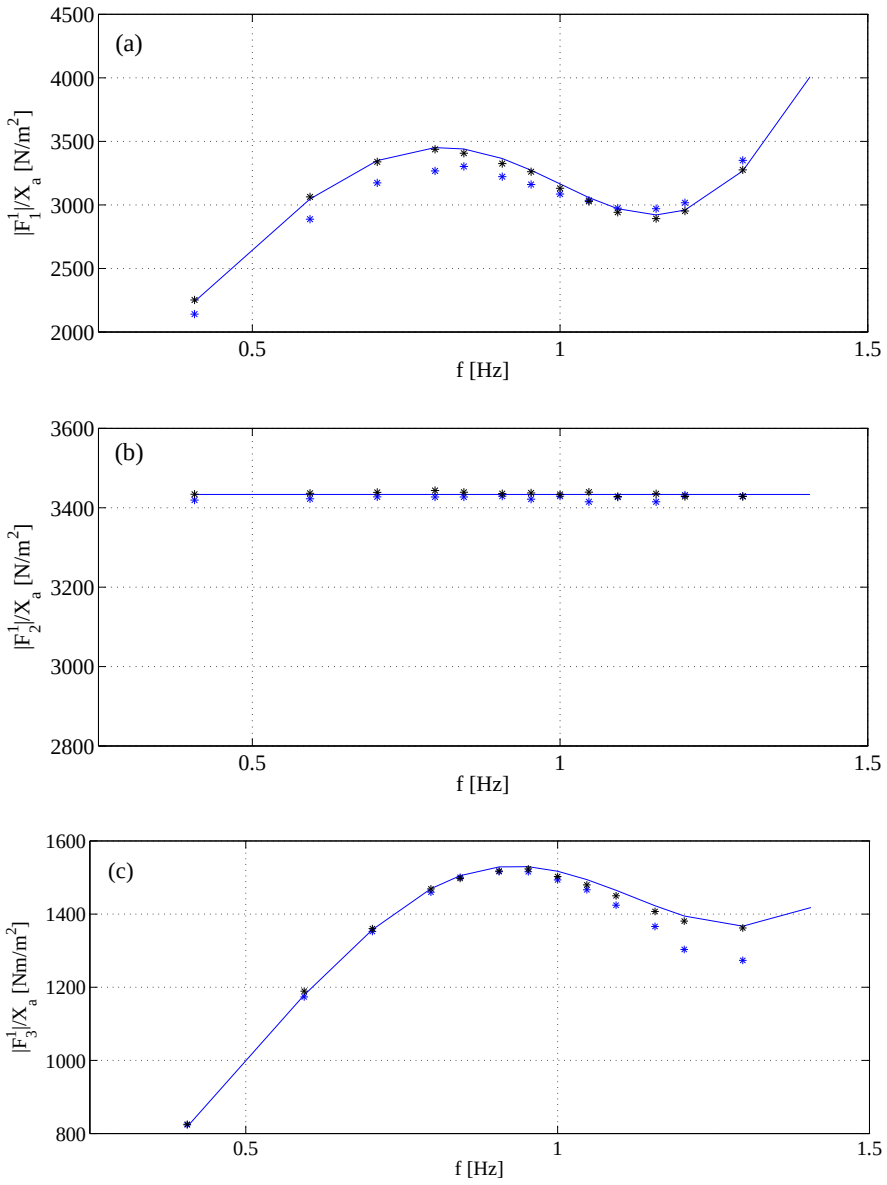


Figure 3.3: Prediction of the first harmonic amplitude of (a) horizontal force, $|F_1^1|$, (b) vertical force, $|F_2^1|$, and (c) moment about the bottom hinge, $|F_3^1|$. —— analytical solution, numerical predictions based upon * Isaacson Method, * Indirect Method

Comparison of forces

In comparing the force on the moving wave maker, both the Isaacson Method and the Indirect Method were used to provide a time-history of the total force. Unfortunately, this force cannot be split into two parts, that are 90° out of phase, in

the same way that the propagating and evanescent waves modes were identified. Figure 3.3 concerns the amplitude of the first harmonic of the force; comparisons being provided between the two numerical approaches (the Isaacson and Indirect methods) and the analytical solution. Within figure 3.3, three subplots are provided: the first addressing the horizontal force, F_1; the second the vertical force, F_2; and the third the moment about the bottom hinge, F_3. In each case, the amplitude is divided by X_a. This aids a comparison over the frequency range even though the terms remain dimensional.

Figures 3.3(a) and 3.3(c) concern $|F_1^1|/X_a$ and $|F_3^1|/X_a$ respectively. In both cases, the data vary with frequency as they are dependent on the generated wave field. In contrast, figure 3.3(b) concerns $|F_2^1|/X_a$ and shows that this is constant over frequency. The reason for this is that the vertical force, $|F_2^1|$, on a moving wave maker represents the weight of the fluid displaced by the wave maker motion. This depends solely on X_a and, as a result, $|F_2^1|/X_a$ is constant in frequency. Not surprisingly, figure 3.3(b) indicates good agreement with both numerical approaches. However, figures 3.3(a) and 3.3(c) show that whilst the Indirect Method agrees extremely well with the analytical theory, the agreement with the Isaacson Method is less good. The explanation for this lies in the use of the backwards finite difference scheme in the Isaacson Method. Given the inaccuracy of the Isaacson Method depicted in figure 3.3, all subsequent validations presented within this chapter consider only the Indirect Method.

Further discussion

Before continuing with the validations, the reader is reminded that the force exerted on a body by the wave field which is generated by the motion of the body is the so-called radiated force. In other words, the forces described in figure 3.3 are related to the wave field depicted in figure 3.2. For example, consider the frequency variation in figures 3.3(a) and 3.2. Clearly, the amplitude sum of the evanescent wave modes is negligible at low frequencies. As a result, the increase in $|F_1^1|/X_a$ mimics the increase in the amplitude of the propagating wave mode; effec-

tively representing an increase in the energy radiated away from the wave maker or the hydrodynamic damping. However, as the frequency of the generated wave field increases, a smaller portion of the water depth has appreciable wave-induced fluid velocities; the latter decaying exponentially for waves in deep water. Consequently, despite the large and increasing amplitude of the propagating wave mode, the horizontal force begins to decrease for $f \geq 0.83$Hz. However, for $f \geq 1.2$Hz, subplot 3.3(a) shows that the force, F_1^1/X_a, sharply increases due to the increasing added mass associated with the high frequency cases. The latter observation is consistent with the increase in the amplitude sum of the evanescent wave modes in figure 3.2. These observations illustrate the coupled hydrodynamic system of a rigid body moving in a fluid.

3.2.2 Radiation of a rectangular body

This section presents a second validation of the numerical model based upon the radiation of surface water waves by a rectangular body moving with a single degree of freedom. The validation is achieved by comparing the predicted amplitude of the propagating wave mode with the results of Black et al. (1971). In this latter study, linearised theory is used to formulate a set of integral equations which describe the far-field amplitude of the waves radiated by an oscillating rigid body. The section begins with a description of the appropriate numerical wave tank and the cases considered. The validation consists of both heave only radiation and pitch only radiation; the former relating to the vertical translation of the body and the latter to the rotation of the body about the y-axis, perpendicular to the $x-z$ plane.

The numerical wave tank

Figure 3.4 shows the numerical wave tank used for the study of wave radiation by a rectangular body. The numerical domain is discretised with a nodal spacing of 0.04m along the free surface boundary. A constant time-step of 0.005s is used

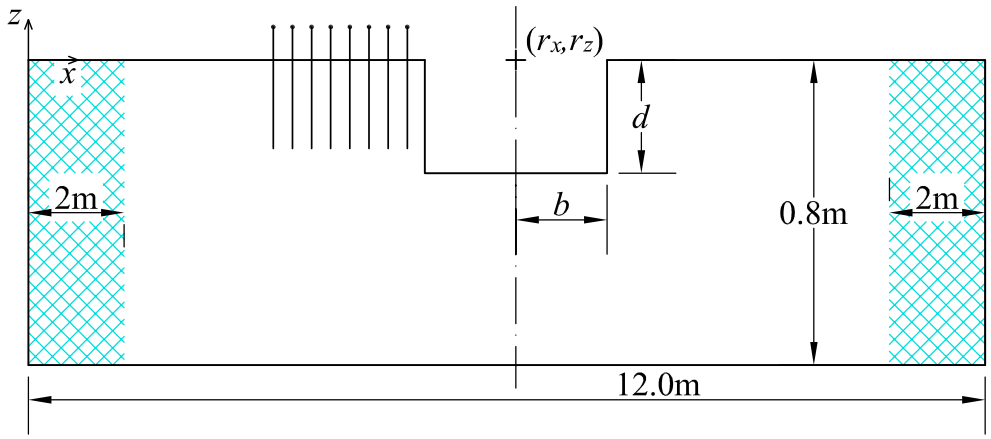


Figure 3.4: Details of the numerical wave tank for the radiation of surface water waves due to the motion of a rectangular body. Note: the vertical lines to the left of the body indicate the position of the wave gauges and the shaded areas indicate the sponge layers.

throughout. Figure 3.4 shows the numerical sponge layers located at either end of the domain; the surface waves propagating away from the moving rectangular body in both directions. The sponge layers are each 2m thick, ensuring that they are effective but are positioned far enough away from the body so as not to adversely affect the resulting wave field close to the body.

The body's centre of mass, (r_x, r_z), is located at the still water level in z and the centreline of the domain in x. The position of the body boundary, Γ_b, varies with the body's geometric properties. Two geometric cases are considered, the values of the draft, d, and the half-beam, b, being presented in Table 3.2. These geometric

	draft, d, [m]	half-beam, b, [m]
Case A	0.4	0.4
Case B	0.4	1.2

Table 3.2: Geometric properties of the rectangular bodies considered.

properties, coupled with the z location of the centre of mass, are identical to two of the cases presented in Black et al. (1971); both cases corresponding to $h/d = 2$, where h is the still water depth.

The frequencies of the rectangular body motion are the same as those used in the wave maker validation; details being given in Table 3.1. However, the displacement of the rectangular body was kept constant over frequency. For the heave only motion, this corresponded to $\hat{\xi}_2$ = 0.025m, while for the pitch only motion, $\hat{\xi}_3$ = 0.025rad.

Heave only radiation

In presenting these results, the linear amplitudes of the generated waves, A, are non-dimensionalised by the heave body displacement, $\hat{\xi}_2$. Figure 3.5 considers the dimensionless amplitude of the propagating wave mode due to the heave only radiation; the numerical predictions being compared to the results of Black et al. (1971) for both Cases A and B (Table 3.2). It should be noted that although the numerical simulations are discrete in the frequencies they address, the number of frequencies considered is large compared to the number of readings taken from Black et al. (1971). Accordingly, the discrete numerical predictions (indicated with small squares) have been connected by lines. Figure 3.5 clearly indicates that the numerically predicted amplitudes of the propagating wave modes agree very well with the results of Black et al. (1971). This observation is true for both Case A and Case B.

Pitch only radiation

Figure 3.6 concerns the pitch only radiation. In this case, the body displacement is expressed in radians and hence the linear amplitude of the propagating wave mode, A, is non-dimensionalised using the product $\hat{\xi}_3 b$. Once again, the data presented in figure 3.6 show that the numerically predicted amplitudes of the propagating wave modes compare well with the results of Black et al. (1971); the agreement being equally good for both body geometries, Cases A and B.

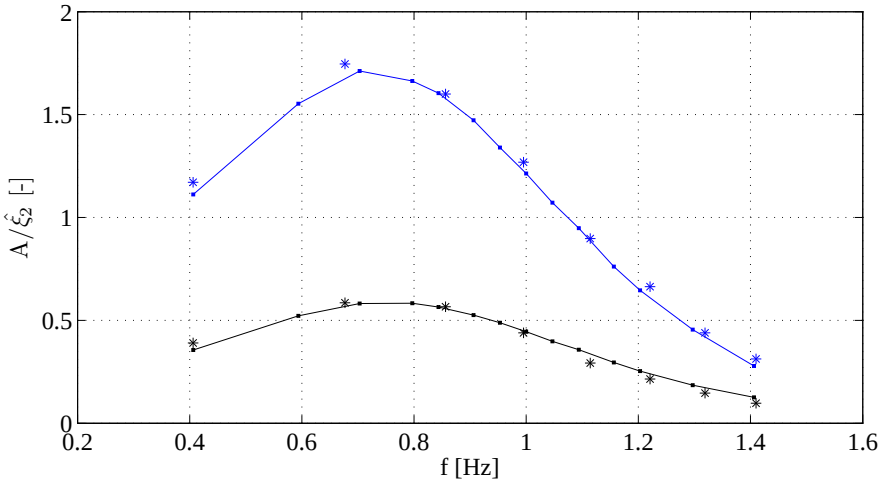


Figure 3.5: Predictions of the non-dimensionalised linear amplitude of the propagating wave mode for heave only radiation, $A/\hat{\xi}_2$; comparisons between numerical calculations and the results of Black et al. (1971). Lines correspond to the BEM numerical predictions and asterix to Black et al. (1971), the black colour denotes Case A and the blue denotes Case B.

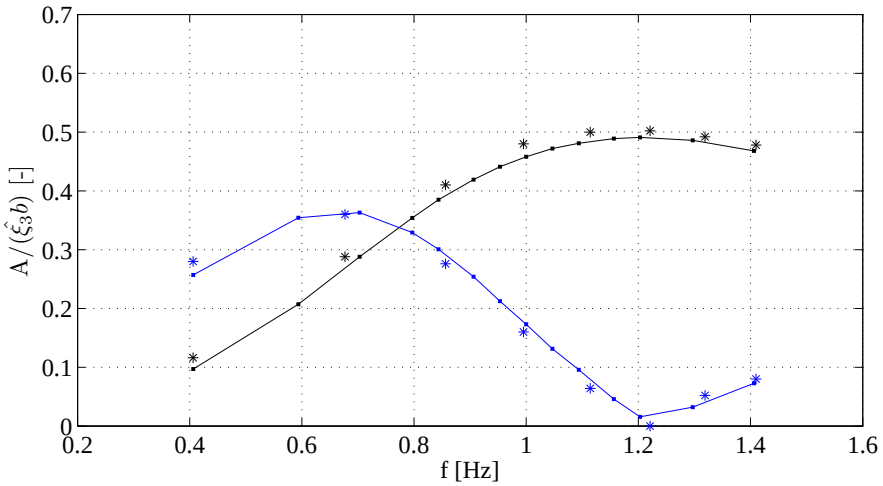


Figure 3.6: Predictions of the non-dimensionalised linear amplitude of the propagating wave mode for pitch only radiation, $A/(\hat{\xi}_3 b)$; comparisons between numerical calculations and the results of Black et al. (1971). Lines correspond to the BEM numerical predictions and asterix to Black et al. (1971), the black colour denotes Case A and the blue denotes Case B.

Further discussion

The data represented in figures 3.5 and 3.6 allow a number of comparisons to be made. First, the amplitude of the propagating wave mode generated by the heave motion, figure 3.5, shows that the wider body (Case B) generates larger waves. Furthermore, the amplitude of the generated wave is seen to decrease for $f > 0.7$Hz in both Cases A and B. Therefore, it may be concluded that the frequency variation is similar between the two cases. In contrast, figure 3.6 concerns the amplitude of the propagating wave mode generated by a pitching motion and presents a very different picture. In particular, the frequency variation for the two cases has very little in common. Indeed, while the asymptotic nature of the data relating to Case A is similar to that of A_p/X_a in wave maker theory (figure 3.2), the pitching motion of Case B generates no propagating waves at around 1.2Hz. This is thought to be a result of the cancellation of the effects on either half of the bottom of the rectangular body; possibly being determined by a ratio of the body's beam and the wavelength of the generated waves.

The absence of an overall trend, as outlined above, demonstrates the complexity of the interaction between a moving body and the surrounding wave field. Clearly, the waves generated by a forced body motion are not only dependent on the degree of freedom of the motion, but also critically dependent on the aspect ratio of the body.

3.3 Validation of force calculations

Having presented the validations relevant to the forced body motion, the rest of this chapter involves the steps leading up to the validation of the wave-induced body motion. The first step relates to the validation of the exciting force, $\mathbf{F}^{exc}$. This is defined as the force that the body would experience if held fixed in its equilibrium position, as discussed in Section 2.5.

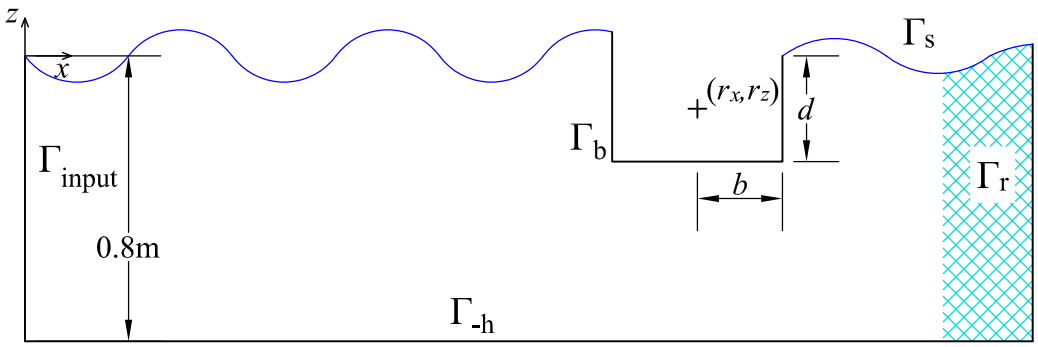


Figure 3.7: Numerical wave tank involving a fixed body. The numerical domain is bounded by the free surface boundary, Γ_s, the fixed body, Γ_b, the input boundary, Γ_{input}, the bed boundary, Γ_{-h} and the end boundary, Γ_r.

3.3.1 The numerical domain

Figure 3.7 represents the numerical domain or wave tank used to simulate wave interactions with a fixed rectangular body. The dimensions of the fixed body are those of Case A considered in the previous section; a half-beam of b = 0.4m, a draft of d = 0.4m and a water depth of h = 0.8m. The numerical wave tank is seen to be defined by the body boundary, Γ_b, the free surface, Γ_s, the bed, Γ_{-h}, the end boundary, Γ_r, and an input boundary, Γ_{input}; the latter used to introduce the incident wave conditions.

In order to avoid the drifting of the nodes along Γ_s due to the non-closed orbits of the fluid particles, the motion of the nodes in the numerical simulations is semi-Lagrangian; the nodes being allowed to move in the vertical direction, but being fixed in the horizontal direction. As a result, the input boundary remains vertical throughout the numerical simulation and the boundary condition along it is expressed in terms of $-\frac{\partial \phi}{\partial x}$; this being the equivalent of $\frac{\partial \phi}{\partial n}$ for a vertical boundary. The incident wave conditions are introduced using the analytically-calculated horizontal fluid velocity, u_{input}.

In accordance with Section 3.2, the input conditions considered herein are regular waves, allowing for simple harmonic decomposition. As a result, $u_{input} = \frac{\partial \phi}{\partial x}$

is calculated using a Stokes' fifth order solution (Fenton 1985). This represents a relatively simple, yet accurate, analytical solution. As before, the results are presented as a variation with frequency. In this case f defines the incident wave frequency, rather than the frequency of a forced motion, and ranges over 0.625Hz < f < 1.25Hz. Across this range, the incident wave amplitude, A_{inc}, is kept constant at A_{inc} = 0.01m. Given this small incident wave amplitude, the values of u_{input} are dominated by the linear terms; the higher order Stokes terms being calculated to avoid unnecessary inaccuracies.

In considering figure 3.7, it should be noted that the fixed body is not central to the numerical wave tank. The reason for this is as follows. In the fixed body simulations, the incident waves are either transmitted beneath the finite-draft body or reflected by it. Unfortunately, the reflected waves travel back towards the input boundary, Γ_{input}, where they cannot be absorbed. This leads to an unwanted contamination of the incident wave conditions. To avoid such difficulties, the upwave section of the numerical wave tank is longer than the downwave section; thereby allowing for the wave field surrounding the body to become fully developed before the reflected waves contaminate the input conditions.

3.3.2 Comparison of forces

A frequency content analysis of the exciting force is undertaken by applying an FFT to the time-history of the force; the data corresponding to fully developed wave conditions and hence ignoring the initial starting transient. Figure 3.8 illustrates the variation with the incident wave frequency, f, of the amplitude of both the first and the second harmonic forces; the former occurring at the incident wave frequency and the latter occurring at twice this frequency. Figure 3.8(a) concerns the amplitudes of (i) the first harmonic horizontal force, $|F_1^1|$, (ii) the first harmonic vertical force, $|F_2^1|$, and (iii) the first harmonic moment, $|F_3^1|$; the latter being taken about the mid-draft of the fixed body on its centreline. Figure 3.8(b) provides a similar plot describing the second harmonic equivalent forces. In

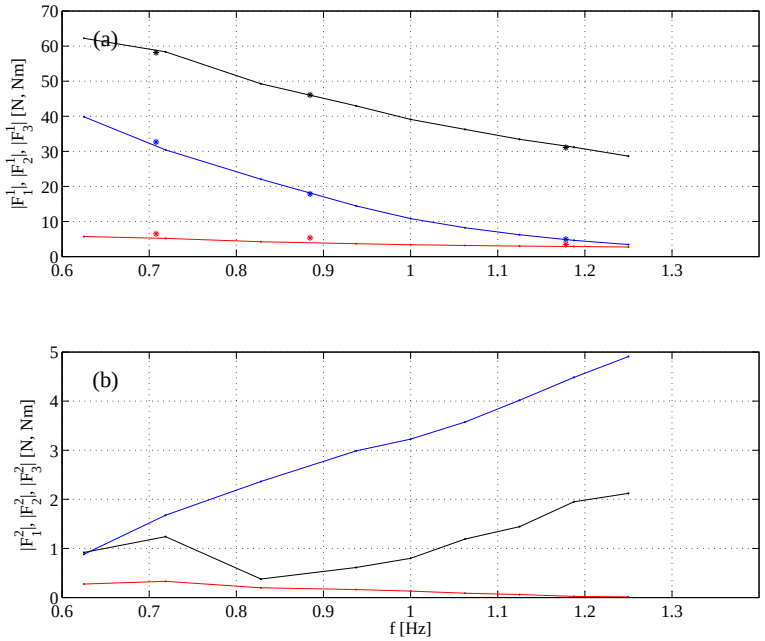


Figure 3.8: Predicted forces acting on a fixed rectangular body (a) first harmonic force with comparisons to Johansson (1989) and (b) second harmonic force. Lines denote the numerical calculations and asterix denote data from Johansson (1989); colour coding is black $|F_1|$, blue $|F_2|$ and red $|F_3|$.

presenting these results, the amplitudes of the first harmonic forces in figure 3.8(a) are directly compared with the values given by Johansson (1989); the latter based upon a similar numerical analysis of a boundary value problem and providing a table of reference values. These comparisons show that the present calculations are in excellent agreement with the earlier results of Johansson (1989).

Figure 3.8(b) shows that the second harmonic of the vertical force grows steadily. Indeed, at f = 1.25Hz it has become more than 140% of the first harmonic vertical force. Second harmonic vertical forces in excess of the first harmonic contribution have also been reported by Sulisz (1993), again for high frequency waves of moderate steepnesses. Although second harmonic forces are beyond the scope of the present validation, it is nevertheless interesting to illustrate their significant contribution despite the linear incident wave conditions.

3.4 Validation of the hydrodynamic properties

The second step leading to the validation of wave-induced body motion concerns the body's hydrodynamic properties. The relationship between these hydrodynamic properties and the wave field generated by a forced body motion has already been discussed in Section 3.2. In contrast, the validation presented below is expressed in terms of decay tests. These concern the body's response to an initial displacement, ξ_0, and can be used to determine the hydrodynamic coefficients of the body; specifically, constant values of the hydrodynamic damping and of the added mass. This is achieved by modelling the response of the body as a free damped oscillation as outlined in Appendix D. The numerical predictions are compared with experimental data; the experimental setup being identical to that used in the validation of the wave-induced motions (Section 3.5 below). The present section outlines the experimental setup and provides details of how the motion of the body is restricted to heave only and pitch only. Finally, the results of the numerical decay tests in heave and in pitch are compared with their experimental equivalents.

3.4.1 Experimental setup

The body considered in the 2D experimental study is a cross-section of a 1:100 scaled model of a Liquid Natural Gas (LNG) tanker; having a half-beam of b = 0.23m and a draft of d = 0.114m at laboratory scale. Figure 3.9(a) illustrates the position of the body in the wave flume. The body is immersed to the value of its draft, 0.114m, and protrudes 0.146m above still water level so that water cannot enter it. The length of the body is equivalent to the beam, 0.46m. The surge motion of the body is prevented using the support structure photographed in figure 3.9(b). This structure spans the width of the narrow flume; the latter corresponding to 0.30m. The model structure or body extends over 0.29m of this width in order to prevent any circulation around it (three-dimensional effects). Accordingly, there is a 5mm gap on either side between the body and the glass

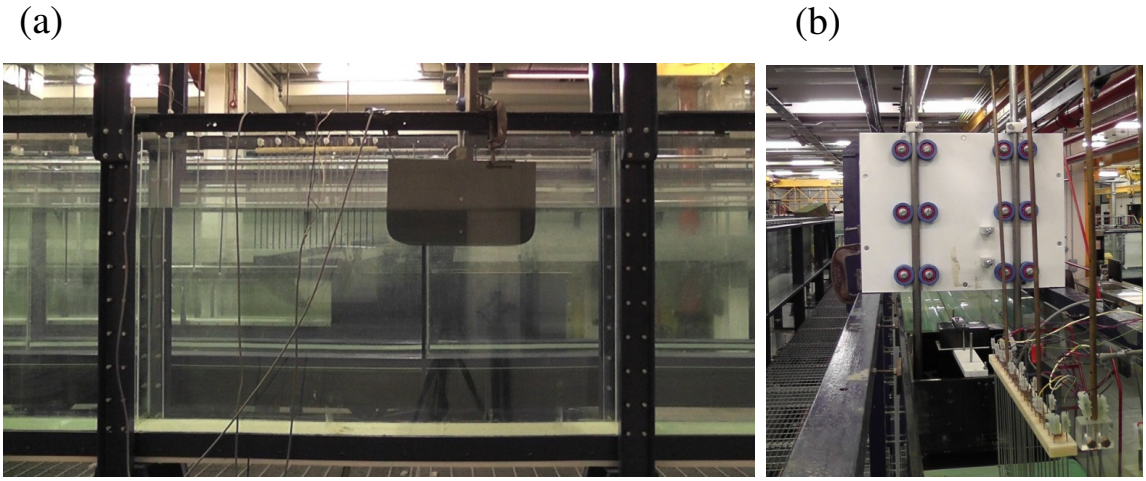


Figure 3.9: Photographs of the 2D experimental setup; (a) the body within the wave flume and (b) the support structure for the body.

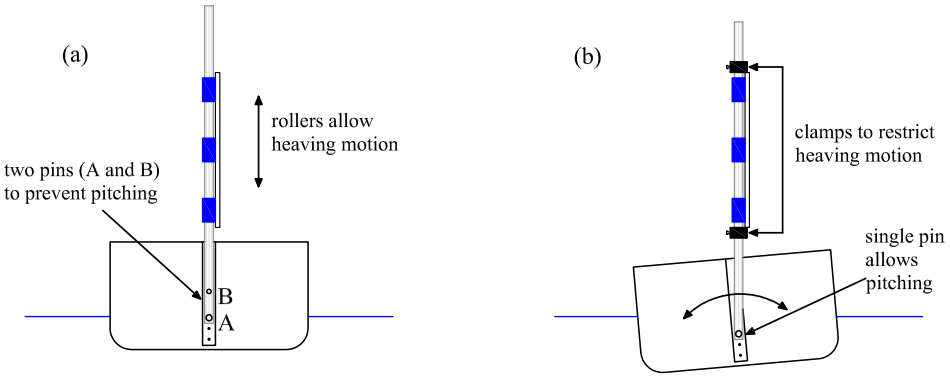


Figure 3.10: Sketches illustrating the arrangement of the experimental setup to restrict the motion of the body to (a) heave only and (b) pitch only.

walls of the flume; allowing the body to move. However, this leads to substantial shear between the ends of the model structure and the glass walls of the flume. The implications of this shear, specifically the role of additional viscous forces not incorporated in the potential flow numerical model, are considered below. Figure 3.9(b) also shows an array of resistance wave gauges. These were used to record the surrounding water surface elevations. An accelerometer and a laser displacement transducer were also used to record the motion of the model structure.

Figure 3.10 is a sketch of a section through the centre of the wave flume.

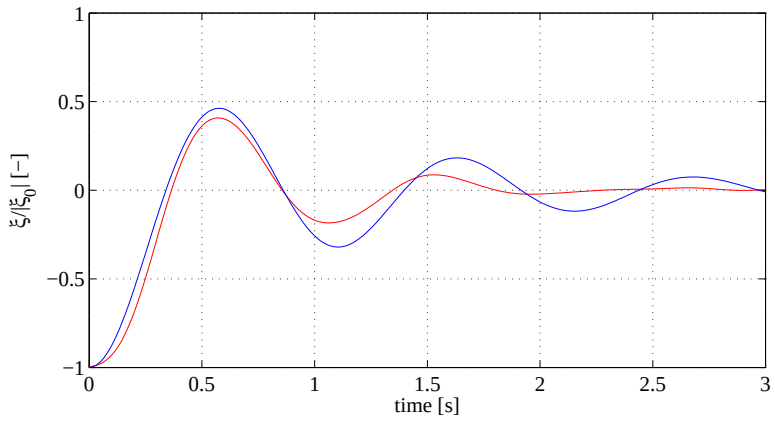


Figure 3.11: Predictions of the heave response to an initial displacement in heave; comparisons between —— numerical predictions and —— experimental data.

It illustrates the means by which the body is supported so that its motion is restricted to heave only motion in subplot (a) and pitch only motion in subplot (b). In figure 3.10(a), pinning the body at two points (A and B) restricts any pitching, while the vertical bars slide between the blue rollers; the position of the rollers (12 in total) being noted in figure 3.9(b). In contrast, in figure 3.10(b) the holders or clamps at the top and bottom of the vertical board restrict vertical (heaving) motion, while the body pitches about a single pin located at its centre of rotation.

3.4.2 Comparison of decay tests

In this case the validation of the numerical predictions is presented in terms of the time-history of the body's response to an initial displacement. The response is non-dimensionalised by the absolute value of the initial displacement, $|\xi_0|$, in an effort to make the extent of the decay more apparent.

Heave only

Figure 3.11 considers the decay test in heave only. It illustrates how, in both the experimental and the numerical cases, the body is given an initial downward heave displacement from which it subsequently recovers to its equilibrium position

	Numerical	Experimental
c_s [kgm^{-1}s^{-1}]	277.4	361.1
m_e [kgm^{-1}]	120.2	89.5

Table 3.3: Comparison between experimental and numerical dynamic properties of a rectangular body moving in heave.

at ξ = 0. The data suggest that the experimental model achieves its equilibrium position sooner than the numerical predictions; the experimental data being more heavily damped and hence undergoing a more significant decay. For example, after the initial displacement at t = 0s, the experimental model displaces beyond the equilibrium position to $0.40|\xi_0|$ and then back down to $-0.18|\xi_0|$. In contrast, the numerical predictions achieve $0.46|\xi_0|$ and $-0.32|\xi_0|$. This difference is due to the fact that the numerical simulations assume an inviscid fluid and, more importantly, frictionless motion of the body.

These effects can be seen more clearly in the values of the hydrodynamic properties obtained from the numerical and experimental heave decay tests using the method outlined in Appendix D. Table 3.3 provides a comparison of the hydrodynamic damping coefficient, c_s, and of the effective mass, m_e; the latter being the sum of the physical mass and the added mass. The table shows that the experimental c_s is significantly larger than the numerical equivalent. The numerical c_s consists solely of the hydrodynamic damping due to the radiated waves, while the experimental c_s has additional viscous damping due to the viscosity of the fluid as well as the friction of the experimental setup. In contrast, it is the numerical m_e that is larger than the experimental equivalent. This observation signifies that the added mass of the numerical body is larger than that of the experimental model; their physical masses being equal. The larger added mass means that the numerical body accelerates more fluid as it moves or that the motion of the numerical body is converted more efficiently into the motion of the surrounding fluid. Consequently, the additional viscous damping in the experimental setup is

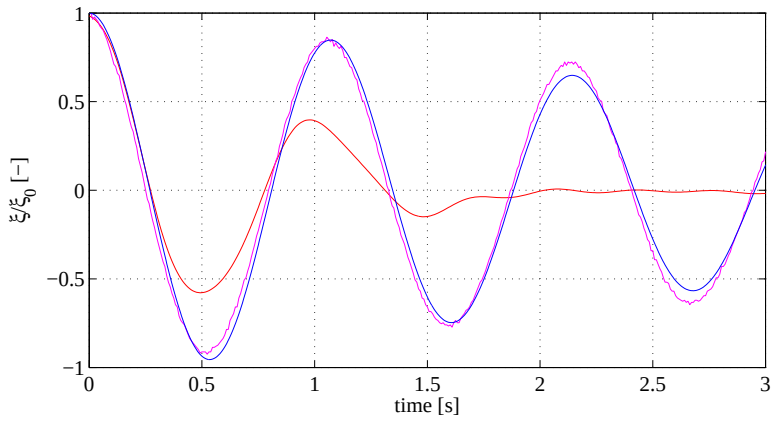


Figure 3.12: Predictions of the pitch response to an initial displacement in pitch; comparisons between —— numerical predictions, —— 2D experimental data and —— 3D experimental data.

thought to be larger than the difference in the two c_s values given in the table because the radition damping of the numerical body is greater than the experimental equivalent.

Pitch only

Figure 3.12 concerns the pitch decay test. The experimental results arising from the setup described in figure 3.9 are denoted as 2D experimental data in figure 3.12. Comparisons between these results and the numerical predictions indicate that the pitching motion is damped out very quickly in the former. This is believed to be due to the inadequacy of the experimental rig; specifically the role of friction at the pinned connection and viscous fluid effects on the side walls of the wave flume. To support this view comparisons are also made with the recorded pitch decay of a three-dimensional (3D) 1:100 scale model of the full LNG tanker; the amidships cross-section being equivalent to the 2D experimental model described earlier. These data are presented in figure 3.12 and are denoted as 3D experimental. In this latter case, the pitch decay of the 3D model was undertaken in a wave basin; full details of which are given in Chapter 5. In undertaking these tests, the 3D model was located in the centre of the wave basin, far removed from any side wall

effects. In considering these results, it is important to note that for consistency the pitch motion refers to the coordinate axes defined in the 2D problem. This contrasts with a 3D representation, in which the x-coordinate is typically aligned with the long axis of the vessel and the motion mode would be referred to as roll. Irrespective of what it is called, pitch in 2D and roll in 3D, figure 3.12 shows that the numerical predictions and the 3D experimental data are in very good agreement.

Further discussion

This section has shown that the experimental decay tests in both heave and pitch can be reproduced by the numerical model, within the bounds of assuming an inviscid fluid and frictionless body motion. In other words, it has illustrated the extent to which the numerical simulations can model the physical processes involved in the 2D experimental study. Furthermore, these results show that the numerical model is stable enough to simulate the bodys response to an initial displacement from its equilibrium position. This is a rigorous test for any numerical simulation.

3.5 Validation of wave-induced motion

Finally, consider the validation of wave-induced motion. With no analytical solution describing the interaction of waves and moving bodies, the validation presented below involves a comparison between numerical predictions and experimental data.

The numerical wave tank used to simulate the wave-induced motion is similar to that used in the fixed body analysis, considered in Section 3.3. The geometry of the body is $b = 0.23$m and $d = 0.114$m. The incident wave frequencies considered range over $0.625\text{Hz} < f < 1.25\text{Hz}$. Across this range, the incident wave amplitude is kept constant at $A_{inc} = 10$mm.

The experimental setup concerning the body motion is exactly as described

for the experimental decay tests in Section 3.4.1. In considering the experimental study of the wave-induced motions, both the body motion and the water surface elevation of the surrounding wave field were recorded. Four incident wave frequencies were considered (f = 0.72Hz, 0.83Hz, 1.00Hz and 1.25Hz). The wave flume, depicted in figure 3.9(a), has the advantage of having one flap-type wave maker at either end. Therefore, although the problem of wave-induced motion is not symmetric, the wave gauges were positioned solely to the left of the moving body. With the wave gauge locations fixed, the incident waves were first generated by the left wave maker. This allowed the upstream (or upwave field) data to be gathered. Once complete, identical incident waves were generated by the right wave maker allowing the downstream (or downwave field) data to be gathered. A total of thirteen resistance wave gauges was used, positioned between 0.05m and 1.4m from the surface of the body. In addition, a reference gauge was positioned close to each wave maker to monitor the incident wave conditions, thereby ensuring the compatibility of the two halves of each test case.

In considering the conduct of the experimental tests, it should be noted that the reference gauges served solely to monitor the repeatability of the experimental runs. The incident wave conditions were measured at the thirteen wave gauges in the absence of the body, where their amplitude was set to A_{inc} = 10mm. The reason for this is as follows. The wave flume is 27m long and the body is positioned close to its midpoint. As a result, the incident waves must travel approximately 12m before reaching the area of interest. Given the width of the wave flume, wave propagation over this distance may result in significant wave decay as a result of the viscous effects on the side walls of the flume. Therefore, the incident waves at the reference gauge may not be representative of those within the area of interest; the two differing by as much as 2mm in the shortest wave case. However, with careful calibration these effects have no material consequence on the measured data.

Comparisons between the numerical and experimental descriptions of both the water surface elevation and the body motion are presented below. These compar-

isons are provided in two parts. Within each part, the body moves with a single degree of freedom; the first part considering heave only and the second pitch only. Given that the decay tests, presented in Section 3.4, illustrated the significance of friction and viscous effects, an additional set of body motion results is presented. These are based upon the linear superposition of the exciting and radiated forces, which can be expressed as

$$\mathbf{F}^{exc} = (\mathrm{M} + \mathrm{M}_a)\,\mathbf{a} + \mathrm{C}_s\mathbf{v} + \mathrm{K}_s\boldsymbol{\xi}, \tag{3.1}$$

where M is the physical mass matrix of the body, M_a is the added mass associated with the body acceleration, $\mathbf{a}$, C_s is the hydrodynamic damping associated with the body velocity, $\mathbf{v}$, and K_s is the spring constant associated with the body displacement, $\boldsymbol{\xi}$. Again, it should be noted that the added mass and the hydrodynamic damping are approximated as constant values. The fixed body analysis, in Section 3.3, presented the validation of $\mathbf{F}^{exc}$. The decay tests, in Section 3.4, provided a comparison of the body's hydrodynamic properties, relating to M_a and C_s. A time-history of $\mathbf{F}^{exc}$ and zero initial conditions of the body velocity and displacement are substituted into equation 3.1 to evaluate the body's acceleration. The use of the Linear Piecewise Analysis (full details given in Appendix D) provides a time-history of the motion of the body based upon the so-called superposition method. This may then be compared to the wave-induced body motion.

3.5.1 Heave only motion

Consider first the amplitude of the first harmonic heave motion, $|\xi_2^1|$. Figure 3.13 presents its variation with the incident wave frequency, f, and contrasts the numerical predictions, the superposition calculations and the experimental data. None of these results are continuous in frequency, but since the number of numerical simulations exceeds the number of experimental runs, the numerical results are joined with lines.

Figure 3.13 illustrates, as expected, that the heave response of the body is

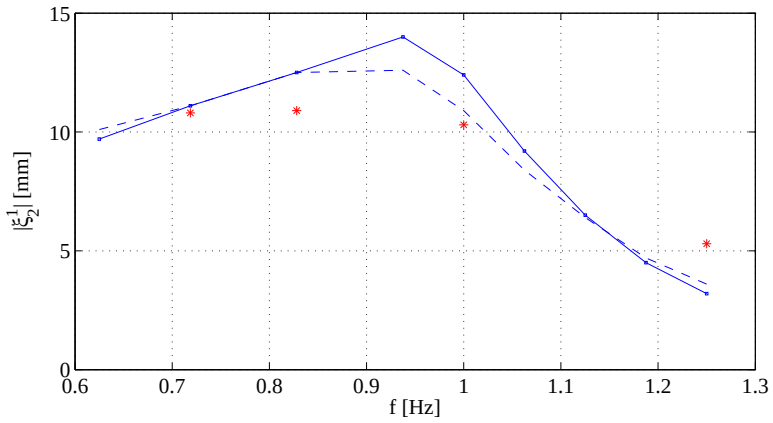


Figure 3.13: Predicted amplitude of the first harmonic of the wave-induced heave motion, $|\xi_2^1|$, for a single degree of freedom system; comparisons between —— numerical prediction, * experimental data, and – – motion determined via the superposition method.

frequency-dependent. Comparisons between the numerical predictions and the laboratory data confirm that the former has a more peaked response. The explanation for this lies in the additional damping due to viscosity and friction in the experimental setup. In contrast, the calculations based upon the superposition method are seen to compare well with the numerical predictions. The reason for this is that the superposition method uses the forces and hydrodynamic coefficients (provided in Table 3.3) derived from the numerical model, which does not incorporate the additional damping. The good agreement between the numerical predictions and the superposition method warrants further discussion.

The difference between the fixed body numerical simulations and those involving the wave-induced heave motion lies in the body boundary condition. Within the fixed body simulations, this boundary condition is defined by $\phi_n = 0$. Consequently, the wave field contains the incident and scattered potentials. In addition to these two potentials, the body boundary condition in the wave-induced motion simulations ($\phi_n = v_2 N_2$) incorporates the radiated potential. The agreement between the superposition motion and the numerical wave-induced motion in figure 3.13 indicates that the radiated potential has little effect on the first order (linear)

body motion. Indeed, the first order effects of the radiated potential are only apparent within the surrounding wave field, full details of which are discussed below.

Figure 3.14 concerns the amplitude of the first harmonic of the water surface elevation, $|\eta^1|$, associated with the heave only motions for the four incident wave frequencies considered in the experimental study; $f = 0.72$Hz in subplot (a), $f = 0.83$Hz in subplot (b), $f = 1.00$Hz in subplot (c), and $f = 1.25$Hz in subplot (d). In each case comparisons are provided between the numerical predictions and the experimental observations. Given that the body motion is restricted to heave, the motion of the nodes within the numerical wave tank is semi-Lagrangian; moving in the vertical direction only and being fixed in the horizontal. Consequently, the time-history of the z coordinate of each node along the free surface boundary can be used directly in the frequency content analysis of the free surface elevation (bypassing the use of numerical wave gauges). The results obtained are plotted against the fixed x location of the appropriate free surface node leading to the illustration of a finely discretised spatial variation. As a result, the numerical surface elevation data are presented as continuous, while the experimental results are presented using discrete asterix. In each subplot the solid black vertical lines at $x \pm 0.23$m indicate the position of the body. Accordingly, $x < -0.23$m corresponds to the upwave field and $x > 0.23$m to the downwave field; the incident waves propagating in the positive x direction.

The spatial variation of $|\eta^1|$ presented in figure 3.14 illustrates the interaction between the incident, scattered and radiated wave components. Taken as a whole the figure shows good agreement in subplots (a) and (d), reasonable agreement in subplot (c) and less convincing agreement in subplot (b). The discrepancies are believed to be due to a combination of the following:

(i) The hydrodynamic properties of the body are different between the experimental and the numerical cases.

(ii) The numerical body radiates waves more easily than the experimental body due to the effects of friction and/or viscosity in the latter case.

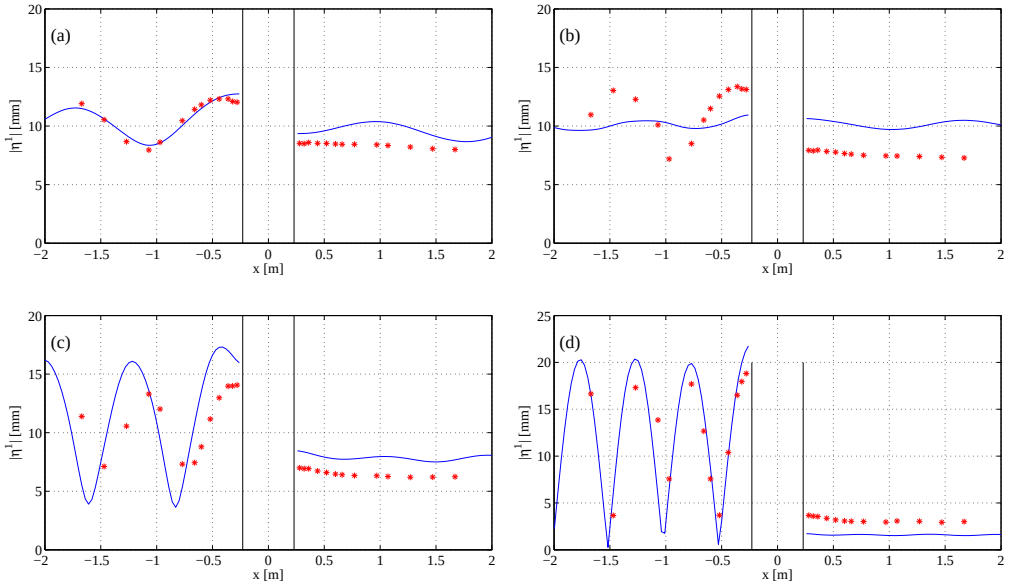


Figure 3.14: Spatial variation of the amplitude of the first harmonic surface elevation within the wave field surrounding a body undergoing wave-induced heave only motion for (a) f = 0.72Hz, (b) f = 0.83Hz, (c) f = 1.00Hz and (d) f = 1.25Hz. Comparisons between —— numerical predictions and * experimental data.

Indeed, for the longest wave case, f = 0.72Hz, the observed and predicted motion in figure 3.13 are almost identical. As a result, the spatial variation of $|\eta^1|$ in figure 3.14(a) is excellent with only a small difference in the downwave amplitudes; the latter thought to be a result of (ii). For the shortest wave case (f = 1.25Hz), the numerically predicted heave motion in figure 3.13 is larger in the experimental data due to (i). Consequently, the experimental data in figure 3.14(d) show less reflection in the upwave field and more transmission in the downwave field. Nevertheless, these differences are relatively small. In contrast, the differences in the two intermediate frequencies, figures 3.14(b) and 3.14(c) are larger and are believed to be due to a combination of (i) and (ii).

A more detailed comparison between the numerical and experimental cases may be achieved by considering the time-history of the water surface elevation at two points within the upwave field (where the spatial variation is more pronounced) for f = 0.72Hz and f = 1.25Hz. The points of comparison are chosen to

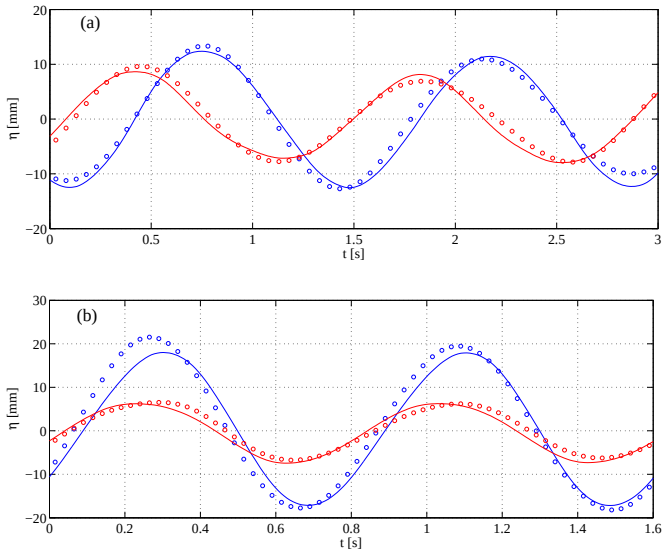


Figure 3.15: Time-history of the free surface elevation, $\eta(t)$, at two points within the wave field upwave of a body undergoing motion in heave only for (a) f = 0.72Hz and (b) f = 1.25Hz; comparison between experimental data, denoted by lines, and numerical predictions, denoted by circles.

be far enough away from the body to avoid the effects of viscosity on the surface of the body and the presence of significant evanescent wave modes. For the long wave, f = 0.72Hz, these points are at x = −0.52m and −1.07m, while for f = 1.25Hz they are x = −0.77m and −0.97m. Figure 3.15 presents the data for f = 0.72Hz in subplot (a) and for f = 1.25Hz in subplot (b); data describing approximately two wave periods being included for each case. In considering the time-histories, $\eta(t)$, the sampling interval in time in the experimental study is substantially smaller than the numerical time-step. As a result, the experimental data are plotted as a continuous line, while the numerical data are presented as discrete circles; the latter corresponding to every tenth time-step for f = 0.72Hz and every fifth for f = 1.25Hz. The results presented within this figure show good agreement; most importantly they show that the relative phase between the points in the upwave field is also modelled correctly.

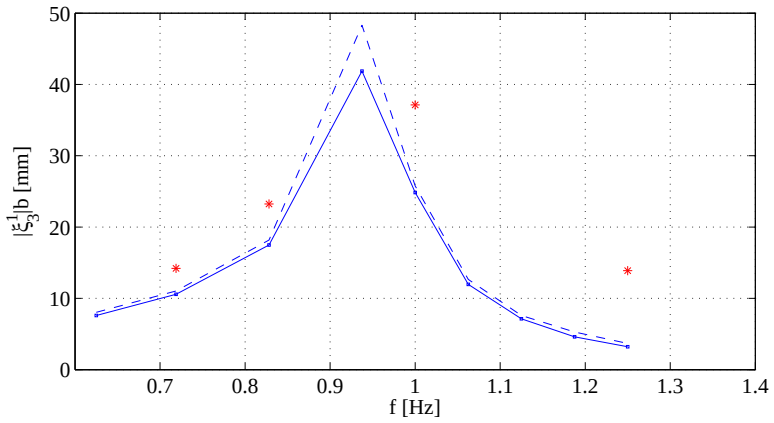


Figure 3.16: Predicted amplitude of the first harmonic of the wave-induced pitch motion, $|\xi_3^1|$, for a single degree of motion system; comparisons between —— numerical prediction, * experimental data, and – – motion determined via the superposition method.

3.5.2 Pitch only motion

Figure 3.16 considers the variation with incident wave frequency of the amplitude of the first harmonic of the angular displacement in pitch, $|\xi_3^1|$. The figure contrasts the experimental and numerical data as well as the results based upon the superposition method. The values presented within the figure correspond to the product of $|\xi_3^1|b$; being approximately equal to the vertical displacement of the bottom corner of the body and therefore comparable to the heave displacement presented in figure 3.13.

Before focusing on the agreement of the experimental, numerical and superposition methods, comparisons between figures 3.13 and 3.16 should be made. First, it is clear that the extent of the vertical motion in pitch only, in figure 3.16, is as much as three times as large as that in heave only, in figure 3.13. Furthermore, comparisons between the figures show that the pitch response is more peaked than the heave response; the ratio of the largest to the smallest $|\xi_3^1|b$ being 14 and the equivalent for $|\xi_2^1|$ being 4.7. These observations reflect the varying degrees of damping seen in the heave only and pitch only decay tests in Section 3.4. As the simulations of the wave-induced motions are more complex than the

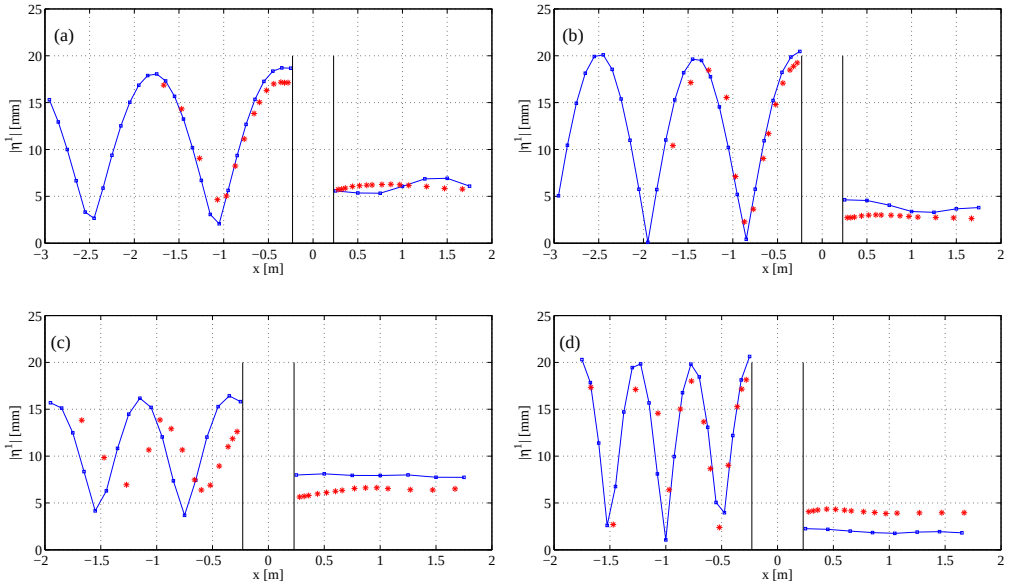


Figure 3.17: Spatial variation of the amplitude of the first harmonic surface elevation within the wave field surrounding a body undergoing wave-induced pitch only motion for (a) f = 0.72Hz, (b) f = 0.83Hz, (c) f = 1.00Hz and (d) f = 1.25Hz. Comparisons between —— numerical predictions and * experimental data.

earlier decay tests (not least because the body motion in the former is a reaction to the surrounding wave field), this result is reassuring. Whilst the comparison between the experimental data and the numerical predictions in figure 3.16 is far from perfect, the general trend is clearly reproduced and the differences may be accounted for in terms of the variation in the two dynamic systems. Furthermore, the comparison between the numerical predictions and the superposition method is clearly encouraging.

With respect to the water surface elevations, the results are again presented as the spatial, x, variation of $|\eta^1|$ for four discrete incident wave frequencies in subplots (a) to (d) of figure 3.17. In this example, both the experimental and the numerical results are discontinuous, although the latter is again joined by lines. Within the pitch motion simulations, the resolution of the numerical data is much reduced. The reason for this is that within these simulations, the motion of the nodes along the rigid body boundary as well as the free surface boundary is fully

Lagrangian; the nodes moving in both x and z. Therefore, the z data from the free surface nodes cannot be plotted against a fixed x location, as required for the purposes of figure 3.17. As a result, the data are generated using numerical wave gauges. Finally, it should be noted that the extent of the upwave field is 3m in subplots (a) and (b), and 2m in subplots (c) and (d). This is due to the differences in the incident wavelengths and the desire to illustrate enough of the upwave field to appreciate the variation within it.

Figure 3.17 illustrates generally good agreement between the numerical predictions and the experimental measurements. The most significant differences are seen in figure 3.17(c) for f = 1.00Hz. In accordance with the earlier discussion, this case also shows the largest departures in the predicted motions (figure 3.16). Nevertheless, the following observations are valid for both the numerical and the experimental cases:

(i) The extent of the variation in the upwave $|\eta^1|$ reduces from figure 3.17(b) to (c).

(ii) The downwave $|\eta^1|$ in figure 3.17(c) has the largest magnitude when compared to the other frequencies presented.

Both (i) and (ii) contradict the variation with frequency of the upwave and downwave field surrounding a fixed body and must therefore be the result of the radiated wave field. Since (i) and (ii) apply to both the experimental and numerical data, it may be concluded that the effects of the radiated waves are correctly modelled in the complex problem involving the interaction of the incident, scattered and radiated potentials.

Figure 3.18 presents the time-history of the surface elevation, $\eta(t)$, at two points within the upwave fields for f = 0.72Hz and f = 0.83Hz; these frequencies exhibiting the largest variation within the upwave field. For f = 0.72Hz, the points are located at x = −0.60m and −0.97m, while for f = 0.83Hz they are located at x = −0.52m and −1.27m. As before, the lines relate to the experimental data and the circles denote the numerical predictions; the latter being presented for every

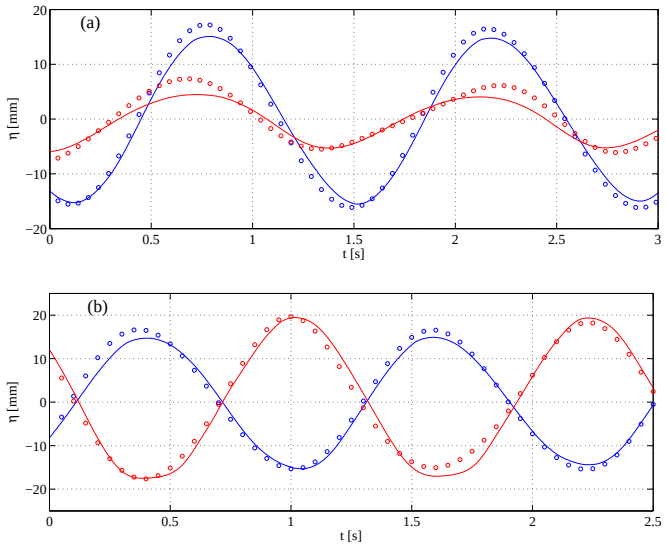


Figure 3.18: Time-history of the free surface elevation at two points within the wave field upwave of a body undergoing motion in pitch only for (a) f = 0.72Hz and (b) f = 1.25Hz; comparison between experimental data, denoted by lines, and numerical predictions, denoted by circles.

tenth time-step in both subplots. Figure 3.18 illustrates that the relative phasing in the numerical predictions agrees well with the experimental data. It should be noted that the two points for the f = 0.83Hz case are consecutive antinodes in the upwave field and, therefore, the variation of their time-histories are almost mirror images as seen by the numerical predictions and the experimental data.

3.6 Conclusions

This chapter has described the validation of the new numerical model designed to simulate the interaction of waves and a moving rigid body. The validations presented vary from the wave fields generated by forced body motions, to the forces on a fixed body, to the replication of experimentally-recorded decay tests and, finally, to the wave field surrounding a body undergoing wave-induced motion in heave only and in pitch only. The bulk of the data presented within the chapter involves linear terms. However, it should be not be forgotten that the model is

fully nonlinear. It has also been shown that a fixed-body analysis may be used to obtain the linear motion of a body undergoing wave-induced motion (in both heave only and pitch only modes). Indeed, the effects of the radiated potential are only apparent in the surrounding wave field. The following chapter will investigate whether this observation is equally valid for the problem of two bodies in close proximity.

4

Two-dimensional analysis of fixed bodies in close proximity

4.1 Introduction

This chapter describes the application of the numerical model (validated in the previous chapter) to the problem of side-by-side offloading of Liquid Natural Gas (LNG); the aim being to establish a basic understanding of the hydrodynamics involved. Side-by-side offloading commonly involves both fixed and floating bodies in close proximity; their separation being of the order of 4m to 6m at full scale. The wave field surrounding a floating body is described in terms of the following potentials: (i) the incident wave potential, (ii) the scattered wave potential due to the presence of the physical body and (iii) the radiated wave potential due to the motion of the body. In an effort to more clearly interpret the interactions involved in side-by-side offloading, certain initial simplifications are applied to the problem in the present study. First, the bodies are assumed to be of infinite length so that a two-dimensional numerical model can be applied. Second, the effect of the radiated potential is eliminated by considering fixed or motionless bodies. The implications of these simplifications are addressed at the end of the present chapter as well as in the following chapter.

The present chapter begins in Section 4.2 with an introduction to earlier studies reported in the literature. Without exception, these are numerical in nature due to the complexity of the problem. The numerical model to be used within the present study was considered in detail in the previous chapters and its description will not be repeated here. Section 4.3 merely introduces the appropriate numerical wave tank and the relevant boundary conditions. This is followed by an outline of how the numerical calculations are to be used in the interpretation of the hydrodynamic interactions.

By way of an introduction, a *single* rigid body of finite draft is considered in Section 4.4. In this simpler case, the results presented include the wave fields both upwave and downwave of the body. Section 4.5 addresses the central problem of two bodies in close proximity. The section begins with a definition of the cases to be considered; providing details of the incident wave frequencies as well as the body geometries. The presence of a second body leads to the development of a third region of the flow, which is subsequently referred to as the gap between the two bodies. The three regions of the flow are therefore the upwave, downwave and gap regions; the latter being very small in its spatial (x) dimension. The comparisons between the cases involving two bodies seek to illustrate the effect of the incident wave frequency, the width of the gap, the beam and the draft of the bodies on the surrounding wave fields. Section 4.6 demonstrates the implications of the fixed-body simplification by considering a case in which one of the two bodies is floating. However, at this stage, the motion of the body is restricted to a single degree of freedom; specifically heave motion or vertical translation.

The present study shows that the hydrodynamics within the gap are very different from those of the upwave or downwave fields. Indeed, the amplitude of the wave motion within the gap is found to reach as much as ten times the amplitude of the incident waves. This resonance occurs at a specific frequency; the value of the frequency being significantly influenced by the gap width and the heave motion. It should be noted that although the numerical model used is fully nonlinear, the results presented within this chapter primarily concern the linear

surface elevation; the incident waves being of relatively small steepness. However, the end of the chapter briefly highlights an example of the nonlinear effects arising within the gap.

4.2 Background

The hydrodynamics within the gap between two bodies in close proximity have been likened to the hydrodynamics within moonpools; the latter being vertical openings through the deck and hull of barges. Molin (2001) considered the two-dimensional (2D) analysis of the water motion in moonpools using linearised potential flow theory, assuming the barge was motionless. Resonant water motion was shown to occur at the natural modes of the moonpool and Molin (2001) presented an approximate method of calculating the frequencies at which these modes occur. Two different types of modes were identified, referred to as the piston and the sloshing modes. Only the piston mode is relevant to the present study due to the narrowness of the gap considered. The piston mode involves the heaving up and down of the water within the moonpool, similar to a heaving rigid body. As a result, the piston mode radiates waves in the surrounding wave field. Since the present study considers both motionless and moving bodies, it is important to distinguish between the radiated potential due to the piston mode and the radiated potential due to the body motion. To avoid confusion, the radiated potential due to the piston mode is referred to as the emitted potential; while the radiated potential due to the body motion remains simply the radiated potential.

Instead of considering the resonant water motion within a moonpool due to wave-induced pressure, Faltinsen et al. (2007) considered the resonant water motion within a moonpool due to the heave excitation of the barge in an otherwise still water environment. Linear potential flow theory was adopted and the forcing amplitude of the barge motion was assumed small. In addition to the theoretical analysis, Faltinsen et al. (2007) presented the results of an experimental study. This showed that the amplitude of the resonant water motion within the moon-

pool was ten times the forcing amplitude in the experimental study and thirteen times in the theoretical analysis. Furthermore, Faltinsen et al. (2007) presented data relating to the amplitude of the water surface elevation within the upwave field. Adopting the definitions introduced above, this region is affected by the radiated potential and the emitted potential. The combined effects were such that the minimum magnitude within the upwave field was observed for frequencies slightly higher than the frequency at which resonant wave motion occured within the moonpool. Faltinsen et al. (2007) also considered the hydrodynamic properties of the barge, reporting significant peaks in the hydrodynamic coefficients of the barge around the resonance frequency; the latter being the frequency at which resonance occurs within the moonpool.

Finally, Kristiansen & Faltinsen (2007) adopted the Boundary Element Method (BEM) within a numerical wave tank to analyse the resonant water motion in the gap between a fixed ship and a terminal due to the wave-induced pressure. In order to overcome the corner problem, which is inherent of any BEM formulation, Kristiansen & Faltinsen (2007) extrapolated the free surface boundary onto the fixed body boundary so that the corner node always remains on the fixed body. However, the gap between two bodies in close proximity is *defined* by the corners, making extrapolation undesirable. The numerical model adopted in the present work is also based upon a BEM formulation. However, the use of multiple fluxes ensures that the free surface boundary remains normal to the fixed body boundary, thereby eliminating the need for extrapolation.

4.3 The numerical model

The numerical model used herein is an application of the multiple-flux BEM, which has been described in detail in Section 2.4.4. Its validation regarding the interaction of waves with a single moving body has been presented in Chapter 3. The section below describes the numerical wave tank (NWT) appropriate to the present study and the boundary conditions applied within it. This is followed by

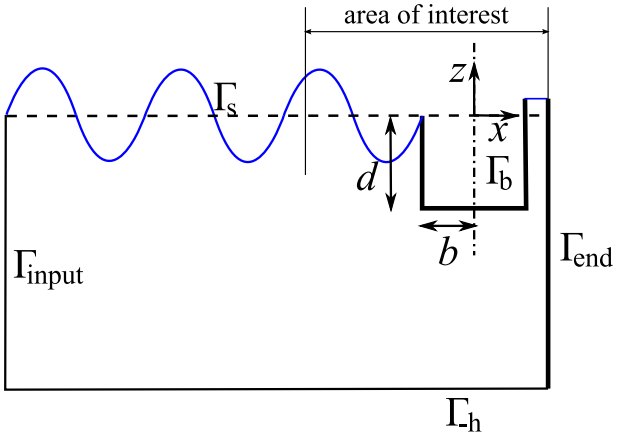


Figure 4.1: Numerical wave tank used for the simulation of wave interactions with a fixed LNG in close proximity to a terminal; the latter modelled as a bottom-mounted Gravity Based Structure (GBS).

an outline of how the numerical outputs are used to illustrate the wave field within the gap, as well as the upwave and downwave fields.

4.3.1 The numerical wave tank

Figure 4.1 illustrates the NWT for the problem involving two fixed bodies in close proximity and defines the area of interest. It is clear from this layout that the majority of the corners are located within the area of interest, highlighting the need for a rigorous treatment of the corners in the BEM formulation.

The NWT in figure 4.1 is enclosed by the boundary Γ. This boundary consists of the bed boundary, Γ_{-h}, the free water surface boundary, Γ_s (denoted in blue), and the input boundary, Γ_{input}, along which the incident wave conditions are applied. Furthermore, the first body boundary, Γ_b, pierces the free surface and is a rectangular approximation of an LNG tanker; its draft, d, and half-beam, b, being defined within the figure. In contrast, the second body boundary, Γ_{end}, extends from the free surface to the bed and represents an LNG terminal; being modelled as a bottom-mounted Gravity Based Structure (GBS). Figure 4.1 depicts the Still Water Level (SWL) as the horizontal dashed line and the centreline of the LNG tanker as the vertical dash-dotted line; the latter corresponding to the origin

of the x-axis. The z-direction is measured positively upwards from the SWL and the incident waves propagate in the positive x-direction.

The reader is reminded that the fully nonlinear nature of the numerical model is achieved through the use of the Mixed Eulerian-Lagrangian (MEL) method. In such an approach, the boundary conditions are satisfied in an Eulerian frame of reference, while the position of the nodes along the moving boundaries of the NWT changes with time; the latter being characteristic of a Lagrangian frame of reference. This is illustrated in figure 4.1 by the fact that the (blue) free surface boundary, Γ_s, fluctuates about the SWL. Since the numerical simulations considered within the present study are restricted to either fixed bodies or bodies moving in heave only, the nodes are described in a *semi*-Lagrangian frame of reference; allowed to move vertically, but fixed in the horizontal direction.

Within the NWT, the bed boundary is impermeable and its boundary condition requires the normal fluid velocity to be zero. This is expressed as

$$\frac{\partial \phi}{\partial n} = 0 \quad \text{on } \Gamma_{-h}, \tag{4.1}$$

where ϕ is the velocity potential and $\mathbf{n}$ defines the outward normal direction; making $\dfrac{\partial \phi}{\partial n}$ or ϕ_n the normal potential flux.

The boundary condition along the input boundary is also expressed in terms of ϕ_n. However, within the semi-Lagrangian simulations, the input boundary remains vertical. Therefore, $\phi_n \equiv -\phi_x$ along the vertical input boundary and

$$\phi_x = u_{input} \quad \text{on } \Gamma_{input}, \tag{4.2}$$

where u_{input} is an analytically-calculated horizontal input velocity. The incident wave conditions considered within the present study are regular waves. Consequently, an accurate yet simple analytical description of u_{input} is the Stokes' fifth order solution given in Fenton (1985). Within the present study, the incident wave frequencies range between $0.625\text{Hz} \leq f \leq 1.31\text{Hz}$ and the incident wave amplitude, A_{inc}, is kept constant over this frequency range at A_{inc}=10mm. Given this small incident wave amplitude, the values of u_{input} are dominated by the linear terms;

the higher order terms being calculated to avoid unnecessary inaccuracies. It is also worth noting that throughout the present work, a scale of 1:100 is applied to the lengthscales; corresponding to a scale of 1:10 in the time- and frequency-scales based on a Froude-number scaling.

On the free water surface, Γ_s, two boundary conditions are applied. The first is the kinematic condition which requires the velocity of the free surface along a normal to the surface to be equal to the fluid velocity along that normal. The second is the dynamic condition which ensures the pressure at the water surface is a constant, equal to the atmospheric pressure. These conditions can both be written in a semi-Lagrangian frame of reference and are given as

$$\frac{\partial \eta}{\partial t} = w - u\frac{\partial \eta}{\partial x} \tag{4.3}$$

and

$$\phi = \int \frac{\partial \phi}{\partial t} \mathrm{d}t = \int \left[-gz - \frac{1}{2}\left(u^2 + w^2\right) + w\left(w - u\frac{\partial \eta}{\partial x}\right)\right] \mathrm{d}t \quad \text{on } \Gamma_s, \tag{4.4}$$

where g is the acceleration due to gravity, (u, w) are the horizontal and vertical fluid velocity components and η is the free surface elevation.

Finally, Γ_{end} and Γ_b are fixed, impermeable, rigid bodies. As a result, the appropriate boundary conditions are equivalent to that applied on Γ_{-h},

$$\phi_n = 0 \quad \text{on } \Gamma_{end} \text{ and } \Gamma_b. \tag{4.5}$$

4.3.2 Numerical results

The results presented within this chapter seek to identify the fundamentals of the interaction of the incident, scattered and emitted potentials. The incident regular wave conditions allow a simple harmonic decomposition via a frequency content analysis based upon the Fast Fourier Transform (FFT) technique. This provides amplitude and phase information from which the first harmonic value can be isolated; the frequency of the first harmonic being equivalent to the incident wave frequency. The interaction of the aforementioned potentials is illustrated

through the spatial (x) variation of the amplitude and phase of the first harmonic of the free water surface elevation, $|\eta^1|$ and $arg(\eta^1)$ respectively. Given the semi-Lagrangian frame of reference, the time history of the z coordinate of each node along the free surface boundary can be used directly in the frequency content analysis. This ensures a good spatial resolution and avoids the use of numerical wave gauges.

The spatial variation of $|\eta^1|$ and $arg(\eta^1)$ establishes a basic understanding of the hydrodynamic interactions. Detailed analysis of these data using the reflection analysis method outlined in Lin & Huang (2004) allows the amplitude of individual components to be identified. Within this method, the spatial location of the free surface nodes and the FFT results based upon the z coordinate of these nodes are used to determine the amplitude and phase of the first harmonic incident and reflected waves. Indeed, the method also identifies the amplitude and phase of the second harmonic incident and reflected wave fields, separating the free and the bound wave components. However, for the purpose of the present work, only the amplitude and phase of the first harmonic incident and reflected waves are considered. The presentation of these results allows for a simpler inter-comparison of the various cases considered.

4.4 Single fixed body of finite draft

By way of an introduction, this section illustrates the interaction of the incident wave potential and the scattered wave potential due to a single body of finite draft, fixed in its equilibrium position. The incident wave conditions are regular waves with an incident wave amplitude of A_{inc} = 10mm in a water depth of h = 0.7m. The dimensions of the rectangular body are d = 0.114m and b = 0.23m; approximately modelling the LNG tanker considered in Chapter 3 and hereafter being referred to as the LNG. Within these calculations, the body is placed at the centre of the NWT and the end condition, Γ_{end}, is replaced by an absorption layer of sufficient thickness to prevent any disturbance of the flow about the body.

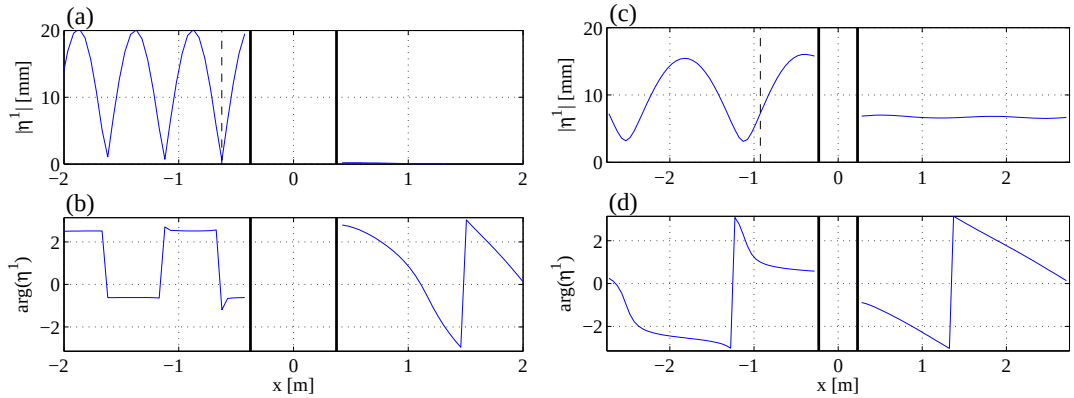


Figure 4.2: Spatial variation of the amplitude and phase of the first harmonic surface elevation for a single fixed body subject to regular waves of frequency, f at (a)&(b) f = 1.25Hz and (c)&(d) f = 0.72Hz; solid black lines indicate the position of the fixed body, dashed black lines indicate the position of $\lambda/4$ from the upstream face of the body. (Note the different horizontal scales adopted for the two frequency cases.)

Figure 4.2 considers the spatial (x) variation of $|\eta^1|$ and $arg(\eta^1)$ within the NWT. Subplots (a) and (b) of the figure present the spatial variation of $|\eta^1|$ and $arg(\eta^1)$ respectively for an incident wave frequency of f = 1.25Hz; while subplots (c) and (d) provide equivalent information for a longer wave case of f = 0.72Hz. Instead of considering the whole NWT, the area of interest is restricted to approximately one wavelength, λ, upwave and downwave of the body. As a result, the extent of the x-axis in the subplots varies between the incident wave frequencies. This causes the beam of the body, outlined in the figure by the solid black vertical lines, to appear different for each frequency. Finally, the dotted black vertical line in subplots (a) and (c) marks a distance of $\lambda/4$ from the upwave face of the LNG.

The upwave $|\eta^1|$ in subplot (a) shows how the incident and scattered potentials interact constructively to give antinodes of approximately $2A_{inc}$ (or 20mm) and destructively to give nodes of approximately zero. The position of the first node is close to the vertical dashed line and the distance between two consecutive nodes or two consecutive antinodes is $\lambda/2$. These are the expected characteristics of a purely standing wave field resulting from the interaction of waves of *equal*

amplitude travelling in opposite directions. These results clearly suggest that, for this short wave case, all of the incident wave energy is reflected. Indeed, confirmation of this is provided by the downwave $|\eta^1|$ in subplot (a) which is negligible, indicating that there is no transmitted wave. The upwave $arg(\eta^1)$ in subplot (b) is also indicative of the phase variation of a purely standing wave; the absence of a gradient indicating zero phase speed. Indeed, this upwave phase is seen to be made up of constant sections with jumps of π between them. The constant sections cover the length between consecutive nodes and are therefore $\lambda/2$ long.

The phase speed of a freely propagating wave is clearly identified by the downwave $arg(\eta^1)$ in subplot (d). This varies between $-\pi$ and π with a relatively constant gradient, which represents the phase speed of the wave being transmitted beneath the LNG. The magnitude of the transmitted wave is seen from the downwave $|\eta^1|$ in subplot (c) to be approximately $0.6A_{inc}$. This (significant) transmission means that less incident wave energy is reflected in the upwave field and that, as a result, the amplitudes of the incident and reflected waves will not be equal. This is apparent in the upwave $|\eta^1|$ in subplot (c), where the antinodes are considerably less than $2A_{inc}$, the nodes are non-zero and the position of the first node is not at $\lambda/4$ from the upwave face of the LNG. Finally, the upwave $arg(\eta^1)$ in subplot (d) displays jumps in the phase rather than a constant gradient, the sections between jumps are not straight and the phase does cover the whole $-\pi$ to π interval. Therefore, the upwave field in the long wave case can be identified as a partially standing wave.

The above description of figure 4.2 suggests that the differences in the spatial variation between the two frequencies may be attributed to wave transmission beneath the body. It therefore follows that the spatial variation can be summarised using the reflection analysis of Lin & Huang (2004). The analysis is applied to two regions, the wave fields upwave and downwave of the body. This leads to the following amplitudes of the first harmonic surface elevation: (i) the upwave incident, $|\eta^1_{up_inc}|$, (ii) the upwave reflected, $|\eta^1_{up_refl}|$, (iii) the downwave incident, $|\eta^1_{down_inc}|$ or transmitted wave, and (iv) the downwave reflected, $|\eta^1_{down_refl}|$. The

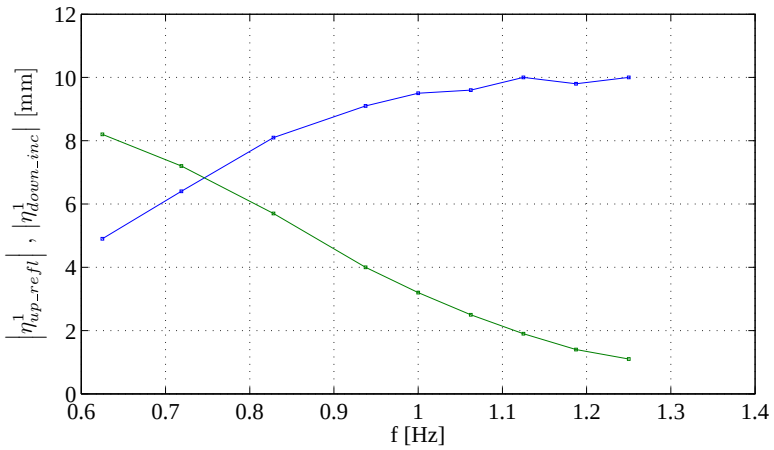


Figure 4.3: Variation with frequency of —— the amplitude of the first harmonic of the reflected wave in the upwave region and —— the amplitude of the first harmonic of the incident wave in the downwave region for a single LNG.

latter indicates the disturbance of the flow due to any unwanted reflections from the downstream boundary, Γ_{end}. The reflected and transmitted wave amplitudes referred to in the description of figure 4.2 are then (ii) and (iii) respectively.

A total of eight incident wave frequencies was considered in the single body simulations, and the reflection analysis was undertaken for each of the eight cases. As expected, the upwave incident amplitude is A_{inc} = 10mm for all the cases, while the downwave reflected amplitude is zero for all the cases. Accordingly, figure 4.3 describes the variation with frequency of the upwave reflected amplitude and the downwave incident or transmitted amplitude. With increasing frequency, the data describe a smooth decrease in the amplitude of the incident wave in the downwave region or the transmitted wave. Most importantly, while the downwave incident amplitude falls to almost zero at the high frequency end, it does not surpass A_{inc} at the low frequency end. This change is accompanied by a smooth increase in the upwave reflected amplitude; the maximum upwave reflected amplitude being approximately equal to the incident wave amplitude, A_{inc}.

From figures 4.2 and 4.3, it can be concluded that with an increase in incident wave frequency, the amplitude of the downwave incident wave reduces while the amplitude of the upwave reflected wave increases. Accordingly, the upwave field

goes from being a partially to a purely standing wave field.

4.5 Two fixed bodies in close proximity

Having presented and discussed the simpler problem involving a single fixed body, this section considers two fixed bodies in close proximity. This represents a more complex problem for the following reasons. Section 4.4 illustrated how a fixed body boundary condition stipulates a standing upwave field, whether purely or partially standing. The presence of two fixed body boundary conditions in the same problem dictates that there will be two stipulated standing upwave fields, and that these will be at odds with each other. This section illustrates the consequences of the competing boundary conditions, as well as the effect of the emitted potential; the latter being due to the resonant wave excitation within the gap. The section begins by outlining the cases considered. Comparisons between these cases seek to identify the characteristics that govern the resonance frequency and the extent of the resonant wave excitation within the gap. Finally, the values of the resonance frequency are compared with those found using the approximation provided by Molin (2001).

4.5.1 Definition of cases

Given the desire to model side-by-side offloading, the bodies considered within the present study are an LNG tanker, a bottom-mounted GBS, and an FLNG or Floating LNG production and storage barge. The LNG tanker is modelled as a rectangular fixed box, with $b = 0.23$m and $d = 0.114$m unless otherwise stated. This geometric approximation is regarded as sufficient for the purposes of the present study. Similarly, the FLNG is modelled as a rectangular fixed box of $b = 0.35$m and $d = 0.216$m. In the case of the FLNG, the rectangular shape and dimensions are based upon a proposal outlined by Noble Denton (2007).

Table 4.1 outlines the six cases considered and defines the properties of the

Case	Upwave body (LNG)		Gap Width	Downwave
	half-beam [m]	draft [m]	[m]	body
1	0.23	0.114	0.06	GBS
2	0.23	0.114	0.12	GBS
3	0.35	0.114	0.06	GBS
4	0.23	0.135	0.06	GBS
5	0.23	0.114	0.06	FLNG
6	As 5 but LNG downwave and FLNG upwave			

Table 4.1: Definition of cases considered.

Case suffix	a	b	c	d	e	f	g	h
f [Hz]	0.625	0.72	0.83	0.94	1.00	1.125	1.25	1.31

Table 4.2: Incident wave frequencies considered and their case suffixes.

fixed bodies involved in each case as well as the width of the gap between them. Table 4.2 lists the discrete incident wave frequencies to be considered within each of the cases in Table 4.1; the combination of geometries and frequencies resulting in a total of 48 cases. The reasons behind the choice of these cases are as follows.

(1) The data arising from Cases 1a to 1h are used to illustrate the effect of varying the incident wave frequency. The results will include both the upwave field and the gap; the latter being bounded by the downwave face of the LNG and upwave face of the GBS (figure 4.1).

(2) Comparison between the results of Cases 1 and 2 demonstrates the effect of increasing the gap width from 0.06m to 0.12m, or (alternatively) the effect of increasing the distance between the upwave faces of the two fixed bodies by 0.06m. The beam of the LNG in Case 3 is 0.24m wider than in Case 1. As a result, both Case 2 and Case 3 involve an increase in the distance between the upwave faces of the fixed bodies. This is achieved in Case 2 by an increase in the gap width, while in Case 3 by an increase in the LNG beam. The

inter-comparison of Cases 1, 2 and 3 aims to identify the uniqueness, if any, of the hydrodynamics within the gap.

(3) Cases 4, 5 and 6 seek to determine the effect of the draft. The draft of the LNG is increased in Case 4, while the second body in Cases 5 and 6 is an FLNG, which is of finite draft (unlike the GBS). The difference between Cases 5 and 6 is the order of the bodies; the LNG being upwave of the FLNG in Case 5 and vice versa in Case 6.

4.5.2 The effect of incident wave frequency

The results of Cases 1a to 1h are presented within this section; the initial emphasis being an illustration of the spatial variation in the upwave field and in the gap. In each of the cases considered, two subplots are presented; subplot (a) considering the spatial variation of $|\eta^1|$ and subplot (b) the equivalent for $arg(\eta^1)$. Within these subplots, the position of the fixed LNG is denoted by the solid black vertical lines. In addition, subplot (a) of each figure contains two additional points of reference. The first is a dashed black line marking a distance of $\lambda/4$ from the upwave face of the LNG, while the second is a dashed red line marking a distance of $\lambda/4$ from the upwave face of the GBS. The purpose of these two dashed lines is to indicate the position of the first node within the standing wave field based upon the two competing boundary conditions. Finally, given that the figures consider the wave field up to approximately one wave length upwave of the fixed LNG, the gap width (0.06m in Case 1) is comparatively small. To ensure that the data within the gap are clearly visible, they are indicated with crosses.

Figure 4.4 considers an incident wave frequency of f = 0.72Hz. This is the same frequency as the long wave case presented in the single fixed body results (Section 4.4). Due to the presence of the GBS, subplots 4.4(a) and 4.4(b) are quite different from subplots 4.2(c) and 4.2(d). Subplot 4.4(a) shows that $|\eta^1|$ downwave of the LNG (now within the gap) is $2A_{inc}$, while subplot 4.2(c) showed a downwave amplitude of $0.6A_{inc}$. The phase variation in subplot 4.4(b) confirms

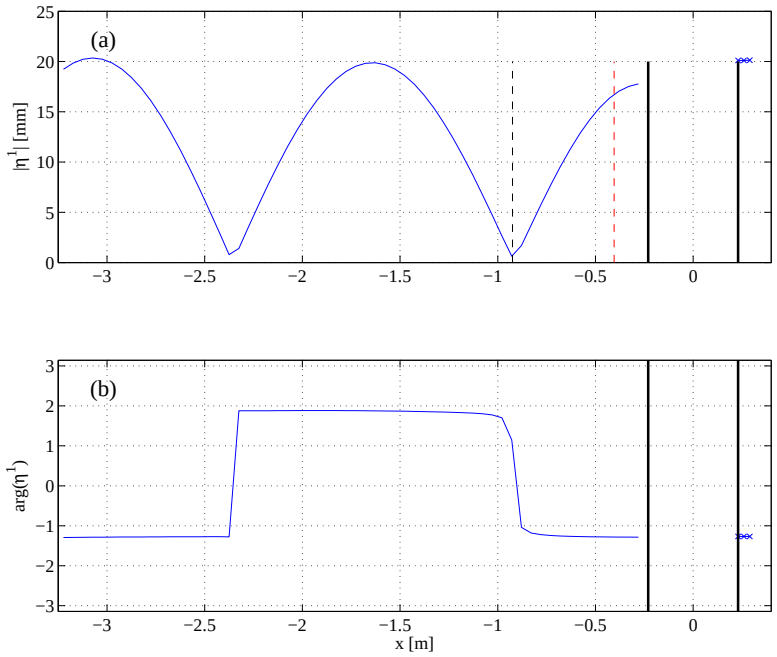


Figure 4.4: Spatial (x) variation of the first harmonic surface elevation (a) amplitude, $|\eta^1|$, and (b) phase, $arg(\eta^1)$ for Case 1b, f = 0.72Hz.

that the wave field upwave of the LNG in Case 1b is purely standing, unlike that in subplot 4.2(d) for a single LNG. The reason for these differences is the presence of the GBS, beyond which there can be no transmission.

The interaction of the two scattered potentials in Case 1b requires further discussion. Subplot 4.4(b) shows that $arg(\eta^1)$ either side of the LNG is equal; signifying that $|\eta^1|$ within the gap and $|\eta^1|$ just upwave of the LNG in subplot 4.4(a) are between consecutive nodes. Considering subplot (a) further, it can be seen that $|\eta^1|$ within the gap (upwave of the GBS) has the magnitude of an antinode, while the first upwave node falls on the dashed black line ($\lambda/4$ from the LNG) and not on the dashed red line. Therefore, despite the fact that $|\eta^1|$ corresponds to an antinode at the upwave face of the GBS, the scattered potential due to the LNG is not negligible. Indeed, it determines the position of the first upwave node.

Figure 4.5 considers a shorter wave of f = 0.83Hz corresponding to Case 1c. As in the previous case, subplot 4.5(b) shows that the wave fields either side of the LNG are still within consecutive nodes and the upwave $arg(\eta^1)$ is indicative

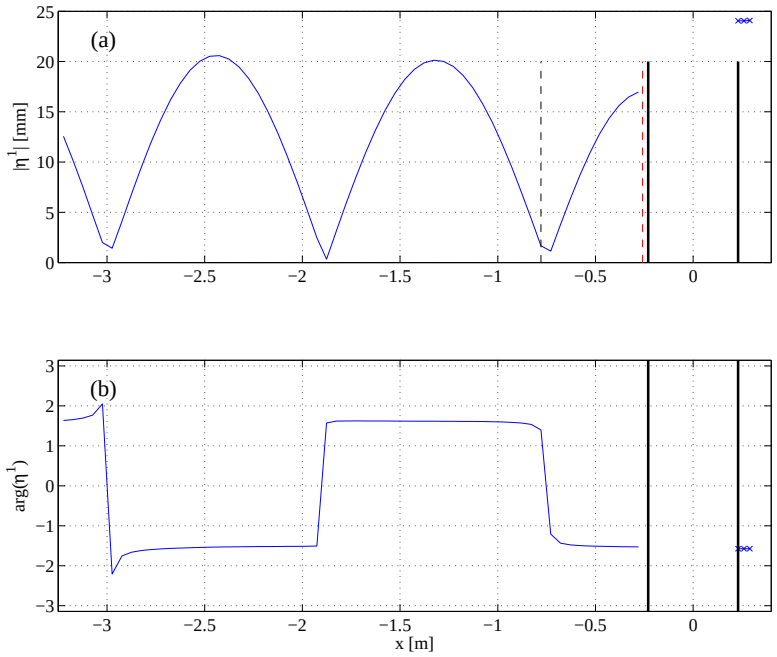


Figure 4.5: Spatial (x) variation of the first harmonic surface elevation (a) amplitude, $|\eta^1|$, and (b) phase, $arg(\eta^1)$, for Case 1c, f = 0.83Hz.

of the phase of a purely standing wave field. Within subplot 4.5(a), the position of the red dashed line coincides with the upwave face of the LNG. This indicates that the scattered potential due to the GBS stipulates a node at the upwave face of the LNG. However, this naturally corresponds to the position of an antinode resulting from the scattered potential due to the LNG. The effects of these competing conditions are immediately apparent in subplot 4.5(a): $|\eta^1|$ at the upwave face of the GBS is $2.4A_{inc}$ and the position of the first upwave node is just under $\lambda/4$ from the LNG. It is clear from these results that the competing boundary conditions can produce larger than expected wave amplitudes within the gap; $|\eta^1| > 2A_{inc}$.

Indeed, the resonant wave excitation within the gap for Case 1 is illustrated in figure 4.6. This concerns an incident wave with f = 1.00Hz, corresponding to Case 1e, and describes a resonant wave excitation of just under $10A_{inc}$. In considering this case, it should be noted that the data used to obtain this result do not represent a steady state. In effect, the amplification within the gap for Case 1e is continuously growing. As a result, a steady state can never be reached because

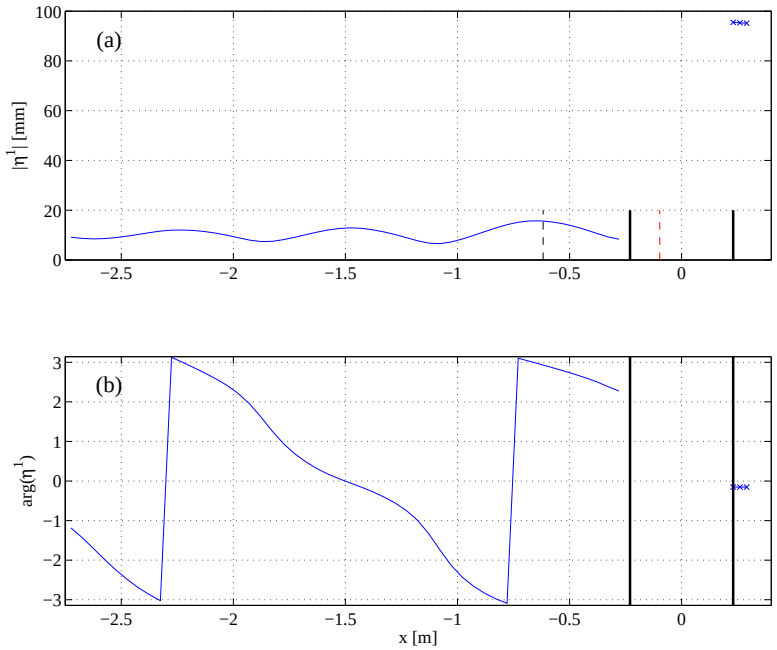


Figure 4.6: Spatial (x) variation of the first harmonic surface elevation (a) amplitude, $|\eta^1|$, and (b) phase, $arg(\eta^1)$, for Case 1e, f = 1.00Hz.

the magnitude of the wave excitation within the gap approaches the draft of the fixed LNG, defined by $11.4A_{inc}$. The large downward motion of the nodes along free surface boundary within the gap causes the elements on the vertical side of the fixed LNG to become very small. As a result, the integrals in the boundary integral equation become singular and the numerical simulation cannot continue. This problem may be overcome through the introduction of a no-slip boundary condition on the rigid body boundaries defining the gap, as discussed below.

The numerical formulation used within the present study assumes an inviscid fluid and an irrotational flow. As such it models the normal stresses acting on the fluid particles. However, as described in Lighthill (1979), the modelling of a real fluid also involves modelling the shear stresses; the latter leading to angular momentum and the rotational motion of the fluid. Although smaller than the normal stresses, shear stresses are significant at solid boundaries and lead to a no-slip boundary condition; the latter requiring the tangential velocity of a fluid particle on the body surface to be zero in the case of a fixed body. Lighthill (1979)

describes how the shear stresses modify angular momentum and, therefore, generate vorticity. Provided that the shear stresses remain small, the vorticity can be diffused within the boundary layer; the diffusion coefficient being equal to the kinematic viscosity. The larger the fluid velocity in the external body of fluid, the larger the shear stress, and when the vorticity can no longer be diffused within the boundary layer, it separates and moves into the body of fluid.

Lewis (1991) argued that surface vorticity (the vorticity that is contained within the boundary layer) can be modelled using a vortex element method. Within this method, the boundary layer is assumed to be infinitesimally thin and can be modelled using vortex elements on the body surface. The fluid particle velocity changes discontinuously from zero on the body to the external fluid velocity across the vortex element. Applications of the vortex element method are presented in Stock & Gharakhani (2010) and for flow around a rigid body in Strickland et al. (2002). However, the incorporation of such a method is outside the scope of the present work; the numerical calculations presented in this and other chapters being based upon an irrotational BEM formulation.

In addition to the resonant amplification within the gap, figure 4.6 illustrates the effect of the emitted potential on the upwave field in Case 1e. The upwave $|\eta^1|$ in subplot (a) has no distinct antinodes or nodes; merely oscillating about the incident wave amplitude of A_{inc} = 10mm. It is also interesting to note from the $arg(\eta^1)$ in subplot (b), that the wave field within the gap is not in phase with the wave field just upwave of the LNG. Furthermore, the upwave $arg(\eta^1)$ is predominantly the phase of a wave propagating in the positive x direction. It therefore appears that the resonant wave motion in the gap leads to an emitted potential whose effect in the upwave field is to largely cancel out the two scattered potentials.

Case 1f concerns a further increase in the incident wave frequency to f = 1.125Hz; being presented in figure 4.7. The upwave $|\eta^1|$ in subplot (a) shows antinodes of approximately $2A_{inc}$ and nodes of approximately zero. The upwave $arg(\eta^1)$ in subplot (b) consists of straight sections. These observations are char-

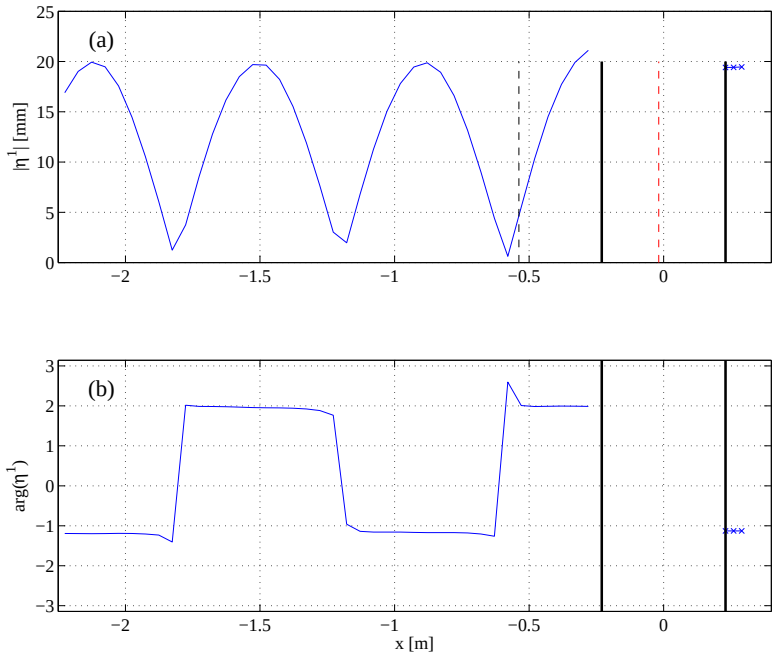


Figure 4.7: Spatial (x) variation of the first harmonic surface elevation (a) amplitude, $|\eta^1|$, and (b) phase, $arg(\eta^1)$, for Case 1f, f = 1.125Hz.

acteristic of a purely standing wave field. However, $|\eta^1|$ within the gap is seen in subplot (a) to be $2A_{inc}$. This confirms that the incident wave energy is not fully reflected by the LNG. Furthermore, subplot (b) shows that the wave fields just upwave of the LNG and within the gap are exactly out of phase; having a phase difference of π. This signifies that in subplot (a), $|\eta^1|$ within the gap and on the upwave face of the LNG are *consecutive* antinodes, possibly with a node existing somewhere between them. Finally, the effects of the two scattered potentials are apparent in the facts that the magnitude of $|\eta^1|$ on the upwave face of the LNG is larger than $2A_{inc}$ and that the position of the first upwave node is just slightly farther than $\lambda/4$ from the upwave face of the LNG.

Having considered the spatial variation of $|\eta^1|$ and $arg(\eta^1)$ for Case 1 at various discrete incident wave frequencies, figure 4.8 summarises the variation over the entire frequency range. This summary is achieved by applying the reflection analysis of Lin & Huang (2004) described previously; the method being applied both within the upwave field and in the gap. In considering these results, it is

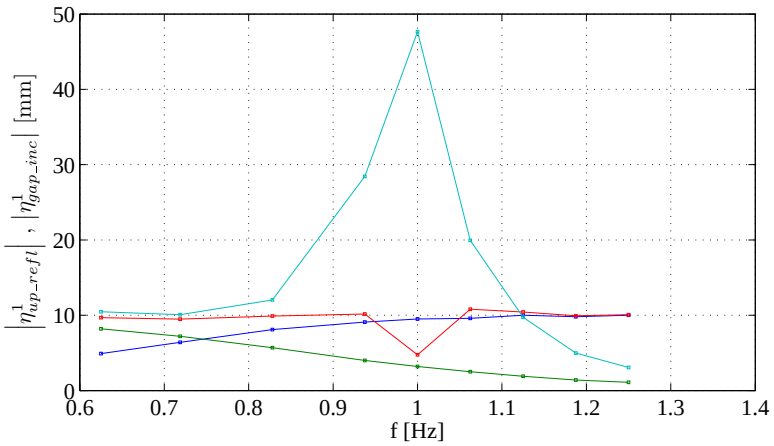


Figure 4.8: Variation with frequency of the amplitude of the first harmonic of the reflected wave in the upwave region and the amplitude of the first harmonic of the incident wave in the gap; — single LNG upwave, — single LNG downwave, — Case 1 upwave, — Case 1 gap.

important to note that within the gap, the amplitude of the reflected wave was always equal to the amplitude of the incident wave for each of the Case 1 data sets. This is to be expected since within the narrow gap width, the phase is always constant across the gap defining a standing wave field for the purposes of the reflection analysis. As a result, figure 4.8 considers the variation over frequency of the amplitude of the reflected wave in the upwave field and the amplitude of the incident wave within the gap. In addition to the Case 1 data, the amplitude of the reflected wave in the upwave field and the amplitude of the incident wave in the downwave field (or transmitted wave) for the single LNG are also included in figure 4.8 to allow direct comparisons.

Within figure 4.8, the amplitude of the incident wave in the gap is exactly half of the amplitude presented in the earlier Case 1 data (figures 4.4 - 4.7). This is to be expected since, as noted above, the incident wave within the gap represents only half of the purely standing wave within the gap. Figure 4.8 also highlights the stark contrast between the smoothly varying results of a single body and those of Case 1; the explanation being the presence of the GBS. Indeed, amplitude of the reflected wave in the upwave field for Case 1 is almost constant at A_{inc}=10mm,

while the amplitude of the incident wave in the gap achieves resonance and then drops off. At the higher frequencies ($f \geq 1.125$Hz), there is very little energy transmitted beneath the single LNG. However, amplitude of the incident wave in the gap for Case 1 within this region lies between $0.5A_{inc}$ and A_{inc}. It can therefore be concluded that the amplitude of the incident wave in the gap is not restricted to either A_{inc} or its single body equivalent. Furthermore, the dip in the amplitude of the reflected wave in the upwave region at the resonance frequency (figure 4.8) illustrates the effect of the emitted potential. These observations confirm that the incident wave within the gap is very different to the incident wave in the region downwave of a single LNG. Indeed, the incident wave energy causes the motion of the fluid within the gap to build up until it has reached a steady state. The magnitude of this motion is independent of the transmitted waves and has been shown to be critically frequency-dependent, possessing a natural frequency. The wave excitation within the gap may, therefore, be described as the response of a rigid body. As a result, the variation with frequency of this wave excitation may be modelled using an approach akin to a Response Amplitude Operator (RAO).

The reduction in the amplitude of the incident wave in the gap beyond the resonance frequency in figure 4.8 means that the amplitudes of the reflected wave in the upwave region and of the incident wave in the gap for Case 1b (f = 0.72Hz) are similar to those for Case 1f (f = 1.125Hz); all being close to A_{inc} = 10mm. However, this is a gross simplification of the data presented in the spatial variation plots. The previous descriptions of figures 4.4 and 4.7, which consider the spatial variation of Cases 1b and 1f respectively, revealed the following. Although of similar magnitude, $|\eta^1|$ either side of the LNG was between consecutive nodes in Case 1b but corresponded to consecutive antinodes in Case 1f. Bearing this in mind, the data describing the amplitude of the reflected wave in the upwave region in figure 4.8 may be split into two regions: below the dip and above the dip. Below the dip, the amplitude of the reflected wave is determined by the bottom-mounted GBS. Above the dip, the amplitude of the reflected wave is determined by the LNG and, in this region, closely resembles its single body equivalent (see

figure 4.8). However, the variation in the position of the first upwave node, as illustrated in the spatial variation plots, is one indication that the hydrodynamics involved may not be quite as clear cut as this suggests. Nevertheless, the ability to summarise the data, as demonstrated in figure 4.8, is clearly beneficial.

4.5.3 The effect of gap width

Within this section, the effect of the gap width is addressed by direct comparisons between the Case 1 and the Case 2 results, details of both are given in Table 4.1. However, as the Case 1 results have been described in detail above, the descriptions below predominantly refer to the Case 2 results. The essential difference

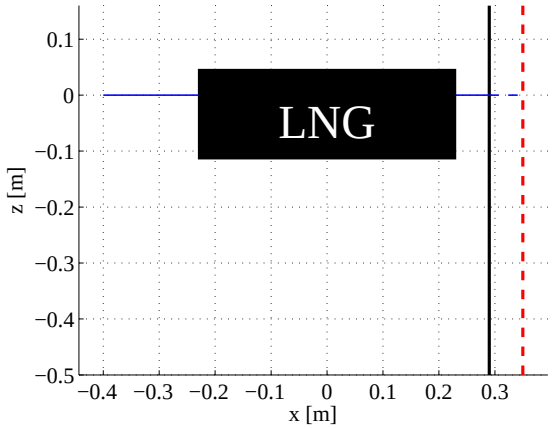


Figure 4.9: Comparison between the Case 1 and the Case 2 numerical wave tanks; —— position of the GBS in Case 1, – – position of the GBS in Case 2.

between the Case 1 and Case 2 NWTs is illustrated in figure 4.9; the vertical and horizontal scales being equal thereby indicating the true aspect ratios of the dimensions involved. With an increase (doubling) of the gap width in Case 2, the solid black line indicates the position of the GBS in Case 1 while the dashed red line indicates its position in Case 2; the position of the LNG being the same in both cases. Within the plots describing the spatial variation, this difference in the position of the GBS is simply portrayed as an extended set of gap data for the Case 2 results.

Figure 4.10 compares the spatial variation of the Case 1c and Case 2c results,

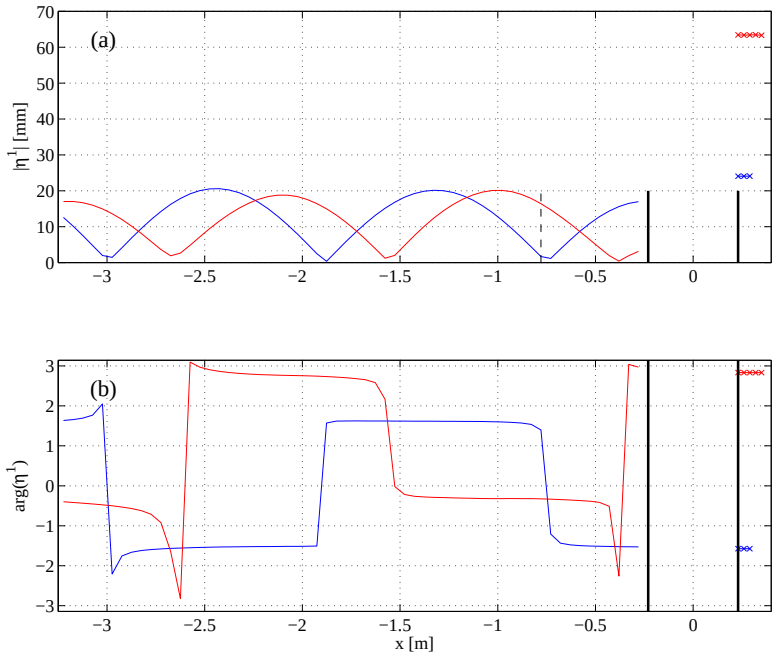


Figure 4.10: Comparison of the spatial (x) variation of the first harmonic surface elevation (a) amplitude, $|\eta^1|$, and (b) phase, $arg(\eta^1)$, between Cases 1c and 2c, f = 0.83Hz; —— Case 1, —— Case 2.

in which the incident wave frequency is f = 0.83Hz. The Case 2 $|\eta^1|$ within the gap is shown in subplot (a) to be $6.3A_{inc}$. This is the largest amplification recorded in Cases 2a to 2h; making f = 0.83Hz the resonance frequency for Case 2. Furthermore, the $|\eta^1|$ data in the upwave region of subplot (a) consist of antinodes of approximately $2A_{inc}$ and nodes of approximately zero; being indicative of a standing wave field. Subplot (b) shows that the wave fields within the gap and immediately upwave of the LNG are in phase. However, subplot (a) shows that in Case 2, $|\eta^1|$ at the upwave face of the LNG is only $0.3A_{inc}$ and the position of the first upwave node is very close to the upwave face of the LNG. These observations illustrate the interaction of the two scattered potentials (one from the LNG and one from the GBS) and the emitted potential. As a result, in stark contrast to the results describing the resonance frequency for Case 1 (Case 1e in figure 4.6) the effects of the emitted potential do not cancel out the effects of the scattered potentials in Case 2c.

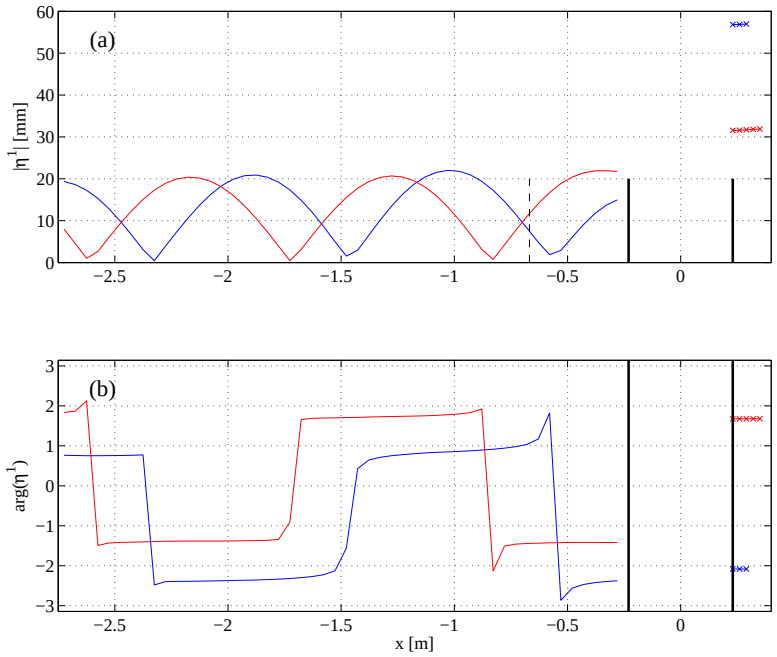


Figure 4.11: Comparison of the spatial (x) variation of the first harmonic surface elevation (a) amplitude, $|\eta^1|$, and (b) phase, $arg(\eta^1)$, between Cases 1d and 2d, f = 0.94Hz; —— Case 1, —— Case 2.

Similar data relating to Cases 1d and 2d are compared in figure 4.11. This corresponds to a frequency of f = 0.94Hz, which is above the resonance frequency in the Case 2 results. The Case 2 $arg(\eta^1)$ in subplot (b) shows that the wave fields either side of the LNG are almost exactly out of phase. Therefore, the $|\eta^1|$ within the gap and just upwave of the LNG in subplot (a) represent consecutive antinodes, with magnitudes of $3.2A_{inc}$ and $2.2A_{inc}$ respectively.

The main purpose of figure 4.11 is to demonstrate the stark differences between the Case 1 and Case 2 data. The reader is reminded that the only difference between the NWTs describing each of these two cases is an additional 0.06m in the gap width between the LNG and the GBS in Case 2; approximately corresponding to a mere $\lambda/30$ with an incident wave frequency of f = 0.94Hz. Subplot (b) shows that the wave fields either side of the LNG are in phase for Case 1, but out of phase for Case 2. This observation signifies that f = 0.94Hz is below the resonance frequency for Case 1 and above it for Case 2. Furthermore, subplot (a) shows that

the position of the first upwave node is closer than $\lambda/4$ for Case 1 and farther than $\lambda/4$ for Case 2. The distance between the positions of the first upwave nodes in Case 1 and Case 2 is approximately $\lambda/7$; more than four times larger than the $\lambda/30$ increase in the gap width. As a result, the differences in the Case 1 and Case 2 data in figure 4.11 are believed to be due to the difference in the resonance frequencies between the two cases. In other words, the differences are driven by the hydrodynamics within the gap.

4.5.4 The effect of the LNG beam

The Case 2 results, described above, show a significant decrease in the value of the resonance frequency with respect to Case 1. In order to determine whether this decrease is the result of doubling the gap width, or of increasing the distance between the upwave faces of the two bodies (the LNG and the GBS), comparisons are made between Cases 1, 2 and 3. In Case 3, the gap width is equal to that of Case 1, but the LNG in Case 3 is 0.24m wider; all other parameters having been kept constant. As a result, the upwave faces of the two bodies are farther apart in Case 3 than in Case 2. The comparison between these cases is presented using the results of the reflection analysis discussed earlier. Accordingly, figure 4.12 illustrates the variation with frequency of the amplitude of the reflected wave in the upwave region, and the amplitude of the incident wave in the gap; data from Cases 1, 2 and 3 being compared directly. As before, the amplitude of the reflected wave within the gap is always equal to the amplitude of the incident wave within the gap and is not included.

For each of the three cases, the amplitude of the incident wave within the gap displays a clear resonance and in the vicinity of this frequency, the amplitude of the reflected wave in the upwave region undergoes a fluctuation about A_{inc} = 10mm. These observations confirm that in all three cases, there is a resonant amplification and its emitted potential has an effect on the upwave field; albeit of varying magnitude. The magnitudes of the resonance, and of the associated

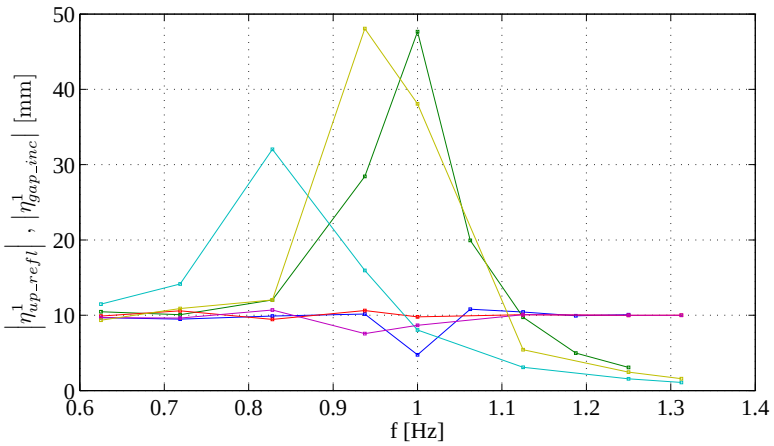


Figure 4.12: Variation with frequency of the amplitude of the first harmonic of the reflected wave in the upwave region and the amplitude of the first harmonic of the incident wave in the gap; — Case 1 upwave, — Case 1 gap, — Case 2 upwave, — Case 2 gap, — Case 3 upwave, — Case 3 gap.

fluctuation, are seen to be most pronounced in Case 1 and least pronounced in Case 2. Furthermore, there is a marked similarity in the data describing all three cases at both the high frequency end and at the very low frequency end of the range considered. However, while the Case 1 and Case 3 results are still comparable at f = 0.83Hz, the Case 2 results are very different.

The resonance frequency identified in figure 4.12 is seen to decrease from 1.0Hz in Case 1, to 0.94Hz in Case 3 and to 0.83Hz in Case 2. These results indicate that the increase in the beam of the LNG in Case 3 has much less effect on the resonance frequency than the increase in the gap width in Case 2; despite the fact that the increase in the beam is substantially larger. The data presented on figure 4.12 add to the argument that the fluid within the gap effectively responds as a rigid body. By doubling the size of this water body in Case 2, the resonance frequency as well as the damping of its response are significantly altered.

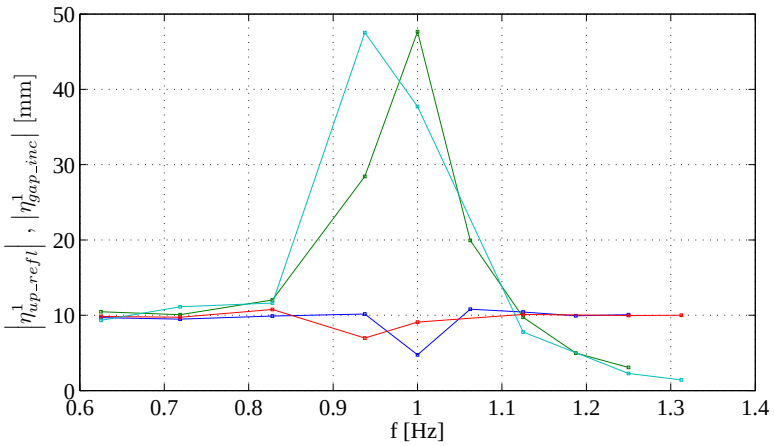


Figure 4.13: Variation with frequency of the amplitude of the first harmonic surface of the reflected wave in the upwave region and the amplitude of the first harmonic of the incident wave in the gap; — Case 1 upwave, — Case 1 gap, — Case 4 upwave, — Case 4 gap.

4.5.5 The effect of draft

The effect of draft can be illustrated using a reflection analysis based on the data gathered in Cases 1 and 4. Figure 4.13 overlays the Case 1 and the Case 4 amplitudes of both the reflected wave in the upwave region and the incident wave in the gap. From this data it is clear that the increase in the draft of the LNG in Case 4 leads to a change in the resonance frequency from 1.00Hz in Case 1 to 0.94Hz in Case 4. In the latter case, the resonance frequency is identical to that identified for Case 3 in figure 4.12. Therefore, it may be concluded that a 52% increase in the beam (Case 3) has an identical effect on the resonance frequency as an 18% increase in the draft (Case 4).

4.5.6 The effect of transmission

The cases presented thus far have all involved a GBS as the second fixed body, beyond which there can be no transmission of wave energy. This section considers the effect of transmission beneath a second fixed body of finite draft, namely an FLNG. Here, there are three regions of interest: the upwave region, the gap and

the downwave region. In the discussion that follows, the results of the reflection analysis for Cases 5 and 6 are compared, together with the single body data described earlier. Since the wave field within the gap is both downwave of the first body and upwave of the second body, the three regions of interest are presented in the two subplots of figure 4.14. Subplot (a) illustrates the variation with frequency of the amplitude of the reflected waves in the upwave region and within the gap. In contrast, subplot (b) illustrates the frequency variation in the amplitude of the incident waves both within the gap and within the downwave region; the former having been transmitted under the first body and the latter transmitted under the second body. It should be noted that, since the majority of the results are below A_{inc} = 10mm, the extent of the vertical axis is limited to $1.6A_{inc}$.

A comparison of the data relating to the gap in figure 4.14 shows that the reflected amplitudes in subplot (a) are identical to the incident amplitudes in subplot (b). This is true across the frequency range for both Case 5 and Case 6. Furthermore, both cases exhibit resonance within the gap at the same frequency, albeit of varying magnitude. Finally, both the Case 5 and the Case 6 data show fluctuations close to the resonance frequency in the amplitude of the reflected wave in the upwave region and, to a larger extent, the amplitude of the incident wave in the downwave region; both effects illustrating the influence of the emitted potential. These observations are similar as those in Case 1 (which includes a bottom-mounted GBS). Therefore, it may be concluded that although the FLNG only extends to a third of the water depth, its presence is sufficient to excite the key hydrodynamics within the gap.

Having discussed the variation of the wave amplitudes within the gap, consider the amplitude of the reflected wave in the upwave region and of the incident wave in the downwave region for Cases 5 and 6, denoted by the green and cyan lines in subplots (a) and (b) respectively in figure 4.14. In both Cases 5 and 6, the amplitude of the reflected wave in the upwave region (subplot (a)) increases with frequency, while the amplitude of the incident wave in the downwave region (subplot (b)) decreases. This trend is also apparent in the single body data.

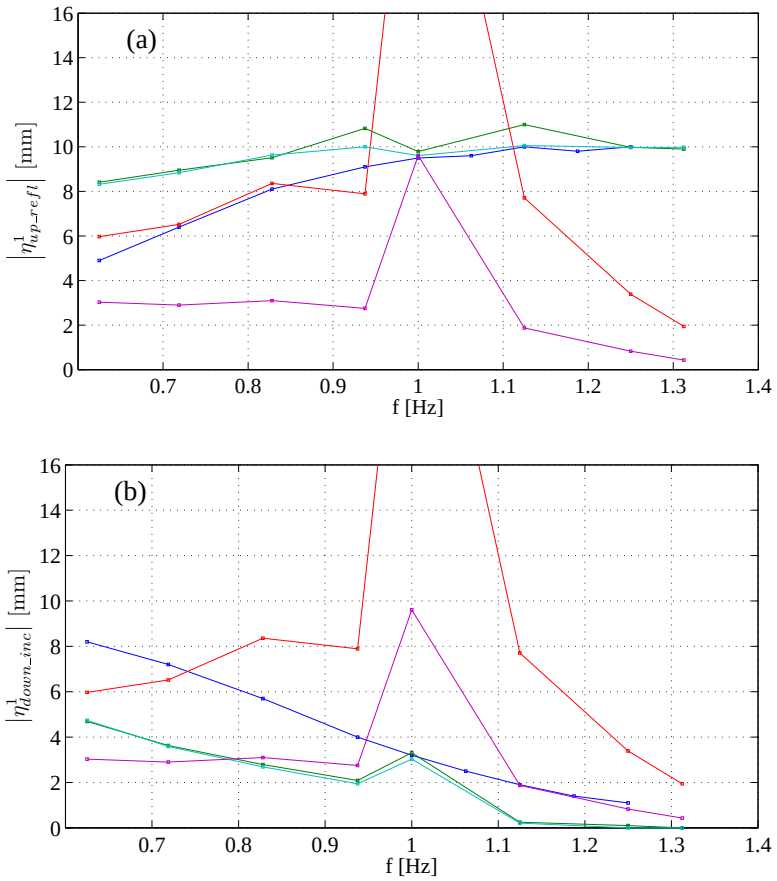


Figure 4.14: Variation with frequency of the first harmonic amplitudes; (a) reflected waves in the upwave region and the gap, (b) incident wave in the downwave region and in the gap; — single LNG, — Case 5, — Case 5 gap, — Case 6, — Case 6 gap.

Therefore, the close agreement between Cases 5 and 6 suggests that the two fixed bodies act as a single body and the order of the bodies (whether the LNG is the upwave or the downwave body) has a negligible effect.

The results of the reflection analysis presented in figure 4.14 give no indication of the relative phasing between the various wave components involved (as discussed previously in the context of figure 4.8). Accordingly, the spatial variation of $|\eta^1|$ and $arg(\eta^1)$ within the NWTs relating to Cases 5 and 6 is considered below. However, in order to facilitate a direct comparison of the cases, the following describes how the differences in the respective NWTs are reconciled.

Figure 4.15 presents a sketch of the NWTs appropriate to Cases 5 and 6,

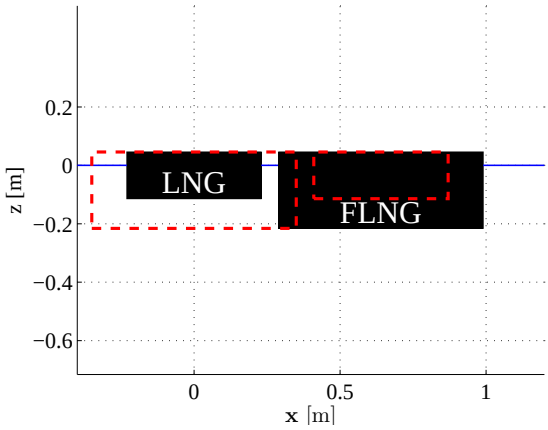


Figure 4.15: Comparison between the Case 5 and the Case 6 numerical wave tanks; — — Case 6.

close to the position of the fixed bodies. From this figure, it is clear that the LNG is the upwave body and the FLNG the downwave body in Case 5, while in Case 6 the bodies are reversed. It has been stated previously that the origin of the x-axis is the centreline of the upwave body. With the beams of the FLNG and the LNG being different, the absolute x position of the free surface nodes in the numerical domains is different between these two cases. This difference is immediately apparent in figure 4.15. In order to directly overlay the upwave region, the gap, and the downwave region, the introduction of a secondary spatial coordinate, $\tilde{x}$, is required. If x refers to the absolute spatial position within the Case 5 domain, $\tilde{x}$ involves some lateral translation of the absolute x coordinates appropriate to the description of the Case 6 domain. The relationship between $\tilde{x}$ and x is defined as follows

$$\tilde{x} = \begin{cases} x + 0.12 & \tilde{x} < -0.23 \\ x - 0.12 & 0.23 < \tilde{x} < 0.29 \\ x + 0.12 & \tilde{x} > 0.99. \end{cases} \tag{4.6}$$

Finally, it should be noted that within the figures given below, the presence of the upwave body (or its translated and scaled equivalent) is depicted using vertical

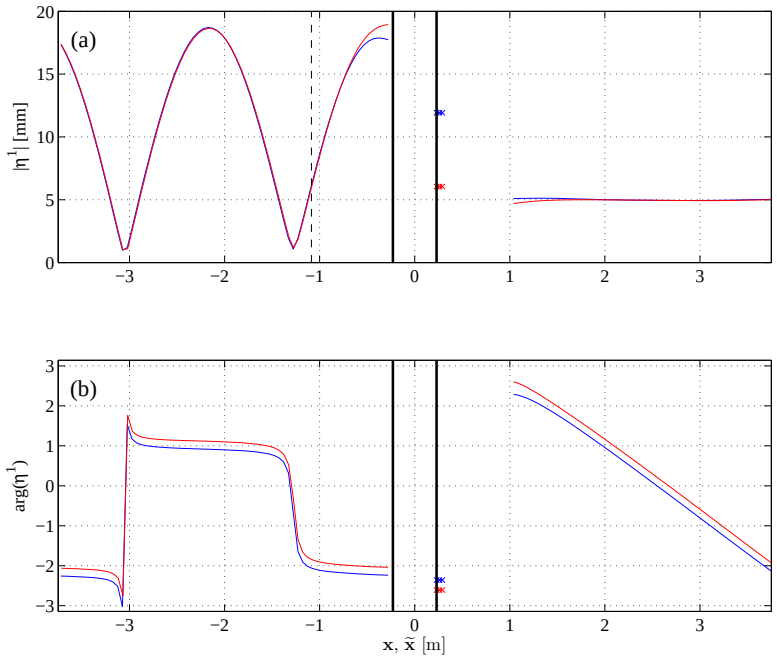


Figure 4.16: Comparison of the spatial variation in x and $\tilde{x}$ of the first harmonic surface elevation (a) amplitude, $|\eta^1|$, and (b) phase, $arg(\eta^1)$, between Cases 5a and 6a, f = 0.625Hz; —— Case 5, —— Case 6; x relating to —— and $\tilde{x}$ relating to – – in figure 4.15

black lines, while the discontinuity between the gap and the downwave data indicates the presence of the downwave body.

Data relating to the lowest incident wave frequency, f = 0.625Hz, are presented in figure 4.16. Subplot 4.16(a) concerns the spatial variation of the amplitude of the first harmonic surface elevation, $|\eta^1|$, and is therefore related to the amplitudes arising from the reflection analysis in figure 4.14 at f = 0.625Hz. A comparison of the data arising from Cases 5 and 6 shows that $|\eta^1|$ in subplot 4.16(a) is effectively identical in both the upwave and the downwave regions. In contrast, $|\eta^1|$ within the gap is shown to be approximately two times larger for Case 5 when compared to Case 6. Subplot 4.16(b) provides information describing the relative phasing, $arg(\eta^1)$, within the three regions of interest. These comparisons confirm that the phasing of the wave components in Case 5 is very similar to that in Case 6. It may therefore be concluded that the results of Cases 5 and 6 are almost identical

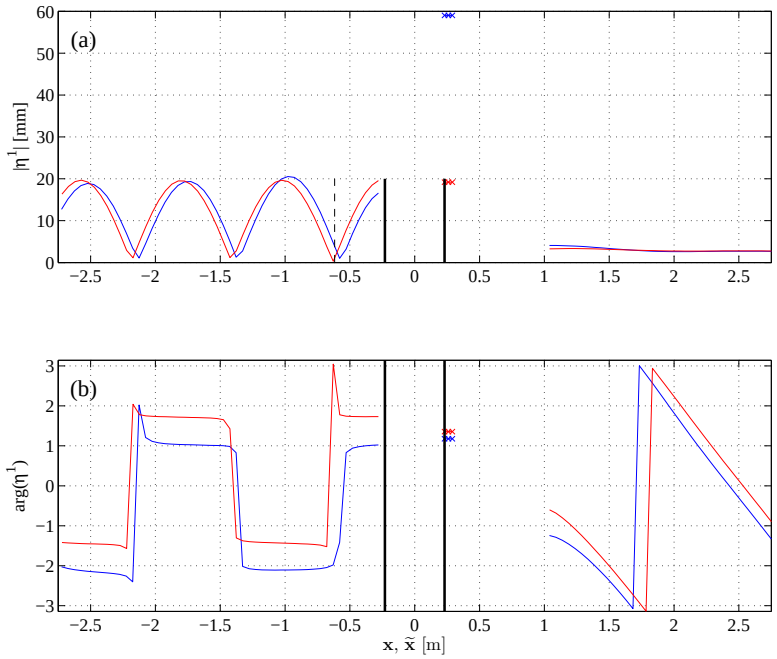


Figure 4.17: Comparison of the spatial variation in x and $\tilde{x}$ of the first harmonic surface elevation (a) amplitude, $|\eta^1|$, and (b) phase, $arg(\eta^1)$, between Cases 5e and 6e, f = 1.00Hz; —— Case 5, —— Case 6; x relating to —— and $\tilde{x}$ relating to – – in figure 4.15

in all aspects, except within the gap.

Figure 4.17 provides a similar sequence of data relating to f = 1.00Hz. This is the frequency at which the fluid within the gap undergoes resonant excitation in both cases. Subplot (a) shows that the resonant excitation is three times larger for Case 5 than for Case 6. Consequently, the effect of the Case 5 emitted potential on the upwave region is more prominent. Indeed, this effect is clearly visible in the $|\eta^1|$ relating to the upwave region of Case 5 in subplot (a); $|\eta^1|$ being less than $2A_{inc}$ at the upwave face of the LNG and the first upwave node being closer than $\lambda/4$ from the LNG. However, subplot (b) shows that the relative phasing between the three regions is very similar for the two cases, despite the differences in $|\eta^1|$ noted above.

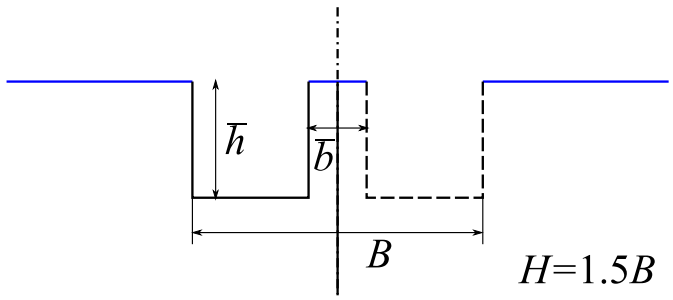


Figure 4.18: Conversion of Case 1 into the equivalent moonpool problem.

4.5.7 Summary of resonance frequency results

A summary of the resonance frequency of the cases presented in Sections 4.5.2 to 4.5.6 is provided below. This summary contrasts the resonant frequencies obtained with the predicted values based upon the approximation outlined in Molin (2001). The latter gives the natural frequency of the piston mode within a moonpool, f_0, as

$$f_0 \approx 2\pi \left(\frac{g}{\overline{h} + \left(\frac{\overline{b}}{\pi}\right)\left(\frac{3}{2} + \ln\left(\frac{H}{2\overline{b}}\right)\right)} \right)^{1/2}, \tag{4.7}$$

where g is the acceleration to due gravity, $\overline{h}$ is the draft of the barge containing the moonpool, $\overline{b}$ is the width of the moonpool, and H is dependent on the width of the barge, B. The sketch provided in figure 4.18 illustrates how these variables (concerning the description of the moonpool) are translated into dimensions relevant to the description of Case 1. Within the figure, the left half describes the Case 1 domain; the solid black rectangular body being the fixed LNG and the solid black vertical line being the upwave face of the GBS. As a fully reflecting boundary, the latter surface may be interpreted as a line of symmetry; the right half of the figure being the mirror image. In this way, the equivalent width of a barge containing a moonpool may be taken as twice the sum of original LNG width and the original gap width. Using this approach, the width of the moonpool is twice the width of the gap defined in Case 1. The equivalent moonpool dimensions for Cases 1 to 6 are presented in Table 4.3, along with the values of f_0, the predicted resonance frequency, and the resonance frequency obtained; the

Case	$\overline{h}$ [m]	$\overline{b}$ [m]	B [m]	f_0 [Hz]	f_{BEM} [Hz]
1	0.114	0.120	1.040	1.01	1.00
2	0.114	0.240	1.160	0.87	0.83
3	0.114	0.120	1.520	0.98	0.94
4	0.135	0.120	1.040	0.97	0.94
5 6	0.165	0.060	1.220	1.01	1.00

Table 4.3: Equivalent moonpool dimensions for Cases 1 to 6, together with a comparison of the predicted and obtained resonance frequencies.

latter being denoted as f_{BEM}.

Within Table 4.3, special attention needs to be drawn to Cases 5 and 6, in which there is no GBS (and hence no line of symmetry). The data presented in Section 4.5.6 provided compelling evidence that the two fixed bodies of finite draft in Cases 5 and 6 effectively act as a single body. Therefore, for the purposes of the present moonpool comparison, $\overline{h}$ is taken as the average draft of the LNG and FLNG, while B is the sum of the LNG beam, the FLNG beam, and the gap width. As a result, the values presented in Table 4.3 for Cases 5 and 6 are identical; the simplified geometric description taking no account of the reversal of the two bodies.

As stated previously, the numerical model applied within this thesis is a time-domain model and the present study involves a coarse resolution in terms of the incident wave frequency. Taking this into consideration, a comparison of f_0 and f_{BEM} in Table 4.3 illustrates very satisfactory agreement. Furthermore, it is clear from Table 4.3 that for the cases considered in the present study, the effect of altering the gap width (Case 2) is most influential in determining the resonance frequency.

4.6 The validity of the fixed-body simplification

The implications of considering fixed bodies to simplify the analysis of side-by-side offloading are addressed within this section. This is achieved through the introduction of Case 7, whose numerical domain is geometrically equivalent to that of Case 1. However, the LNG in Case 7 is able to move, with a single degree of freedom, in heave (ξ_2). In considering the Case 7 setup, it should be noted that there is no use of mooring lines or fenders. The section begins by illustrating the implications of a fixed-body analysis on the surrounding first harmonic wave field. This is achieved by comparing the spatial variation of the surface elevation within the Case 1 and Case 7 NWTs at a number of discrete incident wave frequencies. The section continues by exploring similar implications for the first harmonic body motion, using the vertical forces on the fixed body in Case 1 to predict the heave motion in Case 7. Finally, details of the surrounding wave field for the longest incident wave case in Case 7 are considered; the results illustrating some interesting nonlinear effects within the gap.

4.6.1 The first harmonic wave field

Restricting the Case 7 motion to heave only allows the numerical simulations to be undertaken in a semi-Lagrangian frame of reference, thereby retaining the fine discretisation of the surface elevation data. Furthermore, as heave represents a vertical translation, the amplitude of the first harmonic heave motion, $|\xi_2^1|$, may be directly related to $|\eta^1|$; the latter being the amplitude of the first harmonic vertical motion of the free surface nodes in a semi-Lagrangian frame of reference. Consequently, the data concerning the heave body motion are presented in the figures illustrating the spatial variation of $|\eta^1|$ and $arg(\eta^1)$ within the NWTs of Cases 1 and 7. In the plots, the heave motion is depicted as a discrete point between the vertical solid black lines marking the position of the LNG. Finally, the vertical dashed black line seen in the figures discussed below marks a distance of $\lambda/4$ from the upwave face of the GBS, not the upwave face of the LNG. This is an

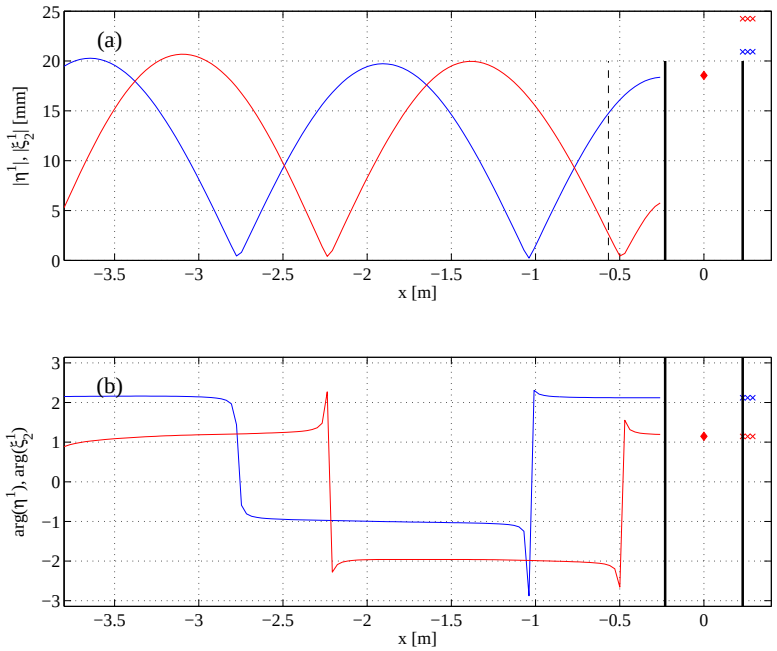


Figure 4.19: Comparison of the spatial (x) variation of the first harmonic surface elevation and body motion (a) amplitude, $|\eta^1|$ and $|\xi_2^1|$, and (b) phase, $arg(\eta^1)$ and $arg(\xi_2^1)$, between Cases 1a and 7a, f = 0.625Hz; —— Case 1, —— Case 7.

important distinction with respect to the spatial variation plots presented within Section 4.5.

Figure 4.19 compares the results of Cases 1a and 7a, corresponding to an incident wave frequency of f = 0.625Hz. Subplot (a) shows that $|\xi_2^1|$ is almost twice the incident wave amplitude, A_{inc} = 10mm. This large body motion is seen to lie between the small $|\eta^1|$ just upwave of the LNG and the larger $|\eta^1|$ within the gap; the latter being just under $2.5A_{inc}$. Furthermore, the position of the first upwave node is only slightly closer than $\lambda/4$ from the upwave face of the GBS. Finally, subplot (b) shows that the phase just upwave of the LNG, the phase of the body motion and the phase of the wave excitation within the gap are all equal. These observations suggest that the heave body motion is, in large part, driven by the standing wave field associated with the presence of the GBS; illustrating the reason why the dashed vertical black line is located at $\lambda/4$ from the upwave face of the GBS within this section.

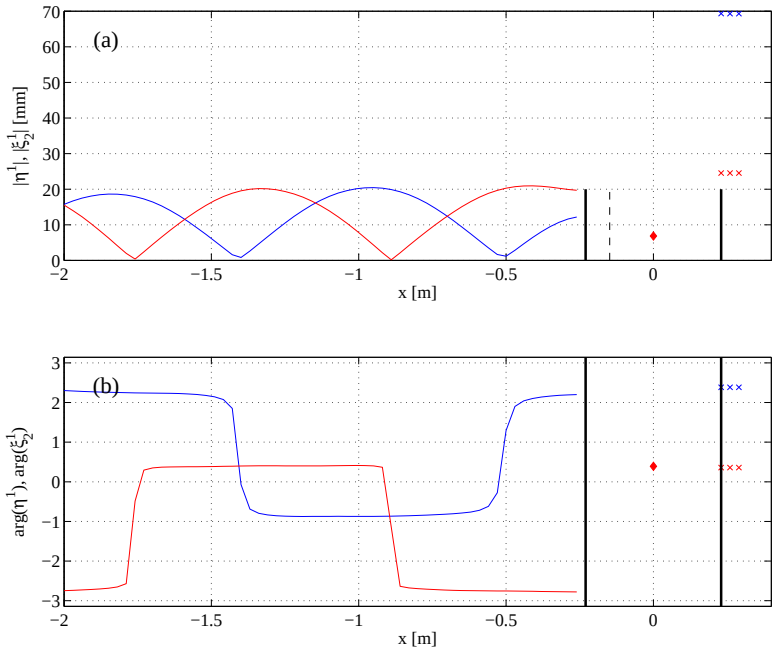


Figure 4.20: Comparison of the spatial (x) variation of the first harmonic surface elevation and body motion (a) amplitude, $|\eta^1|$ and $|\xi_2^1|$, and (b) phase, $arg(\eta^1)$ and $arg(\xi_2^1)$, between Cases 1d and 7d, f = 0.94Hz; —— Case 1, —— Case 7.

The significant differences between the data relating to Case 1 and Case 7 in figure 4.19 illustrate the effect of the radiated potential due to the heave body motion. Indeed, it is possible that, at this incident wave frequency, the effects of the radiated potential cancel out those of the scattered potential due to the LNG. This then allows the effect of the scattered potential due to the GBS to dominate the resulting wave field.

Figure 4.20 provides a similar set of data relating to an incident wave frequency of f = 0.94Hz. In this case, the dashed vertical black line in subplot (a) indicates that the scattered potential due to the GBS defines a node within the boundaries of the LNG. Indeed, subplot (a) shows a much reduced $|\xi_2^1|$ while $|\eta^1|$ either side of the LNG are close to the magnitude of antinodes. The phase variation, depicted in subplot (b), shows that the wave motion in the gap and the body motion are in phase and that both are out of phase with the wave field just upwave of the LNG. Therefore, $|\eta^1|$ either side of the LNG constitute consecutive

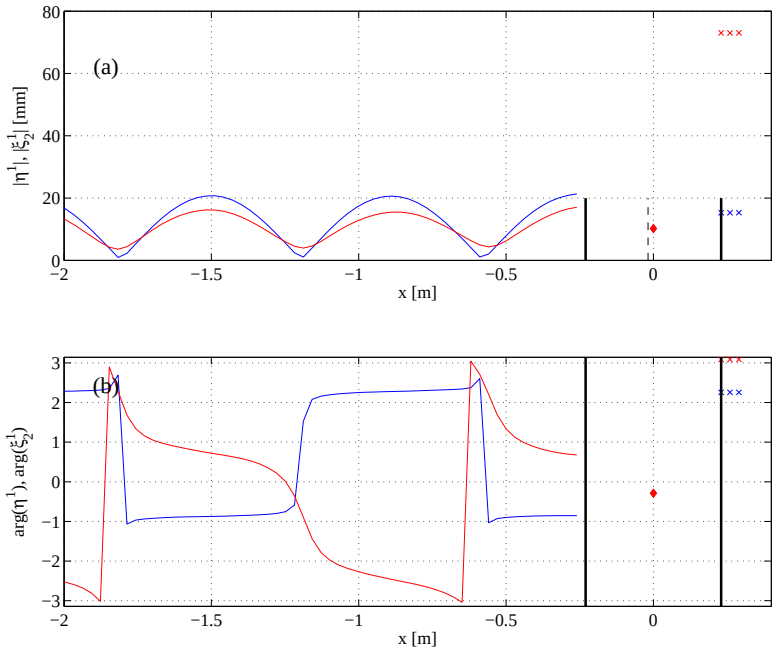


Figure 4.21: Comparison of the spatial (x) variation of the first harmonic surface elevation and body motion (a) amplitude, $|\eta^1|$ and $|\xi_2^1|$, and (b) phase, $arg(\eta^1)$ and $arg(\xi_2^1)$, between Cases 1f and 7f, f = 1.125Hz; —— Case 1, —— Case 7.

antinodes while $|\xi_2^1|$ resembles a node. However, body motion is different to fluid motion. If the LNG were fluid, the first upwave node in subplot (a) would be the second node from the GBS; being a distance of $3\lambda/4$ from the GBS. However, the distance between the GBS and the first upwave node in subplot (a) is found to be approximately 10% smaller than $3\lambda/4$.

Figure 4.21 concerns an incident wave frequency of f = 1.125Hz and corresponds to the resonant wave excitation within the gap for Case 7. This is clearly different to Case 1, for which the resonant wave excitation occurs at f = 1.00Hz (figure 4.6). Subplot (a) of figure 4.21 shows that the resonant wave excitation within the gap for Case 7 is $7.3A_{inc}$. This is smaller than the resonant wave excitation in Case 1, which was just under $10A_{inc}$, but nevertheless is still very significant. Despite the presence of radiated potential from the heaving body motion, the effects of the emitted potential are apparent in the Case 7 results as follows:

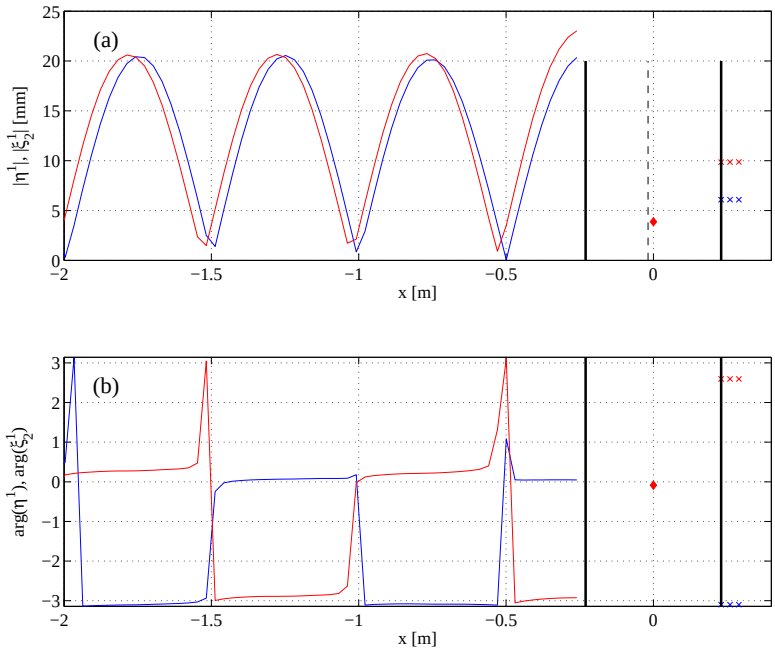


Figure 4.22: Comparison of the spatial (x) variation of the first harmonic surface elevation and body motion (a) amplitude, $|\eta^1|$ and $|\xi_2^1|$, and (b) phase, $arg(\eta^1)$ and $arg(\xi_2^1)$, between Cases 1g and 7g, f = 1.25Hz; —— Case 1, —— Case 7.

(1) The upwave $arg(\eta^1)$ in subplot (b) extends from $-\pi$ to π, between which there is a distinct gradient, albeit not a constant one.

(2) The fluctuations in the upwave $|\eta^1|$, depicted in subplot (a), do not extend over the zero to $2A_{inc}$ range.

Furthermore, subplot (a) of figure 4.21 shows that $|\xi_2^1|$ at the resonance frequency is limited to approximately the incident wave amplitude.

Figure 4.22 considers an incident wave frequency of f = 1.25Hz. This represents a wave that is shorter than that which causes resonance within the gap in Case 7. Subplot (b) shows that the upwave $arg(\eta^1)$ for both Cases 1 and 7 relates to a standing wave mode. Furthermore, the only differences between the upwave Case 1 and Case 7 $|\eta^1|$ in subplot (a) are that the Case 7 data are slightly offset from the Case 1 data, and the Case 7 $|\eta^1|$ just upwave of the LNG is larger than $2A_{inc}$. Indeed, these comparisons indicate that it is only at this very high incident wave frequency that the Case 1 and 7 upwave regions begin to resemble each other.

However, it should be noted that $|\xi_2^1|$ in subplot (a) remains appreciable and that $|\eta^1|$ within the gap for Case 7 is equal to A_{inc}. Finally, subplot (b) shows that the fluid motion within the gap is out of phase with the body motion, which, in turn, is out of phase with the wave field just upwave of the LNG. As a result, when considering a moving body, the fact that $|\eta^1|$ within the gap and the body motion are out of phase indicates that the incident wave frequency is above the resonance frequency.

4.6.2 The first harmonic body motion

Newton's 2^{nd} Law equates the force on a body to its acceleration. However, when that body is moving within fluid (as in Case 7), a coupled hydrodynamic system is formed. Therefore, the expression relating the force and the body motion is given by Cruz (2008) as

$$\mathbf{m} \cdot \mathbf{a} = \mathbf{F}^{exc} - \mathbf{F}^{rad}, \tag{4.8}$$

where $\mathbf{m}$ is the physical mass of the body and $\mathbf{a}$ is its acceleration. $\mathbf{F}^{exc}$ is the exciting force that the body experiences when fixed in its equilibrium position. This force is dependent upon the incident wave potential and the scattered potential. In contrast, $\mathbf{F}^{rad}$ is the radiated force, which is dependent upon the radiated potential and which can be expressed in terms of the body's hydrodynamic properties (see Appendix D). In order to predict the Case 7 heave motion, F_2^{exc} is taken as the vertical force calculated for Case 1 (the fixed equivalent of Case 7). F_2^{rad} is evaluated from a heave decay test; the details of this being given below. The motion determined using this method is referred to as the superposition motion and can be compared to the wave-induced motion for Case 7. Comparisons of this form illustrate the implication of the fixed-body simplification in terms of the predicted first harmonic heave motion.

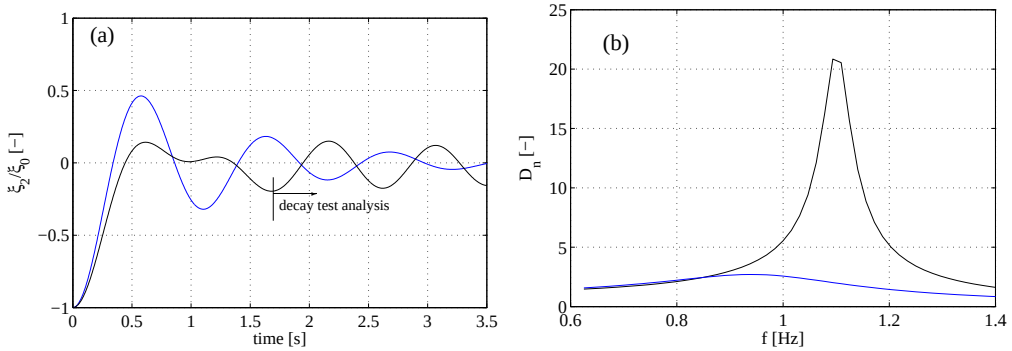


Figure 4.23: Comparison between (a) the time-history of the heave decay test response and (b) the variation with frequency of the dynamic amplification factor, D_n; —— single LNG, —— Case 7 LNG.

Heave decay tests

Before considering the present data, the reader is reminded that Faltinsen et al. (2007) showed that the resonant water motion within a moonpool leads to a peak in the barge's hydrodynamic coefficients. As a result, two decay tests are numerically simulated herein:

(1) the first including a single LNG, hereafter referred to as the single body decay test, and

(2) the second with the LNG located 0.06m upwave of a GBS, hereafter referred to as the Case 7 decay test.

The response of the LNG in the two decay tests is illustrated in figure 4.23(a). This depicts the time-history of the heave motion, ξ_2; the latter being non-dimensionalised by the absolute value of the initial displacement in heave, $|\xi_0|$. The significant differences between the single body and the Case 7 decay tests seen in figure 4.23(a) demonstrate the effect of the second body (the GBS) in close proximity to the LNG. Indeed, for $t < 1.7$s the Case 7 response does not resemble a typical decay test; a possible reason being that the effect of the GBS takes some time to become established. Furthermore, for $t > 1.7$s the decay in the Case 7 response is very slow. The purpose of a decay test is to determine

the hydrodynamic properties of the body (see Appendix D). Due to the unusual nature of the first 1.7s section of the Case 7 decay test, only data lying in the region $t > 1.7$s are used in the analysis of this case.

The hydrodynamic properties of the body can be summarised by considering the frequency variation of the dynamic amplification factor, D_n (see Appendix D for details). The dynamic amplification factor is used in simple harmonic forcing to relate the amplitude of the exciting force to the amplitude of the body motion. For an undamped dynamic system, the magnitude of D_n is infinity at the body's natural frequency; this magnitude decreasing as the damping within the system increases. The variation of D_n with frequency, as evaluated from the two decay tests, is presented in subplot (b) of figure 4.23. The D_n of the single body is shown to be rather flat. This is indicative of the substantial hydrodynamic damping; the response of the single LNG in subplot (a) being reduced to almost zero in as little as 3s. In contrast, there is a significant peak in the amplification factor relating to Case 7 in subplot (b). This occurs at around f = 1.10Hz, which is very close to the incident wave frequency (f = 1.125Hz in figure 4.21) at which resonant wave excitation within the gap was observed for Case 7. It may therefore be concluded that in Case 7 the heave response of the body is driven by the resonant motion of the inviscid fluid within the gap. This also explains why the peak in the D_n for Case 7, in subplot 4.23(b), is so large and why the Case 7 response in subplot 4.23(a) decays very slowly. In undertaking these calculations, the author does recognise that the analysis of the Case 7 decay test appears to neglect the hydrodynamic properties of the physical body itself. Nevertheless, it is encouraging that the numerical model can be used in this simple way to identify the resonance frequency for the complex problem involving a moving body in close proximity to a second fixed body.

As an aside, in order to verify that the Case 7 heave decay test can indeed be used to identify the resonance frequency, a similar decay test was undertaken for a problem involving a much larger gap width of 0.24m. Beyond the initial transient, the frequency of the heave response was seen to decrease. This was

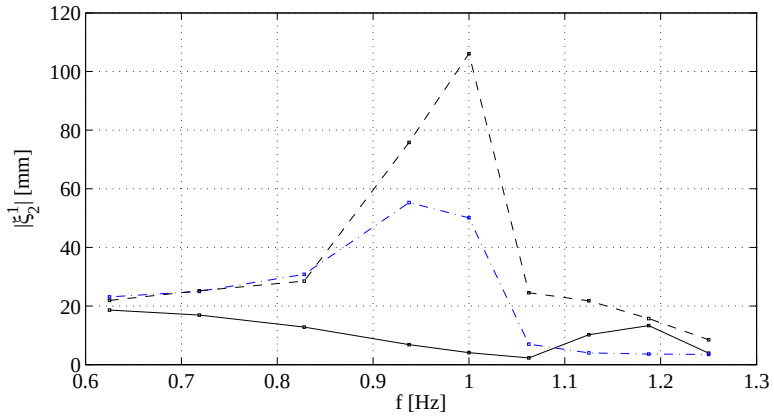


Figure 4.24: Variation with frequency of the first harmonic heave motion; —— Case 7, — — Case 1 with the superposition method based upon the Case 7 decay test, — — Case 1 with the superposition method based upon the single decay test.

exactly as expected due to the effect of increasing the gap width, discussed earlier in Section 4.5.3. More importantly, there was visual evidence of the first sloshing mode. Molin (2001) describes the sloshing modes as involving the backward and forward motion of the fluid between the vertical walls either side of the gap. Furthermore, the spatial (x) variation of the surface elevation within the gap for the first sloshing mode was found to take the shape of a sine wave between $\pi/2$ and $3\pi/2$. In conclusion, the decay test of a moving body in close proximity to a second body may be used to predict both the frequency of the piston mode and the frequency of the first sloshing mode.

Comparison of the predicted heave motion

A comparison of the numerically predicted wave-induced heave motion in Case 7 and the calculations based upon the superposition method is presented in figure 4.24. Two sets of superposition data are presented; one using the hydrodynamic coefficients obtained from the Case 7 decay test and the other using the coefficients obtained from the single body decay test. The figure shows that both sets of superposition data overestimate the Case 7 response, especially around 1Hz; the latter corresponding to the resonance frequency for Case 1. The explanation

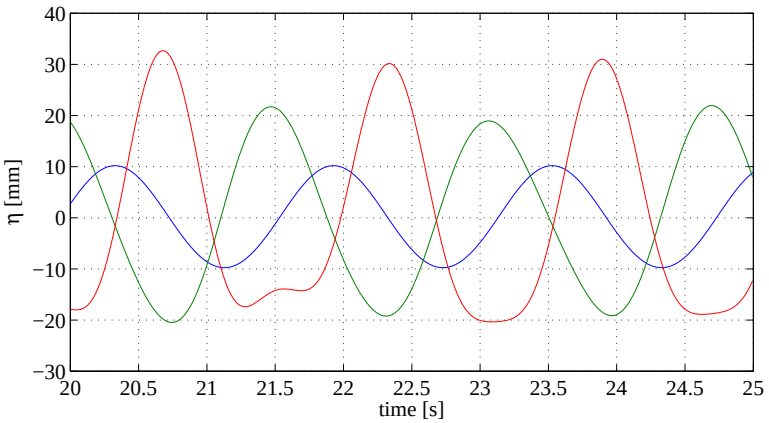


Figure 4.25: Time-history of η at various positions within the numerical wave tank for Case 7a, $f = 0.625$Hz; — input, — antinode, — gap

for this is that the motion of the body forms an important part of the coupled hydrodynamic system and it is not included in either of the superposition methods. The author believes that although the superposition method using single body hydrodynamic coefficients does not include the effect of the presence of the second body in close proximity, its results are more reliable than the superposition method using the Case 7 hydrodynamic coefficients. The latter is thought to be driven by the resonance of the fluid within the gap, which undergoes negligible damping, and therefore leads to an exaggerated response. Evidence of the importance of including the radiated potential (or body motion) is provided in figure 4.24 by the change in the resonance frequency.

4.6.3 The nonlinear wave field within the gap

The presence of nonlinearity within the gap is briefly highlighted by considering the Case 7 data relating to the longest incident wave case, Case 7a with $f = 0.625$Hz. Before considering the data, it should be noted that this is the *least* steep incident wave case considered within the present study. Figure 4.25 concerns Case 7a and overlays the time-history of the total surface elevation, $\eta(t)$, at three positions within the NWT. The first position lies just inside the input boundary, and therefore defines the incident wave conditions, the second lies at the position of the first

upwave antinode, and the third lies within the gap. The time-history at the input indicates a perfectly linear wave varying sinusoidally between $\pm A_{inc}$. Similarly, the data recorded at the antinode indicate the expected standing wave, the fluctuations lying between $\pm 2A_{inc}$ in accordance with linear theory. However, nonlinear effects are clearly present in the time-history of the total surface elevation recorded within the gap; the magnitude of the troughs being (approximately) 10mm less than the magnitude of the crests. This is confirmed by a harmonic decomposition of the data recorded in the gap which reveals the presence of a significant second harmonic; having a magnitude of $0.6A_{inc}$.

At first sight, this observation is unexpected not least because wave nonlinearity is usually associated with the free surface boundary conditions and, therefore, nonlinear effects only become important in steep waves. However, it is interesting to note that the frequency of the second harmonic in figure 4.25 is 2*0.625Hz, which is close to the resonance frequency for Case 7. It therefore appears that the data presented on figure 4.25 add to the argument that the fluid within the gap responds as a rigid body. Specifically, the fluid within the gap undergoes a large excitation at the resonance frequency, irrespective of whether the motion occurs at the first harmonic or the second harmonic of the forcing frequency.

4.7 Conclusions

This chapter has considered the surface elevation within the 2D wave field surrounding two bodies in close proximity; both fixed and moving bodies being considered. The hydrodynamics within the gap between the two bodies were shown to be very different from those in either the upwave or the downwave fields. Indeed, it is argued that the fluid within the gap responds as a rigid body for the following reasons.

(1) The wave excitation within the gap is seen to undergo a resonance. The magnitude of this motion greatly exceeds both the amplitude of the wave transmitted beneath the upwave body as well as the incident wave amplitude.

(2) The resonant wave excitation within the gap leads to a radiated potential, referred to as the emitted potential. This affects the upwave field and, where applicable, the downwave field.

(3) When the LNG is in close proximity to the GBS, its response to an initial heave displacement is driven by the resonance of the fluid within the gap between the two bodies.

(4) The excitation of the fluid within the gap can involve significant nonlinearity, particularly where this corresponds to the resonance frequency.

A principal aim of this chapter has been to determine the characteristics of the two bodies that govern the wave excitation within the gap. This has been achieved by comparing a large number of test cases. The value of the resonance frequency has been shown to be most affected by the gap width and the heave motion of the LNG. The extent of the resonant wave excitation within the gap has been shown to be dependent on the draft of the bodies involved, the upwave body more so than the downwave body. Furthermore, the gap width is important in determining the magnitude of the resonance within the gap.

The consideration of the spatial variation of the surface elevation within the NWT suggested that it is the hydrodynamics within the gap that determine which of the two scattered potentials dominates the upwave field. For incident wave frequencies below the resonance frequency, the upwave field is dominated by the effects of the potential scattered from the GBS. For incident frequencies above the resonance frequency, the potential scattered from the LNG becomes dominant in the upwave field.

Finally, the reader is reminded that the only difference between Case 1 and Case 7 is the heave motion of the LNG. Therefore, a comparison of the Case 1 and Case 7 data illustrates the implications of the fixed-body simplification to a problem involving moving bodies. The present study has shown that the fluid motions within the gap in Cases 1 and 7 have different resonance frequencies. More importantly, it has shown that the heave motion predicted using the vertical

forces calculated in Case 1 is very different to the heave motion calculated in Case 7. Taken as a whole, the results emphasise the importance of incorporating the body motion or the effects of the radiated potential.

5

Three-dimensional analysis of fixed bodies

5.1 Introduction

The work presented thus far has involved a two-dimensional (2D) analysis; considering a single cross-section of the flow. The present chapter concerns the three-dimensional (3D) analysis of the interaction of waves with fixed bodies, including a numerical and an experimental study. A 3D analysis allows both the directional spreading of the incident wave conditions and the complete dimensions of the physical bodies to be incorporated. However, within this chapter, the incident waves remain uni-directional; the aim being to illustrate the effect of the finite length of the bodies. In essence, this chapter seeks to determine which of the 2D results presented in the previous chapters are relevant to the 3D problem.

Studies involving breakwaters provide a common example of the interaction of waves with fixed bodies. Mei & Black (1969) and Kanoria et al. (1999) considered 2D breakwaters, both surface-piercing and submerged. The reflection coefficient, $|R|$, was shown to be dependent on the width of the breakwater. In the case of submerged breakwaters, the variation of $|R|$ with frequency fluctuates, while for surface-piercing breakwaters it does not. Within a 2D analysis the transmission coefficient, $|T|$, is simply determined using $|T|^2 = 1 - |R|^2$. In contrast, the finite length of a fixed body in a 3D analysis leads to the physical process of wave diffrac-

tion, whereby wave energy is transferred into the shadow zone behind the body. This introduces an additional level of complexity to the problem.

Early 3D analysis of breakwaters is found in Penney & Price (1952) and Wiegel (1962), both addressing the problem of waves in a uniform water depth incident upon a semi-infinite breakwater. The analytical solution presented in Penney & Price (1952) includes Fresnel integrals. More recently, these have been replaced by polynomial approximations in the solution presented in McCormick & Kraemer (2002). As a result, the latter solution provides a computationally efficient method of estimating the diffraction coefficient, K_D, within the wave field surrounding a semi-infinite breakwater.

In addressing the case of isolated breakwaters (bodies of finite length), the closed-form analytical solution for a circular cylinder were considered in MacCamy & Fuchs (1954). Arbitrary sections were addressed by Isaacson (1978) using a numerical solution based upon an integral equation technique. Both the surrounding wave field and the force on the body were considered by these authors. Isaacson (1978) included a validation against MacCamy & Fuchs (1954), which showed that the force is adequately reproduced using only eight segments to represent the cylinder. However, four times as many segments were required to yield an estimate of the runup that is within 15% of the closed-form solution; runup being representative of the surrounding wave field. Further studies involving isolated breakwaters have been undertaken by Au & Brebbia (1983) and Briggs et al. (1995). In the latter, the automated coastal engineering system (ACES) numerical code (Leenknecht et al. 1992) was compared to laboratory data recorded along three transects in a 60° sector of the shadow zone. The study involved both regular and irregular wave cases, providing comparisons between the numerical and experimental data. The agreement was found to be worst in the regular wave cases along the transect perpendicular to the edge of the breakwater. Such discrepancies were believed to be due to the large gradients in the wave height that exist along this section.

The numerical study described within the present chapter is a 3D application

of the Boundary Element Method (BEM); the latter being based on the boundary integral equation, applied within a numerical wave tank (NWT). The use of a NWT allows changes in the water depth to be modelled or, in the case of the present study, bodies of finite draft to be included. The so-called corner problem, an inherent difficulty associated with the use of a NWT, is overcome through the introduction of multiple fluxes. An outline of the multiple-flux BEM numerical formulation in 3D is provided in Section 5.2.

The present study represents the first application of this 3D numerical model to problems involving fixed bodies. As a result, careful validation of the numerical predictions is required. This validation involves the description of the water surface elevation within the surrounding wave field. Specifically, Section 5.3 compares the numerical predictions with the analytical theory of semi-infinite breakwaters, based upon McCormick & Kraemer (2002), and with experimental data recorded upwave of a bottom-mounted Gravity Based Structure (GBS).

The numerical predictions of the wave field surrounding a single fixed body in beam seas are presented in Section 5.4.1. The results are used to illustrate the effects of the length of the body, its width and its draft; two incident wave frequencies being considered. The effect of the presence of a second fixed body in close proximity to the first is considered in Section 5.4.2. Due to the long run-times of the 3D numerical model, an experimental study was also undertaken to provide further insights into the problem of two fixed bodies in close proximity. The 2D analysis of this problem, described in Chapter 4, identified very large wave excitations in the gap between the two bodies; the gap width being a key characteristic. The 3D experimental study presented within this chapter considers eight incident wave frequencies and three values of the gap width. Section 5.4.3 describes the experimental setup, through which observations of the surface elevation along the length of the gap are made.

In considering the problem of two fixed bodies in close proximity, the 3D analysis presented herein exhibits resonant wave excitation within the gap at the resonance frequency. Furthermore, the resonance frequency is shown to decrease as

the gap width increases. This behaviour is closely related to the 2D results presented in Chapter 4. In addition, the 3D results suggest that below the resonance frequency the fluid along the whole length of the gap responds as a single entity; this again being comparable to the 2D analysis. However, beyond this frequency, the effects of diffraction become significant and a 2D analysis is no longer valid.

5.2 The multiple-flux boundary element method

The development of the 3D multiple flux BEM formulation has been described in detail in Christou (2009). Archibald (2011) presents both the parallelisation of this numerical model and its validation; the latter involving the description of extreme waves up to, and including, the occurrence of wave over-turning. The description that follows provides an outline of this numerical method, applied to the example of wave interactions with a fixed body of finite draft.

5.2.1 Governing equations

The 3D multiple-flux BEM is appropriate to the description of an incompressible, inviscid fluid undergoing an irrotational flow. The latter allows the gradient of the velocity potential, ϕ, to define the fluid velocity, $\mathbf{u}$, such that $\mathbf{u} = \nabla\phi$, where $\mathbf{u} = (u, v, w)$ denotes the fluid velocity components in the horizontal (x, y) and vertical (z) directions. Adopting the above assumptions, the governing equation, representing mass continuity, can be expressed as the Laplace equation

$$\nabla^2\phi = \frac{\partial^2\phi}{\partial x^2} + \frac{\partial^2\phi}{\partial y^2} + \frac{\partial^2\phi}{\partial z^2} = 0. \tag{5.1}$$

A solution of this equation is given by Green's function $G(p,q) = \dfrac{1}{4\pi r(p,q)}$, where $r(p,q) = |\mathbf{x}_p - \mathbf{x}_q|$; with $\mathbf{x}_p = (x_p, y_p, z_p)$ and $\mathbf{x}_q = (x_q, y_q, z_q)$ respectively define the source and evaluation points on the domain boundary. Using this notation, the Boundary Integral Equation (BIE) is defined by

$$c(p)\phi(p) + \int_\Gamma \phi(q)\frac{\partial G(p,q)}{\partial n}\mathrm{d}\Gamma(q) = \int_\Gamma \left(G(p,q)\frac{\partial \phi(q)}{\partial n}\right)\mathrm{d}\Gamma(q), \tag{5.2}$$

where $c(p)$ is a geometric coefficient reflecting the position of the source point on the boundary (Becker 1992) and $\mathbf{n}$ defines the normal vector, which is positive in the outward direction.

5.2.2 Boundary conditions

With the BIE (equation 5.2) defined in terms of ϕ and $\frac{\partial \phi}{\partial n}$ (or ϕ_n), the boundary conditions within the NWT must be expressed in one or other of these variables. Figure 5.1 provides an isometric projection of the NWT used to simulate waves interacting with a rectangular body of finite length (in y), finite beam (in x) and finite draft (in z). The boundaries making up the NWT include the free surface boundary, Γ_s, the input boundary, Γ_{input}, the fixed body boundary, Γ_b, the radiation boundary, Γ_{rad}, the bed boundary, Γ_{-h}, and the side boundaries, Γ_{refl}. The figure also defines the location of the origin and the x, y and z directions; z being measured positively upwards from the still water level and x aligned with the direction of propagation of the incident waves. Based upon these definitions, the NWT in figure 5.1 concerns the description of a body orientated beam-on to the incident waves. Finally, the nature of the boundary condition specified along each boundary, whether Dirichlet (expressed in terms of ϕ) or Neumann (expressed in terms of ϕ_n), is indicated in the figure; the expression for each of these boundary conditions being described below.

In the present calculations, uni-directional incident wave conditions are specified along the open input boundary. Assuming this boundary remains vertical,

$$\frac{\partial \phi}{\partial n} \equiv -\frac{\partial \phi}{\partial x} = -u_{input} \qquad \text{on } \Gamma_{input}, \tag{5.3}$$

where u_{input} is the analytically-calculated horizontal input velocity. Within the present study, the incident wave conditions are defined as regular waves. Consequently, an accurate but simple analytical description of u_{input} is the Stokes' fifth order solution given in Fenton (1985). The incident wave frequencies considered are f = 0.875Hz and 1.25Hz and the incident wave amplitude is held constant at A_{inc} = 0.01m. Given this small incident wave amplitude, the values of u_{input} are

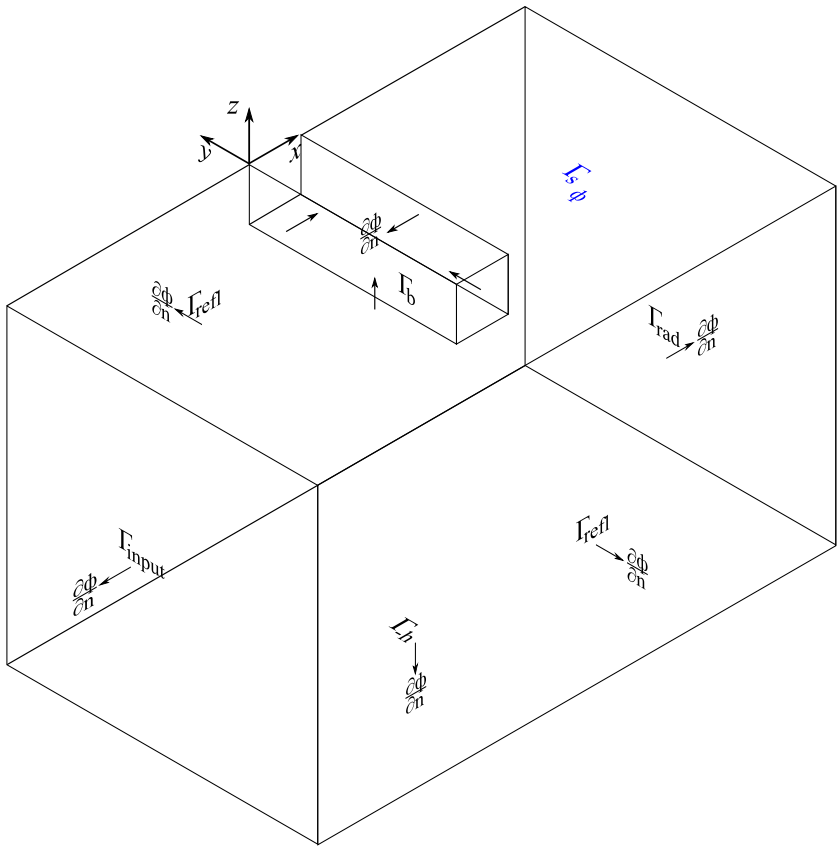


Figure 5.1: 3D numerical wave tank for waves interacting with a fixed body of finite draft subject to beam seas. Individual boundaries are identified and labelled such that Γ_{-h} defines the bed, Γ_{rad} the radiation boundary, Γ_{input} the input boundary, Γ_{refl} the reflecting side boundaries, Γ_b the fixed body and Γ_s the free surface boundary. In each case the appropriate boundary condition is specified.

dominated by the linear terms. Nevertheless, the higher order terms are calculated to avoid unnecessary inaccuracies.

Assuming there is no flow into the bed, the fixed body, or out of the sides of the numerical domain, a zero flux condition can be applied on each boundary such that

$$\frac{\partial \phi}{\partial n} = 0 \qquad \text{on } \Gamma_{-h},\ \Gamma_b \text{ and } \Gamma_{refl}. \tag{5.4}$$

The reflecting nature of the side boundaries (Γ_{refl}) allows the symmetry of the beam-sea problem to be exploited. Accordingly, the fixed body in figure 5.1 has a beam and draft equivalent to that being modelled, but only *half* of its length.

Consequently, the numerical results are mirrored along $y = 0$ to describe the wave field surrounding the complete body.

Having been generated on the input boundary, the incident waves propagate over the length of the domain, interacting with the body. On approaching the downwave end of the domain, they are first damped within a sponge layer of length 0.3m and are then allowed to radiate through the open (and vertical) radiation boundary (Clement 1996) using

$$\frac{\partial \phi}{\partial n} \equiv \frac{\partial \phi}{\partial x} = u_{rad} \qquad \text{on } \Gamma_{rad}, \tag{5.5}$$

where u_{rad} is a horizontal radiation velocity. The evaluation of this velocity is described by Christou (2009) and is based upon the application of the Sommerfeld (1949) radiation condition.

The 3D numerical model is fully nonlinear, requiring the boundary conditions to be applied on the instantaneous position of the moving boundaries. This is achieved through the implementation of the Mixed Eulerian-Lagrangian (MEL) method (Longuet-Higgins & Cokelet 1976). Within this method, the boundary conditions are solved in an Eulerian frame of reference, while the position of the nodes along moving boundaries changes with time; the latter being characteristic of a Lagrangian frame of reference. Within the present study, the only moving boundary is the free surface, Γ_s. In accordance with the physics that govern the description of the free surface, two boundary conditions are applied along Γ_s. The first is the kinematic free surface boundary condition, which requires the fluid velocity normal to the surface to be equal to the velocity of the surface along that normal. The second condition is the dynamic free surface boundary condition which ensures the pressure at the water surface is a constant, or equal to the atmospheric pressure. These conditions can both be written in a semi-Lagrangian frame of reference. Taking due account of the 3D nature of the problem, they are given as

$$\frac{\partial \eta}{\partial t} = w - u\frac{\partial \eta}{\partial x} - v\frac{\partial \eta}{\partial y} \tag{5.6}$$

and

$$\phi = \int \frac{\partial \phi}{\partial t} \mathrm{d}t = \int \left[-gz - \frac{1}{2}\left(u^2 + v^2 + w^2\right) + w\left(w - u\frac{\partial \eta}{\partial x} - v\frac{\partial \eta}{\partial y}\right)\right] \mathrm{d}t \quad \text{on } \Gamma_s, \quad (5.7)$$

where g is the acceleration due to gravity and $\eta(x, y, t)$ is the water surface elevation.

5.2.3 Discretisation

The computational domain outlined in figure 5.1 is discretised into N nodes, forming M isoparametric, bi-quadratic Lagrange elements; each element being made up of nine nodes. It should be noted that in a 3D analysis, there is no universal relationship between N and M. In order to evaluate the terms in the BIE, numerical integration of G and $\frac{\partial G}{\partial n}$ around the elements of the NWT is undertaken by two-dimensional Gauss quadrature. Quadratic shape functions are used to find the appropriate values of the necessary variables at 6 Gaussian integration points. Once the integration is complete, the integral values and the appropriate boundary conditions at each node are substituted into the BIE. This can be expressed as

$$\mathbf{H\Phi} = \mathbf{G\Phi_n}, \quad (5.8)$$

where the diagonal entries of $\mathbf{H}$ absorb the geometric coefficients, $c(p)$. With one velocity potential per node, the sizes of $\mathbf{\Phi}$ and $\mathbf{H}$ are $(N \times 1)$ and $(N \times N)$ respectively. For the multiple-flux formulation, there is one ϕ_n or normal potential flux for every node in each element, therefore the sizes of $\mathbf{\Phi_n}$ and $\mathbf{G}$ are $(9M \times 1)$ and $(N \times 9M)$ respectively.

Within the present NWT, ϕ is unknown along all the boundaries except Γ_s, where ϕ_n is unknown. Consequently, equation 5.8 must be rearranged before it can be solved; the coefficients relating to the known ϕ for the nodes along Γ_s being moved to the right-hand side. Full details concerning the re-arrangement of these equations to produce N independent equations and the nature of the solution procedure are given in Archibald (2011).

5.2.4 Time-marching the solution

As described previously, the MEL method yields a fully nonlinear solution by time-marching the position of the nodes along the moving boundaries. The evolution of the free surface boundary is calculated by time-marching the free surface boundary conditions. In the initial stages of the calculation, this is achieved using three steps of a fourth-order Runge-Kutta scheme. Beyond this point, sufficient information is available to apply a fifth-order Adams-Bashford Moulton time-marching scheme. This latter approach maintains the required accuracy and at the same time limits the necessary computational resources.

The evaluation of the fluid velocity components (u, v, w) along the free surface boundary, Γ_s, requires special attention because this boundary does not remain horizontal. Along Γ_s, the fluid velocity is determined as

$$\begin{aligned} u &= \frac{\partial \phi}{\partial x} = \frac{\partial \phi}{\partial s}\cos\theta_s \cos\alpha_s + \frac{\partial \phi}{\partial m}\cos\theta_m \cos\alpha_m + \frac{\partial \phi}{\partial n}\cos\theta_n \cos\alpha_n, \\ v &= \frac{\partial \phi}{\partial y} = \frac{\partial \phi}{\partial s}\cos\theta_s \sin\alpha_s + \frac{\partial \phi}{\partial m}\cos\theta_m \sin\alpha_m + \frac{\partial \phi}{\partial n}\cos\theta_n \sin\alpha_n, \\ w &= \frac{\partial \phi}{\partial z} = \frac{\partial \phi}{\partial s}\sin\theta_s + \frac{\partial \phi}{\partial m}\sin\theta_m + \frac{\partial \phi}{\partial n}\sin\theta_n, \end{aligned} \tag{5.9}$$

where θ_s, θ_m and θ_n are the angles made by the unit vectors $\mathbf{s}$, $\mathbf{m}$ and $\mathbf{n}$ to the (flat) plane in which the element is described and α_s, α_m and α_n are the azimuthal angles. The gradients ϕ_s and ϕ_m in the two tangential directions are determined using values of ϕ within bi-quartic sliding elements. These sliding elements are made up of 25 nodes; their formation being described in detail in Christou (2009).

In a semi-Lagrangian frame of reference, the nodes along the vertical boundaries within the NWT move according to w, while the nodes along the horizontal boundaries do not move at all. The fixed body (figure 5.1) is made up of three vertical boundaries and one horizontal boundary; the latter defining the bottom (or underside) of the body. If the nodes along the vertical boundaries of the fixed body were to move as described above, they would move past the bottom of the body. However, these nodes are needed to define the position of the vertical sides of the fixed body and, as such, must stay above the bottom of the body. In order to

ensure this, the nodes along the vertical boundaries of the fixed body are divided into vertical columns. Within these vertical columns, the nodes are redistributed linearly between the appropriate free surface and bottom nodes; retaining both the deformation of the free surface and the fixed position of the bottom. It should be noted that this redistribution is only undertaken along the rigid body boundaries and does not affect the free surface boundary.

5.2.5 Outputs

The outputs of the numerical simulations include the spatial coordinates of the nodes, their fluid velocity, their associated potential, ϕ, and the value of their boundary condition. Of these, the spatial coordinates are the easiest to visualise. With the calculations undertaken in a semi-Lagrangian frame of reference, the z coordinate of the nodes along the free surface boundary relates directly to the water surface elevation η (avoiding the need for numerical wave gauges). As a result, the numerical results provided in the present study involve the variation of η within the NWT.

Furthermore, with regular incident wave conditions a simple harmonic decomposition can be achieved using a frequency content analysis based upon a Fast Fourier Transform (FFT) technique. In undertaking such an analysis, the data records must correspond to fully developed wave conditions which are, as yet, undisturbed by reflections from the side walls. Given the linear incident wave conditions, only the amplitude and phase of the first harmonic of the surface elevation is considered; the frequency of this harmonic being identical to the incident wave frequency.

5.3 Validation of the 3D wave field surrounding a fixed body

5.3.1 Comparisons to theoretical solutions for a semi-infinite breakwater

This section concerns the validation of the 3D numerical model applied to the problem of wave interaction with a fixed body. This first example involves a semi-infinite breakwater, as considered by Penney & Price (1952) and McCormick & Kraemer (2002). Both provide theoretical solutions for an infinitesimally thin breakwater of semi-infinite length. In contrast, given the physical basis of the NWT, both these length-scales will be finite in the numerical calculations. Specifically,

(i) The minimum width of the numerical breakwater is four node spacings due to the requirements of the sliding element.

(ii) The length of the numerical breakwater is finite due to the symmetry imposed on the $y = 0$ boundary.

A direct comparison of the semi-infinite breakwater and the breakwater modelled in the numerical calculations within this section is presented in figure 5.2. Within the figure, the red line represents the semi-infinite breakwater, while the shaded rectangle represents the numerical breakwater; the latter having a half-length of 2.94m and a width of 0.28m. Two coordinate axes are described within this figure:

(i) (x, y) referring to the NWT, being consistent with figure 5.1, and

(ii) (x', y') referring to the analytical solution; the origin of this axis being located at the end of the numerical breakwater or $x = 0$m, $y = 2.94$m.

The dashed black lines in figure 5.2 indicate the x-sections along which the transverse (y) variation of the numerical predictions and the analytical solution are

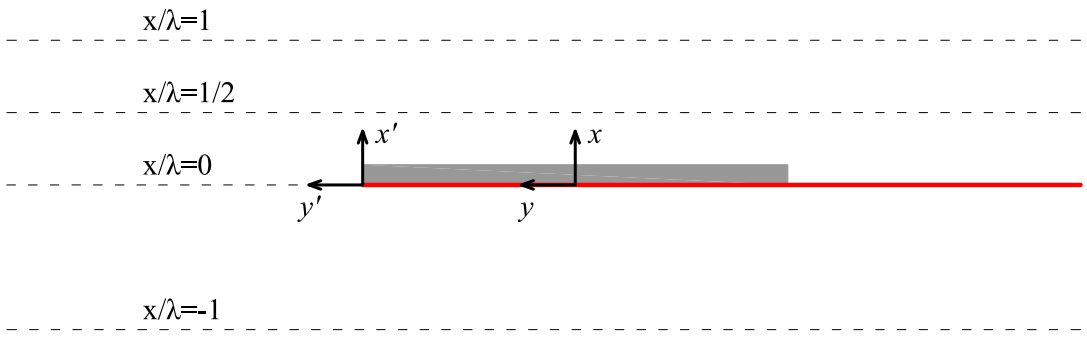


Figure 5.2: Comparison of the semi-infinite analytical breakwater and the numerical breakwater

compared. With the incident waves again propagating in the positive x-direction, it is clear that the validation includes the wave conditions both upwave and downwave of the structure.

The present calculations concern a single incident wave frequency of f = 0.875Hz. With a water depth of h = 0.825m, the corresponding wavelength, λ, is approximately 2m. Consequently, the length of the breakwater in the numerical calculations is $\approx 3\lambda$, while its width is $\approx \lambda/7$. Although this breakwater can certainly be described as long and narrow, it is short in the terms of the analytical solution; for example, Penney & Price (1952) also considered an 'isolated breakwater' of length 10λ. However, the numerical breakwater described above is thought to lie close to the practical limit of the available computational resources; the associated NWT consisting of over 27000 nodes and requiring 6 days to simulate 14s of data.

The comparisons presented below concern the diffraction coefficient, K_D, defined as the ratio of the diffracted wave height to the incident wave height. The analytical solution presented in McCormick & Kraemer (2002) provides a relatively simple means of determining the variation of K_D around the semi-infinite breakwater; resulting from the presence of a pressure gradient at the end of the breakwater, $x' = y' = 0$m. Having implemented this analytical solution, it was

found that $K_D = 1$ at $x' = 0$m for all y'. A possible explanation for this is that the analytical solution is undefined at $x' = 0$m; this location being (simultaneously) upwave and downwave of the infinitesimally thin breakwater. Consequently, when considering the $x/\lambda = 0$ section, the analytical results adopted in the comparisons relate to $x' = -0.01$m.

The transverse variation of K_D is presented in subplots (a) to (d) of figure 5.3; each subplot providing a comparison between the analytical and numerical predictions. In total, the figure considers the four x-sections introduced in figure 5.2; subplot (a) of figure 5.3 being farthest upwave and subplot (d) farthest downwave. In describing the transverse profiles, both the analytical data and the numerical predictions are expressed in terms of y with the data lying in the range $0\text{m} \leq y \leq 6\text{m}$. To achieve this, the numerical data generated in the region $y \leq 0$m are simply mirrored about the plane of symmetry defined by $y = 0$m (figure 5.1). The analytical solution is shifted laterally using the transformation $y = y' + 2.94$m. Adopting this approach, $y < 2.94$m corresponds to the wave field directly upwave or downwave (in the shadow) of the breakwater; while $y > 2.94$m represents the wave field to one side of the head of the breakwater.

Consider first the transverse variation of K_D for $y < 2.94$m in figure 5.3. This lies to the left of the vertical dashed line indicated on each subplot and relates to the wave field in front of the breakwater in subplots (a) and (b), and behind the breakwater in subplots (c) and (d). The single maximum in subplot (a) becomes two maxima in subplot (b), the values of K_D in both subplots ranging between 1.5 and 2.5 ($K_D = 1$ relating to an undisturbed incident wave field). In contrast, the values of K_D in subplots (c) and (d) are significantly smaller, ranging between 0 and 0.5. This is expected since these plots relate to the shadow zone behind the breakwater. These are important trends that are all well modelled by the numerical solution.

Considering the wave field alongside the breakwater, $y > 2.94$m or to the right of the vertical dashed line, K_D is close to one or tends towards one with increasing y. This indicates that the role of diffraction becomes less significant as y

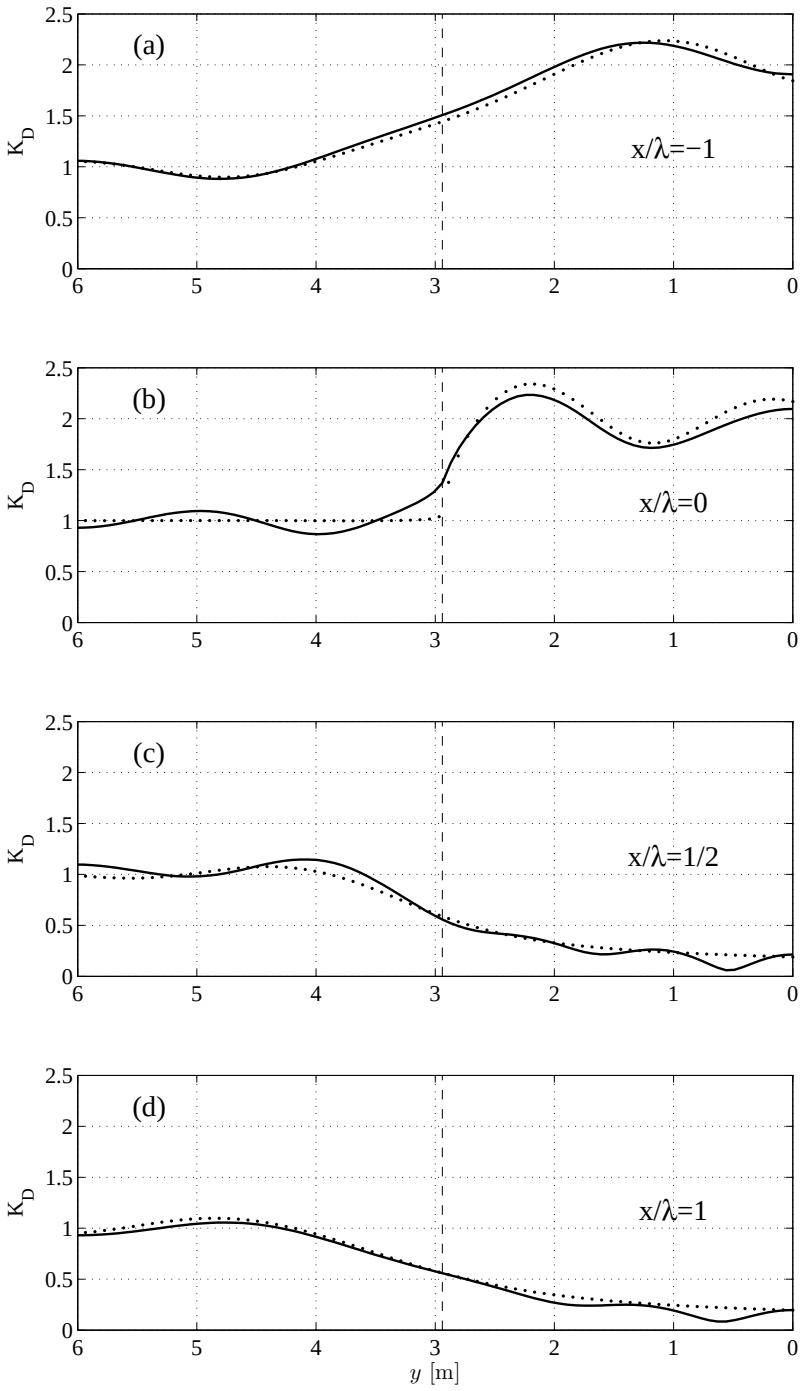


Figure 5.3: Transverse (y) variation of the diffraction coefficient, K_D, for an incident wave frequency of $f = 0.875$Hz: (a) $x/\lambda = -1$, (b) $x/\lambda = 0$, (c) $x/\lambda = 1/2$ and (d) $x/\lambda = 1$; comparisons between numerical predictions and the results of McCormick & Kraemer (2002). Lines correspond to the numerical predictions and dots to the analytical solution of McCormick & Kraemer (2002). Note: the vertical dashed line indicates the location of the head of the breakwater.

increases. Alongside the breakwater, the differences between the numerical predictions and the analytical solution become more significant in subplot (b) and, to a lesser extent, in subplot (c). This is thought to be a consequence of the finite width of the breakwater, and accordingly, the results closest to the breakwater (subplot (b)) are most affected. Finally, it should be noted that within all the subplots, the numerical predictions become horizontal at $y = 0$m. This arises due to the imposed symmetry. In contrast, the breakwater in the analytical solution is semi-infinite. As a result, $y = 0$m has no significance and the data relating to the analytical solution do not become horizontal at this position; the difference being most apparent in subplot (a). Overall, after taking into account the differences between the modelled breakwaters, figure 5.3 shows very good agreement between the numerical predictions and the analytical solution.

5.3.2 Comparisons to experimental data involving a bottom-mounted GBS

The second example concerns the wave field directly upwave of a bottom-mounted GBS; the geometry of this body being similar to an isolated breakwater. In this case, the numerical predictions are compared with experimental data. Two incident wave frequencies, $f = 0.875$Hz and $f = 1.25$Hz, are considered; the incident wave amplitude being held constant at $A_{inc} = 0.01$m.

Experimental setup

The experimental study was undertaken in the Hydrodynamics Laboratory in the Civil and Environmental Engineering Department at Imperial College London. The observations were made in a 3D wave basin, having a plan area of 12m x 20m. Within this series of tests a constant water depth of $d = 0.825$m was maintained throughout the basin and the surface elevation was recorded using resistance-type wave gauges positioned upwave of the GBS. Figure 5.4 provides a plan view of the GBS located within the wave basin. The coordinate axes (x, y) used to define this

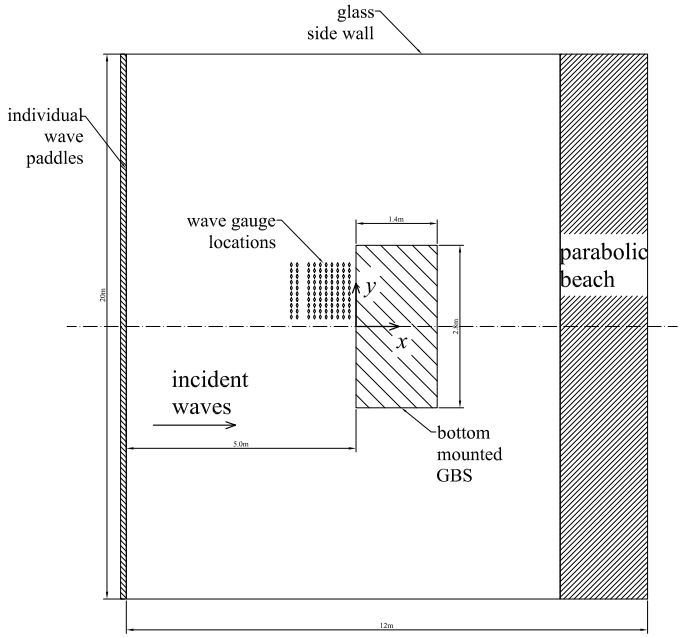


Figure 5.4: Plan view of the bottom-mounted GBS located within the wave basin. (Not to scale.)

arrangement is directly equivalent to that used within the NWT. In particular, the direction of the incident wave propagation is defined by the positive x-axis and the long axis of the GBS is aligned with the y-axis. Within the wave basin, the waves are generated by 56 flap-type wave paddles; being hinged at 0.7m below the still water level. Each paddle is equipped with active force-feedback control and is thus able to absorb reflections from the beach and, more importantly, from the GBS. Furthermore, the evanescent modes, inherent of wave generation, are avoided by positioning the front face of the GBS 5m from the wave paddles. The decay in the magnitude of the evanescent modes with distance from the paddle face (Spinneken & Swan 2009) is such that they will have no influence on the wave behaviour in the vicinity of the GBS. Figure 5.4 also illustrates the 88 wave gauge locations at which the upwave field was recorded; the spacing of the wave gauges being 0.1m. In accordance with the numerical calculations, the symmetry of the problem is again exploited; the recorded data are mirrored about the line of symmetry to describe the transverse (y) variation along the entire length of the

GBS.

The time-history of the water surface elevation, $\eta(t)$, was recorded at each spatial location indicated by the diamonds on figure 5.4. Due to the number of available channels of recording equipment, each column of diamonds illustrates the position of the wave gauges during one experimental run; recording the transverse (y) variation in $\eta(t)$ at one x location. The experimental runs were then repeated with the gauges moved to each of the ten x locations. This process was undertaken for the two incident wave frequencies. With the total data set, for each frequency case, being based upon the accumulation of individual data records, it is important to monitor the repeatability of the incident wave conditions. This was achieved by placing a single wave gauge, referred to as the reference gauge, well away from the influence of the GBS. Records of the incident waves, obtained at this gauge, were found to be highly repeatable; the root-mean-square variations in the incident wave amplitudes being less than 0.0001m (0.1mm).

Comparison of the experimental and numerical data

Figure 5.5 illustrates the spatial (x, y) variation of the amplitude of the first harmonic surface elevation, $|\eta^1|$. Within this figure, the spatial variation is described using coloured contour lines, the magnitudes of $|\eta^1|$ being defined on the colourbar adjacent to each plot. Figure 5.5 presents both the experimental and the numerical data, in subplots (a) and (b) respectively. It should be noted that subplot (a) involves the full extent of the experimental data; the first line of wave gauges being spaced 0.115m from the front face of the GBS. In contrast, subplot (b) involves only the area of the numerical predictions that overlaps with the experimental setup.

Within figure 5.5, the incident waves propagate from the left-hand side and are reflected by the front face of the GBS located at $x = 0$m to result in the standing wave field. The latter is seen to consist of antinodes (depicted in red) and nodes (depicted in blue) occurring alternately in x. The fact that there are concentrated areas of dark red and dark blue signifies that there is a fluctuation about

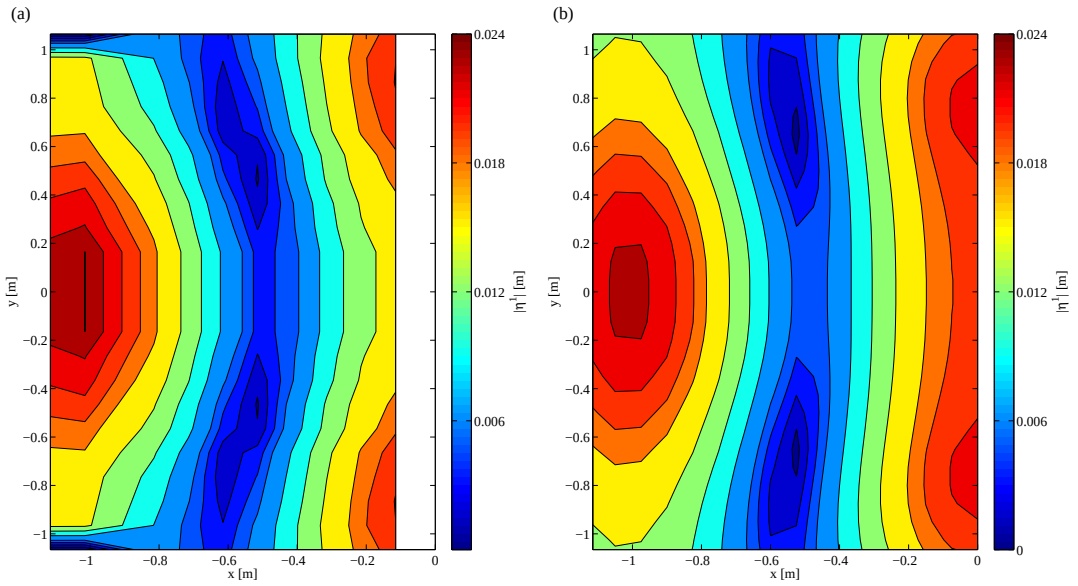


Figure 5.5: Spatial (x, y) variation of the amplitude of the first harmonic of the water surface elevation, $|\eta^1|$, directly upwave of a bottom-mounted GBS for $f = 0.875$Hz; (a) experimental measurements and (b) numerical predictions.

$|\eta^1| = 0.02$m at the antinodes and a fluctuation close to zero at the nodes. In order to emphasise this fluctuation, the discretisation of the contour lines is finer at the extreme ends of the colourbars. Comparing subplots (a) and (b), it is clear that a similar pattern of nodes and antinodes is observed in both the experimental and numerical results. Subplots (a) and (b) also show that the two discernable peaks along the antinode closest to the GBS, merge into a single peak along the second antinode at $x \approx -1$m. The containment of the experimental peak at this second antinode is a result of the lack of recorded experimental data at $y = -1.065$m for the last two x locations (see figure 5.4) and hence the interpolation to zero at these locations.

Figure 5.6 provides the equivalent plot for the $f = 1.25$Hz incident wave case. In this example, the incident wavelength is shorter and hence there is a greater number of antinodes and nodes occurring in x than in the previous figure. Furthermore, the transverse (y) variation is now characterised by three, more distinct, peaks along the antinode closest to the GBS. As before, this transverse variation

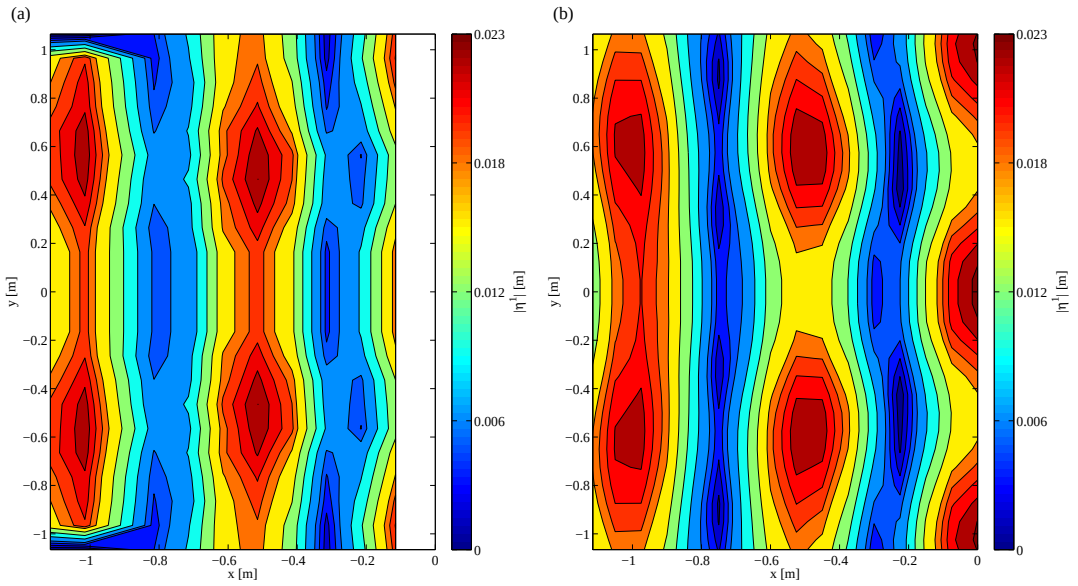


Figure 5.6: Spatial (x, y) variation of the amplitude of the first harmonic of the water surface elevation, $|\eta^1|$, directly upwave of a bottom-mounted GBS for f = 1.25Hz; (a) experimental measurements and (b) numerical predictions.

changes with increasing distance (x) away from the GBS. These observations are present in both the numerical and the experimental data. It should also be noted that the jagged nature of the experimental results in subplot (a) is a direct consequence of the large discretisation in the wave gauge locations, when compared to the incident wave length.

Taken together, figures 5.5 and 5.6 provide an overview of the comparisons between the experimental data and the numerical predictions. In the two figures that follow, figures 5.7 and 5.8, direct comparisons between the two data sets are provided. In both figures, subplot (a) concerns the transverse (y) variation along three x-sections, while subplot (b) denotes the inline (x) variation along three y-sections. In each of these examples, the numerical predictions are represented using lines, while the experimental data are represented using discrete dots. The position of the chosen sections differs between the two frequency cases, but corresponds to the position of the wave gauges in the experimental setup. Although the position of the nodes along the free surface, Γ_s, in the NWT does not exactly

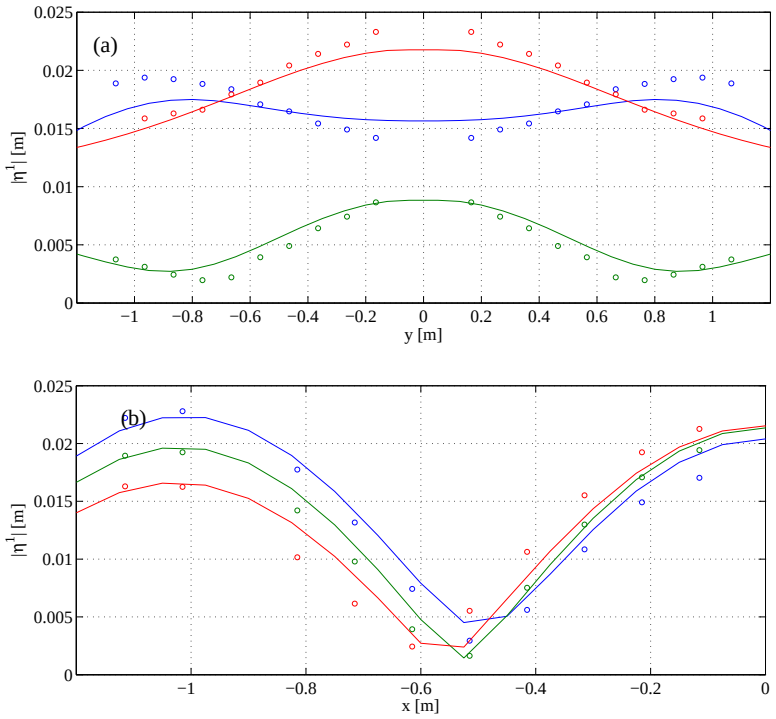


Figure 5.7: Transverse (y) and inline (x) variation of the amplitude of the first harmonic of the surface elevation, $|\eta^1|$, directly upwave of a bottom-mounted GBS for f = 0.875Hz; comparisons between numerical predictions, denoted by lines, and experimental measurements, denoted by dots, at (a) x-sections corresponding to —— x = −0.215m, —— x = −0.615m, —— x = −1.115m and (b) y-sections corresponding to —— y = 0.265m, —— y = 0.565m, —— y = 0.865m.

correspond to the position of the wave gauges, the maximum difference between the two is always less than 0.015m or $\lambda/67$ for the shorter wave case.

Figure 5.7 considers the long wave case, corresponding to an incident wave frequency of f = 0.875Hz. Subplot (a) concerns the transverse variation of $|\eta^1|$ at the two antinodes (x = −0.215m and x = −1.115m) and at the interlaying node (x = −0.615m). The agreement between the numerical predictions and the experimental measurements is clearly demonstrated at each of the three x-sections. Subplot (b) concerns the inline (x) standing wave field at three positions along the length of the GBS, at y = 0.265m, y = 0.565m and y = 0.865m. Since a 2D analysis is essentially an inline analysis, the data presented in subplot (b) most

clearly illustrate the effects of a fully 3D analysis. In other words, it illustrates the effect of the finite length of the body or of the presence of pressure gradients at the ends of the body in a 3D analysis. Within subplot (b), the magnitudes of the two antinodes along any one y-section are not equal; the discrepancy in these magnitudes varying between the three y-sections considered. Furthermore, the antinode with the largest magnitude changes from being at $y = 0.865$m for the first antinode to being at $y = 0.265$m for the second antinode. These observations are apparent in both the numerical predictions and the experimental data. Furthermore, they are clearly in conflict with the expected inline variation arising in a 2D wave field upwave of fully-reflecting body such as the GBS. Whilst there are minor differences between the experimental data and the numerical predictions, it is clear that the numerical predictions are able to capture the essential differences between a 2D and a 3D analysis, specifically the effect of the pressure gradients present in the latter.

Figure 5.8 concerns the short wave case with an incident wave frequency of $f = 1.25$Hz. Due to the shorter wave length, subplot (b) only extends from $-0.75\text{m} < x < 0\text{m}$ in an effort to present the results more clearly. Subplot (a) concerns the transverse variation of $|\eta^1|$ at $x = -0.315$m, -0.515m and -0.615m, while subplot (b) concerns the inline variation of $|\eta^1|$ at $y = 0.265$m, 0.565m and 0.965m. Once again, the numerical predictions reproduce the essential characteristics of the experimental data. Indeed, taking both cases in turn, the agreement between the numerical predictions and experimental measurements is good.

5.4 3D wave interaction with fixed bodies

The comparisons outlined above confirm that the numerical model satisfactorily predicts the 3D wave field surrounding a single fixed body. The present section identifies the key characteristics of the problem that govern this wave field; the cases considered involve variations in the body length, draft and beam, as well as the presence of a second body in close proximity. The results presented include

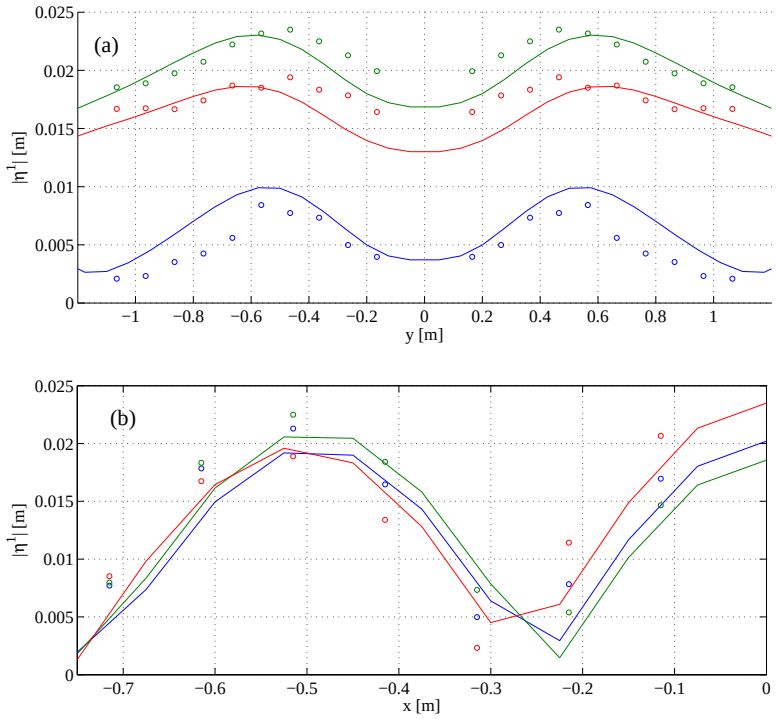


Figure 5.8: Transverse (y) and inline (x) variation of the amplitude of the first harmonic of the water surface elevation, $|\eta^1|$, directly upwave of a bottom-mounted GBS for f = 1.25Hz; comparisons between numerical predictions, denoted by lines, and experimental measurements, denoted by dots, at (a) x-sections corresponding to —— x = −0.315m, —— x = −0.515m, —— x = −0.615m and (b) y-sections corresponding to —— y = 0.265m, —— y = 0.565m, —— y = 0.965m.

both numerical data and experimental measurements. While the former provides information concerning the surrounding wave field, it is limited to two incident wave frequencies. In contrast, the experimental observations are limited to the behaviour over the length of the gap between two bodies in close proximity, but incorporate eight incident wave frequencies and three gap widths.

5.4.1 Wave field surrounding a single fixed body

The figures presented within this section concern a large area of the NWT. In order to distinguish the nature of the wave field involved, specifically whether it is standing or propagating, the spatial variation of both the amplitude and the

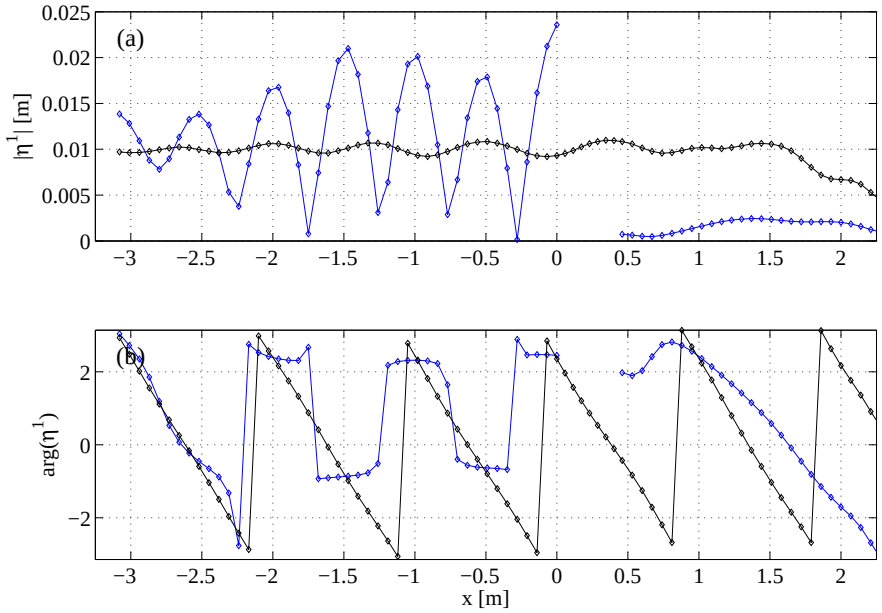


Figure 5.9: Inline (x) variation of first harmonic surface elevation (a) amplitude, $|\eta^1|$, and (b) phase, $arg(\eta^1)$, around a fixed LNG at two y-sections corresponding to the —— centreline (y = 0m), —— edge of domain (y = −3.78m)

phase of the first harmonic surface elevation, $|\eta^1|$ and $arg(\eta^1)$ respectively, are considered. To facilitate the interpretation of such plots, figure 5.9 depicts two y-sections within the NWT containing a single body of finite length, finite width and finite draft. Within the figure, the first y-section corresponds to the centreline (y = 0m) and the second to the edge of the NWT (y = −3.78m).

Figure 5.9 illustrates the inline variation of $|\eta^1|$ and $arg(\eta^1)$ in subplots (a) and (b) respectively. In subplot (a), it can be seen that the centreline data are discontinuous in x; the discontinuity representing the finite width of the single body. In contrast, the edge data are continuous, indicating that the body is of finite length. The additional information required (information that cannot be deciphered from the figure) is that the body is also of finite draft. In considering such a flow, there are three regions of interest:

(i) The wave field upwave of the body, represented in figure 5.9 by the centreline data for x < 0m.

(ii) The wave field downwave of the body, represented by the centreline data for $x > 0.46$m (0.46m corresponding to the beam of the body).

(iii) The wave field alongside the body, represented by the edge data, is continuous in figure 5.9 as this y-section lies beyond the finite length of the body.

The centreline data in figure 5.9(b) indicate that the upwave $arg(\eta^1)$ is predominantly made up of constant sections with jumps of π between them; indicating zero phase speed and therefore a standing wave field. However, these constant sections diminish for $x < -2$m to give an almost constant gradient; the latter representing the phase speed of the propagating incident waves. The presence of a gradient in the phase variation illustrates that the input boundary is, as yet, only slightly disturbed by the waves reflected from the fixed body. In subplot (a), the centreline upwave $|\eta^1|$ close to the body is made up of antinodes and nodes; their magnitudes varying in x for the reasons discussed in Section 5.3. Closer to the input boundary, the fluctuations in $|\eta^1|$ about $A_{inc} = 0.01$m are much smaller. This confirms the reduced influence of the reflected waves on the incident wave conditions at this location. Undisturbed input conditions are apparent in the edge data, corresponding to $y = -3.78$m. Evidence of this is provided by the fact that $|\eta^1|$ is almost constant at A_{inc} in subplot (a) and $arg(\eta^1)$ in subplot (b) is indicative of a pure propagating wave. Finally, the centreline data relating to the downwave field in subplot (b) show that beyond an initial fairly constant phase section, the downwave field involves a propagating wave. However, the downwave $|\eta^1|$ on the centreline in subplot (a) indicates that this wave is of very small magnitude.

Figure 5.9 illustrates just two of the many y-sections within the 3D NWT. The figures within the rest of this section include all of the y-sections by presenting the data in the form of contour plots of $|\eta^1|$ and $arg(\eta^1)$. The former have already been encountered in Section 5.3; the differences between a 2D and a 3D analysis having been attributed to the pressure gradients present at the ends of a body. The results below illustrate how the 3D wave field surrounding a single fixed body

is affected by a range of different pressure gradients.

In figure 5.10, the body depicted using a black rectangle describes a bottom-mounted GBS, which has a finite length of 2.8m but extends to the downwave end of the NWT so that there is no downwave field. Consequently, the only pressure gradient is due to the finite length of the GBS; the pressure gradient being located at (0,±1.4). If l' denotes the half-length of the GBS (1.4m), the total width of the numerical domain is $\approx 2.7l'$ while its total length is $\approx 3.8l'$; $\approx 2.2l'$ of the latter being upwave of the body. The larger upwave region allows the wave field surrounding the body to become fully developed before the reflected waves contaminate the incident wave conditions. Similarly, the total width of the numerical domain ensures that any unwanted reflections from the side walls do not affect the wave field immediately surrounding the body.

Figure 5.10 considers the 3D spatial variation of $|\eta^1|$ in subplots (a) and (c) and of $arg(\eta^1)$ in subplots (b) and (d); (a) and (b) concerning the long wave case with f = 0.875Hz and (c) and (d) the short wave case with f = 1.25Hz. The spatial variation of $|\eta^1|$ in subplot (a) shows the upwave field consisting of antinodes in red and nodes in dark blue; the pattern extending slightly beyond the length of the body. Alongside the body, for $x > 0$m, the turquoise colour indicates the undisturbed incident wave field. To illustrate the interpretation of the contour phase variation in subplot (b), consider the lower right-hand corner which has been identified as the undisturbed incident wave field. The $arg(\eta^1)$ here is seen to be a rainbow pattern made up of equally thick strips of colour indicating a constant variation that goes from dark red (equivalent to π on the colourbar) to dark blue (equivalent to $-\pi$). This rainbow phase pattern indicates a propagating wave travelling in the direction of the colour change from red to blue. Furthermore, the phase variation in the standing wave field upwave of the GBS is seen in subplot (b) to be made up of wide bands of two alternating colours, one cold (blue) and one warm (orange) to cover the jumps of π. As indicated previously, the transverse variation along the antinodes and nodes of the standing wave field in the upwave region changes with distance x away from the body.

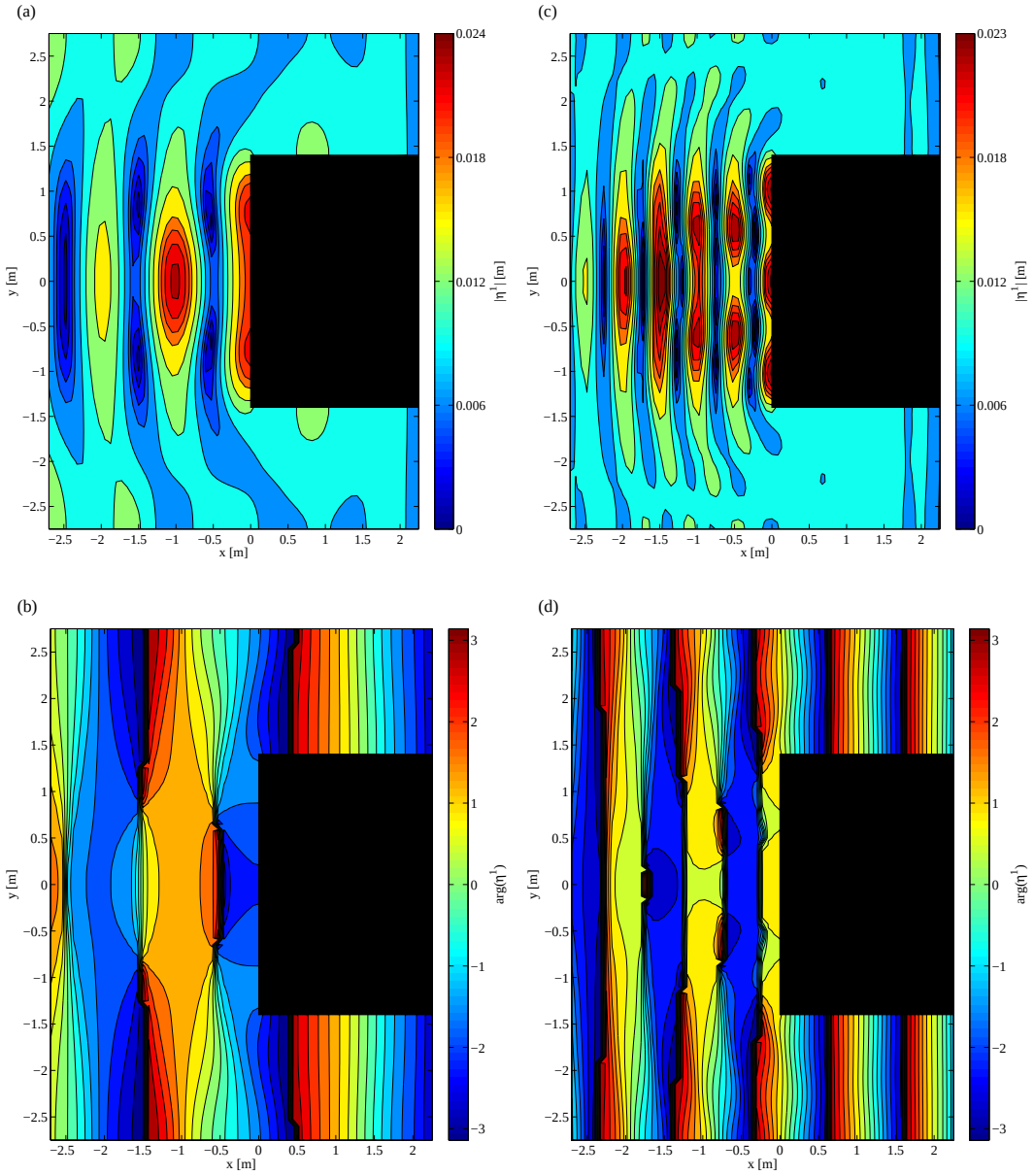


Figure 5.10: Contours of the amplitude, $|\eta^1|$, and phase, $arg(\eta^1)$, of first harmonic of the water surface elevation around a bottom-mounted GBS at (a)&(b) $f = 0.875$Hz and (c)&(d) $f = 1.25$Hz.

The differences between subplots (a) and (c) show that the transverse variation of $|\eta^1|$ in the upwave field is frequency-dependent, suggesting that the number of fluctuations along the antinode closest to the fixed body is dependent on the ratio of the finite body length and the incident wave length. In contrast, subplots (b)

and (d) are rather similar; the only difference being the incident wave length and therefore the width of the rainbow patterns and of the constant bands of colour. This observation suggests that the some important aspects of the nature of the surrounding wave field are independent of frequency.

Figure 5.11 considers the case in which the GBS is of finite *beam* (0.7m) as well as of finite length (2.8m), but still extending over the complete water depth. The introduction of a finite beam leads to a second pressure gradient at (0.7,±1.4), which drives diffraction into the downwave region.

The upwave fields in subplots 5.11(a) and 5.11(c) are similar to the upwave fields in subplots 5.10(a) and 5.10(c) respectively; indicating that the beam of the fixed body has little effect on the wave characteristics in the upwave regions. However, alongside the body for $x > 0.7$m in both subplots 5.11(a) and 5.11(c), the finite beam leads to a reduction in $|\eta^1|$ below $A_{inc} = 0.01$m. This arises because of the diffraction of the incident wave energy into the downwave field. This diffraction is clearly apparent in the phase variation within subplots 5.11(b) and 5.11(d) as follows. The rainbow pattern in the lower right-hand corner in both cases is seen to bend behind the GBS to create a rainbow pattern in the y-direction. This indicates wave propagation in y, with energy transferred into the otherwise still water environment behind the body. This propagating wave subsequently interacts with the wave propagating from the other end of the GBS. These waves are propagating in the opposite direction (as seen by the reverse colour variation in $arg(\eta^1)$) and thus produce a standing wave field.

Figure 5.12 considers two cases of a fixed body that is of finite *draft*, as well as finite beam and finite length. The body in subplots 5.12(a) and 5.12(b) is a model of an FLNG; having a draft of 0.216m, a beam of 0.7m and a length of 2.8m. As a result, the only difference between the FLNG and the GBS in figure 5.11 is the finite draft of the FLNG. The body in subplots 5.12(c) and 5.12(d) is a model of an LNG; having a draft of 0.114m, a beam of 0.46m and a length of 2.8m. Since figure 5.12 considers these two body geometries, it only concerns data relating to the long wave case ($f = 0.875$Hz).

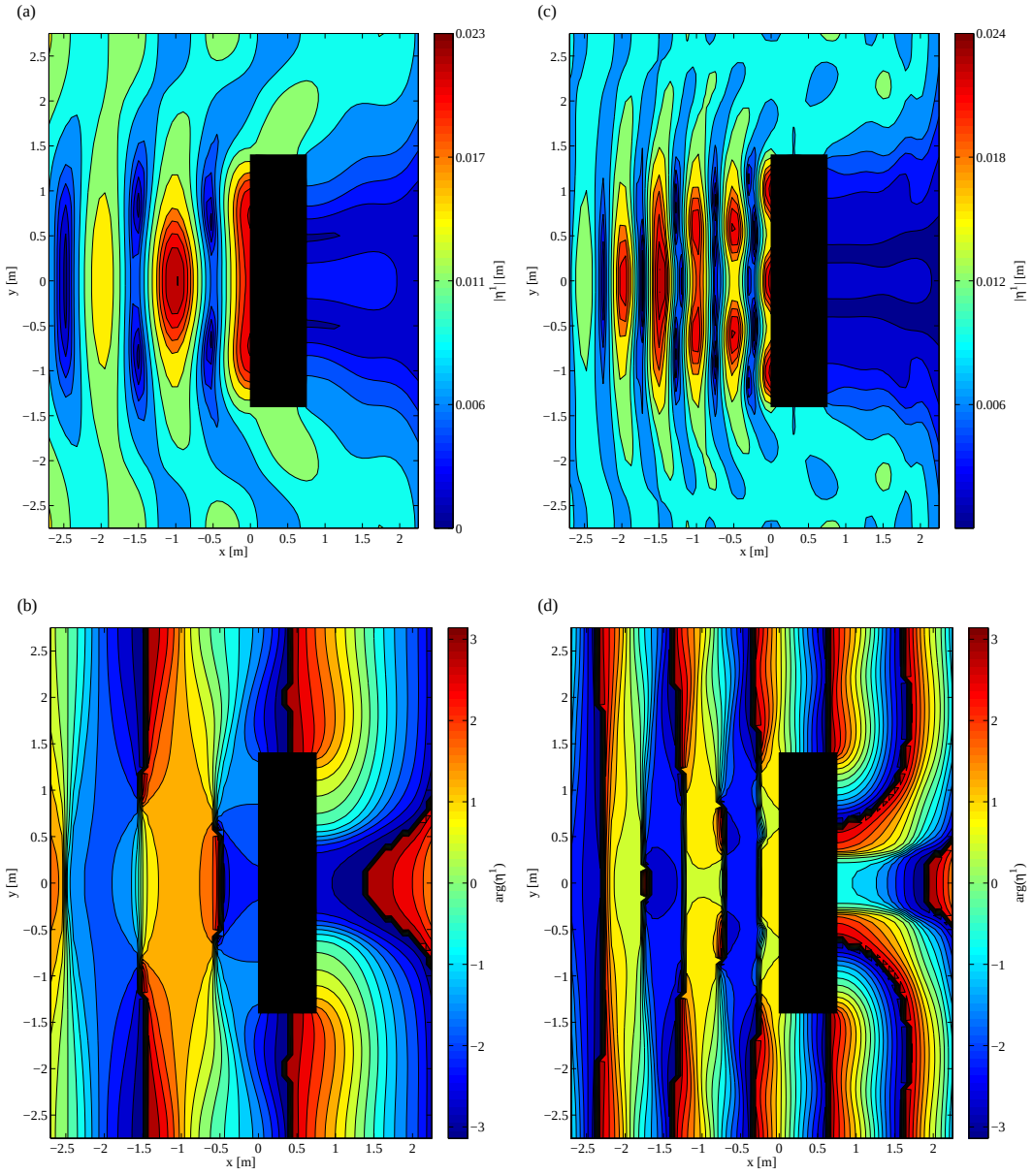


Figure 5.11: Contours of the amplitude, $|\eta^1|$, and phase, $arg(\eta^1)$, of the first harmonic of the water surface elevation around a bottom-mounted GBS of finite beam at (a)&(b) f = 0.875Hz and (c)&(d) f = 1.25Hz.

Consider first a comparison of the upwave fields between subplots 5.11(a), 5.12(a) and 5.12(c). The only discernable difference is that subplots 5.12(a) and 5.12(c) have a constant antinode immediately adjacent to the body rather than the transverse variation (comprising of two local maxima) present on figure 5.11(a).

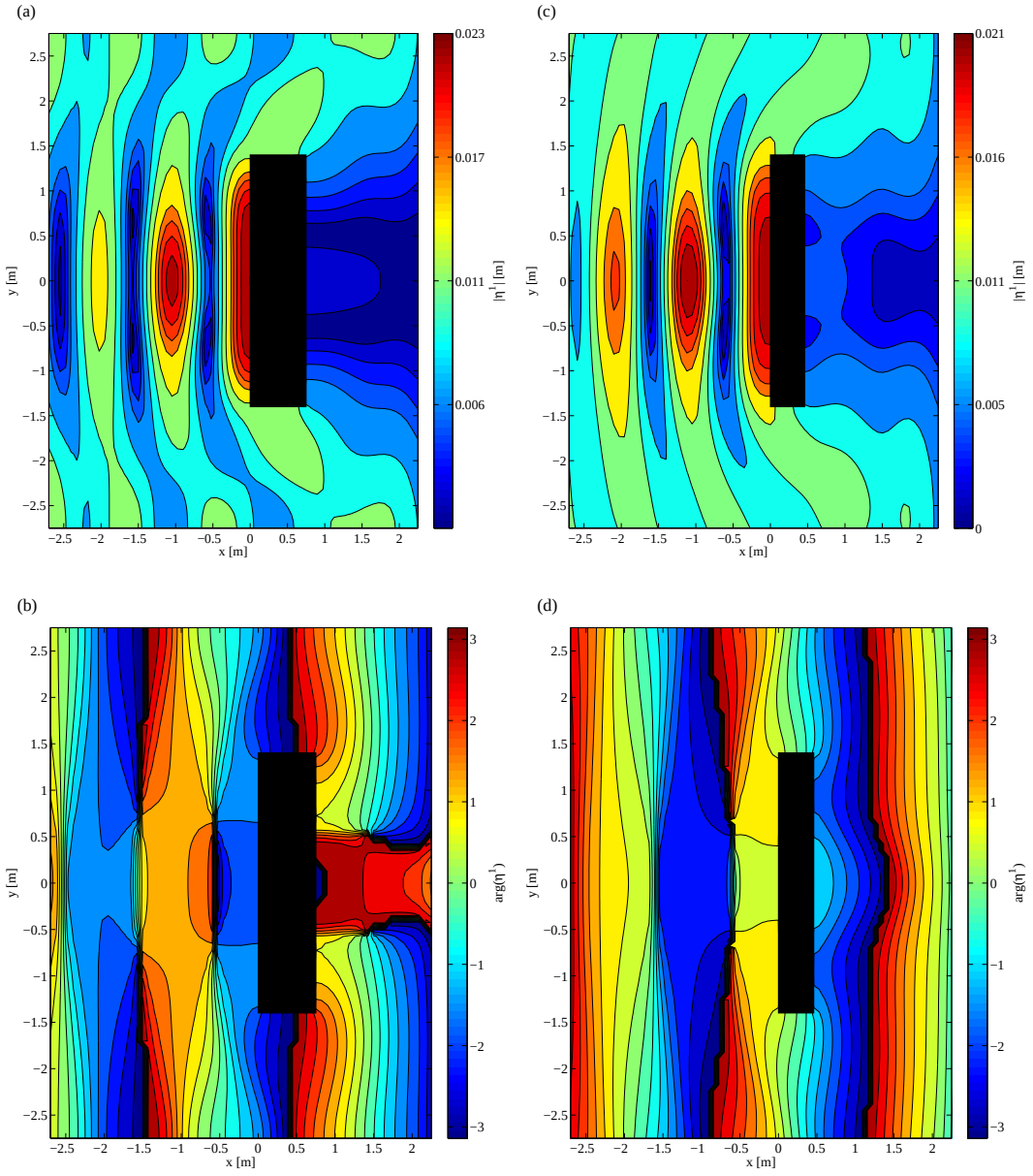


Figure 5.12: Contours of the amplitude, $|\eta^1|$, and phase, $arg(\eta^1)$, of the first harmonic of the water surface elevation around a fixed body of finite draft for f = 0.875Hz; (a)&(b) FLNG and (c)&(d) LNG.

The difference in the downwave fields is more striking. However, because of the small magnitudes involved, this difference is more apparent in the phase variation. Within the downwave region, the difference between subplots 5.11(b) and 5.12(b) arises as a disruption in the rainbow pattern in subplot 5.12(b). This is most

noticeable in the central region and is indicative of the interaction between the wave diffracting into the downwave field and the wave transmitted beneath the FLNG. The difference between subplots 5.11(b) and 5.12(d) is more significant. Indeed, in subplot 5.12(d) the rainbow pattern in x within the downwave $arg(\eta^1)$ is almost constant along the entire width of the domain. This indicates that the wave transmitted beneath the shallow draft of the LNG is dominant, allowing almost no diffraction. In subplot 5.12(c), which considers $|\eta^1|$ surrounding the LNG, the increased wave transmission beneath the body results in a reduction in the magnitude of the first antinode in the upwave field, when compared to the FLNG equivalent in subplot 5.12(a). Evidence of this is provided by the variation in the extent of the colourbars appropriate to subplots 5.12(a) and 5.12(c).

5.4.2 The effect of a second body in close proximity

Having described the wave field surrounding a single fixed body, this section considers how it changes with the introduction of a second fixed body in close proximity. Within the figures given below, each subplot illustrates the spatial variation of the water surface elevation, η, at one instance in time; the value being indicated in the title. Each figure consists of nine subplots, illustrating the variation over one complete incident wave period, T; the interval between subplots being $\frac{T}{9}$. The colours within the subplots indicate the value of η (defined on the adjacent colourbars), while the change in the pattern of these colours between subplots is indicative of the phase variation. The reason for presenting the data in this way is as follows. The NWT used for the simulation of two bodies in close proximity includes an LNG at 0.12m upwave of an FLNG; this setup being hereafter referred to as LNG-FLNG. The use of bi-quartic sliding elements stipulates that there must be five nodes within the 0.12m gap between the two bodies. This leads to a very large node density. Consequently, the size of the numerical domain (having a length of 3.1m) is reduced with respect to that adopted in the previous section. As a result, the waves reflected by the fixed bodies reach the sides of the numeri-

cal domain much sooner, are reflected and have the potential to contaminate the surrounding wave field. Therefore, the long time record describing steady state conditions necessary for a frequency content analysis is not easily attained.

Figure 5.13 concerns the long wave case, corresponding to incident regular waves of frequency f = 0.875Hz. The extent of the colourbar within the figure is determined by the wave excitation within the gap between the bodies. This oscillates between (approximately) $5A_{inc}$ in subplot (c) and $-5A_{inc}$ in subplot (g). Given this large wave excitation within the gap, the surrounding wave fields are predominantly described as cyan and yellow.

In figure 5.13, η just upwave of the LNG and η within the gap are seen to increase from subplot (a) to subplot (b). This corresponds to the arrival of an incident wave crest and the formation of an antinode on the front face of the (upwave) LNG; the largest upwave η defined by a single maximum. The largest η within the gap arises in subplot (c) and also consists of a single maximum. As the wave field evolves, η just upwave of the LNG and η within the gap both decrease through subplots (d) and (e); the smallest upwave η occurring in subplot (f) and the smallest η in the gap occurring in subplot (g). With further advances in the wave cycle, these values increase to approximately zero just upwave of the LNG in subplot (h) and within the gap in subplot (i). Finally, the light green colour upwave of the LNG at $-1.3\text{m} < x < -1\text{m}$ is seen to persist throughout subplots (a) to (i).

The upwave field indicated in figure 5.13 and described above relates to a standing wave field, in which the finite length of the body leads to a transverse (y) variation. This involves a single maximum, making the upwave results of the LNG-FLNG case broadly similar to those involving a single body (described in Section 5.4.1). Based upon the data presented on figure 5.13, the wave field within the gap may be described as following the wave field just upwave of the LNG. Indeed, in some respects it appears to be part of the standing wave field in x. Furthermore, the fluid within the gap may be described as heaving up and down as a single entity, similar to the piston mode introduced in Chapter 4. As

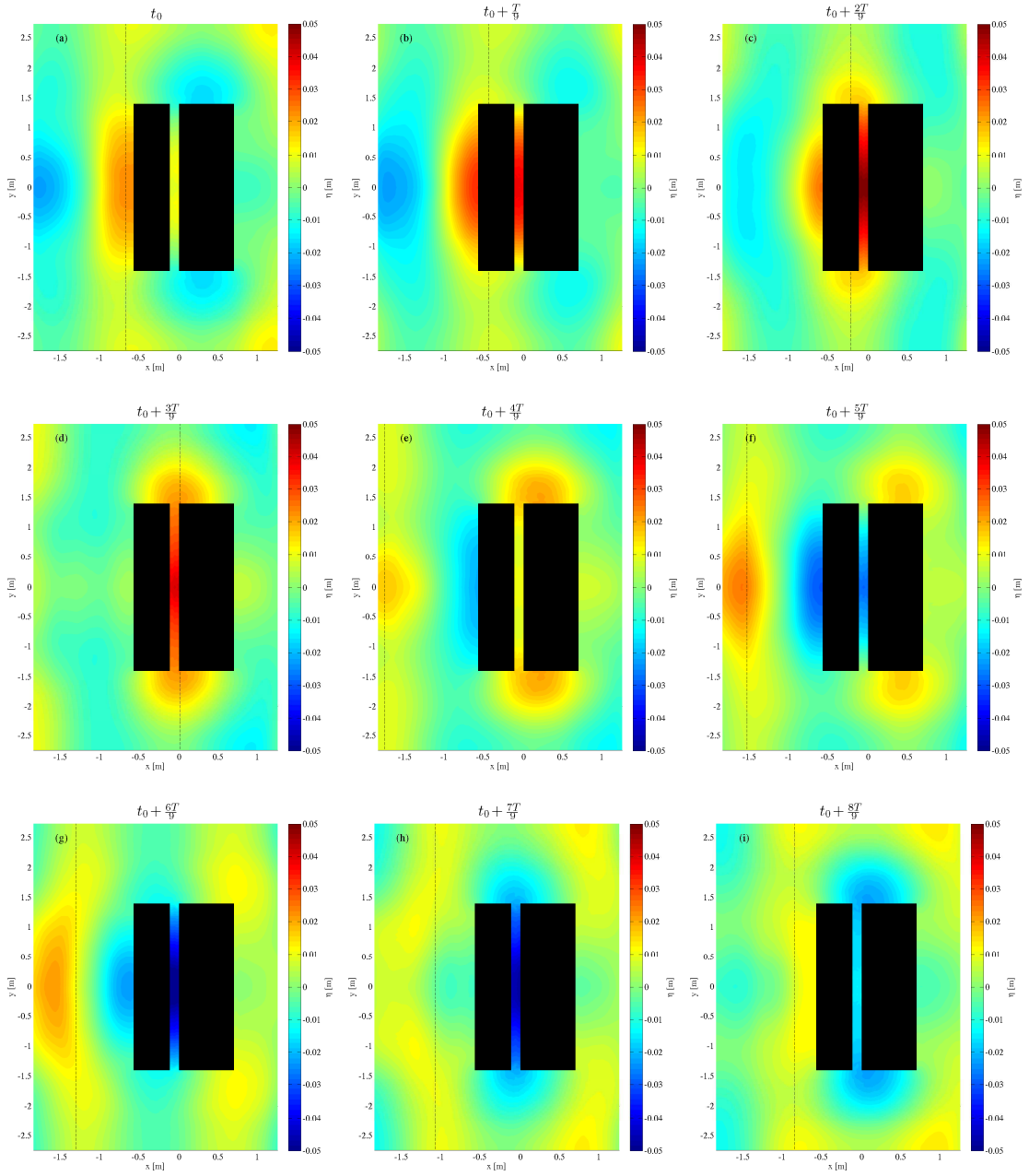


Figure 5.13: Contours of the surface elevation, $\eta(x, y)$, around the LNG-FLNG arrangement at discrete intervals of $\Delta t = T/9$ for $f = 0.875$Hz. Note: the nine subplots cover a complete incident wave period, with t_0 being defined by the arrival of an incident wave crest at $x = -0.68$m (immediately upwave of the LNG) and the position of the incident wave crest is denoted by the dashed line.

a result, f = 0.875Hz is thought to be close to the resonance frequency of the LNG-FLNG case; the latter being the incident wave frequency at which resonant wave excitation occurs within the gap.

Figure 5.14 considers the shorter incident wave frequency of f = 1.25Hz. Comparing figures 5.13 and 5.14, the most obvious difference is the brightness of the colours in figure 5.14. The reason for this is that the upwave field determines the extent of the colourbar in figure 5.14, while in figure 5.13 it was the wave excitation in the gap. The data presented in figure 5.14 relating to the upwave field are similar to the single body results for f = 1.25Hz. In particular, subplot 5.14(a) shows that the transverse variation in the upwave η changes from a sequence of three crests to two troughs with increasing distance from the LNG. As time increases, these crests (or troughs) decrease (or increase) to approximately zero in subplot (d), the process continuing until they become troughs (or crests) in subplot (f). The upwave field is therefore characteristic of a standing wave field arising due to the interaction of an incident and a reflected wave travelling in opposite (x) directions. More importantly, figure 5.14 shows that the wave field within the gap consists of two isolated wave crests (indicated in yellow) visible at either end of the gap in subplot (a). As the interaction evolves, subplots (a) to (i), these crests are seen to grow in amplitude as they travel towards each other in the y-direction. This corresponds to the development of a standing wave field in the transverse (y) direction along the length of the gap; the pattern developing as a result of diffraction from either end of the gap. It can therefore be concluded that although the wave fields in the upwave region and within the gap are both standing wave fields, they are quite distinct, not least because the waves associated with them are propagating in mutually perpendicular directions.

5.4.3 The effect of gap width

The wave excitation within the gap between two fixed bodies in close proximity clearly requires further investigation. However, given the computational effort

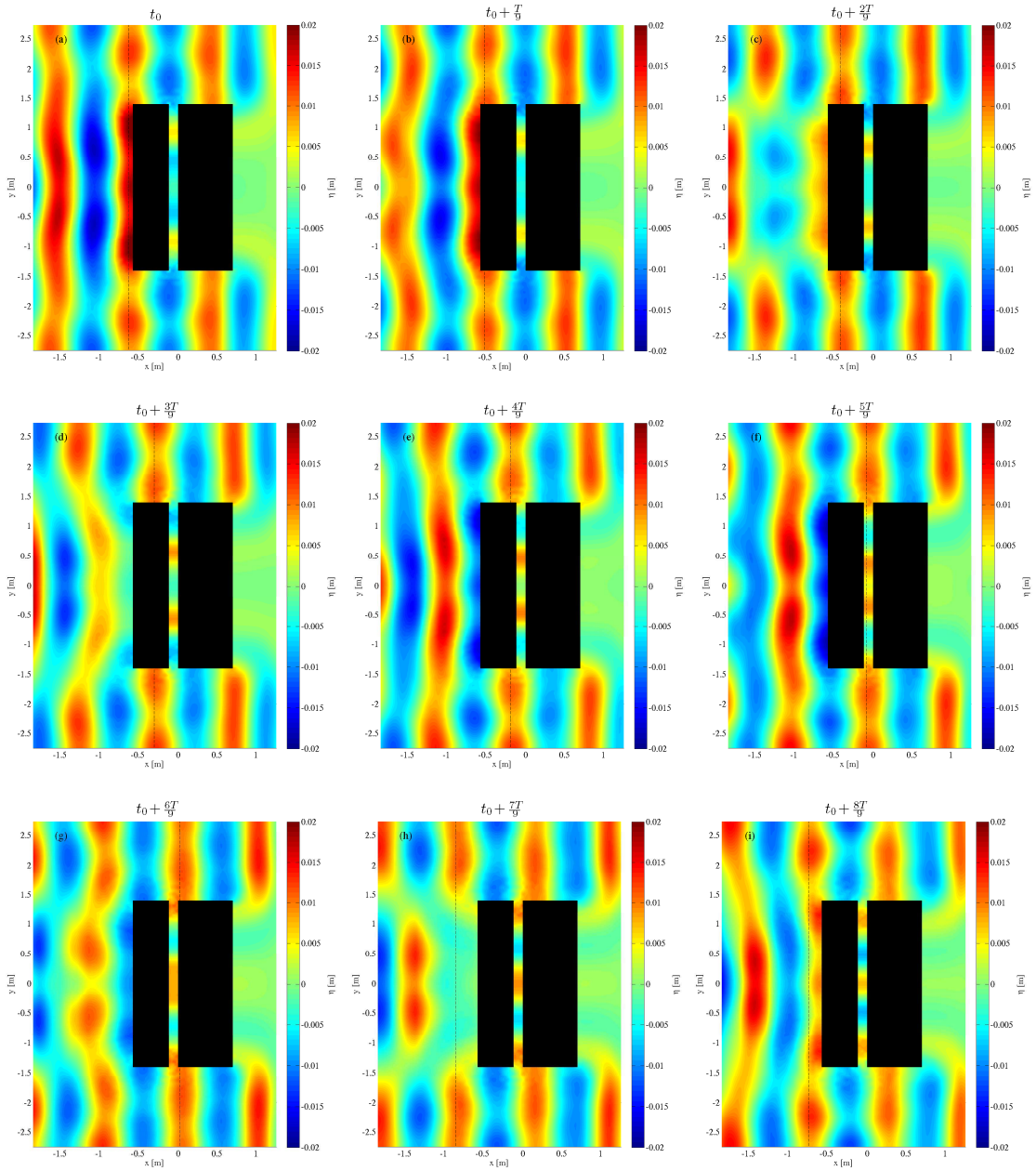


Figure 5.14: Contours of the surface elevation, $\eta(x, y)$, around the LNG-FLNG arrangement at discrete intervals of $\Delta t = T/9$ for $f = 1.25$Hz. Note: the nine subplots cover a complete incident wave period, with t_0 being defined by the arrival of an incident wave crest at $x = -0.64$m (immediately upwave of the LNG) and the position of the incident wave crest is denoted by the dashed line.

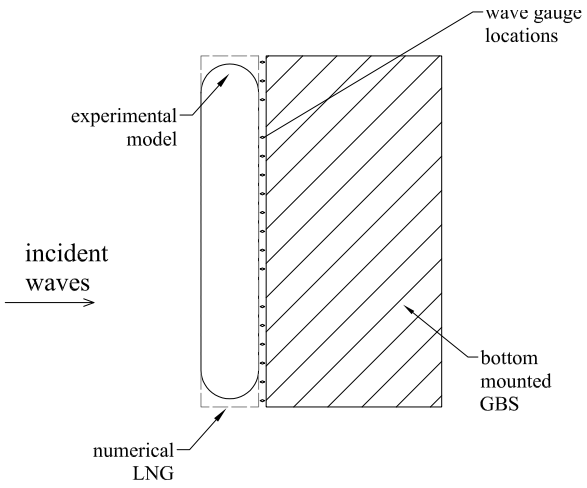


Figure 5.15: Plan view of the experimental setup for a fixed LNG in close proximity to a GBS showing the position of wave gauges along the length of the gap and the comparison of the experimental model and numerical LNG; —— experimental model, – – numerical LNG.

associated with the numerical calculations, this is best achieved within an experimental study. The laboratory observations described within this section were undertaken within the 3D wave basin introduced in Section 5.3.2. All of the data relates to a fixed LNG in close proximity to a bottom-mounted GBS. A model scale of 1:100 was again adopted: the fixed LNG tanker represented by a rectangular box with circular ends (to minimise flow separation), having a draft of 0.135m and a beam of 0.46m. The length of the GBS is 2.8m and a total of three gap widths were considered within the experimental study: 0.08m, 0.06m and 0.04m.

Figure 5.15 provides a plan view of the fixed LNG in close proximity to the GBS. For comparison, the grey dashed line provides the outline of the LNG used in the numerical simulations. The figure also illustrates the position of the 15 wave gauges, having a spacing of 150mm, used to record the transverse variation along the length of the gap. The results gathered from these gauges are the equivalent of a single x-section arising from the numerical simulations presented previously. With only a single experimental run necessary to capture all the data required to define the transverse variation, eight incident wave frequencies were undertaken

lying in the range 0.625Hz $\leq f \leq$ 1.44Hz. Across this range, the incident wave amplitude was held constant at A_{inc} = 0.01m. Having recorded data at 128Hz for a sample length of 64 seconds, an established (or equilibrium) section of each record was identified and a full frequency content analysis undertaken as described in Section 5.2.5.

The transverse (y) variation of the amplitude of the first harmonic of the water surface elevation, $|\eta^1|$, along the length of the gap is presented in figure 5.16. Each subplot concerns a different incident wave frequency, but superimposes the data relating to the three gap widths. Comparing subplots (a) to (d) on figure 5.16, it is clear that the transverse variation is strongly dependent on the incident wave frequency; one maximum occurring within the gap in subplot (a) and five in subplot (d). Furthermore, figure 5.16 shows that the maximum, or resonant, amplification of $|\eta^1|$ over the cases considered is $3.5A_{inc}$ for a gap width of 0.08m, occurring for f = 0.813Hz in subplot (a). In contrast, the value is $4.5A_{inc}$ for the gap widths of 0.06m and 0.04m, both occurring at f = 1.00Hz in subplot (b). Based on these data, it may be concluded that the gap width influences the resonance frequency; an increase in the gap width leading to a decrease in the resonance frequency. Finally, the complete data set suggests that with incident frequencies beyond the resonance frequency, the influence of the gap width reduces and the transverse variation for all gap widths becomes similar. Evidence of this is presented on figure 5.16(d).

Further insights into the nature of the wave excitation within the gap are provided by considering the phase variation of the experimental data. Figure 5.17 illustrates the transverse variation of $arg(\eta^1)$ for a gap width of 0.08m. In this example, data relating to three frequencies (f = 0.813Hz, f = 1.125Hz and f = 1.31Hz) are provided; the resonance frequency having been identified as f = 0.813Hz. Within the figure, the near-constant phase corresponding to the f = 0.813Hz case clearly illustrates that the fluid within the gap responds as a single entity; strong phase coupling existing over the full length of the gap. In contrast, the phase variation in the remaining two cases, f = 1.125Hz and f = 1.31Hz,

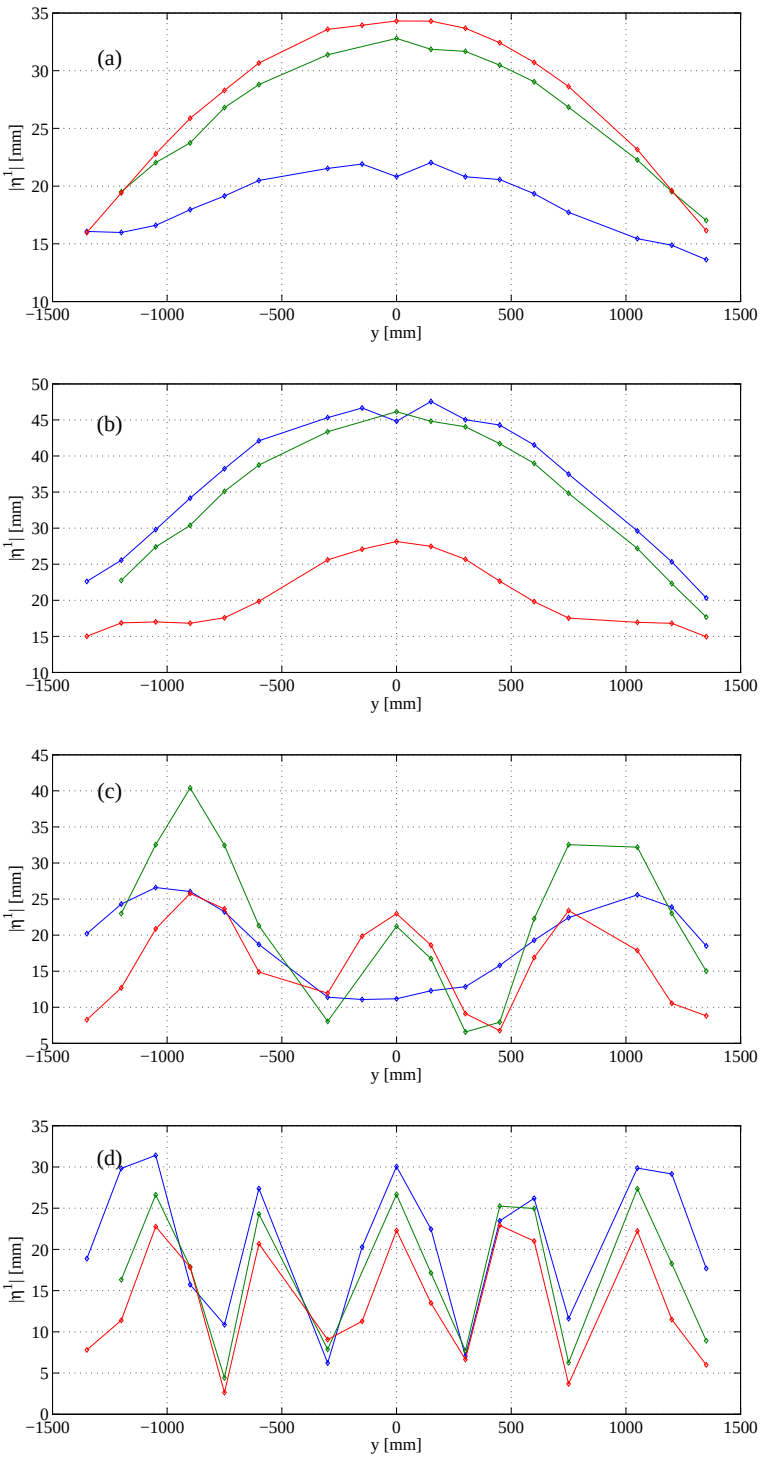


Figure 5.16: Transverse (y) variation of the amplitude of the first harmonic water surface elevation, $|\eta^1|$, arising in the gap between the fixed LNG and the GBS. Comparisons for (a) f = 0.813Hz, (b) f = 1.00Hz, (c) f = 1.125Hz and (d) f = 1.31Hz; and gap widths of — 0.04m, — 0.06m, — 0.08m.

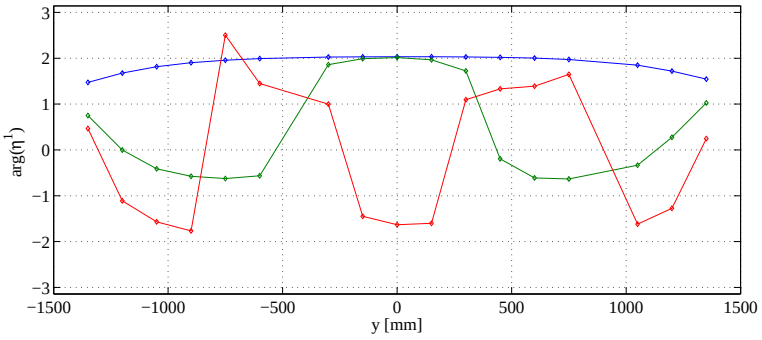


Figure 5.17: Transverse (y) variation of the phase of the first harmonic surface elevation, $arg(\eta^1)$, for a gap width of 0.08m; —— f = 0.813Hz, —— f = 1.125Hz, —— f = 1.31Hz.

is again made up of predominantly flat sections, but with jumps of approximately π between them. This is indicative of a standing wave field in y; the succession of nodes and antinodes arising due to the interaction of waves propagating down the gap due to diffraction at either end.

5.5 Conclusions

The present chapter has described the 3D wave field arising due to the interaction of waves with fixed bodies; the data obtained from both numerical simulations and an experimental study. In respect of the numerical work, this represents the first application of the 3D numerical model to the interaction of waves with fixed bodies. Accordingly, example calculations of a semi-infinite breakwater have been presented to validate the numerical predictions. Although the breakwater incorporated within the numerical model cannot be infinitesimally thin, the fact that the 3D model can simulate a breakwater whose width is made up of a single sliding element attests to the accuracy of the model.

In describing the wave field in the region upwave of a fixed body, the finite length of the body has been shown to lead to fluctuations in both the number and the amplitude of the nodes and antinodes in the standing wave field. The nature of these fluctuations is frequency-dependent or, more specifically, dependent on

the ratio of the body length to the incident wave length. The beam of the body was shown to have little effect on these fluctuations, but the draft of the body influences the degree of wave transmission with implications in both the upwave and the downwave regions.

The introduction of a second fixed body in close proximity leads to a wave field within the gap; the extent of any wave excitation being dependent upon both the incident wave frequency and the gap width. Furthermore, the phase variation of the wave field within the gap suggests that at the resonance frequency, the fluid along the length of the gap responds as a single unit. However, for incident wave frequencies above the resonance frequency, the effects of diffraction into the gap tend to dominate. As a result, while the upwave region is characterised by a standing wave field in x, the wave field within the gap is characterised by a standing wave field in y. This suggests that a 2D description can only model the effects up to the resonance frequency. Beyond this point, the wave field within the gap exhibits transverse variation and must be modelled as fully three dimensional.

6

An experimental study of the effect of vessel motion on the surface elevation in the gap between two bodies

6.1 Introduction

The problem considered within this chapter concerns the offloading of Liquid Natural Gas (LNG) at an offshore terminal; the latter being modelled as a bottom-mounted Gravity Based Structure (GBS). When the LNG transport vessel is moored side-by-side to the GBS, the two bodies are in very close proximity resulting in the formation of a gap that is long and relatively narrow. In practice, the dimensions of this gap are governed by the vessel length (typically > 200m) and available fenders (perhaps 4-8m). The hydrodynamics within this narrow gap, having been discussed previously in Chapters 4 and 5, are also the focus of the present chapter because an understanding of the fundamentals can lead to increased safety during offloading operations.

The interaction of two floating vessels has been investigated by several researchers, with early work (Kodan 1984) considering gap widths comparable to the beam of the vessels. More recently, numerical and experimental work involving

two floating vessels with a gap width appropriate to LNG offloading operations has been carried out by, amongst others, Molin (2001), Kashiwagi (2007), Ha et al. (2004), Koo & Kim (2005), Hong et al. (2005), Pauw et al. (2007) and Sun et al. (2011).

The emphasis within the studies mentioned above is the vessel motion. In contrast, the aim of the present chapter is to illustrate how the linear and nonlinear wave excitation within the gap varies between two fixed bodies in close proximity and a floating body moored side-by-side to a fixed body. This is achieved by presenting two stages of experimental data alongside each other. Both stages involve the bottom-mounted GBS as a fixed body, whilst the second body differs between the stages. In the first stage, the second body is a fixed box-like approximation of an LNG tanker, hereafter referred to as the *fixed box*. The second stage of the experimental study consists of a 1:100 scale model of the LNG tanker Gallea, hereafter referred to as the *floating ship*. As before, all the data are presented at laboratory scale. Having adopted a length-scale of $l_s = 1:100$, Froude-number scaling and the linear dispersion equation give a corresponding time-scale of $t_s = 1:10$.

The experimental study begins with regular incident waves since these allow a simple harmonic decomposition. It then considers data relating to focused wave events. These involve the superposition of many frequency components, the phasing of the components being such that there is a single significant wave event in an otherwise calm sea state. Finally, random sea states are included as they represent the most realistic sea states. In all the incident waves cases considered, it is important to note that the sea states are unidirectional.

The chapter continues with details of the experimental setup and the incident wave cases in Section 6.2. The data relating to the regular wave cases are presented in Section 6.3. These are followed by the focused wave results in Section 6.4 and the random wave results in Section 6.5. The chapter ends in Section 6.6 with some concluding remarks, highlighting the practical implications of the laboratory study.

The results presented herein show that the resonant amplification in the gap can reach six times the incident wave amplitude in both the fixed box and the floating ship stages. However, the incident wave frequency at which this resonant amplification occurs varies significantly between the stages. Furthermore, it is shown that some second-harmonic effects that are evident in both the fixed box and the floating ship cases seem to be enhanced by the body motion. Most importantly, it is shown that these differences persist irrespective of the different types of incident waves.

6.2 Experimental setup

The experimental study was again undertaken in the Hydrodynamics Laboratory in the Civil and Environmental Engineering Department at Imperial College London. The study employed a 3D wave basin having a plan area of 12m x 20m and, for the purpose of the present series of tests, a constant water depth of d = 0.825m. Further details concerning this test facility have been given previously in Chapter 5.

Figure 6.1(a) shows the position of the experimental model in the wave basin for the beam-sea cases; the small insert showing the equivalent arrangement for the head-sea cases. Details of the adopted coordinate axes (x, y) in each of the orientations are also provided; the x-direction always being aligned with the direction of propagation of the incident waves. Figure 6.1(b) provides a plan view comparison of the fixed box and the floating ship, showing that the fixed box is a good approximation of the floating ship; the hydrodynamic properties of the latter being given (at model scale) in Table 6.1.

The fixed box is anchored 6cm from the front face of the GBS (or 6m at full scale) while the floating ship is moored side-by-side; the static fender width again being 6cm. Figure 6.1(c) provides details of the mooring arrangement, including the positions of the mooring lines and fenders. In adopting this arrangement, the scaled tests sought to model a realistic design (Noble Denton 2007) in which the

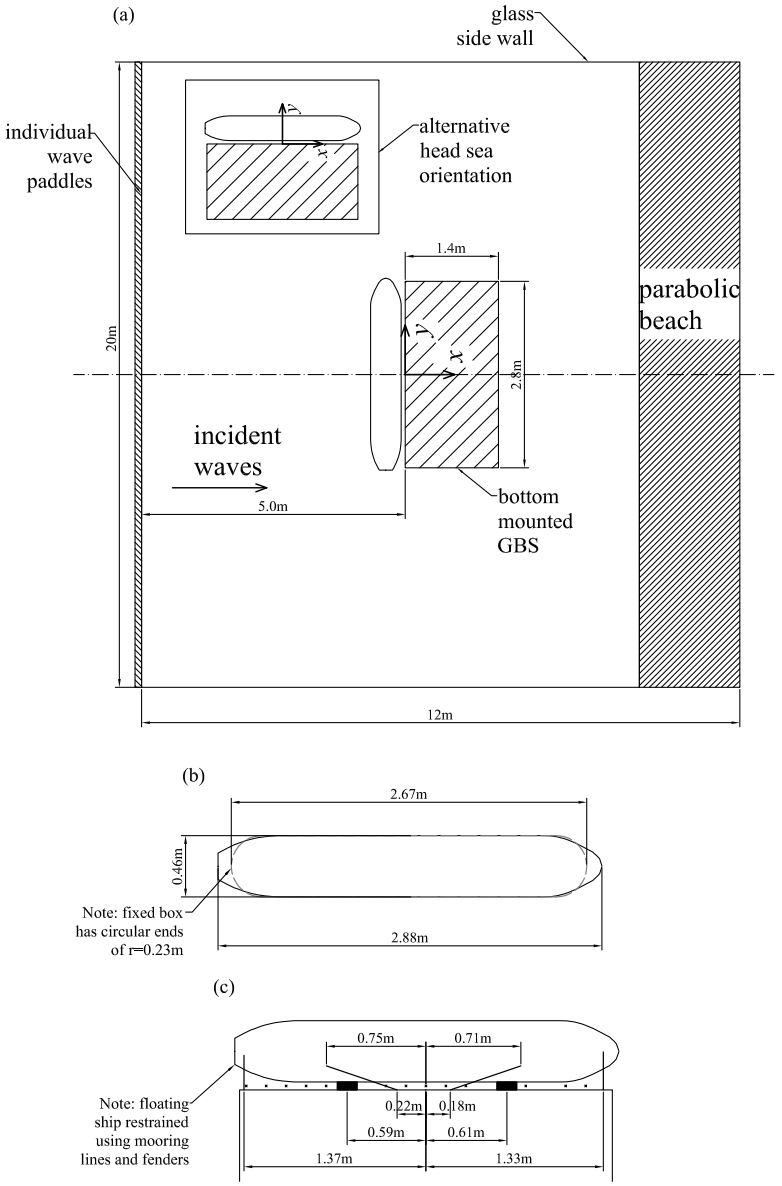


Figure 6.1: (a) Plan view of the experimental setup for the floating ship in the 3D wave basin for the beam-sea cases (not to scale); the insert shows the alternative arrangement for the head-sea cases (b) Plan view showing a comparison between the fixed box and the floating ship, —— floating ship – – fixed box. (c) Plan view of the mooring arrangement of the floating ship to the GBS showing positions of ■ fenders, —— mooring lines and ° wave gauges

beam	0.46m
draft	0.114m
length between perpendiculars	2.21m
natural roll frequency	0.91Hz
natural heave frequency	1.25Hz

Table 6.1: Properties of the experimental model of the LNG tanker Gallea, the floating ship.

spring lines are arranged in pairs and have an effective stiffness of 0.051N/mm and each breast line represents a group of six lines with an effective stiffness of 0.153N/mm. The mooring lines were modelled as tension springs attached to inextensible wire, which was anchored to the GBS and the LNG. The distances between the anchorage points of the mooring lines and the amidships are depicted in figure 6.1(b). In addition, the model fenders were designed to represent Yokohama fenders with a bilinear stiffness; details of how this was achieved at model scale being provided in DHI (2009). Essentially, the fenders were modelled using a cantilevered strip of thin metal. This cantilever was designed to have a stiffness of 0.17N/mm for deflections from 0mm to 13mm, beyond which the stiffness was 0.50N/mm. Figure 6.1(c) also shows that fifteen wave gauges were located along the length of the gap between the two bodies; the centre to centre spacing of the gauges being 15cm at model scale or 15m at full scale. This arrangement of gauges was chosen to enable the description of the spatial variation of the water surface elevation along the gap.

Resistance wave gauges were used to record the time-history of the surface elevation, $\eta(t)$, at each wave gauge location shown in figure 6.1(c). Beyond these locations one wave gauge, referred to as the reference gauge, was positioned away from the influence of the experimental setup in order to monitor the incident waves. For the fixed box experiments, each wave gauge consisted of a pair of parallel free-standing stainless steel rods; the rods being 1.5mm in diameter and

spaced 12mm apart. Previous work has shown that these gauges allow the surface elevation to be measured with an accuracy of ±0.5mm, causing no significant disturbance of the wave field. Unfortunately, in the floating ship experiments, the wave gauges represented an obstacle to the free motion of the ship. To overcome this difficulty, pairs of parallel strips of stainless steel tape were adhered to the front face of the GBS to replicate the rods; the individual strips being 2mm wide and again spaced 12mm apart. Both sets of resistance wave gauges were calibrated by changing their depth of immersion. For the free-standing wave gauges, this is achieved by altering the height at which they are anchored. In contrast, for the stainless steel strip gauges, it was achieved by altering the water depth in the wave basin; the relative change in the water level being accurately measured using the pre-calibrated reference gauge. In this latter case, the absolute accuracy of the strip wave gauges was again estimated to be ±0.5mm.

The incident wave cases include regular waves, focused wave events and random sea states. The regular wave cases totalled 18, with incident wave frequencies ranging from f = 0.625Hz to f = 1.44Hz and a constant incident wave amplitude of A_{inc} = 10mm. The underlying spectra for both the focused wave events and the random sea states were JONSWAP with a peak enhancement factor of γ = 2.5. Within these test cases, the peak frequencies again range from f_p = 0.625Hz to f_p = 1.43Hz. The maximum incident crest elevation of each focused wave event was η_{max} = 10mm and the significant wave height of each random sea state was H_s = 10mm. Across this broad range of incident wave cases, observations were undertaken for the beam-sea and head-sea orientations as described in Table 6.2.

6.3 Regular wave results

In the regular wave cases, a frequency content analysis is again undertaken using a Fast Fourier Transform (FFT) applied to the time-history of the surface elevation, η, recorded at each wave gauge position; the data records corresponding to the fully developed or established wave conditions. Details of this approach, including the

	Fixed box		Floating ship	
	Beam	Head	Beam	Head
Regular	✓	✓	✓	✓
Focused	✓	-	✓	✓
Random	-	-	✓	✓

Table 6.2: Details of observations undertaken in beam and head sea orientations.

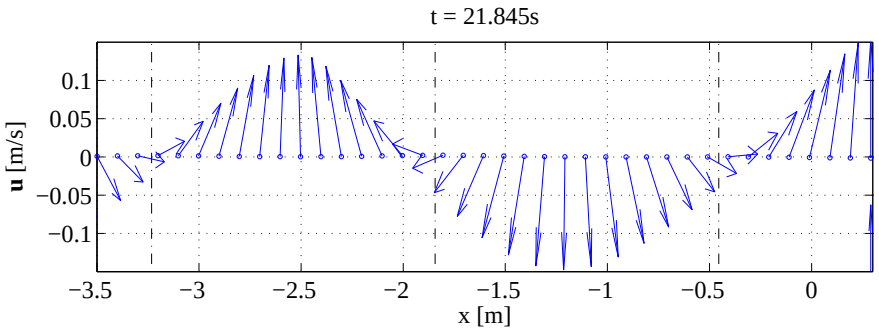


Figure 6.2: Spatial variation of the standing wave fluid velocity vector at the time of largest vertical velocity.

interpretation of the spatial variation of the amplitude, $|\eta|$, and phase, $arg(\eta)$, have been described in Chapter 4. Section 6.3.1 concerns the regular wave results in beam seas, while the head-sea results are presented in Section 6.3.2. As described previously, the aim of the chapter is to illustrate the effect of the body motion on the wave excitation within the gap. With this in mind, each of the figures in these two sections superimpose data relating to the fixed box and the floating ship cases.

Before continuing with this section, consider first the symmetry of a standing wave field generated by numerical test data involving the reflection of incident waves from a vertical wall positioned at x = 0.29m. Figure 6.2 describes the spatial variation of the fluid velocity vector, $\mathbf{u}$, associated with a standing wave field at one instance in time corresponding to the occurrence of the maximum vertical velocity. The position of each dot in figure 6.2 is an indication of its instantaneous surface elevation and since the surface elevation and vertical velocity are 90° out of

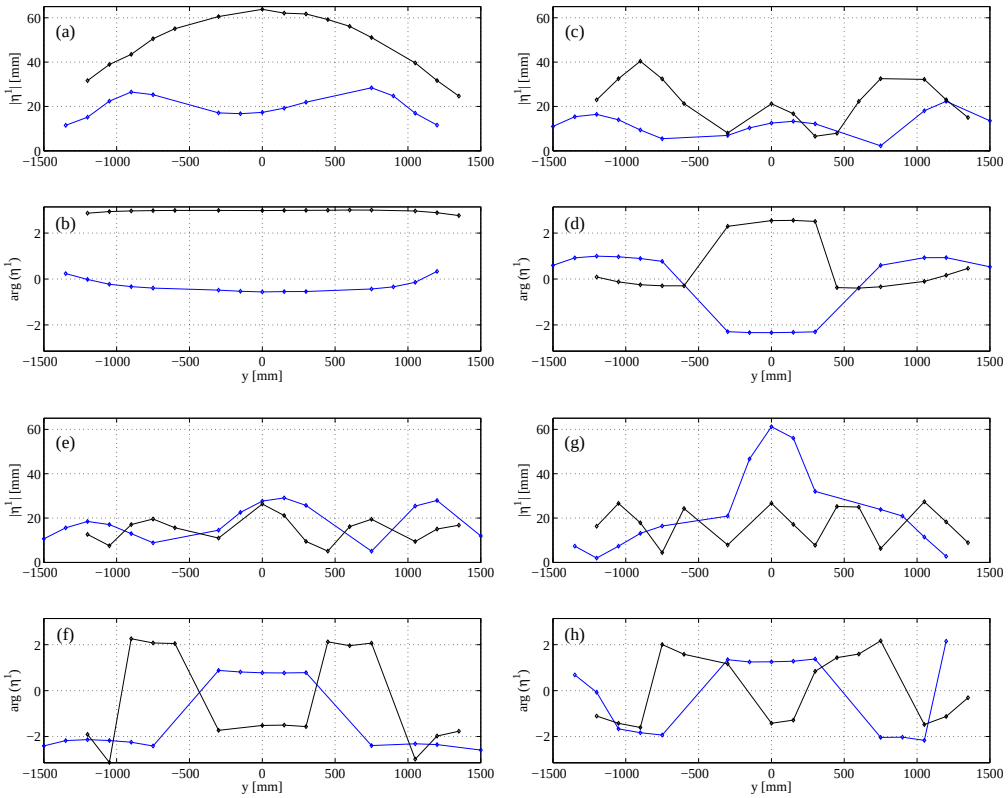


Figure 6.3: Spatial variation of the first harmonic of the surface elevation amplitude, $|\eta^1|$, and phase, $arg(\eta^1)$, for (a)&(b) f = 0.94Hz, (c)&(d) f = 1.125Hz, (e)&(f) f = 1.19Hz, (g)&(h) f = 1.31Hz in beam seas; —— floating ship, —— fixed box.

phase, the position of all the dots at this time is approximately zero. Nevertheless, the locations of the nodes within the standing wave field are indicated by the dash-dotted vertical lines in the figure. The velocity vector at each spatial location in figure 6.2 is depicted using arrows; the latter representing the vector sum of the horizontal and vertical velocity components. In this way, the arrows are purely vertical at the antinodes and purely horizontal at the nodes. From the direction of the arrows in this figure, it is clear that a standing wave is symmetrical about the antinode positions, corresponding to x = −2.61m and -1.16m, and not at the position of the nodes.

6.3.1 Beam-sea cases

Figure 6.3 concerns the spatial variation along the length of the gap of the amplitude and phase of the first harmonic surface elevation for four incident wave frequencies in beam seas. In the case of the fixed box, subplot (a) shows that the amplitude, $|\eta^1|$, is one half of a sine wave, while the phase variation, $arg(\eta^1)$, in subplot (b) is perfectly flat or has no gradient. These results indicate that, at this frequency, the excitation within the gap between the GBS and fixed box is half a standing wave; this spatial variation subsequently being referred to as a first mode. It should also be noted that at this frequency, the maximum amplification within the gap is 6.4 times the incident amplitude, A_{inc}, or $|\eta^1|_{max}$ = 64mm.

With the incident frequency held constant, the amplification associated with the floating ship case in subplot (a) is not as large and the spatial variation depicts what appears to be two half sine waves. This is not, however, a second mode; the floating ship phase in subplot (b) exhibiting no significant variation from that of a first mode. For a second mode to exist, there must be a node at the amidships location, y = 0mm. However, the amidships defines a line of symmetry for the fixed box as well as for the floating ship; differences in the shape of the bow and stern leading to a small loss of symmetry in the latter case. Nevertheless, it has already been shown in figure 6.2 that at positions of symmetry the standing wave field must consist of an antinode, and not a node. Therefore, a second mode cannot exist in either the fixed box or the floating ship cases. As a result, it follows that the floating ship data presented in subplots 6.3(a) and (b) must be interpreted as a transition between modes whose antinodes are located at the amidships; the likely combination being the first and third modes.

A well developed third mode is shown in the fixed box results in subplots (c) and (d). The phase in subplot (d) shows three constant phase sections with jumps of π between them. The length of the constant phase sections is reflected in the distance between the nodes identified in the amplitude, $|\eta^1|$, profiles given in subplot (c). The magnitudes of the three antinodes are not equal and this is

thought to be an effect of the circular ends of the fixed box geometry shown in figure 6.1(b). In the floating ship case, the spatial variation of the amplitude and phase, depicted in figures 6.3(c) and (d), is similar (in shape) to those of the fixed box, but the magnitudes are smaller.

In the floating ship case, the fully developed third mode is shown in subplots (e) and (f). In this case, $|\eta^1|$ in subplot (e) is slightly asymmetric because of the ship's fore-aft asymmetry. In contrast, the phase variation for the fixed box case in subplot (f) shows phase jumps on either end that are larger than π. This indicates a possible transition to a fifth mode. Further evidence of the fifth mode is seen in the fixed box data describing the amplitude and phase in subplots (g) and (h) respectively. In this case, the phase data, $arg(\eta^1)$, relating to the floating ship case in subplot (g) represent the beginning of a fifth mode, but its amplitude in subplot (h) is dominated by the amplification in the amidships section which reaches 6.1 times the incident amplitude, A_{inc}, or $|\eta^1|_{max} = 61$mm.

Having looked in detail at the spatial variation of the first harmonic surface elevation for a selection of incident wave frequencies, now consider how both the linear and nonlinear harmonics of the surface elevation vary over the whole range of incident wave frequencies. In order to achieve this, the spatial variation (depicted for the first harmonic in figure 6.3) must be summarised by a single value. This (representative) value was chosen as the maximum magnitude over the whole length of the gap, irrespective of where it occurs. If f_{inc} defines the incident frequency for a particular test case, the nonlinear harmonics to be considered correspond to the zeroth harmonic or mean shift occurring at $f = 0$Hz, the second harmonic occurring at $f = 2f_{inc}$ and the third harmonic occurring at $f = 3f_{inc}$. Accordingly, figure 6.4 concerns the variation with the incident wave frequency of the maximum amplitude of the zeroth harmonic of the surface elevation $|\eta^0|$ in subplot (a), the first harmonic $|\eta^1|$ in subplot (b), the second harmonic $|\eta^2|$ in subplot (c) and the third harmonic $|\eta^3|$ in subplot (d). In considering these results, it should be noted that the wave steepness, $A_{inc}k$, where k is the incident wave number, increases from 0.02 to 0.08 across the range of the wave cases considered.

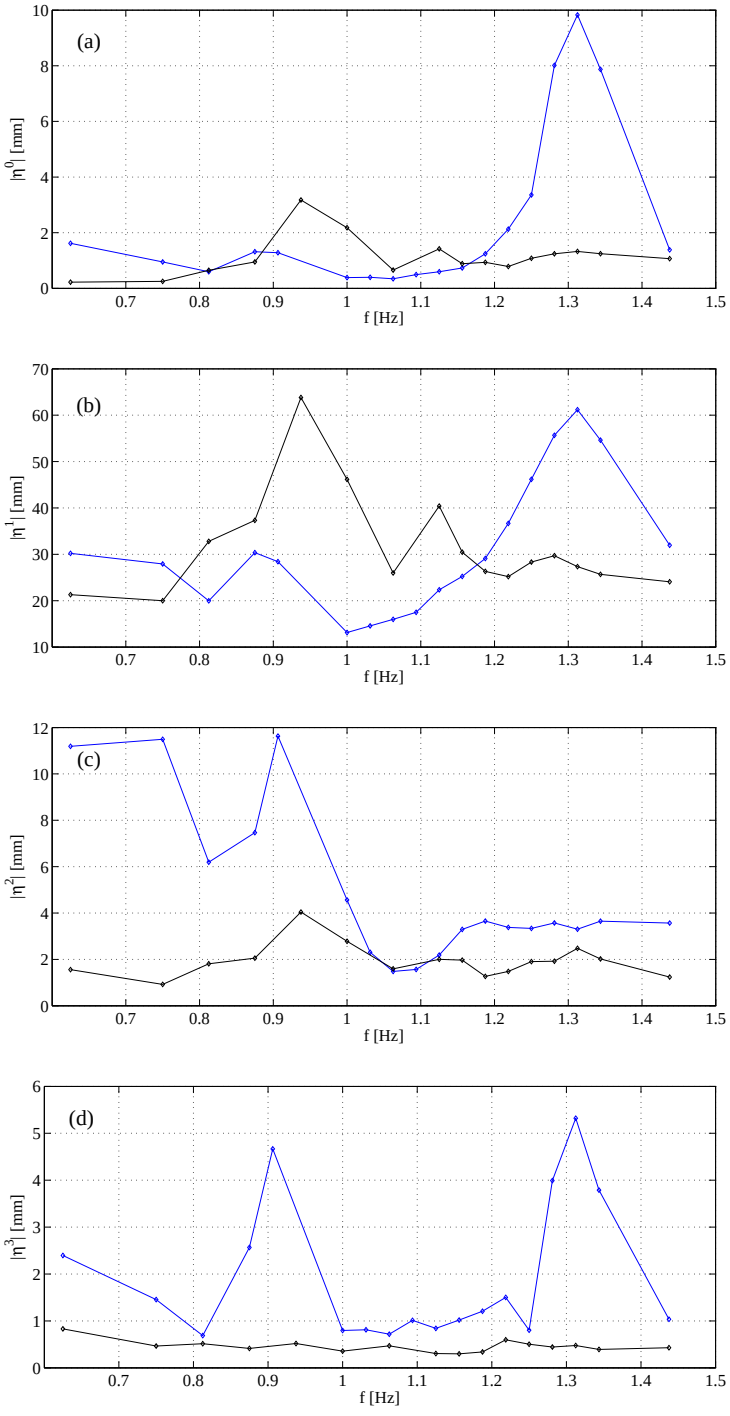


Figure 6.4: Variation with incident wave frequency (f) of the maximum amplitude of the (a) zeroth, (b) first, (c) second and (d) third harmonic of the surface elevation at any point within the gap in beam seas; —— floating ship, —— fixed box.

Consider first $|\eta^1|$ in subplot (b). These data confirm that the largest, or resonant, amplifications within the gap are of a similar magnitude for the fixed box and the floating ship cases, but indicate that they occur at very different frequencies. The fixed box variation shows three peaks at f = 0.94Hz, 1.125Hz and 1.28Hz; corresponding to first, third and fifth modes respectively as seen in figure 6.3. It is therefore clear that with increasing frequency, the magnitude of the amplification in the gap for the fixed box case decreases as the number of modes along the length of the gap increases. In contrast, in the floating ship case the largest amplification in the gap occurs near the end of the frequency range at f = 1.31Hz. Furthermore, there is a notable dip in the amplification at f = 1.0Hz – 1.1Hz, with $|\eta^1|$ approaching A_{inc}.

The nonlinear results presented in subplots (a), (c) and (d) show that the maximum amplitude of the nonlinear harmonics are consistently larger in the floating ship case when compared to those observed in the fixed box case. In particular, the floating ship data describing $|\eta^0|$ and $|\eta^2|$ on figures 6.4(a) and (c) respectively are approximately equal to the incident first harmonic amplitude, A_{inc} = 10mm. Further differences between the fixed box and the floating ship data include the presence of two distinct peaks in the $|\eta^2|$ and $|\eta^3|$ data relating to the floating ship case; the large nonlinear surface elevation amplifications at f = 0.91Hz possibly being due to the large LNG motions at frequencies close to its natural roll frequency. Finally, in the fixed box case, the largest $|\eta^0|$ and $|\eta^2|$ values occur at the same frequency as the largest $|\eta^1|$. Whilst this is also true for $|\eta^0|$ and $|\eta^3|$ in the floating ship case, the largest $|\eta^2|$ (beyond f = 0.91Hz) occurs at the other end of the frequency range at f = 0.625Hz. Here, the incident wave steepness is very small, but the second harmonic frequency at f = 0.625Hz is close to f = 1.31Hz at which the floating ship $|\eta^1|$ is largest.

To shed more light on these maximum values, figure 6.5 reverts back to plots of the spatial variation along the length of the gap. However, these plots involve data corresponding to a mixture of incident frequencies. For the fixed box results in subplots (a), (b), (c) and (d) all of the data relate to f = 0.94Hz. In contrast,

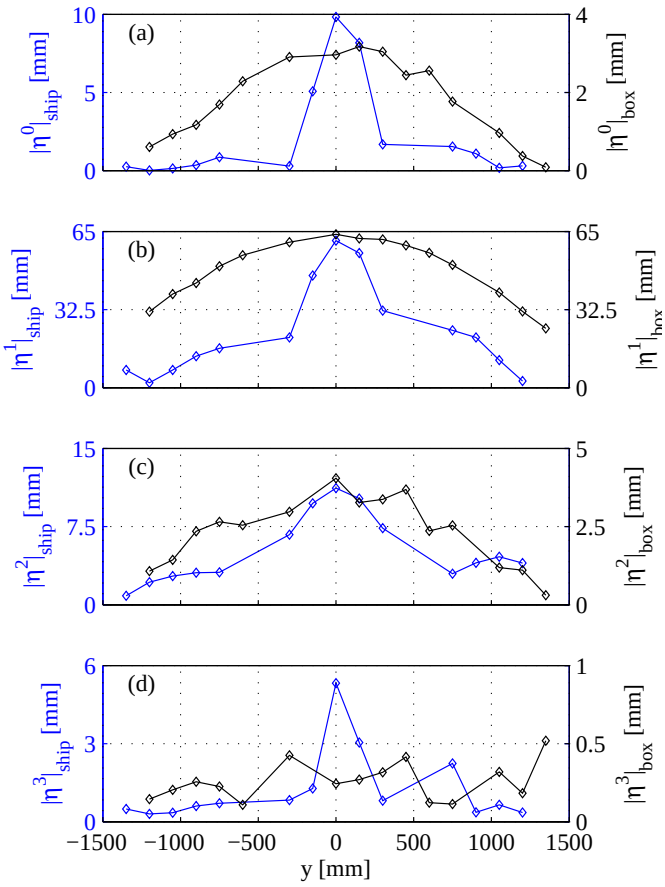


Figure 6.5: Spatial variation of the amplitude of the zeroth to third harmonic surface elevation in beam seas; (a) $|\eta^0(y)|$, (b) $|\eta^1(y)|$, (c) $|\eta^2(y)|$ and (d) $|\eta^3(y)|$ —— floating ship, —— fixed box (see text for details of incident wave frequencies).

the floating ship data in subplots (a), (b) and (d) relate to f = 1.31Hz, while subplot (c) relates to f = 0.625Hz.

With the purpose of figure 6.5 being to compare the spatial variation of the maximum amplifications of the harmonics of the surface elevation, the subplots within this figure have varying vertical scales. Specifically, the left-hand side scales correspond to the magnitudes of the excitation in the vicinity of the floating ship, while the right-hand side scales define the corresponding data appropriate to the fixed box. The relative magnitudes of the floating ship and fixed box results are

then reflected in the extent of their appropriate vertical scales; the former being substantially larger for the nonlinear harmonics.

The fixed box $|\eta^0|$, $|\eta^1|$ and $|\eta^2|$ in figures 6.5(a), (b) and (c) respectively are clearly of the same first mode shape, occurring at the same incident frequency. One possible interpretation of this is that the nonlinear harmonics serve to modify the large first harmonic at this frequency in order to better satisfy the nonlinear free surface boundary conditions. In effect, the nonlinear harmonics operate in a similar fashion to the bound waves in a nonlinear wave theory.

The $|\eta^0|$ and $|\eta^3|$ data relating to the floating ship case in figures 6.5(a) and (d) respectively also occur at the same frequency (f = 1.31Hz) as the $|\eta^1|$ data in figure 6.5(b) and are of a similar shape. Furthermore, despite the fact that $|\eta^2|$ in figure 6.5(c) is at f = 0.625Hz, it too is of a similar mode shape; specifically, the large amplification being concentrated at the amidships section. It therefore appears that the argument outlined in respect of the fixed box data does not hold for the floating ship data. For example, $|\eta^1|$ at f = 0.625Hz is less than half the maximum amplification (seen in figure 6.4(b)) and is of a first mode shape spanning over the whole length of the gap. Instead, given that a frequency of 0.625Hz is very close to half of 1.31Hz, it is thought that the maximum amplification of the surface elevation harmonics within the gap behaves in accordance with an Response Amplitude Operator (RAO). In this way, since the largest amplification of $|\eta^1|$ occurs at f = 1.31Hz, the largest $|\eta^2|$ would occur at f = 0.655Hz. Not surprisingly, a frequency of f = 0.625Hz is sufficiently close that it manages to capture a large part of this latter amplification. Continuing this argument, it is possible that $|\eta^3|$ at f = 0.47Hz would be larger than that recorded at f = 1.31Hz. However, with f = 0.47Hz the incident wavelength is about half of the length of the wave basin and therefore too long to run in practice.

Taken together, figures 6.4 and 6.5 indicate both the importance and the complexity of the nonlinearity involved. Indeed, the present data confirm that although the incident waves may be linear, the excitation of fluid in the gap may incorporate important nonlinear components.

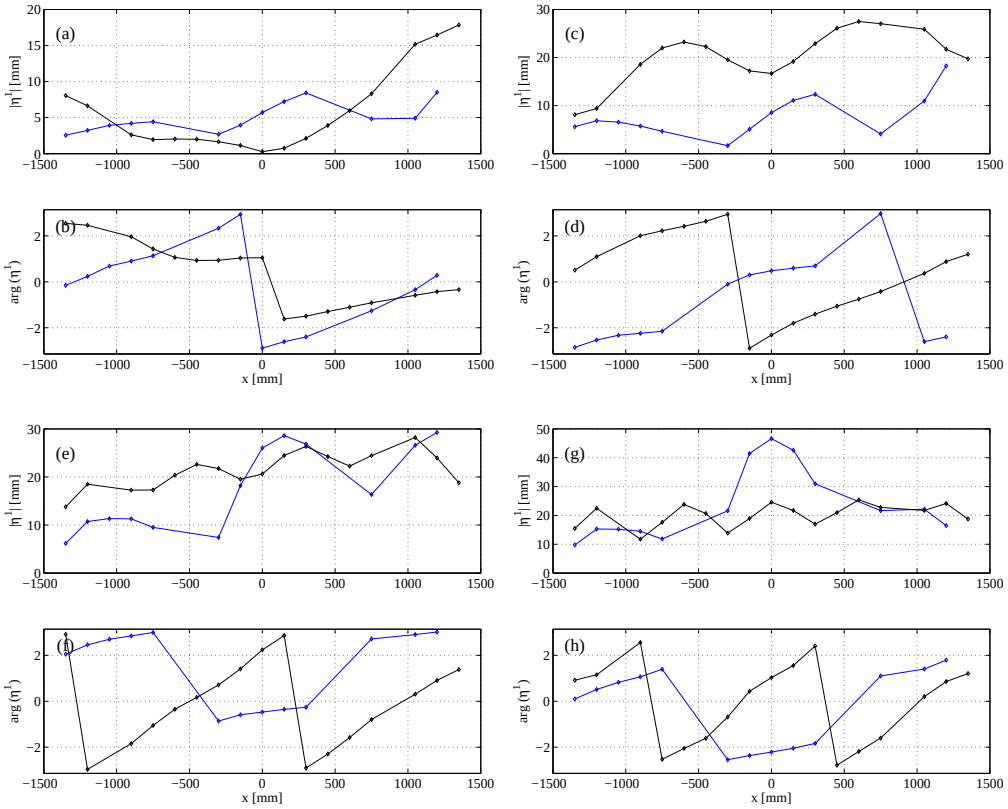


Figure 6.6: Spatial variation of the first harmonic of the surface elevation amplitude, $|\eta^1|$, and phase, $arg(\eta^1)$, for (a)&(b) f = 0.825Hz, (c)&(d) f = 1.06Hz, (e)&(f) f = 1.19Hz, (g)&(h) f = 1.25Hz in head seas; —— floating ship, —— fixed box.

6.3.2 Head-sea cases

Figure 6.6 concerns the head-sea cases; specifically, the spatial variation of the surface elevation over the length of the gap for four incident wave frequencies corresponding to f = 0.825Hz, 1.06Hz, 1.19Hz and 1.25Hz. In each case, separate subplots are provided indicating the spatial variation of the amplitude of the first harmonic of the surface elevation, $|\eta^1|$, and its corresponding phase, $arg(\eta^1)$. Once again, data relating to the fixed box and the floating ship cases are superimposed.

The reader is reminded that the incident waves propagate in the x-direction. Furthermore, the phase variation relating to the floating ship case in subplot (b) describes a wave propagating along the gap. However, the corresponding amplitudes in subplot (a), again relating to the floating ship case, illustrate the interac-

tion of the propagating incident wave and the effect of the gap; the amplitude of the wave being consistently less than the incident wave amplitude of A_{inc} = 10mm. The $|\eta^1|$ of the fixed box case at this frequency (subplot (a)) also shows a significant interaction involving a large amplification for $x > 800$mm and near-zero amplitude for $x < 0$mm. In this case the phase variation (subplot (b)) also shows a marked departure from the expected pattern relating to a propagating wave mode. Indeed, this result (perhaps) suggests that in head seas any wave mode trying to establish itself within the gap must work against the incident propagating wave.

Further evidence of this is provided in the fixed box results presented on figures 6.6(c) and 6.6(d). At this frequency (f = 1.06Hz), the variation in the amplitude of the first harmonic component shows two half sine waves, or crests, whilst the phase variation in figure 6.6(d) indicates a propagating wave. This is referred to as a partial standing wave; the amplitude varying with spatial location, as in a standing wave, but the phase having a clear gradient, as in a propagating wave. A related pattern occurs in the floating ship case, although the phase variation in figure 6.6(d) displays a more noticeable disturbance created by the interaction with the wave modes (propagating and standing) within the gap.

The fixed box results presented on figures 6.6(e) and (f) again relate to a partial standing wave. However, with an increase in the incident frequency, the record now indicates four local maxima or crests. At this frequency the floating ship data describe a similar pattern except the amplitudes in figure 6.6(e) display three local maxima and the phase variation in figure 6.6(f) has a much reduced gradient. In figure 6.6(h) the gradient of the phase variation in the floating ship case is again much reduced. In both cases, this suggests a predominantly standing wave mode. Furthermore, the amplitude of the first harmonic, $|\eta^1|$, in figure 6.6(g) has a dominant amplification over the amidships section. The features in figures 6.6(g) and (h) are very similar to the spatial variation within the gap at a similar frequency in beam seas, details of which are given in figures 6.3(g) and 6.3(h). These results suggest that the nature of the resonant wave excitation within the gap may be less dependent upon the direction of wave propagation than had previously been

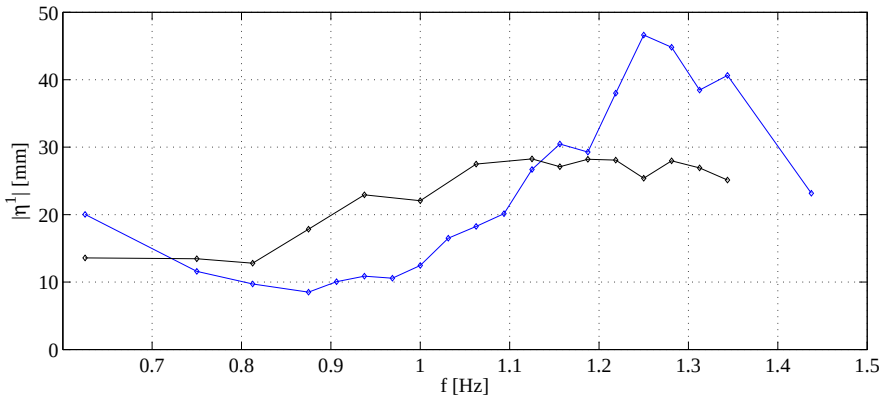


Figure 6.7: Variation with incident wave frequency (f) of the maximum amplitude of the first harmonic of the surface elevation, $|\eta^1|$, at any point within the gap in head seas; —— floating ship, —— fixed box.

expected.

Figure 6.7 concerns the variation with the incident wave frequency, f, of the maximum amplitude of the first harmonic surface elevation at any point along the length of the gap in head seas. These data indicate that in the fixed box case the maximum amplification plateaus beyond 1.0Hz, achieving a magnitude that is relatively small ($|\eta^1|$ = 28mm or $2.8A_{inc}$) in comparison to the fixed box resonant amplification in beam seas ($|\eta^1|$ = 64mm or $6.4A_{inc}$, see figure 6.4(b)). This suggests that in the fixed box case subjected to head seas, the wave modes within the gap struggle to overcome the propagating incident waves.

In contrast, the floating ship data presented in figure 6.7 define a maximum amplification of 4.8 times the incident wave amplitude. Although this is less than the floating ship resonant amplification in beam seas, for which $|\eta^1|_{max} = 6.1A_{inc}$, it occurs at a very similar incident wave frequency in both head seas and beam seas. It therefore appears that in the floating ship case, the orientation of the offloading arrangement with respect to the incident waves has relatively little influence on the resonant wave excitation within the gap.

Finally, figure 6.8 concerns the spatial variation of the largest harmonic amplitudes of the surface elevation in head seas. This is directly comparable to the beam sea data presented in figure 6.5. Within figure 6.8, the fixed box results

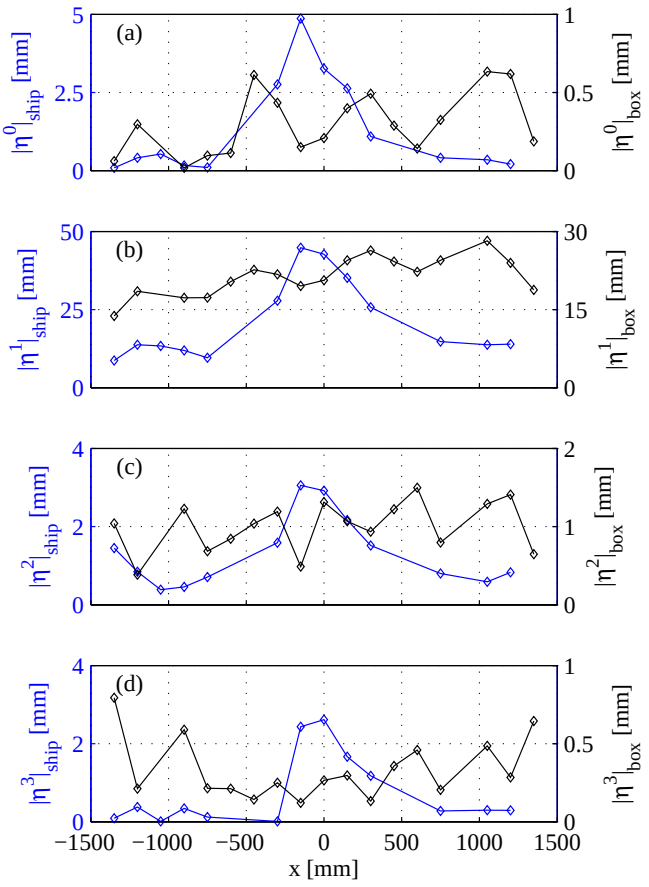


Figure 6.8: Spatial variation of the amplitude of the zeroth to third harmonic surface elevation in head seas; (a) $|\eta^0(x)|$, (b) $|\eta^1(x)|$, (c) $|\eta^2(x)|$ and (d) $|\eta^3(x)|$, —— floating ship, —— fixed box (see text for details of incident wave frequencies).

correspond to f = 1.19Hz for $|\eta^0|$, $|\eta^1|$, $|\eta^2|$ and $|\eta^3|$ in subplots (a), (b), (c) and (d) respectively. The $|\eta^1|$ results in subplot (b) have been seen to represent a partial standing wave with four local maxima or crests; these crests also being present in $|\eta^0|$ in subplot (a).

Figure 6.8 also presents data relating to the floating ship. In this case, $|\eta^0|$, $|\eta^1|$ and $|\eta^3|$ all correspond to f = 1.28Hz in subplots (a), (b) and (d) respectively, while $|\eta^2|$ in subplot (c) arises at f = 0.625Hz. Despite this difference in the incident frequency, all the harmonics depict the same spatial variation; the general

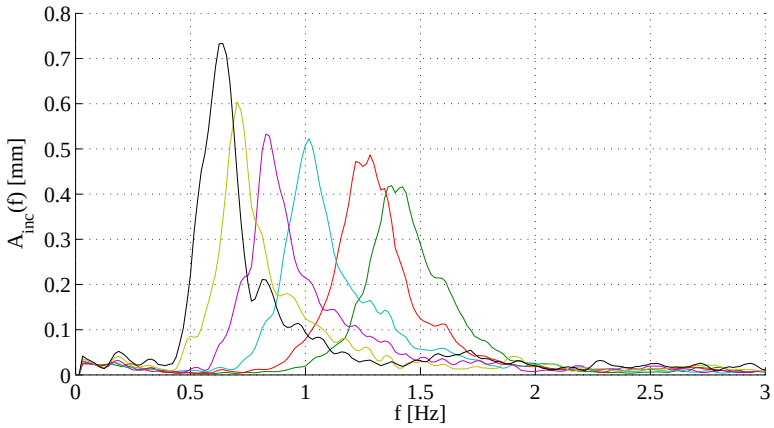


Figure 6.9: Incident amplitude spectra, $A_{inc}(f)$, for focused wave events with varying peak frequencies; — f_p = 1.43Hz, — f_p = 1.25Hz, — f_p = 1.00Hz, — f_p = 0.83Hz, — f_p = 0.714Hz and — f_p = 0.625Hz

form of the data being closely related to that observed in beam seas (figure 6.5). This further confirms that the hydrodynamics within the gap, both linear and nonlinear, are generally unaffected by the orientation of the offloading operation relative to the incident waves.

6.4 Focused wave events

In generating focused wave events, the underlying spectra were defined as JONSWAP with a peak enhancement factor of $\gamma = 2.5$. The phasing of the individual frequency components was pre-determined so as to produce constructive interference (or a large wave crest) at $x = y = 0$mm, and the amplitude of the components adjusted to produce a maximum incident crest elevation of $\eta_{max} = 10$mm. Within this sequence of tests a total of six different frequency spectra were considered, corresponding to a range of spectral peak frequencies lying in the range $0.625\text{Hz} \leq f_p \leq 1.43\text{Hz}$; the amplitude spectra, $A_{inc}(f)$, for each case being presented in figure 6.9.

In accordance with the regular wave study, a time-history of the surface elevation, $\eta(t)$, at each wave gauge location was recorded. For the analysis of focused

waves, a FFT was applied to a 64s interval of the recorded data; the latter defining the chosen repeat period of the generated sea state and therefore sufficient to capture all the frequency components generated by the wave makers. This results in a spectrum describing the amplitude of the frequency components arising at each wave gauge location. Figure 6.10 contrasts the amplitude spectra recorded at each wave gauge location, $A(f)$, with the incident amplitude spectrum, $A_{inc}(f)$, for the case relating to a beam-sea orientation and a spectral peak frequency of $f_p = 0.625$Hz. Given the amount of data included within these plots, the fixed box, figure 6.10(a), and floating ship, figure 6.10(b), results are presented alongside one another to allow for comparisons between the two cases.

With a focused wave event arising due to the constructive interference of many frequency components, the variation in the component wave amplitudes is continuous, as seen in figure 6.10. As a result, it is not possible to isolate key frequencies (such as the first harmonic) and illustrate their spatial variation. Instead, the objective of figure 6.10 is to highlight the occurrence of significant amplifications of the incident spectrum, particularly at frequencies away from the spectral peak. In the fixed box case, figure 6.10(a), there is a notable amplification at $f = 0.94$Hz, while in the floating ship case it occurs at $f = 1.31$Hz. In both cases, these frequencies are identical to those at which resonant amplification occurs in the regular waves cases described in Section 6.3.1. Furthermore, it is also important to note that in figure 6.10(b), there is a reduction of the amplitude spectrum at $f = 1.0$Hz; a similar reduction being observed in the amplitude of the first harmonic of the regular wave $|\eta^1|$ in figure 6.4(b). It therefore appears that despite the significant difference in the incident wave forcing between regular and focused wave events, the surface elevation spectra at the various locations in the gap for a focused wave event with a peak frequency of $f_p = 0.625$Hz exhibit very similar effects to those noted previously in the regular wave cases.

Indeed, the similarity between the regular and focused wave cases is independent of the spectral peak frequency. In order to demonstrate this, figure 6.11 removes the influence of the incident wave spectrum by dividing $A(f)$ at each

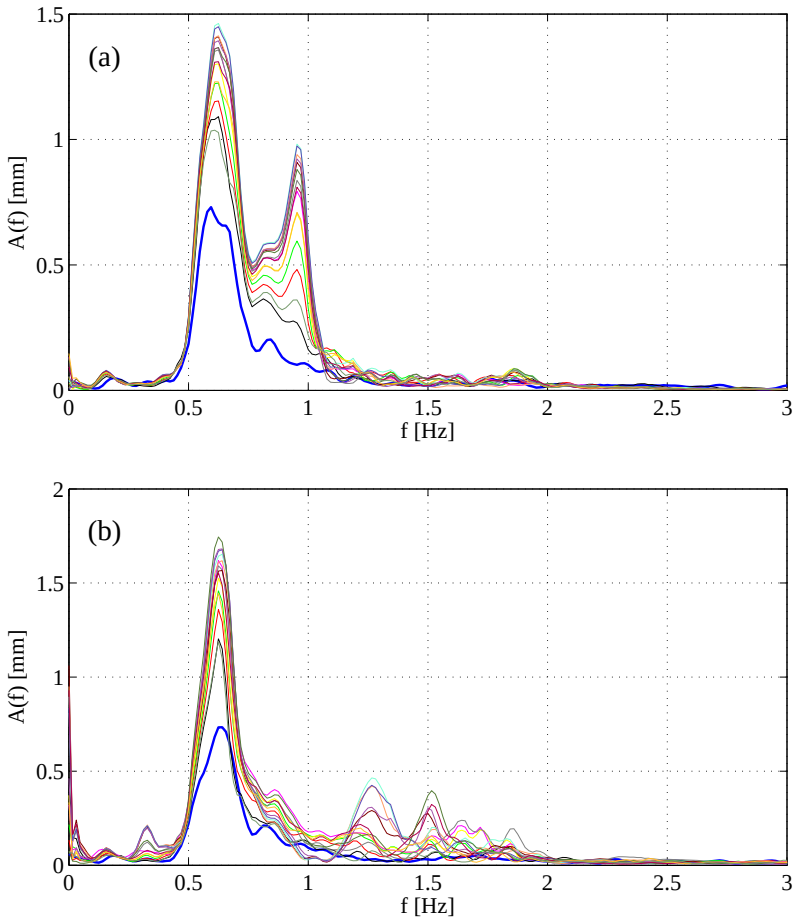


Figure 6.10: Amplitude spectra, $A(f)$, arising at each wave gauge location within the gap and the incident wave spectrum for f_p = 0.625Hz, (a) the fixed box case and (b) the floating ship case in beam seas; ——— incident waves. Note: other colours relate to the various wave gauge locations noted on figure 6.1.

wave gauge location by the corresponding incident amplitude spectrum (shown in figure 6.9) to yield a dimensionless $A(f)/A_{inc}(f)$ ratio. In this way, wave amplifications away from the spectral peak frequency, f_p, are made more apparent, having been divided by a smaller incident amplitude. Figure 6.11 concerns data arising from a single wave gauge located at the amidships, but superimposes data relating to the six peak frequencies. Subplot (a) of figure 6.11 concerns the fixed box in beam seas, subplot (b) the floating ship in beam seas and subplot (c) the floating ship in head seas.

Within figure 6.11, the incident amplitude spectrum defined in figure 6.9 is reduced to a frequency-independent constant of magnitude 1. Taken as a whole, figure 6.11 again identifies two key frequencies: 0.94Hz in the fixed box case (figure 6.11(a)) and 1.28Hz in the floating ship case for both incident wave orientations (figures 6.11(b) and 6.11(c)). In considering these results, it should be noted that the amplification at 0.94Hz in the fixed box case is of a similar magnitude irrespective of the peak frequency. In contrast, the data relating to the floating ship case in beam seas, subplot (b), suggest that the greatest amplification at 1.28Hz occurs for the peak frequencies of f_p = 0.625Hz and 0.714Hz. This is clearly related to the very large $|\eta^2|$ in figure 6.4(c) of the regular wave results.

Figure 6.11(b) also shows that at each of the six spectral peak frequencies, covering a broad range of wave conditions, the ratio $A(f)/A_{inc}(f) < 1.0$ in the vicinity of f = 1Hz. This implies a damping of the wave motion at this frequency. This is consistent with the earlier regular wave results and is believed to be due to the excitation of roll motions. One additional feature of figure 6.11(b), that went unnoticed in the regular wave results, is the additional amplification at (approximately) 0.3Hz; the latter corresponding to $\frac{1}{4}$ of the frequency at which resonant amplification occurs.

A direct comparison between the focused and the regular wave results is presented in figure 6.12. This figure concerns the spectral data relating to all the different wave gauge locations for a single peak frequency (f_p = 0.625Hz). In the case of the focused wave results in subplot (a), non-dimensional data are presented in the form of $A(f)/A_{inc}(f)$ spectra. Likewise, subplot (b) provides a similar dimensionless plot for the regular wave case f = 0.625Hz. All of the data presented on figure 6.12 relate to the floating ship case in beam seas.

A comparison between subplots (a) and (b) of figure 6.12 confirms that both have a negligible amplitude magnification at 0.625Hz (indicated on the figure by the dashed vertical line), but considerable magnitude at twice this frequency. Clearly, the absolute magnitudes of the focused and regular wave data cannot be directly compared because in the regular wave cases the incident spectra, $A_{inc}(f)$,

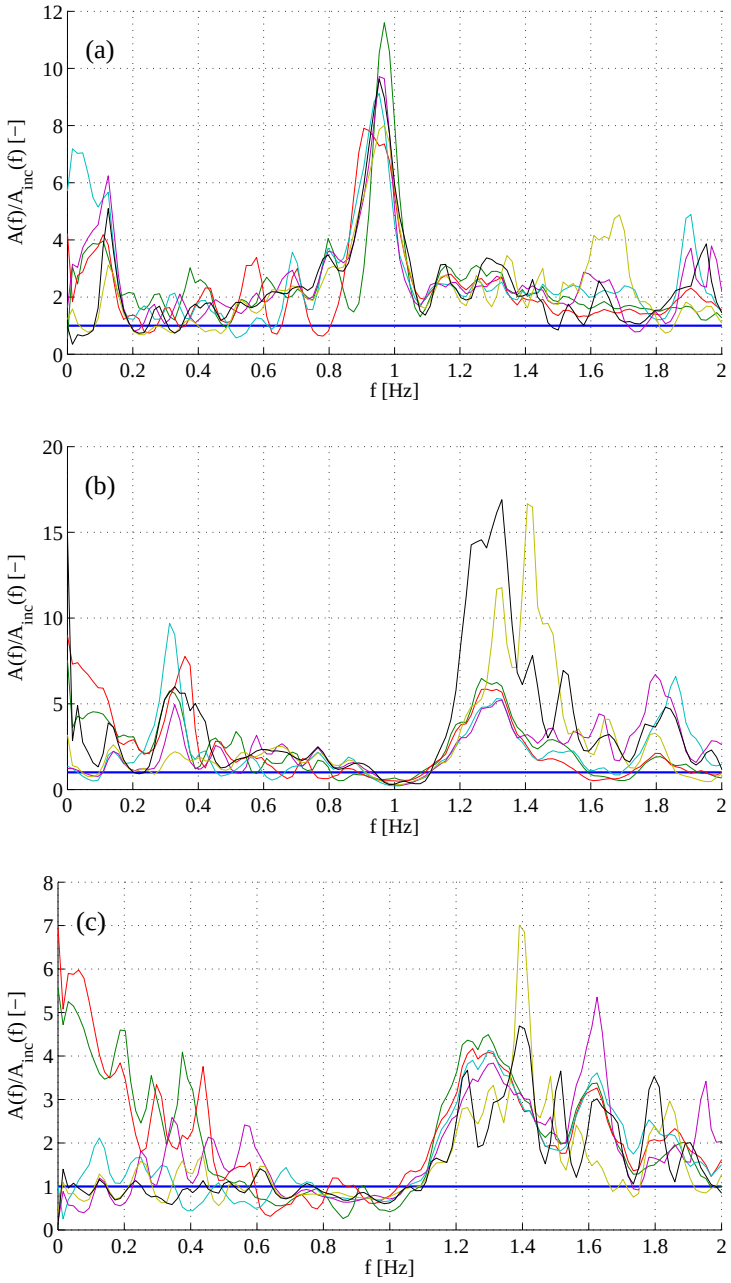


Figure 6.11: Amplification of the spectral amplitudes, $A(f)/A_{inc}(f)$, based on data recorded at the amidships location for focused events of different spectral peak frequencies; (a) the fixed box case in beam seas, (b) the floating ship case in beam seas and (c) the floating ship case in head seas; incident, f_p = 1.43Hz, f_p = 1.25Hz, f_p = 1.00Hz, f_p = 0.83Hz, f_p = 0.714Hz, f_p = 0.625Hz.

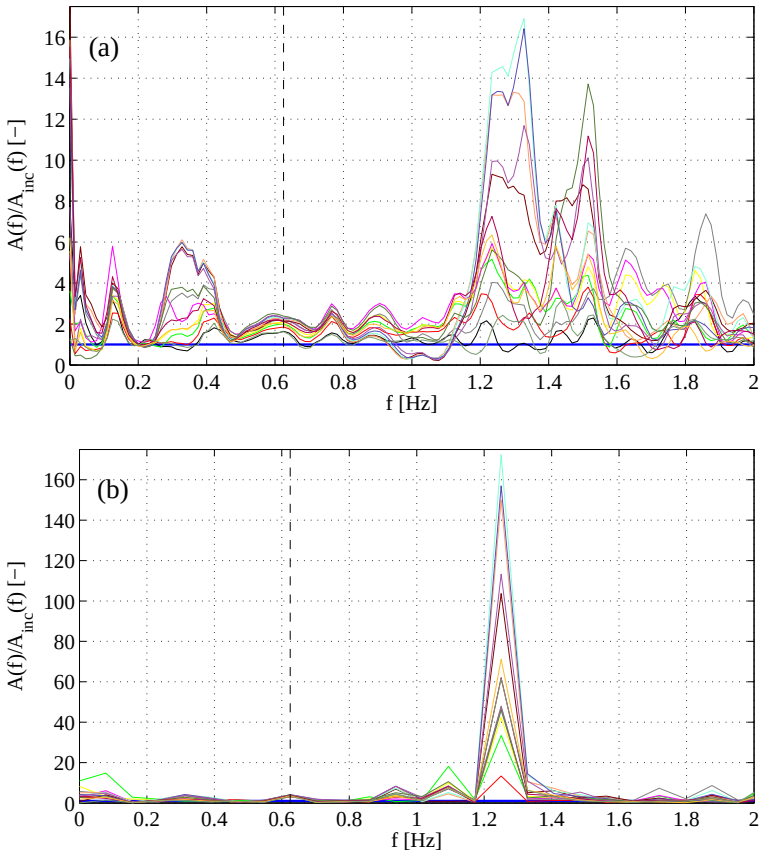


Figure 6.12: Dimensionless amplitude spectra, $A(f)/A_{inc}(f)$, at all wave gauge locations for the floating ship case subject to beam seas, (a) focused waves with f_p = 0.625Hz and (b) regular waves with f = 0.625Hz. Note, in the focused wave event (a), the vertical dashed line indicates the position of the spectral peak frequency, while in the regular wave case (b) it denotes the first harmonic of the incident frequency. — dimensionless incident wave record.

consists of a single first harmonic spike. However, the colours of the lines presented in both examples correspond to the same wave gauge locations and the two subplots show that at f = 1.25Hz their pattern is closely related. Indeed, the ordering of the lines is identical. This indicates that the spatial variation of the additional amplification at f = 1.25Hz in the focused wave events has the same spatial variation as $|\eta^2|$ when the floating ship case is subject to regular waves (figure 6.5(c)). Overall, the data relating to the regular waves and the focused wave events are very closely related.

y [mm]	-1500	-1350	-1200	-900	-750	-150	0	300	750	1050	1500
T_r [s]	147.5	31.1	16.9	12.6	9.7	1.7	1.2	2.6	2.1	3.1	84.3

Table 6.3: Return periods, T_r, for a selection of wave gauge locations

6.5 Random sea states

In the final section of this study, several random sea states were generated. An upcrossings analysis was undertaken on the time-history of the surface elevation, $\eta(t)$, recorded at each wave gauge location and the wave heights between successive upcrossings determined. These data were then ranked and assigned a probability of exceedance. The variation of wave height with probability of exceedance is presented in figure 6.13. This includes data from each wave gauge location, as well as the reference wave gauge recording the incident sea state. Figure 6.13 concerns the floating ship case in beam seas subject to a spectral peak frequency of f_p = 1.25Hz. In this case, the probability of exceedance lines are seen to be self-similar, but of markedly different magnitude. Similar results are found for all the cases considered.

In order to put figure 6.13 into a practical perspective, consider the return period, T_r, of the maximum incident wave height (H_{max} = $2H_s$ = 20mm) at each gauge location. First, a typical wave period, Δt, at each wave gauge location must be found. This is achieved by dividing the duration of the experimental run, or 590s, by the number of upcrossings at each wave gauge location; the latter varying slightly from gauge to gauge. Second, the probability of exceedance value corresponding to H_{max} = 20mm is read off figure 6.13 for each wave gauge location. Finally, T_r is defined by

$$T_r = \frac{\Delta t}{\text{probability of exceedance}}. \tag{6.1}$$

The results of this approach are presented in Table 6.3. At y = −1500mm, a wave height larger than 20mm has a return period of 147.5s whereas at y = 0mm,

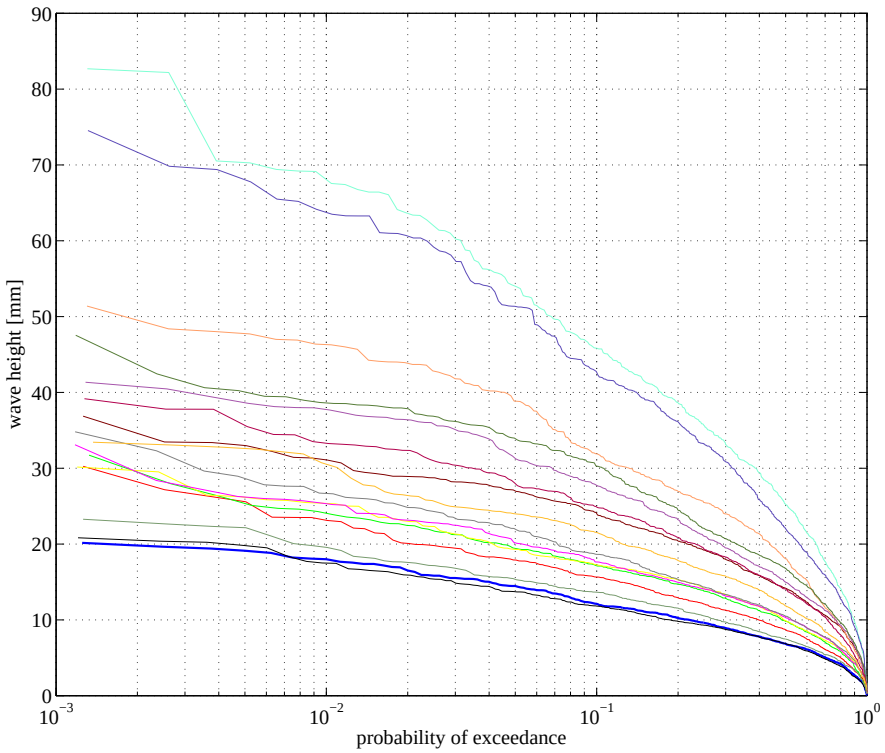


Figure 6.13: Probability of exceedance of wave height, H, in the gap associated with a floating ship in beam seas subject to a random sea state with a spectral peak frequency of f_p = 1.25Hz; ——— incident wave conditions with other colours denoting the data relating to wave gauge locations in the gap.

it is more than 100 times more frequent. In this way, Table 6.3 provides an indication of the more dangerous areas within the gap in which to place equipment, most notably fenders. Figure 6.13 also provides information describing the spatial variation within the gap for an incident spectral peak of f_p = 1.25Hz. As such, it provides equivalent information to that discussed in Sections 6.3 and 6.4.

6.6 Conclusions

This chapter provides a detailed description of the spatial variation of the surface elevation within the gap formed between both a fixed and a floating body in close proximity to a bottom-mounted GBS. It has shown that for a fixed box in beam seas, there is a resonant amplification of the first harmonic surface eleva-

tion, $|\eta^1_{max}|$, at f = 0.94Hz. In contrast, the surface elevation in the gap undergoes a reduction in the floating ship case for incident waves close to f = 0.94Hz. The frequency at which $|\eta^1_{max}|$ occurs for the floating ship case is f = 1.28Hz in both the beam-sea and the head-sea cases. It may therefore be concluded that the motion of the body in the floating ship case significantly increases the frequency at which $|\eta^1_{max}|$ occurs. Furthermore, the similarity between the beam-sea and head-sea cases suggests that the incident wave orientation or, more specifically, the gap end conditions are not the main driving factors behind the resonant amplification in the gap.

At f = 0.94Hz, the fixed box results also display the maximum nonlinearity; the amplitudes of the zeroth and second harmonic surface elevations being a maximum. Similarly, for the floating ship case at f = 1.28Hz the zeroth and third harmonic components also have their maximum amplitudes. In contrast, the largest amplification of the second harmonic surface elevation for the floating ship case occurs for f = 0.625Hz. The shapes of the spatial variation of the first harmonic at f = 1.28Hz and of the second harmonic at f = 0.625Hz are found to be closely related. This suggests that the wave motion within the gap will experience a large excitation at the resonance frequency irrespective of whether the water motion occurs at the first harmonic or the second harmonic of the forcing frequency, f.

The nonlinearity of the floating ship data is more significant than that of the fixed box data in regular waves. Specifically, $\frac{|\eta^0_{max}|}{|\eta^1_{max}|} = \frac{1}{20}$ for the fixed box in beam seas, $= \frac{1}{6}$ for the floating ship in beam seas and $= \frac{1}{10}$ for the floating ship in head seas. Furthermore, $\frac{|\eta^2_{max}|}{|\eta^1_{max}|} = \frac{1}{12}$ for the fixed box in beam seas and $= \frac{1}{5}$ for the floating ship. Finally, while $|\eta^3|$ is negligible in the fixed box case, $\frac{|\eta^3_{max}|}{|\eta^1_{max}|} = \frac{1}{12}$ for the floating ship in beam seas.

Finally, it has been shown that the hydrodynamic interactions leading to an excitation within the gap, occur irrespective of whether the incident waves are regular waves, focused wave events or random sea states. In the chapter that follows, observations will be undertaken to determine whether the findings relating

to the floating ship case are equally valid when considering alternative offloading arrangements in which the LNG transport vessel is moored side-by-side to a body other than a GBS.

7

An experimental study of alternative side-by-side offloading configurations

7.1 Introduction

This chapter considers alternative arrangements arising in the side-by-side offloading of Liquid Natural Gas (LNG). Specifically, it compares the case in which an LNG tanker is moored to a fixed offshore terminal with cases in which the tanker is moored to a floating body. Numerical and experimental work involving two floating vessels has been carried out by, amongst others, Ha et al. (2004) and Koo & Kim (2005). Ha et al. (2004) considered two identical floating vessels and suggested that a reduced surge motion was due to the fact that the hydrodynamic properties of the two vessels were identical. Koo & Kim (2005) highlighted the importance of numerical modelling in the time-domain so that the fenders provide resistance when compressed, but apply no force when not in contact with the moored body. Both contributions also comment that the wave excitation within the gap between the two vessels is the most probable cause of unexpected body motions. However, neither provide detailed measurements of this excitation.

The present chapter seeks to determine the effect of the wave excitation within the gap on the body motion and vice versa; experimental measurements of both

the surface elevation within the gap and the motion of the bodies being presented. Furthermore, the work presented herein considers various experimental setups involving the LNG tanker moored side-by-side to (i) a fixed body (in the form of a bottom-mounted Gravity Based Structure, GBS), (ii) a floating LNG barge (or FLNG) and (iii) a floating body with identical hydrodynamic properties (a second LNG tanker). In each case, the width of the gap between the bodies is identical; the full scale size being determined by the maximum size of the available fenders. In order to develop a basic understanding of the interactions involved, the incident wave conditions are limited to *unidirectional* regular waves and focused wave events. More importantly, the FLNG and the second LNG tanker are externally moored so that they cannot weathervane. The various experimental setups are described in Section 7.2; the similarities and differences between the arrangements being clearly discussed. Section 7.2 also provides details of the incident wave conditions, which include a variation in the wave frequency and the (relative) direction of wave propagation.

Section 7.3 concerns the surface elevation within the gap between the two bodies, the data relating to a sequence of regular wave cases. These cases were chosen because they allow a simple harmonic decomposition; the linear and nonlinear harmonics being considered in turn. The section begins by considering the effect of the incident wave frequency, followed by the effects of the characteristics of the second body, the orientation of the incident waves and the incident wave steepness. Based upon this surface elevation data, the incident wave frequency is shown to be the dominant factor in determining the spatial variation of the wave excitation, while the incident wave steepness highlights the importance of the nonlinearity involved.

The data relating to the vessel motion are presented in Section 7.4. This includes results from both the regular wave cases and the focused wave events. This section also highlights what is believed to be the effect of the wave excitation within the gap on the motion of the moored LNG tanker.

Finally, Section 7.5 compares the surface elevation in the gap with the upwave

beam	0.70m
draft	0.216m
length	4.00m
natural roll frequency	0.77Hz
natural heave frequency	0.74Hz

Table 7.1: Properties of the experimental model of the FLNG barge.

region for a single experimental setup. These comparisons show that the hydrodynamics of these two wave fields are quite different; illustrating the importance of the wave-body interactions when considering two bodies in close proximity.

7.2 Experimental study

The experimental study was again undertaken in the 3D wave basin at Imperial College London; full details of this facility being given in Chapter 5. As before, a length-scale of $l_s = 1:100$ is adopted, and all the data are presented and discussed at laboratory scale. Subplots (a) to (d) of figure 7.1 illustrate the various experimental setups within the wave basin for the beam-sea cases; the small insert in the subplots showing the equivalent arrangement in head seas. Details of the physical and hydrodynamic properties of the FLNG are given in Table 7.1; the equivalent details for the LNG having been given previously in Table 6.1.

Subplot (a) of figure 7.1 concerns the experimental setup of the LNG tanker moored side-by-side to the GBS, hereafter referred to as the GBS-LNG setup. The adopted coordinate axes (x, y) are defined in subplot (a) for each orientation and are relevant to all the experimental setups. Specifically, the x-direction is always aligned with the direction of propagation of the incident waves, while the horizontal y-direction is perpendicular to it. These descriptions are identical to those adopted in earlier chapters, although the figures themselves have been rotated through 90° to facilitate the layout of later comparisons. The GBS in subplot

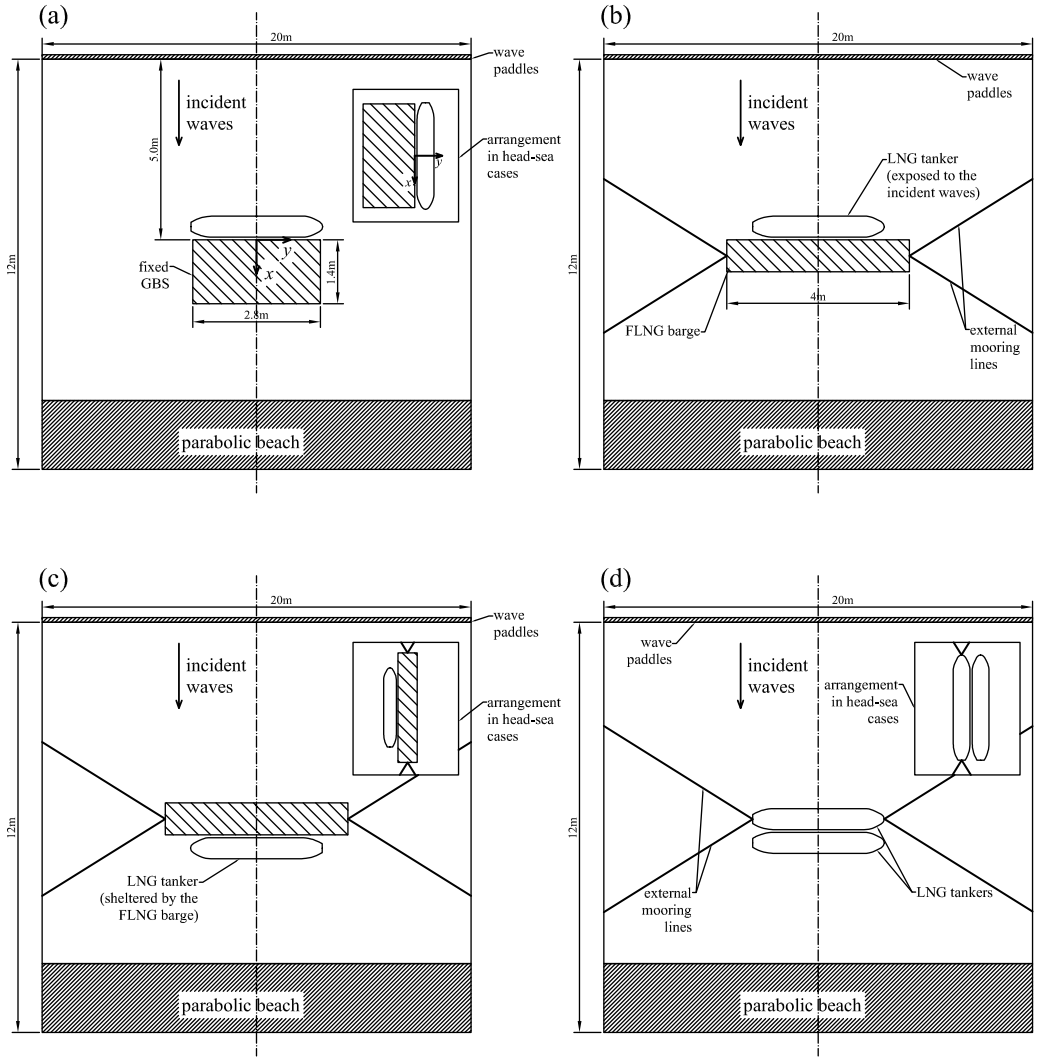


Figure 7.1: Plan view of the experimental setups within the 3D wave basin for the (a) GBS-LNG, (b) FLNG-LNG$_E$, (c) FLNG-LNG$_S$ and (d) LNG-LNG setups in the beam-sea orientation; the insert shows the arrangements of the head-sea orientation, where applicable. In the FLNG-LNG$_E$ setup, the subscript E denotes the fact that the LNG is exposed to the incident waves. In the FLNG-LNG$_S$ setup, the subscript S denotes that the LNG is sheltered by the FLNG.

(a) is *fixed* while the FLNG in subplot (b) is *floating*. However, in this second setup the FLNG is always beam-on to the incident waves; this orientation being maintained through the use of external mooring lines as depicted on the plot. These external mooring lines are tensioned cables running from the centreline of

the vessel and extending to the edges of the wave basin where they are secured by springs. The introduction of this external mooring significantly simplifies the problem by not allowing the floating vessels to weathervane, while at the same time having a minimal effect on the vertical heave and roll motions. The length of the FLNG in subplot (b) is 4m, while the length of the GBS in subplot (a) is 2.8m; the length between perpendiculars of the LNG being 2.21m as described in the previous chapter. It therefore follows that in addition to the fact that the GBS is fixed while the FLNG is floating, the difference in their lengths leads to important changes in the boundary conditions at either end of the gap and possibly the level of wave excitation within it.

Within subplots (b) and (c), the LNG is moored to the FLNG. However, the LNG in subplot (b) is exposed, while it is sheltered in the beam-sea orientation in subplot (c); the former being referred to as FLNG-LNG$_E$ and the latter as FLNG-LNG$_S$. The setup depicted in subplot (d) is referred to as the LNG-LNG setup since it considers an LNG tanker in close proximity to an externally-moored but otherwise identical LNG tanker. Consequently, the hydrodynamic properties of the two floating vessels for the setup described in subplot (d) are the same, while they differ for the vessels in subplots (b) and (c). In all the experimental setups, the details of the mooring arrangement (between the two bodies) are as described in the previous chapter (see Section 6.2).

Within this study, the incident wave cases include regular waves and focused wave events. The frequency of the incident regular waves ranges from long waves at f = 0.625Hz to short waves at f = 1.44Hz. In undertaking these tests, an attempt was made to keep the incident wave amplitude constant over this frequency range at A_{inc} = 10mm. However, this was found not to be possible for the majority of the runs in the FLNG-LNG$_E$ and LNG-LNG setups in the beam-sea orientation, due to the large motions of the vessels. As a result, the incident wave amplitude was reduced to A_{inc} = 5mm. However, even with this reduced amplitude, there were still frequencies at which the runs could not be undertaken. Table 7.2(a) provides details of the incident wave amplitude for each of the experimental se-

tups. It is clear from these data that there is a subset of frequencies at which both the incident wave amplitudes were considered; comparisons between these cases allowing the effect of the incident wave steepness to be addressed. Table 7.2(b) provides details of the maximum crest elevations within focused wave events. In these tests, the underlying wave spectra were JONSWAP, with a peak enhancement factor of $\gamma = 2.5$. Six peak frequencies were considered ranging from $f_p = 0.625$Hz to $f_p = 1.43$Hz and in each case the maximum crest elevation was set at $\eta_{max} = 10$mm.

Within the experimental study, the vessel motion was recorded using 3-component accelerometers. As a result, the data recorded at a fixed location on the vessel combine the effects of the translational and the rotational motion of the body. With the practical application of offloading operations in mind, the accelerometers were placed at the approximate position of the amidships loading manifolds; the latter located on the deck close to the gap (in y) and at the amidships. In this position, in a beam-sea orientation the influence of both the heave and roll motions is accounted for in the recorded vertical component of the acceleration.

The time-history of the water surface elevation, $\eta(t)$, was recorded using the stainless steel strip gauges introduced in Chapter 6; individual gauges being adhered to either the GBS or the floating externally-moored vessel. When adhered to a floating vessel, the recorded data are influenced by both the motion of the surface and the large vertical motion of the vessel. However, the latter could be determined from the recorded vertical component of the acceleration; the accelerometer being positioned close to the gap and therefore above the strip gauges.

The strip gauges were positioned at 150mm spacings to enable a detailed description of the spatial variation of the surface elevation along the length of the gap between the two bodies. This spacing gives a total of 23 wave gauges over the 4m length of the FLNG. Unfortunately, the recording apparatus employed was limited to 14 channels. To overcome this difficulty, all the experimental runs involving the FLNG were undertaken twice; the first set recording $\eta(t)$ at the strip gauge locations along one half of the FLNG and the second set recording $\eta(t)$

(a)

f [Hz]	Incident Wave Amplitude, A_{inc}, [mm]						
	GBS-LNG		FLNG-LNG$_E$	FLNG-LNG$_S$		LNG-LNG	
	Beam	Head	Beam	Beam	Head	Beam	Head
0.625	10	10	5	5&10	5&10	5	5&10
0.75	10	10	5	-	5&10	5	5&10
0.81	10	10	5	-	5&10	5	5&10
0.875	10	10	5	10	10	5	10
0.91	10	10	-	5&10	5&10	-	5&10
0.94	-	10	5	10	10	-	10
0.97	-	10	5	10	10	5	10
1.00	10	10	5	5&10	5&10	5	5&10
1.03	10	10	5	10	10	5	10
1.06	10	10	5	10	10	5	10
1.09	10	10	5	10	10	5	10
1.125	10	10	5	5&10	5&10	5	5&10
1.16	10	10	5	10	10	5	10
1.19	10	10	5	10	10	5	10
1.22	10	10	5	10	10	5	10
1.25	10	10	5	10	10	5	10
1.28	10	10	5	10	10	5	10
1.31	10	10	5	5&10	5&10	5	5&10
1.34	10	10	5	10	10	5	10
1.44	10	10	5	5&10	5&10	5	5&10

Table 7.2: Details of the incident wave cases considered; (a) regular waves and (b) focused wave events.

(b)

f_p [Hz]	Maximum crest elevations, η_{max}, [mm]						
	GBS-LNG		FLNG-LNG$_E$	FLNG-LNG$_S$		LNG-LNG	
	Beam	Head	Beam	Beam	Head	Beam	Head
0.625	10	10	10	10	10	10	10
0.714	10	10	10	10	10	10	10
0.83	10	10	10	10	10	10	10
1.0	10	10	10	10	10	10	10
1.25	10	10	10	10	10	10	10
1.43	10	10	10	10	10	10	10

Table 7.2: Details of the incident wave cases considered; (a) regular waves and (b) focused wave events.

along the other half of the FLNG. The repeatability of the incident waves between the two runs was monitored using a free-standing wave gauge positioned at the edge of the wave basin; the location of this gauge being chosen such that $\eta(t)$ was unaffected by the experimental setup as described in Chapter 5. In contrast, for the LNG-LNG setup the variation of the cross-sectional shape of the LNG tanker meant that the spatial variation could only be recorded over 600mm either side of the amidships.

7.3 Surface elevation within the gap

7.3.1 The effect of incident wave frequency

This section concerns the effect of the incident wave frequency on the wave excitation within the gap. First, the spatial variation of the surface elevation corresponding to a selection of discrete incident regular wave frequencies is considered. Figure 7.2 presents data relating to the two setups involving the FLNG in beam seas; FLNG-LNG$_E$ and FLNG-LNG$_S$ outlined in figures 7.1(b) and 7.1(c) respectively. Four incident wave frequencies are presented within Figure 7.2, ranging

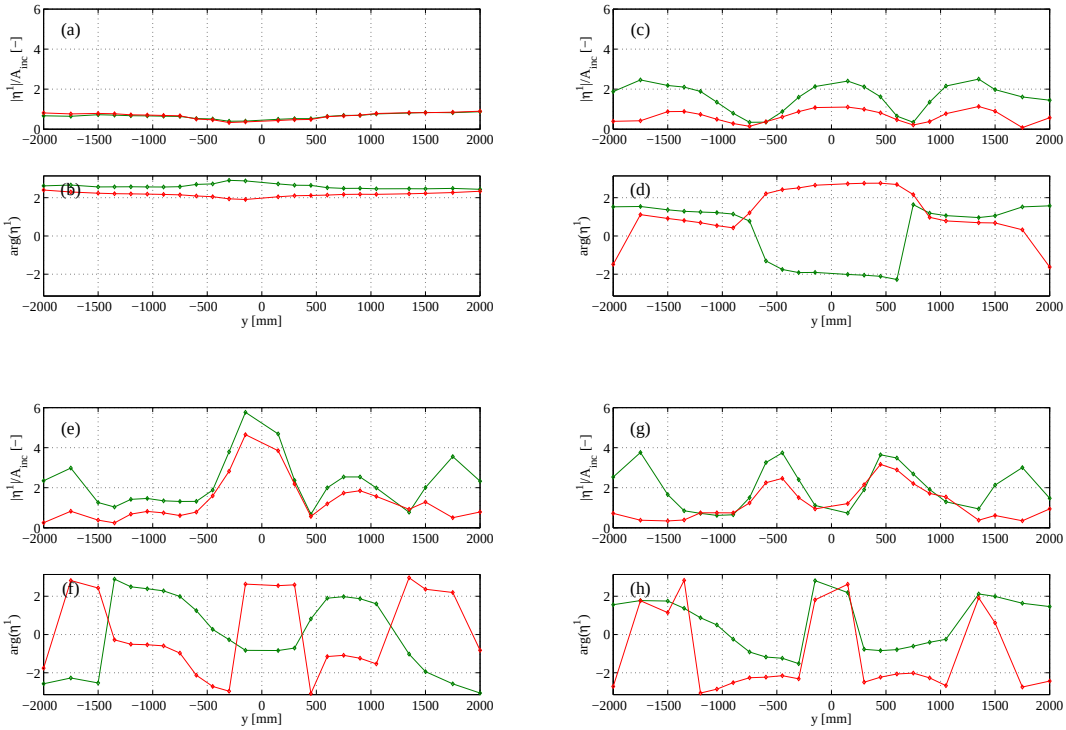


Figure 7.2: Spatial variation of the first harmonic of the surface elevation amplitude, $|\eta^1|$, and phase, $arg(\eta^1)$, for (a)&(b) f = 0.625Hz, (c)&(d) f = 1.09Hz, (e)&(f) f = 1.31Hz, (g)&(h) f = 1.44Hz in beam seas; —— FLNG-LNG$_E$, —— FLNG-LNG$_S$

from the longest wave case in subplots (a) and (b) to the shortest wave case in subplots (g) and (h). Each pair of subplots presents the spatial variation of the amplitude and phase of the first harmonic of the surface elevation, $|\eta^1|/A_{inc}$ and $arg(\eta^1)$ respectively. As described previously, these data are obtained from a Fourier analysis (FFT) of the time-history of the surface elevation recorded at the strip gauge locations.

In accordance with the previous chapter, figure 7.2 indicates a progression from a first mode in subplots (a) and (b) to a third mode in subplots (c) and (d) to fifth modes in subplots (e), (f) and (g), (h). The phase plots presented in this figure (subplots (b), (d), (f) and (h)) are made up of predominantly straight sections, indicating standing wave modes. However, while the constant phase sections in subplot (d) are all of similar length, this is not the case in subplot (h); the con-

stant phase sections at the amidships for both the FLNG-LNG$_E$ and FLNG-LNG$_S$ setups being shorter than those that occur to either side. Furthermore, the magnitudes of the antinodes in subplot (c) are equal along the length of the gap. In contrast, subplot (e) shows a dominant antinode at the amidships, while in subplot (g) the amidships antinode is substantially smaller than those either side of it and the magnitudes of the end antinodes are only appreciable for the FLNG-LNG$_E$ setup. Indeed, the antinode at the amidships in subplot (g) is difficult to identify. This may, in part, be due to the fact that a strip gauge could not be placed at y = 0mm because this also corresponds to the joint between the two halves of the experimental model of the FLNG. The existence of an antinode at amidships is further discussed in relation to the LNG-LNG setup in Section 7.3.3 below. The explanation for the significant variation in the magnitudes of the antinode along the length of the gap is believed to be a consequence of the difference in the lengths of the LNG and FLNG vessels, coupled with the fact that the LNG tanker is asymmetric fore and aft.

7.3.2 The effect of the second body

In order to demonstrate the effect of changing the properties of the second body, the results of all four experimental setups in beam seas are presented below. In order to achieve the required comparisons, the spatial variation at each frequency is initially represented by a single maximum of the total surface elevation at any point along the length of the gap. This is referred to as $|\eta_{max}|$ and is non-dimensionalised by the incident amplitude to give $|\eta_{max}|/A_{inc}$. The variation of $|\eta_{max}|/A_{inc}$ with the incident wave frequency for each of the four setups is presented in figure 7.3. This serves as an overview of the results arising in the beam-sea cases.

Figure 7.3 indicates that the largest wave excitation in the gap, corresponding to $|\eta_{max}|/A_{inc}$ of 7.6, occurs for the GBS-LNG setup with an incident wave frequency of f = 1.31Hz. The second largest amplification corresponds to $|\eta_{max}|/A_{inc}$ = 6.4 for the FLNG-LNG$_E$ setup with the same incident wave frequency.

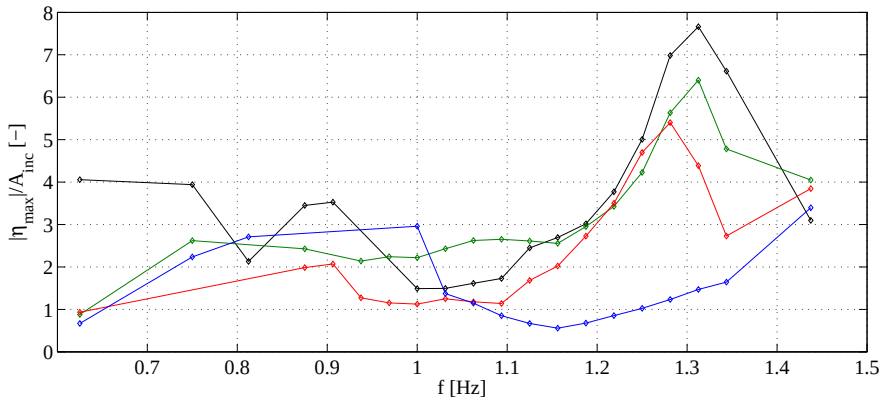


Figure 7.3: Variation with incident regular wave frequency (f) of the non-dimensionalised maximum of the total surface elevation, $|\eta_{max}|/A_{inc}$, at any point within the gap in beam seas; —— GBS-LNG, —— FLNG-LNG$_E$, —— FLNG-LNG$_S$, —— LNG-LNG

This is followed by $|\eta_{max}|/A_{inc}$ = 5.4 for the FLNG-LNG$_S$ setup at f = 1.28Hz and $|\eta_{max}|/A_{inc}$ = 3.4 for the LNG-LNG setup at f = 1.44Hz. In considering these results, it is believed that the largest wave excitation occurs for the GBS-LNG setup because: (i) the GBS extends over the entire water depth and (ii) it is fixed in position. In the remaining setups, the motion of the second body is believed to absorb some of the incident wave energy; resulting in a lower wave excitation within the gap.

Next, consider the variation with frequency when the total surface elevation is split into its harmonic components. The relevant amplitudes of these harmonics are the mean shift or zeroth harmonic $|\eta^0|$, the first harmonic $|\eta^1|$, the second harmonic $|\eta^2|$ and the third harmonic $|\eta^3|$. In Figure 7.2 it was clear that $|\eta^1|$ exhibits a spatial variation along the length of the gap. However, setting aside the spatial variation, figure 7.4 presents the maximum value of the amplitude of each harmonic, irrespective of the position within the gap at which it occurs.

Before considering figure 7.4, Table 7.3 summarises the data presented on figures 7.3 and 7.4. Specifically, it provides the largest, or resonant, amplification of the dimensionless total surface elevation and of the harmonic amplitudes, again non-dimensionalised with respect to the incident wave amplitude. It is clear from

	$\lvert\eta_{max}\rvert/A_{inc}$	$\lvert\eta^1_{max}\rvert/A_{inc}$	$\lvert\eta^0_{max}\rvert/A_{inc}$	$\lvert\eta^2_{max}\rvert/A_{inc}$	$\lvert\eta^3_{max}\rvert/A_{inc}$
GBS-LNG	7.6	6.1	1.3	1.1	0.5
FLNG-LNG$_E$	6.4	5.8	0.4	1.7	0.3
FLNG-LNG$_S$	5.4	4.6	0.5	0.8	0.2
LNG-LNG	3.4	3.1	0.2	1.6	-

Table 7.3: Resonant amplifications of the total surface elevation and of its harmonic components, non-dimensionalised with respect to the incident wave amplitude, for the experimental setups in beam seas. (Note: these data relate to the maximum values irrespective of where they occur along the gap and at which incident wave frequency.)

these data that the largest component of the total surface elevation is the first harmonic. However, the magnitudes of the nonlinear terms are by no means negligible.

In order to identify at which frequencies the resonant amplifications given in Table 7.3 occur, figure 7.4 concerns the variation with frequency. Within this figure, subplot (a) relates to $|\eta^0_{max}|/A_{inc}$, subplot (b) to $|\eta^1_{max}|/A_{inc}$, subplot (c) to $|\eta^2_{max}|/A_{inc}$ and subplot (d) to $|\eta^3_{max}|/A_{inc}$. Evidence that the first harmonic is the largest component of the total surface elevation is provided by the fact that the trends in subplot (b) of figure 7.4 are almost identical to those seen in figure 7.3. A comparison of subplots 7.4(a), 7.4(b) and 7.4(c) shows that the variation with frequency of $|\eta^0_{max}|/A_{inc}$ and $|\eta^1_{max}|/A_{inc}$ are very similar, while that of $|\eta^2_{max}|/A_{inc}$ is quite different. In particular, the resonant magnitudes of these two nonlinear terms, given in Table 7.3, occur at opposite ends of the frequency range. As a result, although the largest component of $|\eta_{max}|/A_{inc}$ (depicted in figure 7.3) is clearly related to $|\eta^1_{max}|/A_{inc}$ (depicted in subplot 7.4(b)), the above observation illustrates that separate nonlinear terms account for the differences between $|\eta_{max}|/A_{inc}$ and $|\eta^1_{max}|/A_{inc}$ at the two ends of the frequency range. For example, it is the $|\eta^2|$ component that accounts for the increase of $|\eta^1_{max}|/A_{inc}$ = 1.0 to $|\eta_{max}|/A_{inc}$ = 2.6 at f = 0.75Hz for the FLNG-LNG$_E$ setup or $|\eta^1_{max}|/A_{inc}$ = 3.0

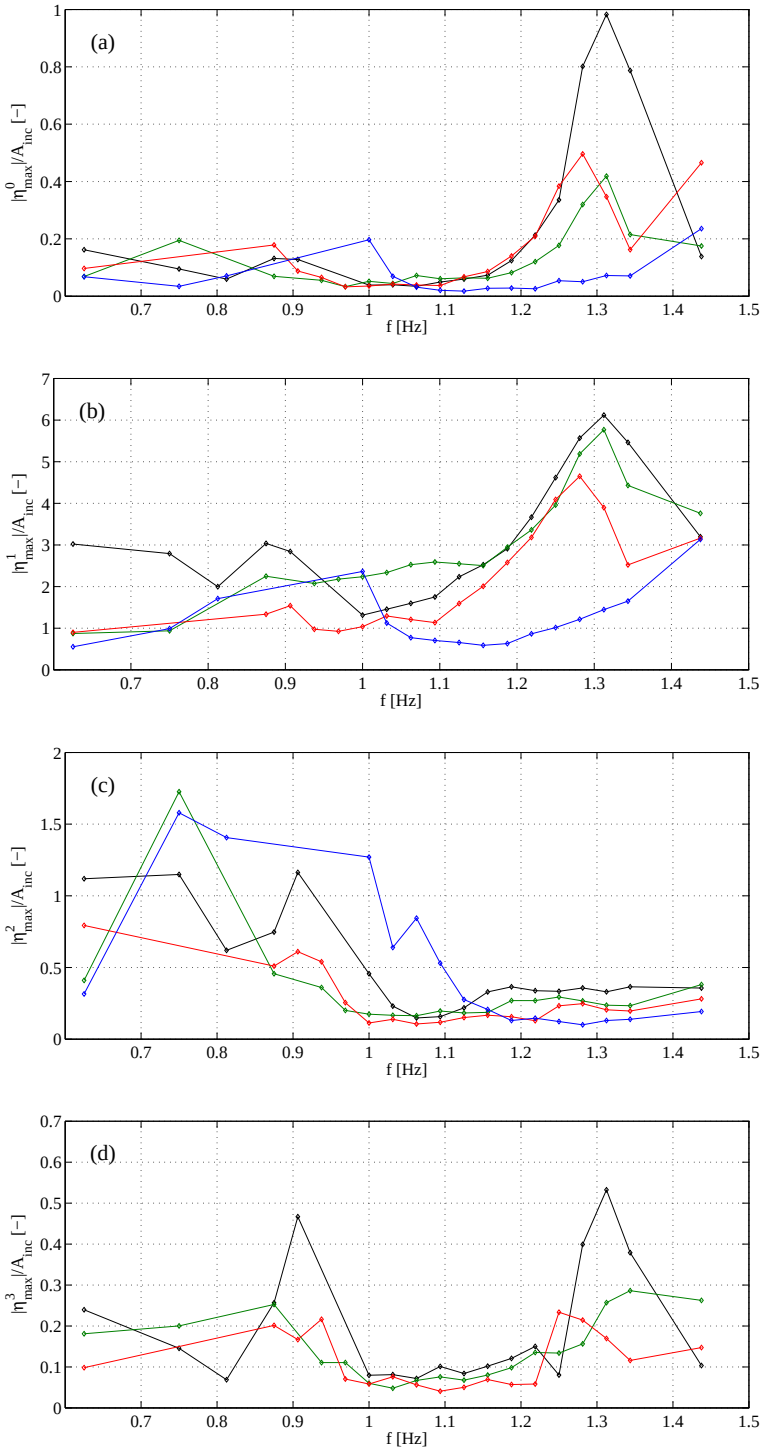


Figure 7.4: Variation with incident wave frequency (f) of the non-dimensionalised maximum amplitude of the (a) zeroth, (b) first, (c) second and (d) third harmonic of the surface elevation at any point within the gap in beam seas; —— GBS-LNG, —— FLNG-LNG$_E$, —— FLNG-LNG$_S$, —— LNG-LNG

to $|\eta_{max}|/A_{inc}$ = 4.0 at f = 0.625Hz for the GBS-LNG setup. In contrast, the $|\eta^0|$ component is responsible for the increase of $|\eta^1_{max}|/A_{inc}$ = 4.6 to $|\eta_{max}|/A_{inc}$ = 5.4 at f = 1.28Hz for the FLNG-LNG$_S$ setup. Finally, subplot 7.4(d) shows that for the GBS-LNG setup the resonant $|\eta^3_{max}|/A_{inc}$ occurs at f = 1.31Hz. Its contribution as well as that of $|\eta^0|$ account for the increase in $|\eta^1_{max}|/A_{inc}$ = 6.1 to $|\eta_{max}|/A_{inc}$ = 7.6 at f = 1.31Hz for the GBS-LNG setup. These results clearly indicate that although the nonlinear terms are smaller than their linear equivalents, they can have a significant effect at some frequencies.

For further insight, consider the spatial variation of the various harmonic amplitudes at some of the key frequencies mentioned above. Table 7.4 provides the details of the cases considered in figure 7.5. Subplot (a) of Figure 7.5 presents

	f [Hz]		
	$\|\eta^0\|/A_{inc}$	$\|\eta^1\|/A_{inc}$	$\|\eta^2\|/A_{inc}$
GBS-LNG	1.31	1.31	0.625
FLNG-LNG$_E$	1.31	1.31	0.625
FLNG-LNG$_S$	1.28	1.28	0.625
LNG-LNG	1.44	1.44	0.75

Table 7.4: Incident wave frequencies at which the resonant amplification of the non-dimensionalised harmonic components of the surface elevation occur for the experimental setups in beam seas. The spatial variation of these cases in considered in figure 7.5.

the data corresponding to $|\eta^0|/A_{inc}$, subplot (b) to $|\eta^1|/A_{inc}$ and subplot (c) to $|\eta^2|/A_{inc}$. In considering the values in Table 7.4, it is clear that subplot (c) relates to the lower end of the frequency range, while subplots (a) and (b) relate to the higher end. Furthermore, it is interesting to note that the incident frequencies considered for the second harmonic in subplot (c) are close to half of those considered in subplots (a) and (b). Despite this frequency difference, figure 7.5 clearly shows that the shape of the spatial variation for all the setups in all of the subplots is remarkably similar; specifically, the data all describe a dominant amplification

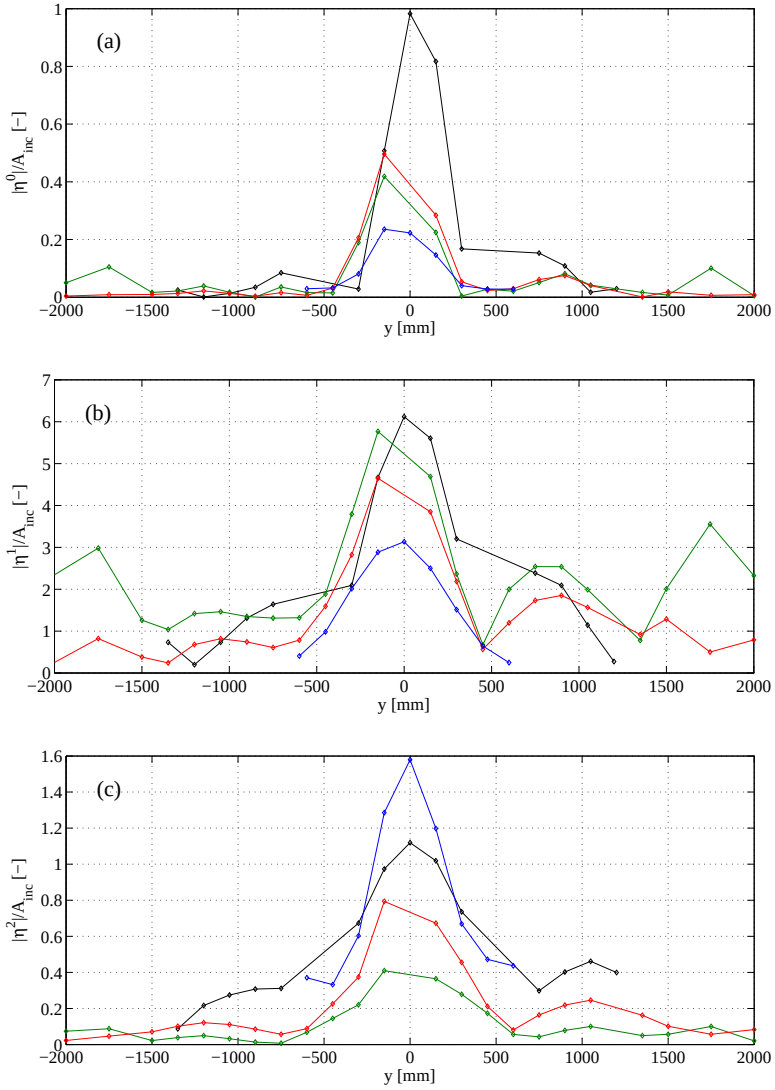


Figure 7.5: Spatial variation of the largest non-dimensionalised amplitude of the zeroth, first and second harmonic surface elevation in beam seas (see Table 7.4 for incident wave frequencies); (a) $|\eta^0|/A_{inc}|$, (b) $|\eta^1|/A_{inc}$ and (c) $|\eta^2|/A_{inc}$ —— GBS-LNG, —— FLNG-LNG$_E$, —— FLNG-LNG$_S$, —— LNG-LNG

	f [Hz]		
	$\lvert\eta^0\rvert/A_{inc}$	$\lvert\eta^1\rvert/A_{inc}$	$\lvert\eta^2\rvert/A_{inc}$
GBS-LNG	1.28	1.28	0.625
FLNG-LNG$_S$	1.34	1.34	0.625
LNG-LNG	1.44	1.44	0.81

Table 7.5: Incident wave frequencies at which the resonant amplification of the non-dimensionalised harmonic components of the surface elevation occur for the experimental setups in head seas. The spatial variation of these cases in considered in figure 7.6.

over the amidships section. In the previous chapter it was concluded that the fluid motion within the gap experiences a large excitation at the resonance frequency irrespective of whether the fluid motion occurs at the first or the second harmonic. Figure 7.5 illustrates that the characteristics of the second body have no effect on this conclusion.

7.3.3 The effect of orientation

The results presented in Chapter 6 showed that although the wave modes in the gap in the head-sea cases are a combination of propagating and standing wave modes, the frequency at which largest amplification in the gap occurs for the head-sea cases is strikingly similar to that for the beam-sea cases. Furthermore, it was shown that the shape or spatial variation of the excitation was closely related.

Figure 7.6 concerns the head-sea cases, describing the spatial variation of $|\eta^0|/A_{inc}$, $|\eta^1|/A_{inc}$ and $|\eta^2|/A_{inc}$ in subplots (a), (b) and (c) respectively; the data relating to the largest amplification in each case and the corresponding frequencies being defined in Table 7.5. In each case, the frequencies relating to $|\eta^2|/A_{inc}$ are approximately half of the frequencies relating to $|\eta^1|/A_{inc}$. More importantly, the relevant frequencies are close to their beam-sea equivalents given in Table 7.4. Subplot 7.6(b) shows that the spatial variation of $|\eta^1|/A_{inc}$ for the different setups is not only similar in shape but also similar in magnitude. The latter observation is

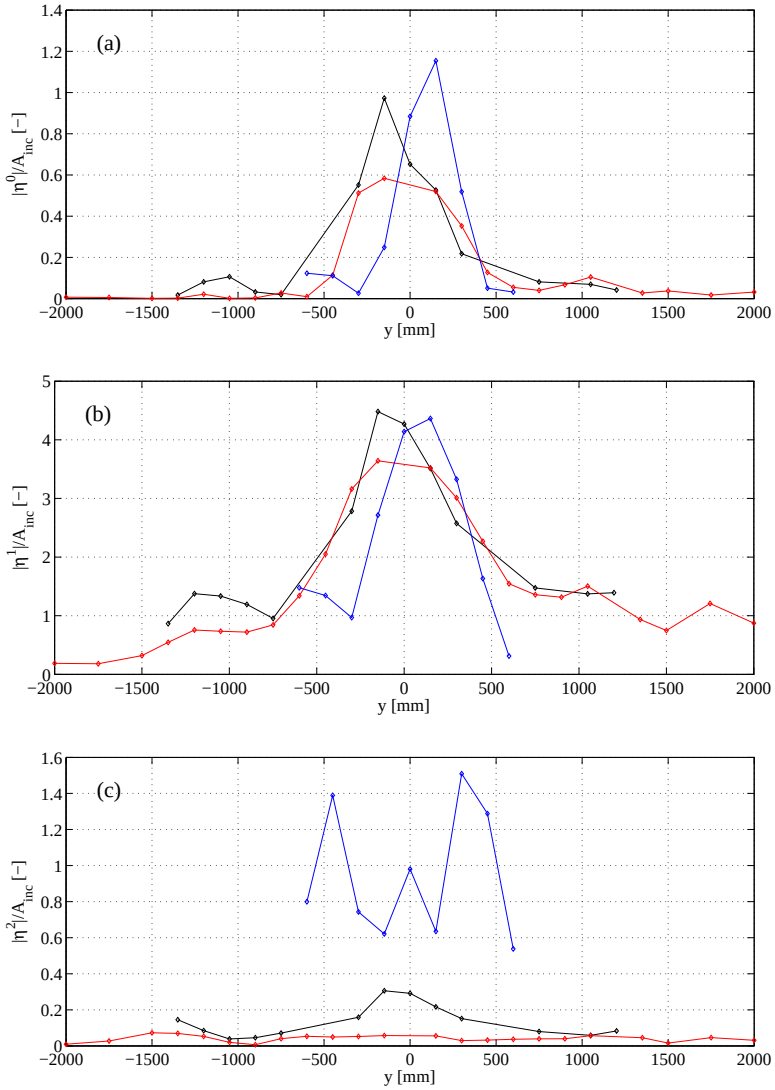


Figure 7.6: Spatial variation of the largest non-dimensionalised amplitude of the zeroth, first and second harmonic surface elevation in head seas (see Table 7.5 for incident wave frequencies); (a) $|\eta^0|/A_{inc}|$, (b) $|\eta^1|/A_{inc}$ and (c) $|\eta^2|/A_{inc}$ —— GBS-LNG, —— FLNG-LNG$_S$, —— LNG-LNG

in contrast to the beam sea data depicted in figure 7.5(b). The explanation for this is believed to be as follows. In the head-sea cases, the incident waves propagate down the length of the gap, while in the beam-sea cases they are reflected by the bodies. Therefore, because the second body merely defines one of the sides of the gap in the head-sea cases, its characteristics (whether physical or hydrodynamic

properties) are less influential in head seas than in beam seas.

Considering the nonlinear harmonics, subplots 7.6(a) and 7.6(c) show that the shapes of $|\eta^0|/A_{inc}$ and $|\eta^2|/A_{inc}$ are similar to the shape of the first harmonic occurring at the same frequency in the former (subplot (a)) and at the opposite end of the frequency range in the latter (subplot (c)). In particular, the data relating to $|\eta^2|/A_{inc}$ for the LNG-LNG setup in subplot 7.6(c) are similar to $|\eta^1|/A_{inc}$ for the FLNG-LNG$_S$ setup in subplot 7.2(g). However, the availability of data at y = 0mm in the LNG-LNG setup in subplot 7.6(c) makes the presence of the amidships antinode more apparent. Furthermore, subplot 7.6(c) shows that $|\eta^2|/A_{inc}$ for the LNG-LNG setup greatly surpasses that recorded in the GBS-LNG setup; the FLNG-LNG$_S$ setup having no substantial second harmonic amplification. In contrast, the magnitudes of $|\eta^0|/A_{inc}$ for the three setups in subplot 7.6(a) are similar. This perhaps suggests that the difference in $|\eta^2|/A_{inc}$ in subplot 7.6(c) is the result of the large discretisation in the chosen incident wave cases at the lower end of the frequency range. This leads to an even larger discretisation in twice these values; the latter being relevant to the resonance of $|\eta^2|/A_{inc}$ and allowing for the possibility that some of these resonant effects have been missed.

7.3.4 The effect of wave steepness

Wave steepness is usually defined in terms of $A_{inc}k$, where k is the wave number. In a wave theory, the wave steepness highlights those cases in which the nonlinear harmonics will become significant. In the present study, $A_{inc}k$ varies from 0.01 at the low end of the frequency range to 0.08 at the high end; the change being due, in large part, to the variation of k. In contrast to a wave theory, the largest nonlinear terms in the description of the wave excitation within the gap have been shown to occur at opposite ends of the frequency range; $|\eta^2_{max}|/A_{inc}$ occurring at the lower end and $|\eta^0_{max}|/A_{inc}$ at the higher end. As a result, it was concluded that the best way to illustrate the effect of wave steepness on all the harmonics was via a subset of wave cases involving two incident amplitudes (varying A_{inc} for a

constant k value). This approach was applied over the entire frequency range; full details being presented in Table 7.2.

Before discussing these results, consider briefly the fundamentals of a first and second order analysis using the example of a nonlinear wave theory. Most wave theories assume an infinite series solution to the Laplace equation in terms of $A_{inc}k$; resulting in the expression for the surface elevation as

$$\eta = \sum_{l=1}^{\infty} \frac{(A_{inc}k)^l}{k} \cos(2l\pi ft). \tag{7.1}$$

Consequently, for $l = 1$, η^1 is directly proportional to A_{inc} and linear theory will result in *equal* non-dimensionalised $|\eta^1|/A_{inc}$ for both the $A_{inc} = 10$mm and the $A_{inc} = 5$mm cases. The second harmonic components in a second order wave theory are proportional to the square of $A_{inc}k$. As a result, increasing A_{inc} by a factor of 2 increases the magnitude of these wave components by a factor of 4. It therefore follows that a second order theory can only account for an $|\eta^2|/A_{inc}$ in the $A_{inc} = 10$mm case that is twice as large as that in the $A_{inc} = 5$mm case; the same argument being applicable to η^0.

Figure 7.7 overlays data relating to the two incident wave amplitudes for the FLNG-LNG$_S$ setup in beam seas. The data are non-dimensionalised, describing the spatial variation of $|\eta^0|/A_{inc}$, $|\eta^1|/A_{inc}$ and $|\eta^2|/A_{inc}$ in subplots (a), (b) and (c) respectively. In each subplot, the data relate to the incident wave frequency resulting in the largest recorded amplification of each harmonic; $f = 1.44$Hz, $f = 1.31$Hz and $f = 0.625$Hz respectively.

Considering the linear component first, figure 7.7(b) shows that the data relating to both incident amplitudes are almost co-incident. This indicates that the increase in the incident wave steepness does little to alter the amplification of the first harmonic of the surface elevation at any point within the gap. It may therefore be concluded that the first harmonic results are predominantly linear, with slight departures due to third and higher order effects. However, subplots (a) and (c) show increases in $|\eta^0|/A_{inc}$ and $|\eta^2|/A_{inc}$ that are greater than a factor of 2; indicating the potential importance of higher order effects.

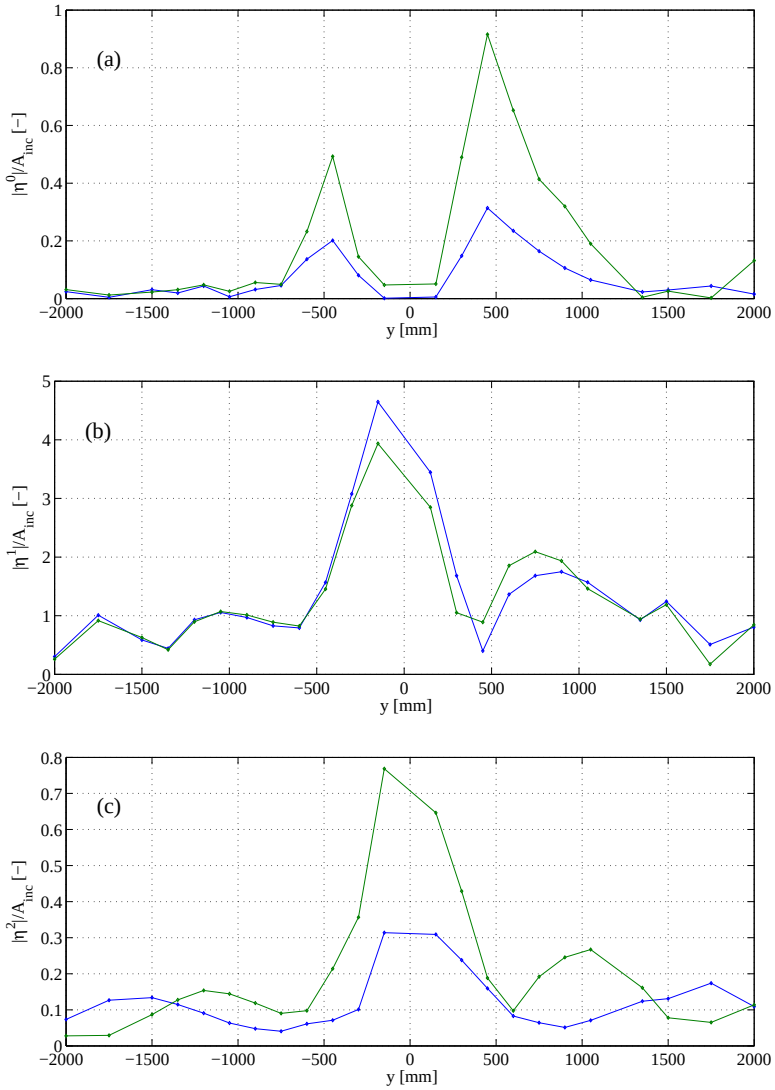


Figure 7.7: Spatial variation of the non-dimensionalised harmonic amplitudes of the surface elevation (a) zeroth harmonic for f = 1.44Hz, (b) first harmonic for f = 1.31Hz and (c) second harmonic for f = 0.625Hz for FLNG-LNG$_S$ in beam seas; —— A_{inc} = 5mm, —— A_{inc} = 10mm

7.4 Vessel motion

7.4.1 The effect of the second body

The data presented in figure 7.8 relate to the amplitude of the first harmonic of the horizontal acceleration in x, $|a_x^1|$, of the LNG tanker in the beam-sea cases.

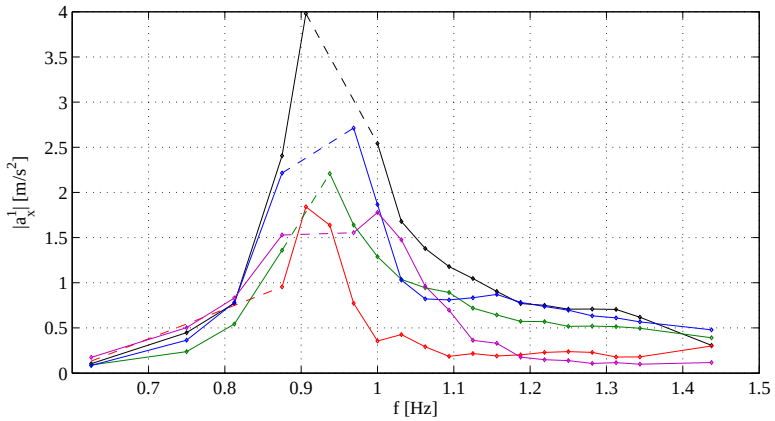


Figure 7.8: Variation with incident frequency of the amplitude of the first harmonic of the horizontal x acceleration, $|a_x^1|$, of the LNG vessel for the regular wave cases in beam seas; —— GBS-LNG, —— FLNG-LNG$_E$, —— FLNG-LNG$_S$, —— LNG-LNG moored, —— LNG-LNG sheltered.

The data within the figure relate to the regular wave tests outlined in Table 7.2, covering a frequency range of 0.625Hz $\leq f \leq$ 1.44Hz and is derived using a simple harmonic decomposition. It should be noted that the horizontal acceleration, a_x, is the largest component of the acceleration in beam seas; the roll and sway motions of the vessel contributing to its magnitude. Figure 7.8 illustrates the variation of $|a_x^1|$ with the incident wave frequency and contrasts the motion of the LNG tanker for the GBS-LNG, FLNG-LNG$_E$, FLNG-LNG$_S$ and the LNG-LNG setups; in the latter setup, data being presented for both the externally-moored LNG and the sheltered LNG. In each case, the dashed portion of the frequency range indicates those conditions in which the motion of the vessels was excessive, hindering the successful completion of the experimental run.

Figure 7.8 shows that the largest recorded accelerations arise in the GBS-LNG setup. The explanation for this is thought to lie in the fact that the GBS extends over the entire depth of the water column and therefore, allows no transmission of incident wave energy beneath it. The smallest LNG motion at the low-frequency end of the range occurs in the FLNG-LNG$_E$ setup. Although the LNG is exposed to the incident waves in this setup, it is believed that the motion of the FLNG

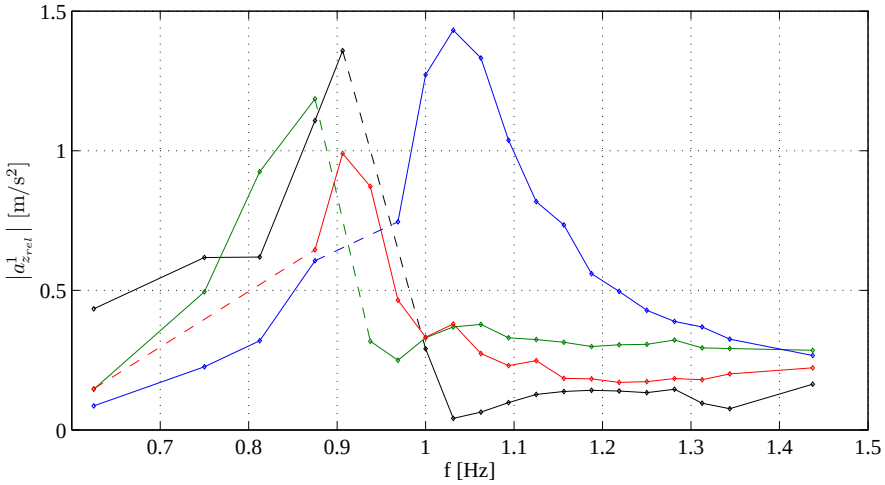


Figure 7.9: Variation with incident wave frequency of the amplitude of the first harmonic of the relative vertical acceleration, $|a^1_{z_{rel}}|$, for regular waves in beam seas; —— GBS-LNG, —— FLNG-LNG$_E$, —— FLNG-LNG$_S$, —— LNG-LNG.

attracts most of the incident wave energy in this low-frequency range not least because its natural roll frequency is low; the latter being 0.77Hz as seen Table 7.1. Indeed, the large FLNG motion at the lower end of the incident wave frequency range prevents these cases from being run for the FLNG-LNG$_S$ setup.

In figure 7.8 the only recorded data lying in the range 0.85Hz < f < 0.95Hz relate to the FLNG-LNG$_S$ setup. This clearly illustrates the sheltering abilities of the FLNG. However, the LNG response occurring at f = 0.906Hz is seen to be larger than that at f = 0.875Hz, indicating the importance of the dynamic amplification factor even when the vessel is sheltered. Furthermore, there is striking similarity between the response of the sheltered LNG for the LNG-LNG and FLNG-LNG$_S$ setups beyond 1.2Hz. This observation shows that the hydrodynamic properties of the sheltering body do not affect its sheltering abilities at high incident wave frequencies. The explanation for this lies in the fact that with increasing incident frequencies, more wave energy will be reflected and this becomes less sensitive to the draft.

Figure 7.9 considers the variation with frequency of the first harmonic amplitude of the relative vertical acceleration, $\left|a^1_{z_{rel}}\right|$, in beam seas; a_z being driven by a

combination of heave and roll. For the GBS-LNG setup, this is equivalent to the vertical acceleration of the LNG because the GBS is fixed, while it is the difference between the vertical accelerations of the two vessels in the remaining setups. For the GBS-LNG and FLNG-LNG$_E$ setups, figure 7.9 shows that the largest relative vertical accelerations occur at the frequency at which the experimental runs become unstable. However, this is not the case for the FLNG-LNG$_S$ and LNG-LNG setups, which have previously been shown to become unstable around the natural roll frequency of the FLNG and the LNG respectively (hydrodynamic properties of the FLNG are given in Table 7.1 and of the LNG in Table 6.1). A further similarity between the FLNG-LNG$_S$ and LNG-LNG setups that can be seen in figure 7.9 is the fact that the largest relative vertical acceleration occurs somewhat above the natural roll frequency of the externally-moored vessel. As described previously in Section 7.2, the FLNG-LNG$_E$ and GBS-LNG setups involve the LNG being exposed to the incident waves, while in the FLNG-LNG$_S$ and LNG-LNG setups the LNG is sheltered. The observations described above suggest that it is with respect to the relative motion (figure 7.9) rather than the motion of the LNG (figure 7.8) that the effect of the LNG being sheltered vs exposed becomes apparent.

In Chapter 6 it was shown that data arising from the incident focused wave events provide a convenient basis on which to consider the occurrence of nonlinear effects. This is a consequence of the fact that the FFT analysis of a focused wave event results in a continuous spectrum of data, unlike the discrete spikes arising from the analysis of a regular wave case. Figure 7.10 presents acceleration data relating to a focused wave event with a peak frequency of f_p = 0.714Hz in beam seas. It should be noted that this peak frequency is close to the natural roll frequency of the FLNG. Within this figure, the spectra illustrate the frequency content of both the horizontal acceleration in x, a_x, and the vertical acceleration, a_z. Subplot (a) relates to the FLNG-LNG$_E$ setup and subplot (b) to the FLNG-LNG$_S$ setup; the two subplots addressing both the LNG and the FLNG motions.

In subplots 7.10(a) and 7.10(b), the response marked (1) denotes the response at the peak frequency; the latter being marked by a dashed vertical line in the

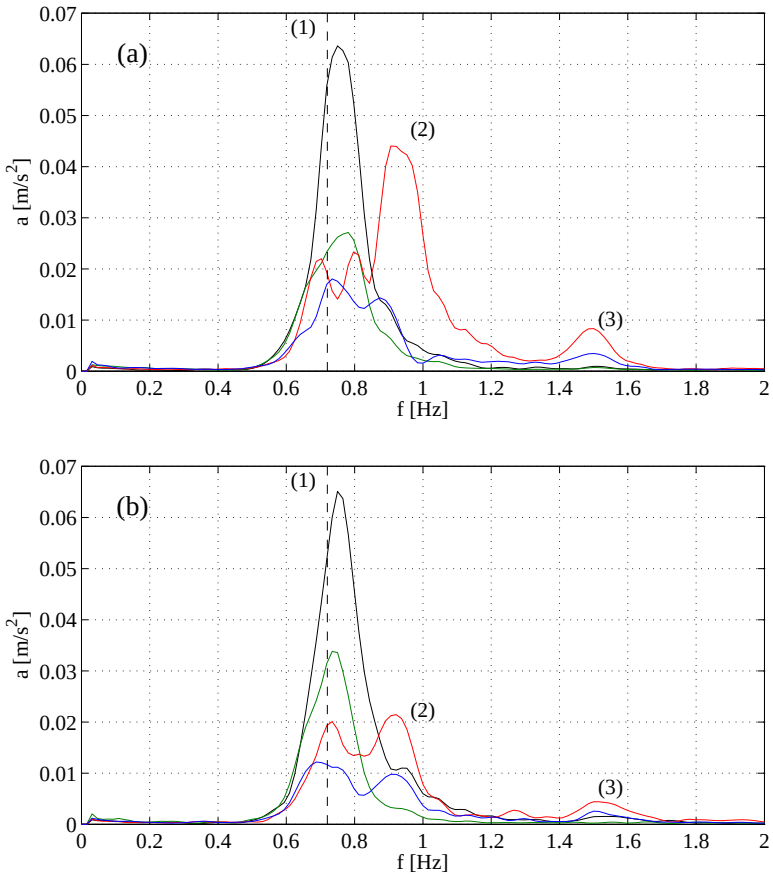


Figure 7.10: Spectra defining the motion of the FLNG and LNG vessels subject to focused waves with a spectral peak frequency for f_p = 0.714Hz in a beam-sea orientation for (a) FLNG-LNG$_E$ and (b) FLNG-LNG$_S$; —— a_x FLNG, —— a_z FLNG, —— a_x LNG, —— a_z LNG

figure. The response at (1) is clearly observed to be larger for the FLNG than the LNG, reflecting the fact that this peak frequency is close to the FLNG natural roll frequency. Beyond this peak frequency response, there is an additional LNG response marked (2), arising at the natural roll frequency of the LNG. The difference in the magnitudes of the LNG response at (1) and (2) is more significant in subplot (a) than in subplot (b). This arises because of the sheltering provided by the FLNG in the FLNG-LNG$_S$ setup. Both these observations are expected. As a result, it is the LNG response at (3) that is most noteworthy; occurring at a frequency close to twice the natural roll frequency of the FLNG.

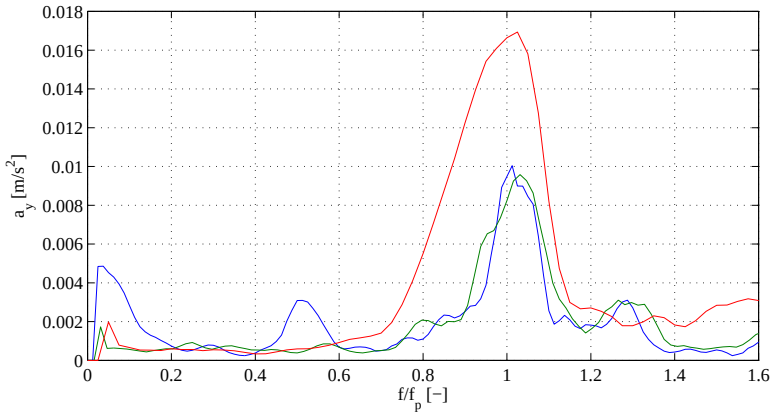


Figure 7.11: Frequency content of the horizontal y acceleration, a_y, of the LNG for the GBS-LNG setup in head-sea focused wave events; —— f_p = 1.25Hz, —— f_p = 1.00Hz, —— f_p = 0.625Hz. The horizontal axis is in terms of the normalised f/f_p.

It should be noted that this LNG response is only observed in the FLNG-LNG$_E$ and FLNG-LNG$_S$ setups at f_p = 0.714Hz. Since this peak frequency is close to the natural roll frequency of the FLNG, it is believed that the LNG response at (3) is the effect of connecting two vessels of varying hydrodynamic properties. At this frequency, the motion of the FLNG controls the tension of the mooring lines and the compression of the fenders (which are attached to it) and hence a component of the forcing on the LNG. The data presented on figure 7.10 suggest that this forcing leads to unexpected higher order LNG motions. This reinforces the need to carefully model the coupled nature of a two vessel system and to incorporate the deformation of the fenders as described in Koo & Kim (2005).

7.4.2 The effect of wave excitation within the gap

The vessel motion considered thus far has illustrated the effect of varying the properties of the second body. This section presents the effect of the wave excitation within the gap on the vessel motion. Due to the large vessel motion in the beam-sea cases, no clear evidence was found to suggest that the resonant wave excitation within the gap leads to any additional vessel motions. However, figure 7.11 considers the GBS-LNG setup in a head-sea orientation and concerns the hor-

izontal acceleration of the LNG in the y-direction, a_y. In a head-sea orientation, this corresponds to a combination of the roll and sway motions with respect to the body axes. The spectra presented in figure 7.11 illustrate the frequency content of a_y for three different focused wave events; the latter defined by spectral peak frequencies of f_p = 1.25Hz, 1.00Hz and 0.625Hz. Direct comparisons between these cases is achieved by normalising the frequency axis and presenting the variation of a_y with f/f_p.

The data presented in figure 7.11 show that the largest response at the peak frequency occurs for f_p = 0.625Hz. More importantly, for f_p = 1.25Hz there is an additional response at half the peak frequency (f/f_p = 0.5); the magnitude of this response being about 30% of the peak frequency response. Furthermore, there is a second additional response at $f/f_p \approx 0$; the magnitude of this response being almost half that of the peak frequency response. Since these additional responses only arise for the case in which the spectral peak frequency is close to the frequency at which there is large wave excitation within the gap, these results are believed to highlight the effects of the wave excitation in the gap and its role in determining (or modifying) the vessel motion.

7.5 Surface elevation in the upwave region

In addition to recording the surface elevation within the gap, data was also recorded over a 4m × 2m area in the upwave region of the FLNG-LNG$_S$ setup for six incident regular wave frequencies. Figure 7.12 defines the orientation of the (x, y) coordinate axes and provides an overview of the location of the wave gauges within this upwave area. As before, the direction of the incident wave propagation is aligned with the positive x-direction, but the origin of the coordinate axes is now set as the *upwave* face of the FLNG. The spacing of the wave gauges in the y-direction is defined as Δy = 100mm; giving 41 sections over the region $-2.0\text{m} \leq y \leq 2.0\text{m}$. In the x-direction, the gauge spacing varies from Δx = 100mm for $-1.0\text{m} \leq x \leq -0.15\text{m}$ to Δx = 200mm for $-2.0\text{m} \leq x \leq -1.0\text{m}$. No measurements

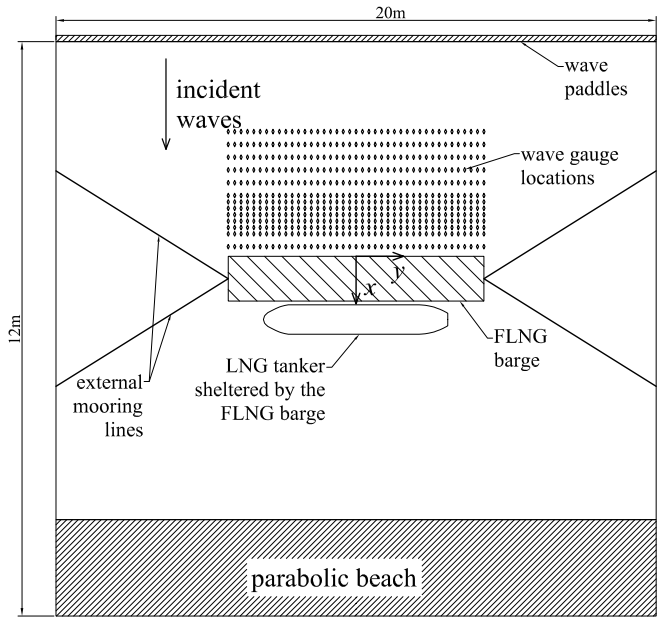


Figure 7.12: Plan view of the FLNG-LNG$_S$ setup showing the area within which measurements of the upwave region were undertaken.

were undertaken within the region $-0.15\text{m} < x \leq 0\text{m}$ to avoid clashes between the moving FLNG and the free-standing wave gauges. The incident wave amplitude considered was A_{inc} = 10mm and the incident wave frequencies varied from f = 0.625Hz to f = 1.44Hz; the corresponding wave lengths being 3.86m and 0.76m respectively. The variation in the spacing of the wave gauges in the x-direction reflects the effort made to capture an appreciable fraction of the longest incident waves, while at the same time capturing enough detail of the shortest wave case. The total number of wave gauge locations within the area depicted in figure 7.12 is 533; the required data assembled from 41 experimental runs. In undertaking these tests, the repeatability of the incident wave conditions was monitored as described in Chapter 5.

Figure 7.13 provides a detailed comparison of the spatial variation in y, or transverse variation, of the amplitude of the first harmonic of the surface elevation, $|\eta^1|$, at three x locations. These locations are positioned within the gap between the two bodies, at $x = -150$mm (which corresponds to the position clos-

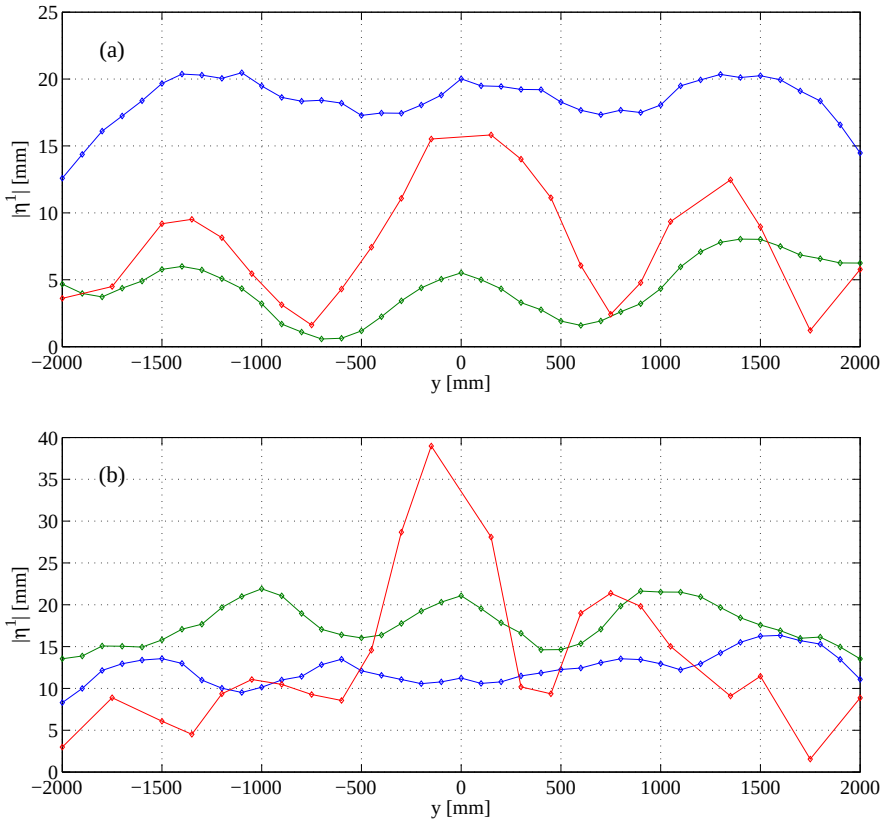


Figure 7.13: Spatial variation of the amplitude of the first harmonic of the surface elevation, $|\eta^1|$, for the FLNG-LNG$_S$ setup in the upwave region and within the gap between the two bodies, (a) f = 1.125Hz and (b) f = 1.31Hz; —— x = −150mm, —— x = −950mm, —— within the gap.

est to the FLNG) and at x = −950mm. In considering these data, it should be noted that for the data relating to the x = −150mm and x = −950mm sections, the spatial variation is made up of one y value per experimental run; the continuous nature of the data confirming the repeatability of the experimental runs. Figure 7.13 includes two subplots; each considering a different incident wave frequency.

For an incident wave frequency of f = 1.125Hz, subplot (a), the x = −150mm section corresponds to the position of an antinode in the upwave region and consequently $|\eta^1|$ is close to 20mm or $2A_{inc}$. In contrast, the x = −950mm section is close to a nodal position and $|\eta^1|$ is much reduced. At both of these locations the transverse variation in $|\eta^1|$ exhibits three peaks that are approximately of equal

magnitude. Interestingly, the transverse variation within the gap also has three peaks. However, in this case the magnitude of the central peak, the amidships peak, is approximately 30% larger than those on either side.

A more significant amplification within the gap at the amidships is apparent in subplot (b). These data relate to an incident wave frequency of f = 1.31Hz, which is close to the frequency at which resonant amplification of $|\eta^1|$ occurs within the gap for the FLNG-LNG$_S$ setup. In contrast, the x = −950mm location (which corresponds to the largest recorded antinode within the upwave region) shows three peaks of equal magnitude along the 4m length. In making these comparisons, it is clear that the large wave excitation over the amidships section, first introduced in Section 7.3, is a result of the unique hydrodynamics within the gap.

Figure 7.14 concerns the spatial (x, y) variation of $|\eta^1|$ over the entire area depicted in figure 7.12, as well as within the gap between the two vessels. This is described using coloured contour lines, the values of $|\eta^1|$ being defined on the colourbar adjacent to each subplot. A total of six subplots are presented, one for each of the six incident wave frequencies considered. Previously, subplot 7.13(b) indicated that the resonant wave excitation is specific to the gap. As a result, the extent of the colourbars within figure 7.14 is determined by the largest magnitude within the upwave region and not within the gap. Accordingly, the deep red colour visible within the gap of subplots (e) and (f) indicates that the amplification here greatly surpasses that within the upwave region. Finally, the position of the FLNG and the LNG vessels is superimposed for reference within each subplot. Although the length of the vessels is correctly scaled, their beams are distorted in x in order to facilitate the presentation of the data.

Comparisons between the subplots of figure 7.14 clearly show that the amplification within the upwave region is smallest for the longest incident wave case in subplot (a) and increases with frequency through subplots (b), (c) and (d). Beyond this point, the amplification remains fairly constant. This increase in amplification arises due to the combination of two factors; the decrease in the FLNG motion and, perhaps more importantly, a decrease in the wave energy transmitted

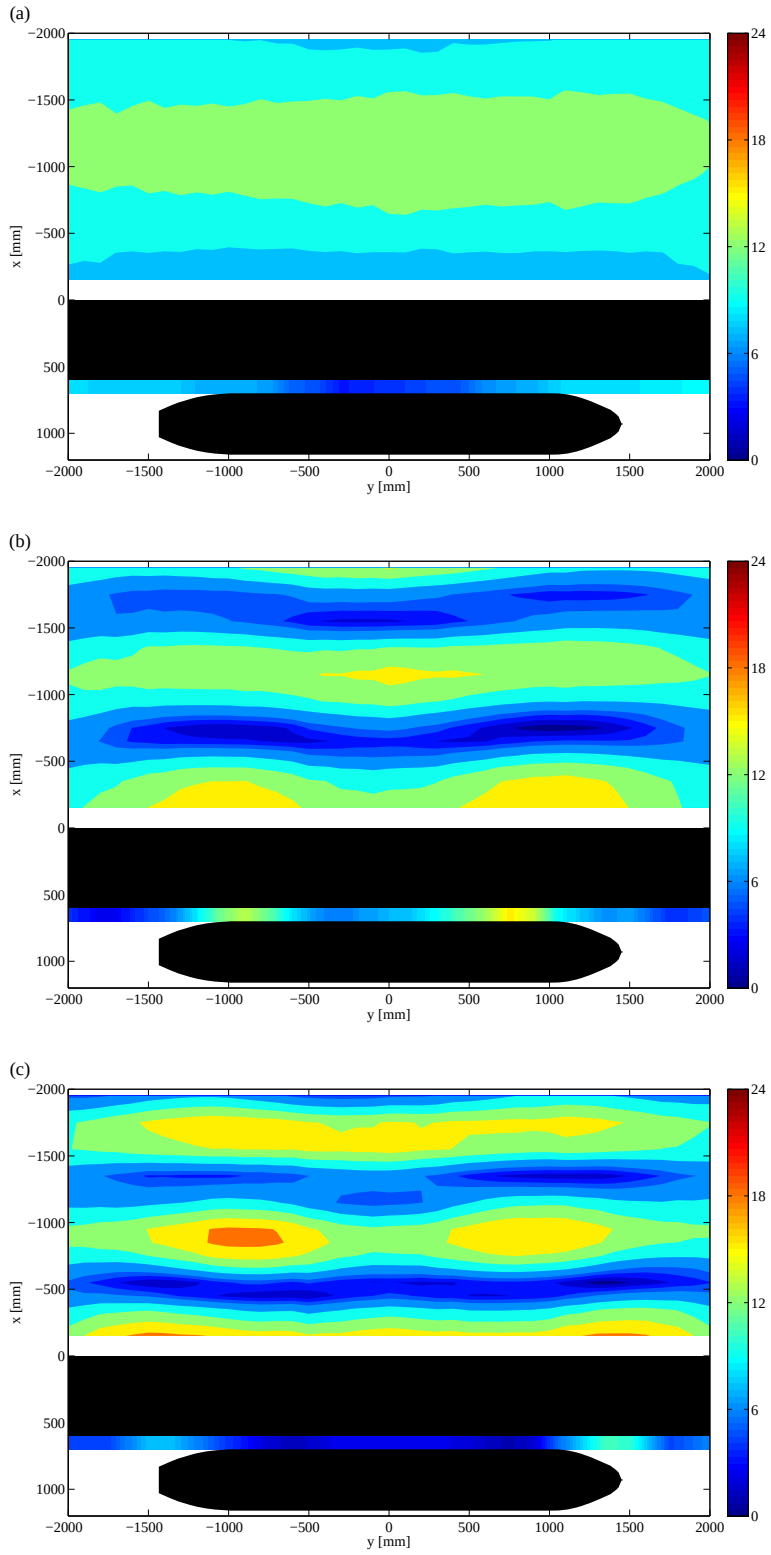


Figure 7.14: Contours of the amplitude of the first harmonic of the surface elevation, $|\eta^1|$, within the upwave area identified in figure 7.12 and in the gap; (a) f = 0.625Hz, (b) f = 0.906Hz, (c) f = 1.000Hz, (d) f = 1.125Hz, (e) f = 1.313Hz and (f) f = 1.438Hz.

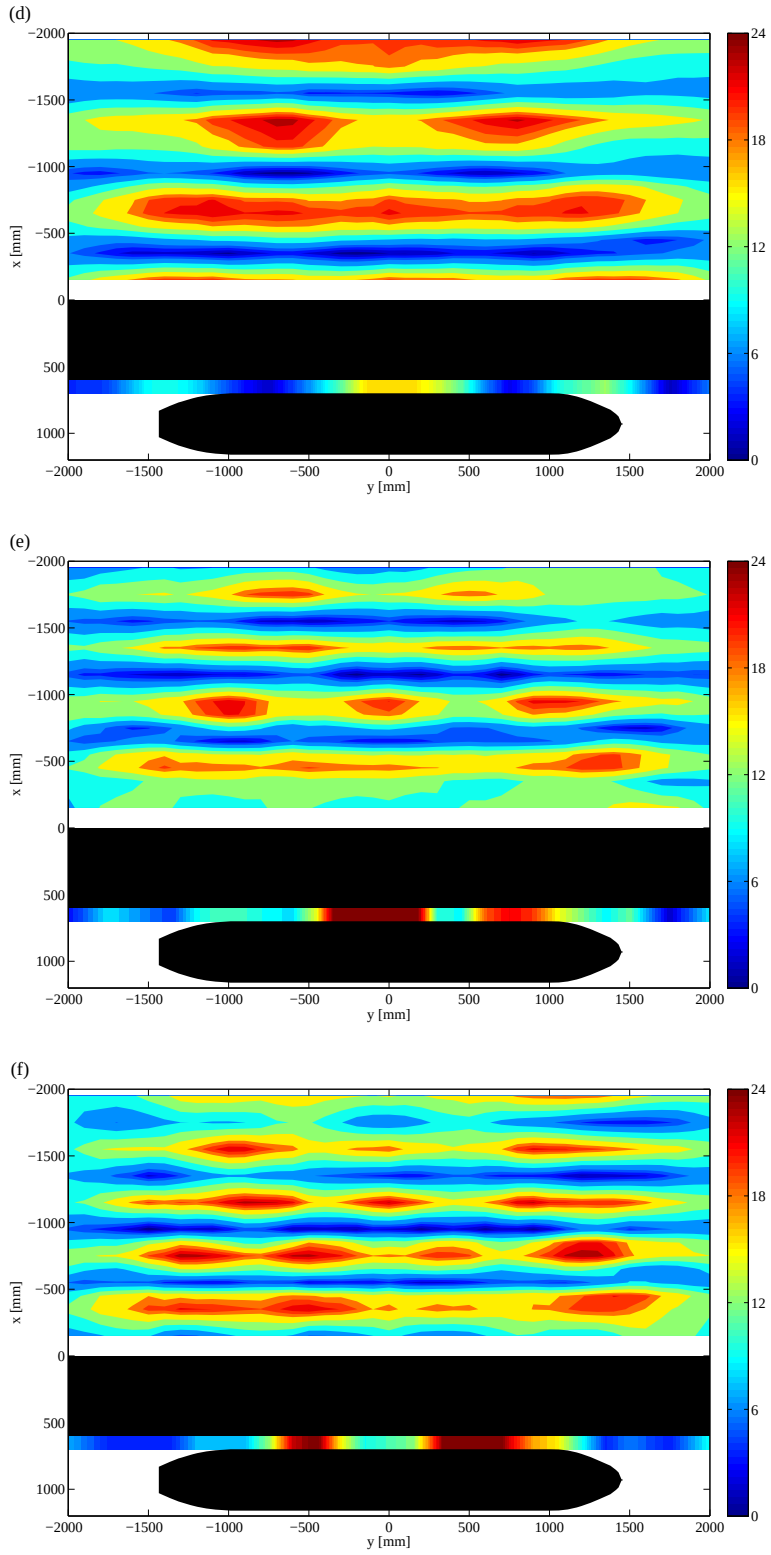


Figure 7.14: (Continued) Contours of the amplitude of the first harmonic of the surface elevation, $|\eta^1|$, within the upwave area identified in figure 7.12; (a) f = 0.625Hz, (b) f = 0.906Hz, (c) f = 1.000Hz, (d) f = 1.125Hz, (e) f = 1.313Hz and (f) f = 1.438Hz.

beneath the FLNG. Despite the appreciable FLNG motion in the long wave cases of subplots (a) and (b), the transverse variation of the upwave region displays similar trends to those shown in Chapter 5. In particular, with an increasing incident wave frequency there is an increase in the number of local maxima along the length of the antinode in the upwave field and this number decreases with distance from the FLNG.

Finally, it is interesting to note that the first recorded antinode at $x = -450$mm and $x = -350$mm in subplots (e) and (f) respectively has a poorly defined transverse variation when compared to the adjacent or second line of antinodes. One possible explanation for this is the presence of the large wave excitation within the gap at these incident wave frequencies. This is indicated by the dark red contours and suggests that the large wave excitation within the gap causes a disturbance to the upwave region close to the FLNG. This is an important result which is consistent with earlier observations made in Chapter 4.

7.6 Conclusions

This chapter has considered several practical alternatives to side-by-side offloading, in which an LNG tanker was moored alongside a fixed Gravity Based Structure (GBS), a floating LNG barge (FLNG) and a second LNG tanker. In each case observations described the spatial variation of the surface elevation both within the gap between the two bodies and in the upwave region. In addition, data describing the vessel motions were also described. With regard to the data describing the surface elevation within the gap, the conclusions drawn in the previous chapter have been shown to be valid for the alternative side-by-side offloading arrangements. This suggests that the incident wave frequency remains the most significant factor controlling the excitation of the fluid within the gap, irrespective of the characteristics of the second body.

With regard to the vessel motion, it was found that the largest LNG motion arises when the tanker was moored alongside the fixed GBS. When moored along-

side the FLNG in a sheltered configuration (FLNG-LNG$_S$), the largest LNG motions were reduced by as much as 50%. However, unexpected higher order motions of the LNG were observed in those setups where the hydrodynamic properties of the two floating bodies differ significantly (FLNG-LNG$_E$ and FLNG-LNG$_S$). Finally, evidence has also been provided to suggest that the large wave excitation within the gap leads to unexpected low frequency motions of the LNG for the GBS-LNG setup in head seas.

Within this chapter, many parallels have been drawn to results presented in previous chapters. The final chapter describes how the full range of results provided in the thesis tie together to provide the fundamentals of the wave interactions with multiple bodies in close proximity.

8

Concluding remarks

8.1 Introduction

The aim of this thesis has been to establish a basic understanding of the nonlinear interaction of waves with multiple bodies in close proximity; the work being directly applicable to the side-by-side offloading of Liquid Natural Gas (LNG). This has been achieved through two-dimensional (2D) and three-dimensional (3D) numerical analysis and experimental studies. The present chapter summaries both the work undertaken and the major conclusions. It ends with proposals of future work.

8.2 Work undertaken

The 2D numerical work included the development of a model that can predict the fully nonlinear interactions of waves with floating bodies. This involved the incorporation of the Indirect Method (Wu & Eatock-Taylor 1996) into the 2D multiple-flux Boundary Element Method (BEM) originally outlined by Hague (2006) and Christou (2009). The resulting model describes the total velocity potential, simultaneously accounting for the effects of

(i) the incident potential, describing the incoming wave conditions,

(ii) the scattered potential, due to the presence of the physical bodies, and

(iii) the radiated potential, due to the motion of these bodies.

The model's prediction of the interaction of (i) with (ii) has been validated by considering the wave-induced force on a fixed body. The validation of (iii) has included both the wave field generated by the prescribed motion of the body and the decay of a body's response to an initial displacement. Finally, the interaction of (i), (ii) and (iii) has been validated through the problem of the wave-induced motion of a body in regular waves.

Following a full validation, the 2D numerical model was applied to the study of two fixed bodies in close proximity. In considering this problem, the calculations have sought to investigate the importance of: the incident wave frequency, the gap width (or spacing between the two fixed bodies), the beam of the upwave body, the draft of the upwave and of the downwave body and the heave motion of one of the bodies. However, before the conclusions arising from this 2D analysis can be applied with any conviction to the problem of side-by-side offloading, the effect of the finite length of the bodies must also be ascertained. This latter task was undertaken using the separately-developed 3D multiple-flux BEM model.

The work involving this 3D numerical model represents the first application of this model to simulations involving fixed bodies. As a result, some initial validation was required. This concerned the wave field surrounding a semi-infinite breakwater and that upwave of a bottom-mounted Gravity Based Structure (GBS); comparisons with both available solutions and laboratory data confirming the accuracy of the model implementation. The subsequent 3D analysis involving various single fixed bodies was undertaken to illustrate the effect of the body length, width and draft on the spatial variation of the surrounding wave field. Finally, the effect of a second fixed body in close proximity to the first was also considered.

The 3D experimental work began with a study involving a fixed box-like approximation to an LNG tanker in close proximity to a GBS. Further studies involved scale models of an LNG tanker and a floating LNG barge (FLNG). The

inter-comparison of the various experimental setups sought to determine the effect of varying the physical and hydrodynamic properties of the bodies involved.

8.3 Physical insights

The conventional approach to predicting wave-induced motion involves using forces obtained from a fixed-body analysis, together with constant values of the body's hydrodynamic coefficients calculated from a decay test. The validation of the new 2D numerical model showed that it can predict the forces on a fixed body as well as the response of a body in a decay test. As a result, the conventional approach was applied on the numerical results to predict the linear wave-induced motion of a single LNG and of an LNG in close proximity to a GBS. In the case of the single LNG, it was found that the conventional approach provides a reasonable estimate of the motion of the LNG. However, this was not the case for the LNG in close proximity to a GBS. The explanation for this lies in the fact that while the radiated potential can be neglected in the estimation of the motion of a single body, it must be incorporated into the analysis of a problem involving two bodies in close proximity.

In the 2D numerical analysis of fixed bodies in close proximity, large amplification of the first harmonic of the water surface elevation, $|\eta^1|$, was observed within the gap at the so-called resonance frequency. The 3D experimental study of a similar setup involving fixed bodies illustrated that the resonance frequency of the fluid within the 3D gap is similar to that of the 2D gap. However, the variation of $|\eta^1|$ with frequency within the 3D gap exhibits multiple peaks beyond this resonance frequency. These peaks were not reproduced in the 2D numerical analysis, suggesting they are the result of effects in the transverse (y) direction. The data obtained from the 3D numerical analysis of two fixed bodies in close proximity provided the explanation for this observation. Specifically, these calculations showed that the occurrence of resonance within the gap is fundamentally an inline process. However, at higher incident wave frequencies, transverse effects

dominate.

The resonance frequency has been found to be dependent on the gap width; an increase in the gap width acting to decrease the resonance frequency. This effect was seen in both the 2D numerical data and the 3D experimental studies. Furthermore, both sets of analysis illustrated that when comparing a problem that involves two fixed bodies in close proximity with one that involves a floating body in close proximity to a fixed body, the resonance frequency is higher in the latter case. Finally, the 2D and the 3D analysis have both shown that there is large amplification of the fluid motion within the gap at the resonance frequency, irrespective of whether this motion is of the first or of the second harmonic. As a result, although the incident wave conditions may be linear, the excitation of the fluid in the gap may incorporate important nonlinear components. It is therefore important to be able to model the complex nature of this nonlinearity.

The consideration of various 3D experimental setups, involving the LNG tanker in alternative side-by-side arrangements, has illustrated that neither the orientation of wave attack (beam seas vs head seas) nor the characteristics of the second body (physical or hydrodynamic properties) have a significant effect on the resonance frequency. However, evidence has been provided to suggest that when the LNG tanker is moored to the FLNG (a body with different hydrodynamic properties), it undergoes unexpected higher order motion. The nature of this excitation is such that it cannot be described by existing design procedures.

8.4 Further work

The work presented within this thesis has involved both numerical modelling and experimental observations and has provided practical insights into the problem of the side-by-side offloading of LNG. Accordingly, the suggestions for further work, outlined below, address these three aspects of the work, concluding with a final section describing wider applications of the tools developed.

8.4.1 Numerical modelling

The present 2D numerical studies have concentrated on the effects of the body motion in heave only, with some consideration of the pitch motion for a single body. An obvious next step in an ongoing study would be to consider the effects of the pitch motion of a body in close proximity to a second fixed body. The reason for this is that the pitch only motion and the heave only motion of a single body have been shown in Chapter 3 to produce very different effects, for both forced and wave-induced motions. Subsequent work should also consider the third (and final) degree of freedom. This would involve the surge motion (horizontal translation) and therefore, the incorporation of the necessary restriction to this motion mode by modelling the effects of mooring lines and fenders.

Having considered the three degrees of freedom (in 2D) individually, further work should consider a body responding in multiple modes. The resulting effects would be due to the coupling of the motion and the potential nonlinear interactions, and should include the wave excitation within the gap as well as the motion of the body. Finally, different configurations should be considered; including two bodies with very different hydrodynamic properties. The latter would be interesting not least because this case has been shown to lead to unexpected higher order motion of the moored body in Chapter 7.

In terms of the 3D modelling, the calculations are currently limited to fixed bodies. Additional development of the 3D BEM model should begin with the calculation of the force on a single body; the present 2D work having shown how this can best be achieved. Subsequently, the 3D model should be extended to predict wave-induced body motions; first with a single degree of freedom and then multiple degrees. Further development would involve the introduction of multiple bodies in close proximity and the appropriate moorings between them. In this case, the aspect ratio of the gap between the two bodies (long but narrow) leads to a very large node density within the gap and difficult resolution issues. As a result, the 3D BEM model would benefit from the introduction of alternative element shapes.

It should be noted that the validation of the model over these suggested stages of development is essential and should be based on quantitative comparisons to diffraction-radiation codes (WAMIT, for example) and experimental observations.

For the case of multiple bodies in close proximity, the new 3D BEM model could be used to address the issues of directional seas and the effect of the incident wave orientation relative to the vessels. Although some aspects of the wave excitation within the gap have been shown to be independent of orientation, careful consideration of the latter is required to fully understand the effects. Particular attention should be paid to the vessel motion in terms of the coupling between multiple motion modes and the relative motion of the bodies. Furthermore, the effect of weathervaning of the externally moored vessel must also be investigated.

Finally, any further numerical modelling must address the importance of viscous effects. For example, comparisons between the 3D BEM model and full CFD (Computational Fluid Dynamics) codes could be undertaken; the purpose being to assess the influence of the fluid viscosity in respect of both the wave excitation and the vessel motions. As a result, a view could be taken on the cost vs benefit of committing to full CFD calculations. In particular, the role of the roll damping must be investigated and possiblility of incorporating a hybrid model explored.

8.4.2 Experimental studies

Within the present work, the emphasis of the experimental studies has been the wave excitation within the gap. Building on this basis, future experimental studies should focus on the motion of the vessels. In addition, the measurement of the forces in the mooring lines and the fenders should be undertaken. As before, the aim would be to establish a fundamental understanding of the interactions involved and how they influence the relative motion of the bodies. Furthermore, directionally-spread incident wave cases should be considered and the second vessel should be turret-moored; the latter allowing it to weathervane with the possible incorporation of slow drift motions.

A separate, but equally important, aspect to the problem of side-by-side offloading is the vessel approach. The work in Chapter 5 has illustrated that the wave field surrounding a single body may be very different to the incident wave conditions. Indeed, the assessment of an adequate weather window must take into account both the side-by-side offloading conditions and the vessel approach/departure. The latter effect must be considered not least because the manoeuvring operation is widely regarded as being the most troublesome aspect of the offloading operation. Finally, any future laboratory study must also incorporate the effects of the wind and the currents acting simultaneously with the waves.

8.4.3 Practical guidance

The work presented herein has identified the gap width as a key factor in determining the wave excitation within the gap. The spacing between the two vessels in side-by-side offloading is more than an order of magnitude smaller than that adopted in tandem offloading; the latter, the preferred option for oil offloading; involving the connection of the transport vessel's bow to the stern of the floating barge. In the context of LNG, tandem offloading cannot be considered a practical solution in the medium term. This is due to the need to support the cryogenic hoses above the water surface. Given these difficulties, it would be interesting to determine the benefits of a larger gap width in side-by-side offloading operations; the intention being to propose an optimal mooring and fender arrangement. Furthermore, if this arrangement were flexible, forecast met ocean conditions could be used to determine the spacing of the vessels that would lead to the safest conditions. For example, the moored vessel could be positioned at the frequently occurring nodal points in the upwave field; thereby minimising its heave motion.

8.4.4 Wider applications

Beyond the specific application to side-by-side offloading, the developed numerical models could be used to investigate a wide range of problems. An obvious candidate would involve the study of nonlinear wave-structure interactions. Within this practically important category of problems, topical issues include:

(i) The optimal design of 3D wave makers, a key point being the nonlinear effects arising in shallow water wave generation. Such problems are fundamental to the generation of a desired sea state and hence impact all physical model testing.

(ii) The evaluation of the forces on a single body in extreme seas. Earlier work has indicated both unexpected high-frequency wave scattering (Sheikh & Swan 2005) and associated fluid loading (Masterton 2007). The dynamics that result from such effects are commonly referred to as 'springing' in the case of a Tensioned Leg Platform (TLP) and 'ringing' in a Gravity Based Structure (GBS). In both cases, practically important effects could be understood and predicted using appropriate numerical solutions.

(iii) The introduction of the forward speed of a vessel, allowing the development of a fully nonlinear ship load model.

In considering these applications, the key issues are centered around the modelling of the largest most nonlinear waves and the need to undertake long random simulations; the latter being neccessary to derive the statistics of a particular occurrence. Unfortunately, both requirements are at present limited to the necessary computational effort; the efficiency of the numerical implementation being fundamental to a successful application.

9

Appendices

Appendix A. Linear wave maker theory

The first order solution of the velocity potential in wave maker theory is

$$\phi = \frac{1}{2}\left(\frac{igX_a}{\omega}\sum_{s=0}^{\infty} c_s \frac{\cosh k_s\left(z+h\right)}{\cosh k_s h} e^{i(\omega t - k_s x)} + c.cc\right), \tag{A.1}$$

where

$$c_j = \sinh k_s h \frac{\Lambda_1\left(k_s\right)}{\Lambda_2\left(k_s\right)}, \tag{A.2}$$

and

$$\begin{aligned} \Lambda_1\left(k_s\right) &= \sinh k_s h - \tfrac{d+l}{h+l}\sinh k_s d + \tfrac{1}{h+l}\tfrac{\cosh k_s d - \cosh k_s h}{k_s}, \\ \Lambda_2\left(k_s\right) &= \frac{1}{2}\left(k_s h + \sinh k_s h \cosh k_s h\right), \end{aligned} \tag{A.3}$$

where d and l are used to define the geometry of the wave maker; for the purposes of a flap-type, bottom-hinged wave maker both d and l are equal to zero.

The first order force is given by

$$\mathbf{F} = -\rho \int_{\Gamma_b} \phi_t \mathbf{n} \mathrm{d}\Gamma. \tag{A.4}$$

Equation A.4 is useful only for numerical analysis where the components of $\mathbf{n}$ are given in equation 2.11 and the integration is carried out using weighting functions. For the analytical solution, however, each force component must be considered

separately. The horizontal force, F_1, is

$$\begin{aligned} F_1 &= -\rho \int_{z=-h}^{0} \phi_t \mathrm{d}z \\ &= \frac{\rho}{2}\left(\frac{gX_a}{k} \sum_{s=0}^{\infty} c_s \frac{\sinh k_s\left(z+h\right)}{\cosh k_s h} e^{i(\omega t - k_s x)} + c.c. \right). \end{aligned} \tag{A.5}$$

The vertical force, F_2, is the only present in the numerical model and is equal to the weight of the displaced fluid as the wave maker moves. Its magnitude is

$$|F_2| = \frac{\rho g X_a h}{2}. \tag{A.6}$$

F_2 does not have an equivalent in the analytical theory because the analytical wave maker boundary does not move as was discussed in Section 2.3.3.

The moment about the wave maker hinge, F_3, is given by Spinneken & Swan's (2009) as

$$\begin{aligned} F_3 &= T \\ &= -\rho \int_{z=-h}^{0} \phi_t \left(h - d + z\right) \mathrm{d}z \\ &= \frac{1}{2}\left(\rho g X_a \sum_{s=0}^{\infty} \frac{c_s}{k_s^2} \Gamma_1(k_s) e^{i\omega t} + c.c. \right), \end{aligned} \tag{A.7}$$

where

$$\Gamma_1(k_s) = \frac{k_s\left(h-d\right)\sinh k_s h - \cosh k_s h + \cosh k_s d}{\cosh k_s h} \tag{A.8}$$

Appendix B. The Isaacson Method

Newton's Second Law is given as

$$\begin{aligned} m_j a_j &= F_j \\ &= \int_{\Gamma_b} p n_j \mathrm{d}\Gamma \\ &= \int_{\Gamma_b} -\rho \left[gz + \phi_t + \frac{1}{2} \left(\nabla \phi \right)^2 \right] n_j \mathrm{d}\Gamma \end{aligned} \tag{A.9}$$

Recalling that the chain rule gives

$$\frac{d\phi}{dt} n_j = \frac{d\left(\phi n_j\right)}{dt} - \phi \frac{dn_j}{dt}, \tag{A.10}$$

the substitution of equation A.10 into equation A.9 gives

$$m_j a_j = -\rho \int_{\Gamma_b} \left[gz + \frac{1}{2} \left(\nabla \phi \right)^2 \right] n_i - \rho \int_{\Gamma_b} \frac{d}{dt} \left(\phi n_i \right) + \rho \int_{\Gamma_b} \phi \frac{dn_i}{dt}. \tag{A.11}$$

Further,

$$m_j a_j + \int_{\Gamma_b} \left(\rho \frac{d\left(\phi n_j\right)}{dt} \right) \mathrm{d}\Gamma = \int_{\Gamma_b} \left[\rho \phi \frac{dn_j}{dt} - \rho \left(gz + \frac{1}{2} \left(u^2 + w^2 \right) \right) n_j \right] \mathrm{d}\Gamma, \tag{A.12}$$

$$\left(m_j v_j + \rho \int_{\Gamma_b} \phi n_j \mathrm{d}\Gamma \right)_{t_0 + \Delta t} = H_j, \tag{A.13}$$

where

$$H_j = \left(m_j v_j + \rho \int_{\Gamma_b} \phi n_j \mathrm{d}\Gamma \right)_{t_0} + \frac{\Delta t}{6} \left[\left(h_j \right)_{t_0} + 2 \left(h_j \right)^{(1)}_{t_0 + \Delta t/2} + 2 \left(h_j \right)^{2}_{t_0 + \Delta t/2} + \left(h_j \right)^{(3)}_{t_0 + \Delta t} \right] \tag{A.14}$$

$$h_j = \int_{\Gamma_b} \left[\rho \phi \frac{dn_j}{dt} - \rho \left(gz + \frac{1}{2} \left(u^2 + w^2 \right) \right) n_j \right] \mathrm{d}\Gamma. \tag{A.15}$$

Equation A.13 is used as the expression for v_j, which is used to give the body boundary condition in ϕ as

$$\begin{aligned} \left(\frac{\partial \phi}{\partial n} \right)_{t_0 + \Delta t} &= \sum_{j=1}^{3} n_j \left(v_j \right)_{t_0 + \Delta t} \\ &= \sum_{j=1}^{3} n_j \frac{H_j}{m_j} - \sum_{j=1}^{3} \frac{\rho}{m_j} n_j \int_{\Gamma_b} \left(\phi n_j \right)_{t_0 + \Delta t} \mathrm{d}\Gamma \end{aligned} \tag{A.16}$$

Substituting this body boundary condition into the Boundary Integral Equation term over Γ_b

$$\begin{aligned}\int_{\Gamma_b}\left\{G\frac{\partial\phi}{\partial n}-\frac{\partial G}{\partial n}\phi\right\}\mathrm{d}\Gamma &= \int_{\Gamma_b}\left\{G\left(\sum_{j=1}^{3}n_j\frac{H_j}{m_j}-\sum_{j=1}^{3}\frac{\rho}{m_j}n_j\int_{\Gamma_b}\phi n_j\mathrm{d}\Gamma\right)-\frac{\partial G}{\partial n}\phi\right\}\mathrm{d}\Gamma \\ &= \int_{\Gamma_b}\left\{G\sum_{j=1}^{3}n_j\frac{H_j}{m_j}-G\sum_{j=1}^{3}\frac{\rho}{m_j}n_j\int_{\Gamma_b}\phi n_j\mathrm{d}\Gamma-\frac{\partial G}{\partial n}\phi\right\}\mathrm{d}\Gamma\end{aligned} \tag{A.17}$$

Consideration of the above equation shows that the first term is known, while the second and third terms are in terms of ϕ and therefore unknown. Note the double integral in the second term. As there are two terms expressed in terms of ϕ, the elements of the influence matrix, $\mathbf{A}$, and of the known matrix, $\mathbf{b}$, regarding the moving body are

$$A_{pq}=\int\left(\frac{\partial G}{\partial n}\right)_{pq}\mathrm{d}q-\sum_{l=N_s+1}^{N_b}\left(\frac{\partial G}{\partial n}\right)_{pl}\sum_{j=1}^{3}\frac{\rho}{m_j}\left(n_j\right)_l\int\left(n_j\right)_q\mathrm{d}q\quad q=1,...,N_b \tag{A.18}$$

$$b_p=\sum_{q=1}^{N_b}\int G_{pq}\mathrm{d}q\sum_{j=1}^{3}\left(n_j\right)_q\frac{H_j}{m_j}. \tag{A.19}$$

The summation over l in the expression for A_{pq} in equation A.18 represents the second integral of the double integral noted in equation A.17; being expressed as a sum for clarity purposes.

Appendix C. Acceleration potential

The expression for the velocity of a fluid particle on the surface of a moving body

$$\mathbf{u} = \mathbf{v_0} + \boldsymbol{\omega} \times \mathbf{x}' + [\mathbf{v}], \tag{A.20}$$

which, recalling that $\mathbf{u} = \nabla\phi$, gives

$$[\mathbf{v}] = \nabla\phi - \mathbf{v_0} - \boldsymbol{\omega} \times \mathbf{x}'. \tag{A.21}$$

The acceleration of the same fluid is

$$\mathbf{a} = \mathbf{a_0} + \dot{\boldsymbol{\omega}} \times \mathbf{x}' + \boldsymbol{\omega} \times (\boldsymbol{\omega} \times \mathbf{x}') + [\mathbf{a}] + \mathbf{2}\boldsymbol{\omega} \times [\mathbf{v}], \tag{A.22}$$

The full expression of the complex vector product terms in equation A.22 is as follows

$$\begin{aligned} \boldsymbol{\omega} \times (\boldsymbol{\omega} \times \mathbf{x}') = {} & (\omega_y\omega_x y' - \omega_y^2 x' - \omega_z^2 x' + \omega_z\omega_x z')i \\ & + (\omega_z\omega_y z' - \omega_z^2 y' - \omega_x^2 y' + \omega_x\omega_y x')j \\ & + (\omega_x\omega_z x' - \omega_x^2 z' - \omega_y^2 z' + \omega_y\omega_z y')k, \end{aligned} \tag{A.23}$$

$$\begin{aligned} 2\boldsymbol{\omega} \times [\mathbf{v}] &= 2\boldsymbol{\omega} \times (\nabla\phi - \mathbf{v_0} - \boldsymbol{\omega} \times \mathbf{x}') \\ &= \begin{vmatrix} i & j & k \\ 2\omega_x & 2\omega_y & 2\omega_z \\ \frac{\partial\phi}{\partial x} - v_{0x} - \omega_y z' + \omega_z y' & \frac{\partial\phi}{\partial y} - v_{0y} + \omega_x z' - \omega_z x' & \frac{\partial\phi}{\partial z} - v_{0z} - \omega_x y' + \omega_y x' \end{vmatrix} \\ &= \left[2\omega_y\left(\frac{\partial\phi}{\partial z} - v_{0z} - \omega_x y' + \omega_y x'\right) - 2\omega_z\left(\frac{\partial\phi}{\partial y} - v_{0y} - \omega_x z' + \omega_z x'\right)\right] i \\ &\quad + \left[2\omega_z\left(\frac{\partial\phi}{\partial x} - v_{0x} - \omega_y z' + \omega_z y'\right) - 2\omega_x\left(\frac{\partial\phi}{\partial z} - v_{0z} - \omega_x y' + \omega_y x'\right)\right] j \\ &\quad + \left[2\omega_x\left(\frac{\partial\phi}{\partial y} - v_{0y} - \omega_x z' + \omega_z x'\right) - 2\omega_y\left(\frac{\partial\phi}{\partial x} - v_{0x} - \omega_y z' + \omega_z y'\right)\right] k, \end{aligned} \tag{A.24}$$

where (i, j, k) is the unit vector is (x, y, z). In 2D analysis, $(\omega_x, \omega_y, \omega_z) = (0, 0, \xi_3)$; $(v_{0x}, v_{0y}, v_{0z}) = (\xi_1, \xi_2, 0)$; $\left(\frac{\partial\phi}{\partial x}, \frac{\partial\phi}{\partial y}, \frac{\partial\phi}{\partial z}\right) = (u, v, w)$. Therefore, equations A.23 and A.24 are simplified to

$$\boldsymbol{\omega} \times (\boldsymbol{\omega} \times \mathbf{x}') = -\left(\xi_3^2 x'\right) i - \left(\xi_3^2 z'\right) j \tag{A.25}$$

and

$$2\boldsymbol{\omega} \times [\mathbf{v}] = [2\xi_3 (w - \xi_2 + \xi_3 x')]\, i - [2\xi_3 (u - \xi_1 - \xi_3 z')]\, j \tag{A.26}$$

respectively. In the Boundary Value Problem (BVP) in terms of the acceleration potential, Φ, the moving body boundary condition is $\frac{\partial \Phi}{\partial n} = \mathbf{a} \cdot \mathbf{N}$, where (using equations A.22, A.25, A.26)

$$\mathbf{a} \cdot \mathbf{N} = \sum_{j=1}^{3} a_j n_j + n_1 \left[\xi_3^2 x' - 2\xi_3 \left(w - \dot{\xi}_2\right)\right] + n_2 \left[\xi_3^2 z' + 2\xi_3 \left(u - \dot{\xi}_1\right)\right] \tag{A.27}$$

However, because Φ does not satisfy Laplace, the BVP must be in terms of ϕ_t. Therefore, in order to derive the moving body boundary condition for the ϕ_t BVP, the expression of $\frac{\partial}{\partial n}\left(\frac{\nabla^2 \phi}{2}\right)$ must be defined. Instead of considering the Cartesian (x, y, z), consider the polar (r, θ). Tanizawa (1995) defines

$$\frac{\partial}{\partial r}\left(\frac{\nabla^2 \phi}{2}\right) = \frac{\partial \phi}{\partial r}\frac{\partial^2 \phi}{\partial r^2} + \frac{\partial \phi}{r \partial \theta}\left(-\frac{1}{r}\frac{\partial \phi}{r \partial \theta} + \frac{1}{r}\frac{\partial^2 \phi}{\partial r \partial \theta}\right) \tag{A.28}$$

Recalling that Laplace in polar coordinates is expressed as

$$\frac{\partial^2 \phi}{\partial r^2} + \frac{1}{r}\frac{\partial \phi}{\partial r} + \frac{1}{r^2}\frac{\partial^2 \phi}{\partial \theta^2} = 0, \tag{A.29}$$

it follows that equation A.28 becomes

$$\frac{\partial}{\partial r}\left(\frac{\nabla^2 \phi}{2}\right) = -\frac{1}{r}\left[\left(\frac{\partial \phi}{\partial r}\right)^2 + \left(\frac{\partial \phi}{r \partial \theta}\right)^2\right] + \frac{\partial \phi}{\partial r}\left(-\frac{\partial^2 \phi}{r^2 \partial \theta^2}\right) + \frac{\partial \phi}{r \partial \theta}\frac{\partial}{r \partial \theta}\left(\frac{\partial \phi}{\partial r}\right) \tag{A.30}$$

Further,

$$\frac{\partial}{\partial r} \equiv \frac{\partial}{\partial n}, \quad \frac{\partial}{r \partial \theta} \equiv \frac{\partial}{\partial s}, \quad \frac{1}{r} \equiv k_n \equiv 0, \tag{A.31}$$

where k_n is the local curvature of the body and equal to zero everywhere for a rectangular body. Substituting the equivalent terms from equation A.31 into equation A.30 gives

$$\frac{\partial}{\partial n}\left(\frac{\nabla^2 \phi}{2}\right) = \frac{\partial \phi}{\partial n}\left(-\frac{\partial^2 \phi}{\partial s}\right) + \frac{\partial \phi}{\partial s}\frac{\partial}{\partial s}\left(\frac{\partial \phi}{\partial n}\right). \tag{A.32}$$

Therefore, the moving body boundary condition for the ϕ_t BVP is

$$\begin{aligned}\frac{\partial \phi_t}{\partial n} = &\sum_{j=1}^{3} a_j n_j + n_1 \left[\xi_3^2 x' - 2\xi_3 \left(w - \dot{\xi}_2\right)\right] + n_2 \left[\xi_3^2 z' + 2\xi_3 \left(u - \dot{\xi}_1\right)\right] \\ &+ \frac{\partial \phi}{\partial n}\left(-\frac{\partial^2 \phi}{\partial s}\right) + \frac{\partial \phi}{\partial s}\frac{\partial}{\partial s}\left(\frac{\partial \phi}{\partial n}\right).\end{aligned} \tag{A.33}$$

Appendix D. Free damped oscillation

A free damped oscillation is often referred to as an impulse response function, where the moving body is given an initial displacement, ξ_0, or an initial velocity, v_0, in a single degree of freedom. The subsequent body response, ξ, is expressed as

$$\xi = \left(C_1 \cos \sigma_d t + C_2 \sin \sigma_d t\right) e^{-\delta t}, \tag{A.34}$$

where $C_1 = \xi_0$ and $C_2 = \frac{v_0 + \xi_0 \delta}{\sigma_d}$, $\sigma_d = \frac{2\pi}{T_d}$ is the damped frequency in terms of the damped period, T_d, and δ is a damping coefficient. The damping, δ, is calculated as

$$\delta = \frac{1}{2\pi} ln \left(\frac{\xi_n}{\xi_{n+1}}\right), \tag{A.35}$$

where ξ_n and ξ_{n+1} are consecutive crests or consecutive troughs in the time history of the body's response. The natural frequency, σ_n, is then expressed as

$$\sigma_n = \frac{\sigma_d}{\left(1 - \delta^2\right)}. \tag{A.36}$$

Further, the effective mass m_e (the sum of the physical mass, m, and the added mass, m_a,) is

$$m_e = \frac{k_s}{\sigma_n^2}, \tag{A.37}$$

where k_s is the spring constant in heave. The hydrodynamic damping coefficient, c_s, is given as

$$c_s = 2 m_e \sigma_n \frac{\delta}{2\pi}, \tag{A.38}$$

and a further damping coefficient, ζ, may be expressed as

$$\zeta = \frac{c_s}{2 \sigma_n m_e}. \tag{A.39}$$

The coefficients m_e, c_s and k_s are used within the equation of motion

$$F = m_e \ddot{\xi} + c_s \dot{\xi} + k_s \xi. \tag{A.40}$$

However, for harmonic loading, the above equation may be simplified through the use of the dynamic amplification factor, D_n,

$$D_n = \frac{1}{\left\{\left[1 - \left(\sigma/\sigma_n\right)^2\right]^2 + \left[2\zeta\sigma/\sigma_n\right]^2\right\}^{1/2}}, \tag{A.41}$$

where σ is the forcing frequency of the loading. The expression of D_n shows that it is a function of frequency and its value is dependent on the damping within the dynamic system, ζ, and how close σ/σ_n is to 1; being largest when the latter ratio is equal to 1. Consequently, D_n is used to equate the amplitude of the body's response to the amplitude of the harmonic loading, F, as

$$\xi = D_n F; \tag{A.42}$$

thus summarising the hydrodynamic properties of the moving body.
If the time-history of the loading, $F_j(t)$, in a single degree of freedom (j) is known instead of its amplitude, the response of the body may be obtained from the Linear Piecewise Method. In this method, the initial displacement of the body is assumed to be zero

$$\xi_j(1) = 0. \tag{A.43}$$

The body displacement after the first time step, Δt, is given as

$$\xi_j(2) = CF(1)/m + DF(2)/m, \tag{A.44}$$

and all subsequent displacement at the time steps (it) is

$$\begin{aligned}\xi_j(it) = {} & AF(it-2)/m + (C-B)F(it-1)/m + DF(it)/m \\ & + 2e^{-\zeta\sigma_n\Delta t}\cos(\sigma_d\Delta t)\xi(it-1) - e^{-2\zeta\sigma_n\Delta t}\xi(it-2),\end{aligned} \tag{A.45}$$

where

$$A = \frac{1}{\sigma_n^2}e^{-\zeta\sigma_n\Delta t}\left\{\frac{1+2\zeta}{\sigma_n\Delta t}e^{-\zeta\sigma_n\Delta t} - \frac{2\zeta}{\sigma_n\Delta t}\cos(\sigma_d\Delta t) + \frac{1-2\zeta^2}{\sigma_d\Delta t}\sin\sigma_d\Delta t\right\}, \tag{A.46}$$

$$B = A + \frac{1}{\sigma_n^2}e^{-\zeta\sigma_n\Delta t}\left\{\cos(\sigma_d\Delta t) - \frac{\zeta}{\sqrt{1-\zeta^2}}\sin(\sigma_d\Delta t) - e^{-\zeta\sigma_n\Delta t}\right\}, \tag{A.47}$$

$$C = \frac{2\zeta}{\sigma_n^3\Delta t} - \frac{1}{\sigma_n^2}e^{-\zeta\sigma_n\Delta t}\left\{\frac{1+2\zeta}{\sigma_n\Delta t}\cos(\sigma_d\Delta t) - \left(\frac{1-2\zeta^2}{\sigma_d\Delta t} + \frac{\zeta}{\sqrt{1-\zeta^2}}\right)\sin\sigma_d\Delta t\right\}, \tag{A.48}$$

and

$$D = -C + \frac{1}{\sigma_n^2}\left\{1 - e^{-\zeta\sigma_n\Delta t}\left(\cos(\sigma_d\Delta t) - \frac{\zeta}{\sqrt{1-\zeta^2}}\sin(\sigma_d\Delta t)\right)\right\}. \tag{A.49}$$

Bibliography

Airy, G. B. (1845), *Wave and tides*, Encyclopedia Metropolitana.

Archibald (2011), Modelling of extreme ocean waves using high performance computing, PhD thesis, Imperial College London.

Archibald, S. (2008), Numerical investigation of wave and wave-structure interaction, Technical report, Imperial College London.

Au, M. & Brebbia, C. (1983), 'Diffraction of water waves for vertical cylinders using boundary elements', *Applied Mathematical Modelling* **7**, 106–114.

Bai, W. & Eatock-Taylor, R. (2006), 'Higher-order boundary element simulation of fully nonlinear wave radiation by oscillating vertical cylinders', *Applied Ocean Research* **28**(4), 247 – 265.

Becker, A. A. (1992), *The Boundary Element Method in Engineering: A Complete Course*, McGraw-Hill.

Black, J. L., Mei, C. C. & Bray, M. C. G. (1971), 'Radiation and scattering of water waves by rigid bodies', *Journal of Fluid Mechanics* **46**, 151–164.

Brebbia, C. A. & Dominguez, J. (1992), *Boundary Elements: An Introductory Course, 2nd edn.*, Computational Mechanics Publications (McGraw-Hill).

Briggs, M. J., Thompson, E. F. & Vincent, C. L. (1995), 'Wave diffraction around breakwater', *Journal of waterway, port, coastal, and ocean engineering* **121**, 23–34.

Christou, M. (2009), Fully Nonlinear Computations of Waves and Wave-structure Interaction, PhD thesis, Imperial College London.

Christou, M., Hague, C. & Swan, C. (2009), 'The reflection of nonlinear irregular surface water waves', *Engineering Analysis with Boundary Elements* **33**(5), 644 – 653.

Christou, M., Swan, C. & Gudmestad, O. (2008), 'The interaction of surface water waves with submerged breakwaters', *Coastal Engineering* **55**(12), 945 – 958.

Clement, A. (1996), 'Coupling of two absorbing boundary conditions for 2d time-domain simulations of free surface gravity waves.', *Journal of Computational Physics* **126**, 139151.

Cointe, R., Geyer, P., King, B., Molin, B. & Tramoni, M. (1990), 'Nonlinear and linear motions of a rectangular barge in a perfect fluid', *Proceedings of the 18th Symposium on Naval Hydrodynamics* pp. 85–99.

Cruz, J. (2008), *Ocean Wave Energy: Current Status and Future Perspectives (Green Energy and Technology)*, Springer.

Dean, R. & Dalrymple, R. (1991), *Water Wave Mechanics for Engineers and Scientists*, World Scientific, Singapore.

DHI (2009), Shallow water model tests, safe offload report, safe-d4-3-dhi-04(1), Technical report.

Faber, F., Bliault, A., Resweber, L. & Jones, P. (2002), Floating LNG solutions from the drawing board to reality, *in* 'Offshore Technology Conference, Texas'.

Falnes, J. (2005), *Ocean Waves and Oscillating Systems*, Cambridge University Press.

Faltinsen, O. M., Rognebakke, O. F. & Timokha, A. N. (2007), 'Two-dimensional resonant piston-like sloshing in a moonpool', *Journal of Fluid Mechanics* **575**(-1), 359–397.

Fenton, J. D. (1985), 'A fifth-order stokes theory for steady waves', *Journal of Waterway, Port, Coastal, and Ocean Engineering* **111**, 216–234.

Grilli, S. & Svendsen, I. (1990), 'Corner problems and global accuracy in the boundary element solution of nonlinear wave flows', *Engineering Analysis with Boundary Elements* **7**(4), 178 – 195.

Grilli, S. T., Skourup, J. & Svendsen, I. A. (1989), 'An efficient boundary element method for nonlinear water waves', *Engineering Analysis with Boundary Elements* **6**(2), 97 – 107.

Ha, M. K., Kim, Mun S.and Park, J. J. & Lee, J. H. (2004), First- and second-order hydrodynamic forces and moments on two offshore floating structures in waves, *in* 'Proceedings of the Fourteenth International Offshore and Polar Engineering Conference, ISOPE', pp. 711–718.

Hague, C. H. (2006), Fully nonlinear computations of directional waves, including wave breaking, PhD thesis, Imperial College London.

Hague, C. & Swan, C. (2009), 'A multiple flux boundary element method applied to the description of surface water waves', *Journal of Computational Physics* **228**, 51115128.

Hong, S., Kim, J., Cho, S., Choi, Y. & Kim, Y. (2005), 'Numerical and experimental study on hydrodynamic interaction of side-by-side moored multiple vessels.', *Ocean Engineering* **32**, 783–801.

Isaacson, M. (1978), 'Vertical cylinder of arbitrary section in waves', *Journal of Waterway, Port, Coastal and Ocean Division, ASCE* **104**, 309.

Isaacson, M. D. S. Q. (1982), 'Nonlinear-wave effects on fixed and floating bodies', *Journal of Fluid Mechanics* **120**, 267–281.

Johansson, M. (1989), Barrier-type Breakwaters: Transmission, Reflection and Forces, PhD thesis, Chalmers University of Technology, Goteborg.

Kanoria, M., Dolai, D. P. & Mandal, B. N. (1999), 'Water-wave scattering by thick vertical barriers', *Journal of Engineering Mathematics* **35**, 361–384.

Kashiwagi, M. (2000), 'Nonlinear simulations of wave-induced motions of a floating body by means of the mixed eulerian-lagrangian method', *Journal of Mechanical Engineering Science, Proc. of the Institution of Mechanical Engineers Part C* **214**, 841–855.

Kashiwagi, M. (2007), 3D calculation of multiple floating bodies in proximity using wave interaction theory., *in* 'Proceedings of the 17th International Conference on Offshore and Polar Engineering, ISOPE'.

Kodan, N. (1984), The motions of adjacent floating structures in oblique waves new orleans, *in* 'Proceedings of the Third Offshore Mechanics and Arctic Engineering Conference, OMAE', pp. 206–213.

Koo, B. & Kim, M. (2005), 'Hydrodynamic interactions and relative motions of two floating platforms with mooring lines in side-by-side offloading operation', *Applied Ocean Research* **27**(6), 292 – 310.

Koo, W. (2003), Fully Nonlinear Wave-Body Interactions by a 2D Potential Numerical Wave Tank, PhD thesis, Texas A&M University.

Kristiansen, T. & Faltinsen, O. M. (2007), Resonant water motion between a ship and a terminal in shallow water, *in* 'Proceedings of the 26th International Conference on Offshore Mechanics and Arctic Engineering, OMAE'.

Landweber, L. (1961), *Motion of immersed and floating bodies. In Handbook of Fluid Dynamics.*, McGraw-Hill.

Lee, J.-F. (1995), 'On the heave radiation of a rectangular structure', *Ocean Engineering* **22**(1), 19 – 34.

Leenknecht, D., Szuwalski, A. & Sherlock, A. (1992), *Automated Coastal Engineering System; Users Guide Version 1.07.*

Lewis, R. (1991), *Vortex Element Methods for Fluid Dynamic Analysis of Engineering Systems*, Cambridge University Press.

Lighthill, J. (1979), Waves and hydrodynamic loading, *in* 'Proceedings of 2nd International Conference on the BehBehaviour of Offshore Structures'.

Lin, C.-Y. & Huang, C.-J. (2004), 'Decomposition of incident and reflected higher harmonic waves using four wave gauges', *Coastal Engineering* **51**(5-6), 395 – 406.

Longuet-Higgins, M. S. & Cokelet, E. D. (1976), 'The deformation of steep surface waves on water. i. a numerical method of computation', *Proceedings of the Royal Society of London. A. Mathematical and Physical Sciences* **350**(1660), 1–26.

MacCamy, R. & Fuchs, R. A. (1954), Wave forces on piles: a diffraction theory, Technical report, U.S. Army Corps of Engineers, Beach Erosion Board.

Masterton, S. (2007), Forces on structures, PhD thesis, Imperial College London.

McCormick, M. & Kraemer, D. (2002), 'Polynomial approximation for fresnel integrals in diffraction analysis', *Coastal Engineering* **44**, 261–266.

Mei, C. C. (1994), *The applied dynamics of ocean surface waves*, World Scientific, Singapore.

Mei, C. C. & Black, J. L. (1969), 'Scattering of surface waves by rectangular obstacles in waters of finite depth', *Journal of Fluid Mechanics* **38 (3)**, 499–511.

Miles, J. W. (1967), 'Surface-wave scattering matrix for a shelf', *Journal of Fluid Mechanics Digital Archive* **28**, 755–767.

Molin, B. (2001), 'On the piston and sloshing modes in moonpools', *Journal of Fluid Mechanics* **430**(-1), 27–50.

Newell, M. (2003), Safe transfer of LNG between a floating production or storage barge to a transportation vessel at an exposed offshore location, *in* 'AIChE Spring National Meeting, New Orleans'.

Noble Denton (2007), Study of alternative FLNG hull forms, Safe Offload Report, SAFE-P1-3-NDE-01(1), Technical report.

Pauw, W., Huijsmans, R. & Voogt, A. (2007), Advances in the hydrodynamics of side-by-side moored vessels., *in* 'Proceedings of the 26th International Conference on Offshore Mechanics and Arctic Engineering, OMAE'.

Penney, W. & Price, A. T. (1952), 'The diffraction theory of sea waves and the shelter afforded by breakwaters, Part I', *Trans. Royal Society London* pp. 236–253.

Pytel, A. & Kiusalaas, J. (2001), *Engineering Mechanics: Dynamics*, second edn, Thomas Learning.

Schäffer, H. A. (1996), 'Second-order wavemaker theory for irregular waves', *Ocean Engineering* **23**(1), 47 – 88.

Sen, D. (1993), 'Numerical simulation of motions of two-dimensional floating bodies', *Journal of Ship Research* **37, 4**, 307–330.

Sheikh, R. & Swan, C. (2005), 'The interaction between steep waves and a vertical, surface-piercing column.', *Journal of Offshore Mechanics and Arctic Engineering* **127(1)**, 31–38.

Sommerfeld, A. (1949), *Partial Differential Equation in Physics*, New York: Academic Press.

Spinneken, J. & Swan, C. (2009), 'Second-order wave maker theory using force-feedback control. Part I: A new theory for regular wave generation', *Ocean Engineering* **36**(8), 539 – 548.

Stock, M. J. & Gharakhani, A. (2010), A GPU-accelerated boundary element method and vortex particle method, *in* '40th Fluid Dynamics Conference and Exhibit'.

Stokes, G. G. (1847), 'On the theory of oscillatory waves', *Transcripts of the Cambridge Philosophical Society* **8**, 441455.

Strickland, J., Porter, V., Homicz, G. & Gossler, A. (2002), 'A vortex code for flow over rigid or flexible bluff bodies', *Journal of Turbulence* **3**, N42.

Sulisz, W. (1993), 'Diffraction of second-order surface waves by semi-submerged horizontal rectangular cylinder', *Journal of Waterway, Port, Coastal and Ocean Engineering* **119**, 160–171.

Sun, L., Eatock Taylor, R. & Taylor, P. (2011), 'Wave driven free surface motion in the gap between a tanker and an FLNG barge', *submitted to Applied Ocean Research Special Edition* .

Tanizawa, K. (1995), 'A nonlinear simulation method of 3D body motions in waves', *Journal of the Society of Naval Architects of Japan* **178**, 179–191.

Vinje, T. & Brevig, P. (1981), 'Nonlinear ship motions.', *Proceedings of the Third International Conference on Numerical Ship Hydrodynamics, Paris, France.* pp. 257–268.

Wiegel, R. L. (1962), 'Diffraction of waves by a semi-infinite breakwater', *Journal of the Hydraulics Division American Society of Cviil Engineers* **88(I)**, 27–44.

Wu, G. & Eatock-Taylor, R. (1996), 'Transient motion of a floating body in steep waves.', *Proceedings of the 11th International Workshop on Water Waves and Floating Bodies.* pp. 219–223.